2016

Modeling heat and mass transfer in reacting gas-solid flow using particle-resolved direct numerical simulation

Bo Sun
Iowa State University

Modeling heat and mass transfer

in reacting gas–solid flow using particle-resolved direct numerical simulation

by

Bo Sun

A dissertation submitted to the graduate faculty

in partial fulfillment of the requirements for the degree of

DOCTOR OF PHILOSOPHY

Major: Mechanical Engineering

Program of Study Committee:

Shankar Subramaniam, Major Professor

Rodney O. Fox

Theodore Heindel

Mark Mba Wright

Alberto Passalacqua

Iowa State University

Ames, Iowa

2016

DEDICATION

I would like to dedicate this thesis to my mom Jingmei Huang and to my father Jinsheng Sun without whose support I would not have been able to complete this work. I would also like to thank my friends and family for their loving guidance during the writing of this work.

TABLE OF CONTENTS

LIST OF TABLES

LIST OF FIGURES

ACKNOWLEDGEMENTS

I would like to take this opportunity to express my thanks to those who helped me with various aspects of conducting research and the writing of this thesis. First and foremost, Dr. Shankar Subramaniam for his guidance, patience and support throughout this research and the writing of this thesis. His insights and words of encouragement have often inspired me and renewed my hopes for completing my graduate education. I would also like to thank my committee members for their efforts and contributions to this work. I thank Dr. Baskar Ganapathysubramanian, Dr. Michael G. Olsen, and Dr. Zhijian Wang (currently in Univeristy of Kansas) for great suggesions for my research. I sincerely thank Dr. Donald L. Koch in Cornell University for providing brilliant ideas and discussions. I would additionally like to appreciate Dr. Sudheer Tenneti for his guidance throughout the initial stages of my graduate career. My special thanks to my group mates (Dr. Sergiy Markutsya, Dr. Vidyapati, Dr. Ravi Kolakaluri, Dr. Mohammad Mehrabadi, Eric Murphy, Christopher Schmitz, Karthikeyan Devendran) and my ISU colleagues (Dr. Meng Li, Dr. Long Chen, Dr. Shang Xu, Dr. Kaige Wang, Dr. Varun Vikas, Dr. Hari Krishna Kodali, Mahdi Ramezani, Fenglei Qi, Songzhe Xu, Anthony Fontanini, Spencer Pfeifer, Yiran Xu) for great discussions and help.

I would also like to acknowledge the supports from the following grants and organizations: Department of Energy grant (DE-AC02-07CH11358), National Science Foundation (award CBET 1034307 and CBET 1336941), the University of Illinois at Urbana-Champaign and its National Center for Supercomputing Applications (Great Lakes Consortium), the Extreme Science and Engineering Discovery Environment (XSEDE) (supported by National Science Foundation grant number ACI-1053575).

ABSTRACT

Reacting gas–solid flows occur in nature and many industrial applications. Emerging carbon-neutral and sustainable energy generation technologies such as CO_2 capture and biofuel production from fast pyrolysis of biomass are examples of reacting gas–solid flows in industry. Fundamental scientific understanding of reacting gas–solid flows is needed to overcome technological barriers for the successful development of these technologies. Multiphase computational fluid dynamics (CFD) simulations are increasingly being used for scale-up of reactors from laboratory to pilot to full-scale plants, and also for evaluation of different design options. Device-scale CFD simulations of reacting gas-solid flow are based on statistical descriptions that require closure models for interphase exchange of momentum, heat, and species. The predictive capability of multiphase CFD simulations depends on the accuracy of the models for the interphase exchange terms. Therefore, multiphase CFD simulations require accurate physics-based multiphase flow models of heat and mass transfer as well as chemical reaction rates. Particle-resolved direct numerical simulation (PR-DNS) is a first-principles approach to provided transformative insights into multiphase flow physics for model development. PR-DNS of reacting gas–solid flows can provide accurate quantifications of gas–solid interactions.

The primary objective of this work is to develop improved closure models for CFD simulations in reacting gas–solid flows using the PR-DNS approach. A computational tool called particle-resolved uncontaminated-fluid reconcilable immersed boundary method (PUReIBM) has been developed as a part of this work to perform PR-DNS of heat and mass transfer in reacting gas-solid flows. A pseudo-spectral (PS) version of the PUReIBM simulation of flow past a fixed homogeneous particle assembly and freely evolving suspension of particles with heat transfer has provided PR-DNS data that are used to develop closure models in the Eulerian-Eulerian two-fluid average fluid temperature equation and probability density function transport equation, and validate the assumptions in multiphase flow statistical theories.

A fully finite-difference (FFD) version of PUReIBM is also developed to account for wall-bounded flow. The FFD PR-DNS is validated by a suite of test cases and used to perform a detailed comparison with experimental data by using the same setup. In order to extend unclosed models to account for wall effect, wall effect on drag and heat transfer of particle assemblies are studied using FFD PR-DNS. In order to validate the assumption of the isothermal particle in the case of flow past a fixed bed of particles, a preliminary study of the transient heat transfer from a single particle is performed by FFD PR-DNS. A better understanding of the role of heat and mass transfer in reacting gas–solid flow is gained by using FFD PR-DNS to simulate mass transfer in flow past a sphere with a first-order chemical reaction on the particle surface for low and high Reynolds number. These capabilities of the PR-DNS approach provide insight into flow physics and have provided data that has been used to develop improved heat transfer models for gas-solid flow.

CHAPTER 1. OVERVIEW

1.1 Background

A gas–solid flow represents the flow of gas through solid particles, which is commonly encountered in nature as well as in industrial processes. In nature, a snowstorm in the winter impacts the economy and society by damaging agriculture and impeding transportation (Gordon and Taylor (2009)). In industrial applications, carbon-neutral technologies such as chemical looping combustion (Shen et al. (2008)) and CO_2 capture (Abanades et al. (2004); Yi et al. (2007)) that use carbonate sorbent particles to absorb CO_2 offer the promise of carbon-neutral energy generation to reduce greenhouse gas emissions. Another example of the use of gas–solid flow is in sustainable energy generation technologies from renewable sources such as biomass pyrolysis that are a promising way to reduce the nation's dependence on fossil fuels.

In sustainable energy generation technologies such as biofuel production from biomass particles, heat and mass transfer between gas and solid phases as well as chemical reaction kinetics are important phenomena. For instance, pyrolysis of biomass is one of the ways to extract bioenergy from biomass particles, resulting in the production of bio-oil over a range of operating temperature. Pyrolysis is a thermochemical conversion technology that involves heating the organic material in biomass in the absence of oxygen (nitrogen is the gas phase). The product yields from the pyrolysis processes depend on the operating temperature in the biomass reactor (Brown (2011)). Fast pyrolyzers are designed to maximize the production of bio-oil in a product stream that typically comprises 50-70% bio-oil, 10-30% biochar, and 15-20% syngas by mass. This is accomplished by high heating rates at operating temperature around $500°C$. Other processes such as slow pyrolysis of biomass produce mainly charcoal at the operating temperature around $500°C$ with lower heating rates (approximately 35% biochar, 30% bio-oil,

and 35% syngas by mass), whereas gasification of biomass is designed to maximize production of syngas and produce very little char or bio-oil at the operating temperature $750^{\circ}C - 1000^{\circ}C$ (Bridgwater et al. (1999); Wright et al. (2008); Laird et al. (2009)). Among the pyrolysis processes, biomass fast pyrolysis is one of the most promising technologies to produce bio-fuel (Brown (2011)) since bio-oil is finally upgraded into biofuel.

In order to maximize biofuel production, the design of reactors for biomass fast pyrolysis requires high heat transfer rates (generating the heat required for the fast pyrolysis process) and controlled reaction temperature (operating temperature). For a fixed-geometry reactor, three parameters are typically used to control the process of fast biomass pyrolysis: (i) inlet temperature of nitrogen gas, (ii) flow rate of nitrogen gas, and (iii) feed rate of biomass. It is worth noting that these three parameters are related to three non-dimensional parameters. The flow rate and inlet temperature of nitrogen gas can be related to the Reynolds number and Nusselt number. Once the solid phase and the gas phase are mixed, the feed rate of biomass can be related to the solid volume fraction. If the flow rate of nitrogen gas is fixed, considering the gas–solid system as a heat exchanger in which nitrogen gas transfers heat to biomass (the temperature of nitrogen gas is higher than the biomass particle temperature initially), the relation between flow rate of nitrogen gas and biomass particles is determined by

$$\dot{m}_b Q = \dot{m}_g c_{pg} \left(T_{g,in} - T_{g,out} \right), \tag{1.1}$$

where $\dot{m}_b$ is the flow rate of biomass particles, $\dot{m}_g$ is the flow rate of nitrogen gas, c_{pg} (J/kg-K) is the specific heat capacity of nitrogen gas, Q (J/kg) is the heat required for fast pyrolysis of biomass, $T_{g,in}$ (K) and $T_{g,out}$ (K) are the inlet and exit temperatures of nitrogen gas, respectively. Given the flow rate of biomass particles, and measurement of the inlet and outlet temperature of nitrogen gas in this gas–solid system, the heat energy Q for maintaining controlled reaction temperature can be determined. The heat energy Q normally includes the heat energy required to take the biomass particles to the reaction temperature and the energy required to initiate and complete the pyrolysis reactions.

However, this energy balance analysis gives only a global estimate for the design of the system due to absence of information regarding the temperature distribution and the local

temperature gradient representing high heat transfer rates inside this system. In biomass fast pyrolysis, the temperature distribution and the local temperature gradient through the reactor are strongly influenced by hydrodynamic fields in this reacting gas–solid flow. This complex coupling between momentum, heat and mass transfer processes can be seen in Fig. 1.1. Due to biomass particle motions, there exist locally intense velocity fluctuations in the gas phase (Mehrabadi et al. (2015)). These gas–phase velocity fluctuations contribute significantly to local mixing of the temperature and species fields. This mixing results in the variation of temperature or species gradients. Therefore, local mixing can influence the product yield since chemical reaction in both gas and solid phases are Arrhenius type with strong nonlinear dependence on temperature.

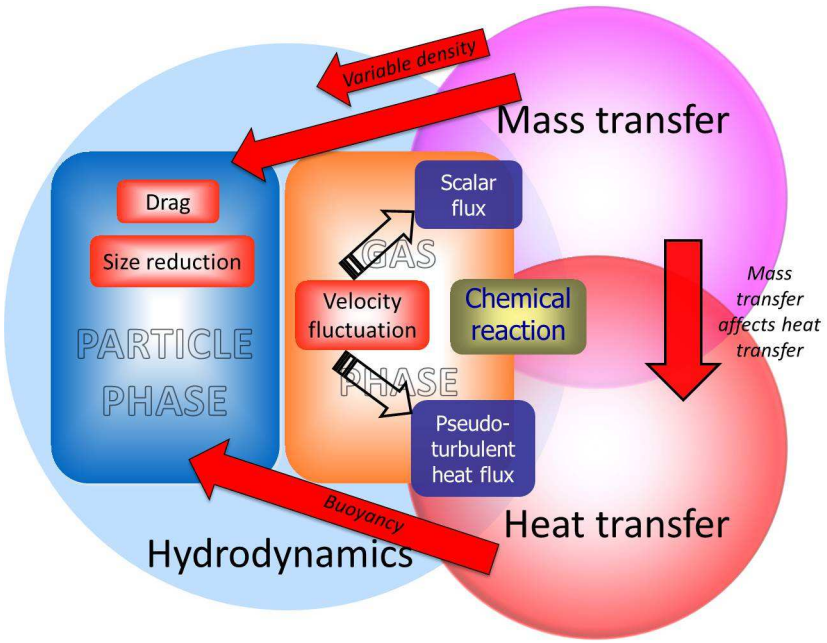

Figure 1.1: A example of coupling between momentum, heat and mass transfer in reacting gas-solid flow encountered in biomass pyrolysis.

The intensity of local mixing also determines how fast the biomass particles can be heated up to the desired reaction temperature in which the biomass particles mostly convert into the expected product yields. Once biomass particle temperature reaches the desired reaction temperature, chemical reactions start to convert the biomass particles into different products. Since the reaction rates representing chemical reaction in biomass fast pyrolysis are of the

Arrhenius form, they are highly temperature-dependent. For instance, in the process of tar vapor reaction into gas, reaction rate constants that related to reaction rates vary from $10^{-12}s^{-1}$ at temperature 300K to $10^{-1}s^{-1}$ at temperature 800K. Since the chemical reaction source term is a function of the reaction rate constants, this huge variation in reaction constants requires knowledge of the temperature distribution. In addition, since the mass transfer between biomass particles (solid phase) and gas is accompanied by heat release (or absorption) during chemical reactions, gas-solid heat transfer is affected by mass transfer (see Fig. 1.1). This effect of mass transfer on heat transfer is difficult to analyze in a global energy balance. ***Therefore, accurate representation of the detailed information on the reaction rate in both fluid and solid phases as well as the coupling between heat and mass transfer is needed.***

In spite of the lack of detailed information on heat and mass transfer, many efforts to design and optimize the gas–solid reactors have been made using theoretical and experimental studies for gas–solid flow (as discussed in Section 1.2). However, because theoretical studies are restricted to simple problems, and experimental studies are expensive and cannot provide complete quantitative information inside the reactors, accurate prediction of gas–solid flow still remains a challenge for industrial applications. In order to overcome these difficulties, multiphase computational fluid dynamics (CFD) is a cost-effective tool that is increasingly being used in the design of technological applications as shown in Fig. 1.2. CFD models for simulating biomass fast pyrolysis have been developed using commercial (Papadikis et al. (2009a); Boateng and Mtui (2012)) as well open-source software (Xue et al. (2011, 2012)). Although the CFD model predictions for a laboratory-scale reactor are in reasonable agreement with experimental measurements of product yields for cellulose and red-oak pyrolysis at the reactor outlet for selected operating conditions, there is considerable scope for improvement of the CFD model for design and scale-up of industrial-scale reactors.

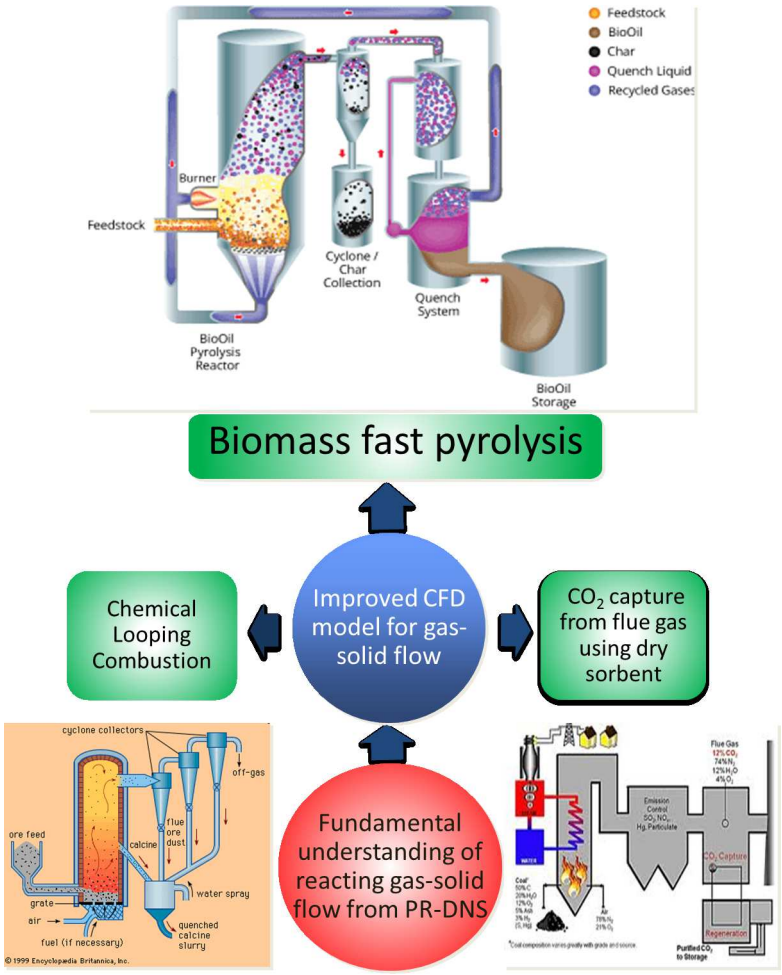

Figure 1.2: Impact of improved understanding of reacting gas–solid flow. Multiphase CFD simulations are increasingly being used to improve design of industrial applications such as chemical looping combustion, biomass fast pyrolysis, and CO_2 capture. The fundamental understanding of reacting gas-solid flow using particle-resolved direct numerical simulation (PR-DNS) will improve closure models for multiphase CFD simulations.

Device-scale CFD simulations can be performed using the Eulerian-Eulerian (EE) two-fluid (TF) approach (Anderson and Jackson (1967); Drew (1983)) in which averaged equations for conservation of mass, momentum, energy and species are written for each phase, with coupling terms representing the interphase interactions, or the transported probability density function (PDF) approach (Zhu et al. (2000); Minier and Peirano (2001); Pai and Subramaniam (2009); Subramaniam (2013)) in which transport equations for the PDF of a set of variables

represent the hydrodynamic and/or thermo-chemical state of each phase. These equations contain unclosed terms that need to be modeled, and the predictive capability of multiphase CFD simulations depends on the models for interphase exchange of species, momentum, and heat. While numerical accuracy is also very important in multiphase CFD simulations (Pai and Subramaniam (2006); Garg et al. (2009)), it is fair to say that even numerically accurate simulations cannot be predictive without the correct physical sub-models. Therefore, multiphase CFD simulations require accurate physics-based multiphase flow models of heat and mass transfer as well as the chemical reaction source term.

One of the critical hurdles in the development of heat and mass transfer models for multiphase flow is the absence of temperature and species measurements inside the particle-laden flow for model validation. Detailed experimental measurements alone cannot improve multiphase flow models. To provide insight into the microscale physico-chemical interactions and develop improved models for CFD simulation of biomass fast pyrolysis, particle-resolved direct numerical simulation (PR-DNS) of time–dependent three–dimensional velocity, temperature, and species fields is developed in this thesis. PR-DNS is a first-principles high-fidelity simulation method that has already provided transformative insights into multiphase flow physics for model development (Tenneti and Subramaniam (2014)). It is used as a promising tool to provide fully characterized microscale data on reaction rates in both gas and particle phases as well as on the coupled gas–solid heat and mass transfer for development of multiphase CFD models for reacting gas–solid flow.

1.2 Existing work

The key modeling requirements that emerge from multiphase CFD study are the need for physics-based closures. The unclosed terms appearing in CFD simulations are divided into: (1) interphase exchange (e.g., drag, Nusselt number), (2) spatial flux (e.g., covariance of gas-phase velocity fluctuations), (3) diffusion (e.g., average heat conduction), (4) source terms (e.g., chemical reaction sources in species mass fraction), and (5) source terms due to interphase mass transfer (see Eq. J.12 in Appendix J). A summary of these terms is provided in Table 1.1.

In the EE TF approach, standard models are available for many of these terms (Benyahia et al.

(2012)) but some terms (such as transport of temperature-velocity covariance) are often neglected in CFD simulations. Recent PR-DNS studies by several researchers (Hill et al. (2001a,b); Beetstra et al. (2007b); Yin and Sundaresan (2009); Tenneti et al. (2010, 2011)) have yielded computational drag laws that have improved existing models. The PR-DNS approach that is used in this thesis has also recently been used to develop models for drag (Tenneti et al. (2011)), pseudo-turbulent kinetic energy (Mehrabadi et al. (2015)), and the source of granular temperature (Tenneti (2013)) in the hydrodynamic problem of gas–solid flow (see Table 1.1). These models shown in the green boxes in Table 1.1 can be easily incorporated into multi-fluid CFD codes.

In this thesis, closure models for heat and mass transfer in reacting gas–solid flow are developed for the EE TF approach using the PR-DNS approach. CFD of heat and mass transfer in reacting gas–solid flow that solve for the average scalar (temperature and species) transport equation requires models for (1) average interphase scalar (heat and mass) flux, (2) transport of the scalar-velocity covariance, (3) conduction in the gas phase, (4) chemical reaction source term in both gas phase and interphase, and (5) source terms due to nonzero interphase mass transfer such as blowing effect from particle surface (see Table 1.1). In the existing standard model for heat (mass) transfer, the average interphase heat (mass) flux is calculated from a Nusselt (Sherwood) number correlation that quantifies the dependence on solid volume fraction ε_s and the Reynolds number based on mean slip velocity. The heat and mass transfer correlations (Kunii and Smith (1961); Littman et al. (1968); Cybulski et al. (1975); Gunn (1978)) that are currently used in state-of-the-art multiphase CFD simulations (Syamlal et al. (1993)) were developed to fit experimental data that were obtained in the late 1970s (Cybulski et al. (1975); Gunn and Desouza (1974); Wakao et al. (1977); Wakao and Kaguei (1982)). The second unclosed term–the transport of the scalar-velocity covariance–is often neglected. This term can be relevant to pseudo-turbulent or turbulent scalar diffusivity that is analogous to that in single-phase turbulence. In gas-solid heat transfer from fixed bed of particles, the ratio of pseudo-turbulent or turbulent thermal diffusivity to the molecular diffusivity is found to have a Pe^n dependence (Koch and Brady (1985); Kuwahara et al. (1996); Pedras and de Lemos (2008); Jeong and Choi (2011); Özgümüş et al. (2013)), where Pe is the Péclet number, and n

is an exponent that depends on the dominant mechanism of thermal dispersion. Average heat conduction (or species diffusion) in the gas phase is normally modeled in term of average temperature (or species mass fraction) gradient (Benyahia et al. (2012)). In addition, the average chemical reaction source term is related to the reaction rate constant that in the simplest model would be evaluated at the average temperature. The source term resulting from the nonzero interphase mass transfer may be considered in an improved Sherwood number correlation. This term (5) are outside the scope of this thesis.

In the transported PDF approach to gas-solid flow without zero interphase mass transfer, a composition PDF transport equation for two-phase flow requires closure models for (1) the interphase scalar (heat and mass) flux conditional on composition, (2) velocity fluctuation conditional on composition (the scalar-velocity covariance can be obtained by the integral of this term), (3) mixing in the gas phase conditional on composition (diffusion term). The existing models for these unclosed terms are extensions of the closure models for single-phase flow (Pope (2000); Fox (2003); Haworth (2010)). The mixing terms and velocity fluctuation conditional on composition for two-phase flow are normally modeled by the interaction by exchange with the mean (IEM) models (Fox (2003)) and a gradient-diffusion model that introduces a turbulent diffusion term (Marchisio et al. (2001); Carrara and DesJardin (2006, 2008)), respectively. Vegendla et al. (2009) modeled interphase heat/mass transfer term in the two-point composition PDF transport equation for gas-solid flow in terms of heat/mass transfer coefficient and temperature/concentration difference between solid and gas phases. Although single-phase closure models (Vegendla et al. (2009)) have been extended to model the unclosed terms of the composition PDF transport equation in gas-solid flow and provided the reasonable results, the extension of single-phase closure models needs to be validated. Therefore, in EE TF and transported PDF approaches, the challenge is to develop accurate models for these unclosed terms in the equations based on the microscale physicochemistry.

In order to address the critical challenge in developing models for heat and mass transfer in reacting gas–solid flow, theoretical analysis and experimental measurements have been attempted. However, it is difficult to develop models that are valid over a wide range of solid volume fraction and mean slip Reynolds number based on theoretical and experimental meth-

ods for gas–solid heat and mass transfer. In this section, the existing theoretical, experimental, and numerical studies on heat and mass transfer in gas–solid flow are summarized.

Table 1.1: Models for unclosed terms have already been available (green) and need to be improved or proposed (orange) from PR-DNS of reacting gas–solid flow. Models for unclosed terms are not discussed in this thesis (gray).

	Momentum		Heat	Mass
	Gas Phase	Particle Phase		
Spatial flux	Velocity covariance		Temperature-velocity covariance	Velocity-species covariance
Source term Without mass transfer	Buoyancy	Granular temperature	Heat of reaction	Average reaction rate
Interphase exchange	Drag	Drag	Gas-solid heat flux	Gas-solid mass flux
Diffusion term			Axial conduction model	Axial diffusion
Source term due to interphase mass transfer	Mass transfer	Mass transfer	Mass transfer	Mass transfer

1.2.1 Theoretical solutions

In order to obtain analytical solutions for gas-solid flow, theoretical studies of heat and mass transfer in gas–solid flow are limited to creeping flow past an isolated sphere, ordered spheres, or flow past random assemblies of spheres. Analytical solutions for heat transfer (Acrivos and Taylor (1962); Taylor (1963a)) and mass transfer (Taylor (1963b); Hartunian and Liu (1963); Gupalo and Ryazantsev (1972)) on an isolated sphere were obtained used matched asymptotic expansions for Stokes flow and low Reynold number ($\mathrm{Re} \ll 1$). In the solutions for mass transfer (Taylor (1963b); Hartunian and Liu (1963); Gupalo and Ryazantsev (1972)), the Sherwood number was calculated based on the first-order and second-order chemical reaction at the sphere surface. The limiting case of heat transfer with isothermal particle or mass transfer with fast reaction ($\mathrm{Re} \to 0$, $\mathrm{Pe} \to 0$) in the analytical solutions also give a useful reference value for the Stokes Nusselt number or Sherwood number, which is known analytically to be 2 (Clift et al. (1978)). Creeping flow past ordered spheres was also studied by Pfeffer and Happel (1964). They performed an analytical study using an idealised concentric "unit cell" with as-

sumed fluid temperature boundary conditions at its frictionless "free surface" or outer radial (fluid) boundary. They noted that while in an actual packed bed these fluid envelopes will be distorted, for the analysis they assumed a spherical cell. This assumption is hard to justify especially at higher solid volume fraction because distortion of the fluid envelopes can significantly change the scalar gradients. Nevertheless, the unit cell solutions are assumed to be representative of packed and fluidized beds. Using the free surface model, Pfeffer and Happel (1964) obtained an average Stokes Nusselt number value of about 13 for Stokes flow in a particle bed with a solid volume fraction of 0.6. Sorensen and Stewart (1974) studied fully-developed creeping flow through a simple cubic arrangement of spheres using stream-function expansions and a variational approach for the velocity field, and approximating functions and a collocation procedure for the temperature field. However, their non-standard Nusselt number definitions that is a function of Péclet number and bulk temperature cannot be easily compared with other results.

The analytical treatment of heat and mass transfer in flow past random assemblies of particles is nontrivial since governing equations for heat and mass transfer problems normally behave non-linearly with random particle configurations. Due to the averaging procedure over different configurations of particles drawn from an ensemble at the same solid volume fraction, the boundary conditions at particle surfaces need to be imposed at random locations. Average quantities such like average Nusselt or Sherwood number corresponding to gas–solid heat or mass transfer depend on the gradients of the resulting random temperature or concentration fields at particle surfaces. Gunn (1978) estimated the average surface heat flux based on the difference in phase-averaged temperature in gas and solid phases and an average length scale obtained from an assumed distribution of flow channel widths. His analytical results of Nusselt number for fixed bed of particles were restricted at low Reynolds number. Koch and Brady (1985) solved the convection-diffusion equation for mass (heat) transfer in Stokes flow through fixed beds using an asymptotic analysis that is valid in the dilute limit (low solid volume fraction). In their analysis, Koch and Brady (1985) assumed a linear concentration profile that varies slowly (on the length scale of the one-particle problem) in the axial direction. Koch and Brady (1985) obtained the dependence of the effective diffusivity on

the Péclet number and the ratio of the particle-fluid solubilities (particle-fluid thermal ratio inertia). Koch's work provides early evidence that in fixed particle beds the presence of bulk convective motion induces fluid velocity fluctuations (mechanical dispersion) because of the presence of particles, and this is an important factor affecting macrotransport. Acrivos et al. (1980) found that under the condition that solid volume fraction of particles is far larger than the square of Péclet number, the fluid heating produced a significant nonlinear temperature gradient throughout a fixed bed of particles. In other words, in slow flow the fluid heating effect is significant in a fixed bed of particles. At finite Reynolds number, the non-linearity of the governing equations and the randomness in particle positions and velocities pose significant obstacles to theoretical analysis.

1.2.2 Experimental measurements

Due to the limitations of theoretical analysis, experimental measurements of gas–solid flow are often used to provide correlations. Experimental measurements of gas–solid heat and mass transfer are also challenging because of limited optical access. Various experimental techniques, such as axial heat conduction (Kunii and Smith (1961)), step response (Handley and Heggs (1968)), frequency response (Littman et al. (1968); Gunn and Desouza (1974)), and shot response (Shen et al. (1981); Wakao et al. (1977)) have been used to study heat transfer in gas–solid fixed-bed reactors over the last several decades (Wakao and Kaguei (1982)). However, these experimental studies report values for the Nusselt number or Sherwood number in packed beds ($\varepsilon_s \approx 0.6$) that differ by three or four orders of magnitude (Wakao and Kaguei (1982)). Since most experimental measurements of heat and mass transfer in gas–solid flow are intrusive, flow disturbances caused by the probes are a source of uncertainty. Furthermore, the gas–solid heat transfer rate is inferred from point-wise temperature measurements using simplified one–dimensional models of heat transfer that are based on assumptions such as the neglect of axial conduction in the fluid phase. Therefore, the validity of the assumptions implicit in these simplified one–dimensional models used in the inferential procedure is also a source of uncertainty.

Recently, non-intrusive laser optical measurement techniques including particle image ve-

locimetry (PIV) and planar laser-induced fluorescence (PLIF) are developed for research and diagnostics into flow and combustion processes. These techniques are capable of measuring an entire two-dimensional cross section of the flow field simultaneously with a high degree of accuracy. For instance, combination of PIV and PLIF allows us to visualize and measure the concentration and temperature field in fluid flow. With index of refraction matching to avoid the light refraction and resulting image distortions, the flow inside a bed of particles can be visualized, which cannot be measured using traditional experimental techniques.

However, these non-intrusive techniques such as PIV and PLIF have their limitations. For instance, regular PIV only gives two components of velocity in a two dimensional plane. Even though stereoscopic PIV can be used for visualization of all three components of velocity field, this technique is still limited to measurement in a two dimensional plane. For PLIF measurement of concentration, fluorescence can arise from other species, especially from hydrocarbons in high pressure reacting flows. Also, since the fluorescence of the dye is a function of the laser light intensity, temporal and spatial variation of laser light intensity needs to accounted for.

Although the challenges in experimental measurement still limit the accuracy of the results from experiments, for the practicing engineer Nusselt (Sherwood) number correlations have been developed to provide relatively simple functional forms to estimate the average interphase heat or mass flux in reacting gas–solid flow based on experimental data. For instance, in a fixed particle bed, based on the findings of Gunn and Desouza (1974), Wakao et al. (1979) reevaluated published data on unsteady heat transfer and combined those with re-assessed steady-state heat transfer data, to develop the following correlation for the Nusselt number in packed beds:

$$\mathrm{Nu} = 2 + 1.1\mathrm{Pr}^{1/3}\mathrm{Re}^{0.6}. \tag{1.2}$$

This correlation yields an average Stokes Nusselt number of exactly 2 for a packed bed. To account for effect of the solid volume fraction, Gunn (1978) proposed a single correlation for particle-to-fluid heat and mass transfer in fixed beds using experimental data, which is written

as the following function of Reynolds number Re, bed porosity ε_b, and Prandtl number Pr:

$$\mathrm{Nu} = (7 - 10\varepsilon_b + 5\varepsilon_b^2)(1 + 0.7\mathrm{Re}^{0.2}\mathrm{Pr}^{1/3}) + (1.33 - 2.4\varepsilon_b + 1.2\varepsilon_b^2)\mathrm{Re}^{0.7}\mathrm{Pr}^{1/3}. \tag{1.3}$$

This correlation is valid in the bed porosity range $0.35 \leq \varepsilon_b = 1 - \varepsilon_s \leq 1.0$ and $\mathrm{Re} \leq 10^5$. It has been widely used in CFD simulations of two–phase flows (Syamlal et al. (1993)) to simulate heat and mass transfer in gas–solid flows. For the case of mass transfer, the Schmidt number is substituted for the Prandtl number, resulting in a correlation for the Sherwood number.

Besides the development of the correlation for interphase transfer using experimental data, various experimental techniques for measuring the solute concentration field have been reviewed by Delgado (2006). A similar review of experimental techniques for measuring the temperature field is given by Özgümüş et al. (2013). These field data have been used to calculate hydrodynamic dispersion and thermal dispersion in porous media or packed beds for gas-solid flow, respectively. The hydrodynamic dispersion or thermal dispersion is defined based on the concentration-velocity covariance by Koch and Brady (1985) or the temperature-velocity covariance by Kaviany (2012) and Whitaker (1999), and a gradient-diffusion model. Empirical correlations have been proposed for the calculation of the hydrodynamic or thermal dispersion coefficients over the entire range of practical values of Schmidt number (or Prandtl number) and Péclet number.

1.2.3 PR-DNS Simulation

The aforementioned limitations of theoretical and experimental methods motivate us to use PR-DNS approach to provide insight into the physico-chemical interactions and develop improved closure models for multiphase CFD simulations. PR-DNS approach is a first-principles, model-free method that has already provided transformative insights into multiphase flow physics for model development (Tenneti and Subramaniam (2014)). The principal features involved in any PR-DNS methodology are that i) solving the fluid flow by imposing appropriate boundary conditions at the particle surfaces, ii) computing the fluid dynamic forces acting on the particles, and iii) evolving the velocities and positions of the particles due to the action of the fluid forces and additional forces due to interparticle interactions such as colli-

sions. It is important to note that unlike point-particle direct numerical simulation (PP-DNS) approach (Squires and Eaton (1991); Elghobashi and Truesdell (1993); Boivin et al. (1998); Sundaram and Collins (1999); Mashayek and Taulbee (2002)) that treat a size particle as a point particle and use the drag model to compute the drag of a particle, the particle velocities are evolved by explicitly computing the fluid forces acting on the particles and does not use any drag model.

Development of PR-DNS methodology needs to address two main challenges. One is how efficiently to solve for a flow that is subject to boundary conditions at moving particle surfaces. The other is how to develop models for different gas-solid flow regimes based on PR-DNS. When PR-DNS is used to develop models for averaged quantities, multiple independent simulations (MIS) of microscale realizations corresponding to the same macroscale system need to be preformed to guarantee that the statistical description for gas-solid flow is correct.

Recently, various PR-DNS methodologies have been developed to overcome these challenges. The methodologies can be broadly categorized as those that rely on a body-fitted mesh (Nomura and Hughes (1992); Hu et al. (2001); Bagchi and Balachandar (2003, 2004); Burton and Eaton (2005)) to impose boundary conditions at particle surfaces and those that employ regular Cartesian grids (Peskin (1981); Yusof (1996); Scardovelli and Zaleski (1999); Patankar et al. (2000); Glowinski et al. (2001); Ladd and Verberg (2001); Oguz and Prosperetti (2001); Sharma and Patankar (2005); Uhlmann (2005); Kim and Choi (2006); Tabaczynski (2001); Apte et al. (2009); Garg (2009); Lucci et al. (2010)). These methods are briefly summarized in Garg et al. (2010b) and Tenneti et al. (2011). The principal disadvantage with body-fitted mesh approaches is that repeated re-meshing and solution projection are required for moving interfaces. For methods using regular Cartesian grids, there is no re-meshing that result in much faster solution times for moving particle simulations. However, because the grid does not conform to the particle surface, special strategies are needed to generate an accurate solution by imposing boundary conditions on the particle surface. Once the interpolation strategies represent the particle surface accurately, PR-DNS methodologies have the capability to solve the flow around complex solid-phase geometries quickly.

PR-DNS of gas-solid flows can provide accurate quantification of gas-solid interaction and

has been used by several researchers to build computational drag models (Hill et al. (2001a,b); Van der Hoef et al. (2005); Beetstra et al. (2007a); Yin and Sundaresan (2009); Tenneti et al. (2011)). In recent years, several researchers have also extended PR–DNS to investigate heat and mass transfer in gas–solid flow. Two-dimensional PR–DNS studies (Yu et al. (2006); Feng and Michaelides (2009)) on simulating gas–solid flow in an infinite channel with an isothermal particle have been reported. Massol et al. (2004) studied heat transfer in a fixed array of monodisperse spheres using three-dimensional PR–DNS. However, their formulation uses a source/sink term that is strictly valid only for those cases where fluid heating is negligible during the time it takes the flow to transit the computational domain. This restriction holds only for dilute suspensions at high Reynolds number (Acrivos et al. (1980)). Deen et al. (2012) and Tavassoli et al. (2013) used three-dimensional PR–DNS with inflow and outflow boundary conditions to compute the gas–solid heat transfer coefficient and Nusselt number that are compared with Gunn (1978) correlation. Deen et al. (2014) also simulated coupled heat and mass transfer in a fixed bed of particles with chemical reaction at the surface of the particles in time and compared the PR-DNS results with one-dimensional heterogeneous model.

Recently, Tenneti et al. (2011) and Garg et al. (2010b) have developed a PR–DNS approach based on the Particle-resolved Uncontaminated-fluid Reconcilable Immersed Boundary Method (PUReIBM) that is used to solve for flow past arbitrary arrangements of solid spherical particles. PUReIBM is a PR-DNS approach for gas–solid flow where the Navier-Stokes equations with no-slip and no-penetration boundary conditions on each particle's surface are solved using a forcing term that is added to the momentum equations. Complete details of the PUReIBM hydrodynamic solver are discussed by Tenneti et al. (Tenneti et al. (2011); Tenneti (2013); Tenneti et al. (2010); Tenneti and Subramaniam (2014)) and Garg et al. (2010b).

1.3 Research objectives

The principal goal of this work is to use the PR-DNS approach to provide ***detailed information on the coupling between heat and mass transfer in both fluid and solid phases***. The PR-DNS approach enables the development of predictive models for momentum, heat and mass transfer in reacting gas–solid flow. The specific research objectives of this thesis

that will lead us to this goal in Fig. 1.3 are described as follows: 1) develop the PR-DNS approach to account for heat and mass transfer in reacting gas–solid flow; 2) develop the PR-DNS approach to account for walls and validate the PR-DNS approach by comparisons with numerical and experimental data; 3) quantify and model unclosed heat transfer terms in the TF fluid temperature equation and the composition PDF transport equation using PR-DNS data; 4) quantify and model mass transfer on particles in reacting gas–solid flow using PR-DNS data; and 5) validate the assumptions in multiphase flow statistical theories using PR-DNS data. These specific research objectives are described below in further detail.

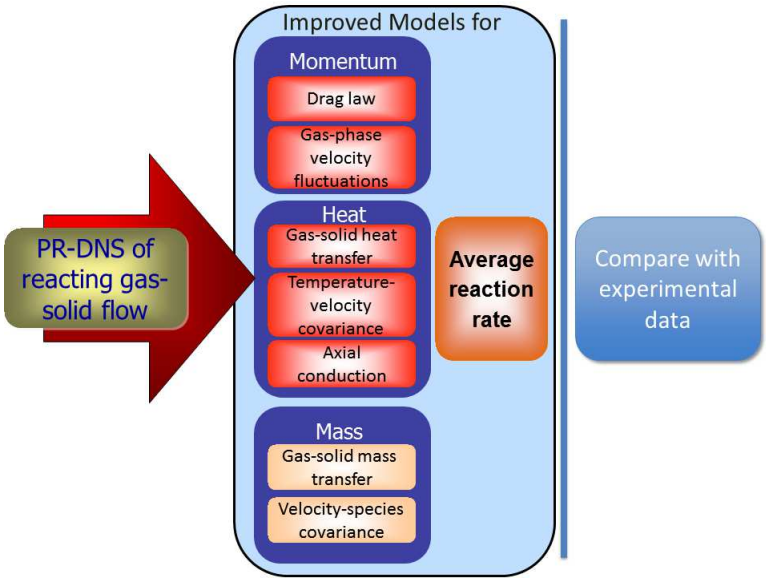

Figure 1.3: Schematic showing specific research objectives leading to the development of a two–fluid model for reacting gas-solid flow. The PR-DNS approach is used to produce data of velocity, temperature and species fields. The data obtained from performed PR-DNS will be used to propose closure models for the average gas-solid transfer, axial conduction in the fluid phase, transport of velocity-temperture covanience. Another objective of this work is to use PR-DNS to provide data to compare with experimental data.

1.3.1 Development of the PR-DNS approach

In order to study heat transfer in gas–solid flow, the hydrodynamic solver of PR-DNS developed by Tenneti *et al.* (Tenneti et al. (2011); Tenneti (2013); Tenneti et al. (2010)) and Garg et al. (2010b) is extended to solve the fluid temperature equation as shown in Chapter 2. The PR-DNS approach is based on a pseudo-spectral (PS) scheme with the immersed

boundary method (PS PR-DNS). Using this PR-DNS approach, fluid heating is accounted for in thermally fully–developed flow with periodic domains using a thermal self–similarity condition (Tenneti et al. (2013)). The scalar solver of PS PR-DNS is validated by comparing the PR-DNS results with analytical solutions, and existing experimental and numerical data.

Although the convergence and accuracy of PS PR-DNS are validated in a suite of test cases, its applications are restricted by periodic boundary conditions. In order to overcome these difficulties, a fully finite-difference (FFD) scheme version of PR-DNS is developed in Chapter 7. The momentum and scalar transport equations are solved using a fully finite–difference scheme in all directions in FFD PR-DNS instead of using Fourier transforms in the cross-stream directions as in PS PR-DNS. This allows us to implement various boundary conditions such as inflow/outflow boundary condition to simulate a wall-bounded flow. The hydrodynamic and scalar solvers of FFD PR-DNS are developed and validated in several test cases in Chapter 7. The FFD PR-DNS solvers are also parallelized to perform simulations of a large domain with high grid resolutions such as simulation of the experimental test section in Chapter 8. A complete test section of the experiments provided by Mahdi Ramezani and Michael G. Olsen in Iowa State University is simulated by FFD PR-DNS and the side-by-side comparison between numerical and experimental data is reported for the purpose of the validation of the FFD PR-DNS approach. In order to study mass transfer in gas–solid flow, the scalar solver of FFD PR-DNS is extended to study mass transfer with surface chemical reactions in Chapter 10. The third type boundary condition that involves the first-order surface chemical reaction and species diffusion is imposed on the surface of particles. The PR-DNS results are validated by 2D analytical solution for low Reynolds number.

1.3.2 Quantification and model development for reacting gas–solid flow

Model development for multiphase CFD simulations requires physics-based closures for unclosed terms (corresponding to the cells in Table 1.1). Using PS PR-DNS, a drag model and a granular temperature model have been proposed by Tenneti et al. (2011), and a model for fluid velocity covariance has been proposed by Mehrabadi et al. (2015) using homogeneous particle assembly simulations (see green cells in Table 1.1). In this thesis, model development

for the other unclosed terms (see orange cells in Table 1.1) in the two–fluid equation is discussed based on PR-DNS data for temperature and species fields.

To solve the average fluid temperature equation of the two–fluid equations requires closure models for (I) the average gas–solid heat transfer, (II) transport of the temperature-velocity covariance, (III) conduction in the gas phase, and (IV) chemical reaction source term (third column in Table 1.1). In Chapter 3, the average gas–solid heat transfer (term I) is first quantified using sufficiently many realizations of PS PR-DNS data for steady flow past a homogeneous fixed particle assembly. A model for the average gas–solid heat transfer is then developed in terms of the Nusselt number and the bulk fluid temperature over a wide range of solid volume fractions and Reynolds numbers based on mean slip velocity. The improved model for average gas–solid heat transfer is also compared with the existing standard model. The transport of the temperature-velocity covariance (term II, the second cell in the first row of Table 1.1) is currently neglected in EE TF CFD simulations but models for velocity covariance (the first cell in the first row of Table 1.1) have been recently proposed by Mehrabadi et al. (2015) using PS PR-DNS. Mehrabadi et al. (2015) found that velocity covariance is significantly important compared with the kinetic energy associated with the mean slip velocity. In Chapter 4, the temperature-velocity covariance and its transport are quantified, and its magnitude is compared with the average gas–solid heat transfer using PS PR-DNS data. Then a model for temperature-velocity covariance is proposed by introducing pseudo–turbulent thermal diffusivity that is analogous to the turbulent diffusivity in single-phase turbulence. The dependence of the effective diffusivity (the ratio of pseudo–turbulent thermal diffusivity to molecular thermal diffusivity) on Péclet number is quantified. This dependence is explained using a wake scaling analysis. In Chapter 4, the average conduction in the fluid phase (term III) is also quantified and modeled in terms of the bulk fluid temperature. A budget analysis of these terms in the average fluid temperature equation in a steady gas-solid flow is preformed to quantitatively compare the importance of these terms in this gas–solid heat transfer problem.

In the transported PDF approach, the composition PDF transport equation for two-phase flow also contains unclosed terms even though (IV) the chemical reaction source term in the gas-phase is closed. In Chapter 6, the composition PDF transport equation for two-phase

flow is derived and its unclosed terms as (I) the average gas–solid heat transfer conditional on composition, (II) velocity fluctuation conditional on composition, (III) gas-phase mixing conditional on composition are identified. Then possible closure models for these unclosed terms are discussed. Since the mixing time scale that represents the rate of mixing of scalar (temperature or species) in the gas phase is an important parameter in single-phase closure models, its values for different solid volume fractions are also extracted from PS PR-DNS data.

Analogous to the heat transfer problem, the average species mass fraction equation for mass transfer problem also includes (1) average gas–solid mass transfer, (2) transport of the species-velocity covariance, (3) diffusion in the gas phase, and (4) average reaction rate (fourth column in Table 1.1). Unlike the heat transfer problem, mass transfer is often coupled with heat transfer in reacting gas–solid flow. For the purpose of model development for mass transfer in gas–solid flow, the mass transfer problem needs to be simplified. In Chapter 10, the mass transfer problem in gas–solid flow is decoupled from heat transfer, and simulated using FFD PR-DNS. Preliminary results are obtained for the case of steady flow past a sphere with a first-order chemical reaction on the sphere surface over a range of Reynolds number. Heat transfer is neglected in this simulation. The FFD PR-DNS results are then compared with 2D analytical solutions of the mass transfer problem at low Reynolds number. The Sherwood number obtained from PR-DNS data is also compared with existing Sherwood number correlations with and without chemical reactions. Mass transfer with heat transfer in fixed beds of particles needs to be simulated to develop models for average gas-solid mass transfer, but that is deferred to future work. Once the PR-DNS data from mass transfer problem is ready, the model for transport of the species-velocity covariance and diffusion in the gas phase (see the third column in Table 1.1) can be developed using a similar approach as in the heat transfer problem.

The above models for unclosed terms are developed based on homogeneous fixed particle assemblies in a thermal fully–developed flow. However, in a real fixed bed reactor, the system is bounded by the walls of reactor. In order to extend the proposed models to account for wall effect on the fixed particle beds, the FFD PR-DNS is also used to simulate a flow past a particle assembly in a square duct in Chapter 7. Preliminary FFD PR-DNS results are provided to

analyze the wall effect on hydrodynamics and heat transfer.

1.3.3 Validity of assumptions in multiphase flow theories and closure models

The PR-DNS data are not only used to develop improve closure models but also allow us to validate the assumptions in multiphase flow theories and assumptions for closure models. Scale separation between macroscales and microscales in continuum theories of multiphase flow is assumed on the basis that the characteristic length scale of macroscopic quantities is larger than that of organized mesoscale structure (characterized by higher order statistics such as the particle pair correlation or two-point correlations in the fluid). In Chapter 5, the assumption of scale separation implied in continuum theories of multiphase flow is validated by using PS PR-DNS results of gas-solid heat transfer in freely evolving suspensions and fixed bed of particles. The key feature of the gas-solid heat transfer problem–the inhomogeneity of the temperature field is in the streamwise direction–results in the inhomogeneous variation of the mean or bulk fluid temperature along the streamwise direction. Using a length scale obtained from the inhomogeneous temperature field, a criterion for scale separation in the gas-solid heat transfer problems is proposed.

Since quantification of unclosed terms in the average fluid temperature equation in Chapters 3 and 4 is based on the data obtained from the homogeneous fixed assemblies of isothermal particles in a thermal fully–developed flow, this raises the question whether or not the statistical quantities such as average Nusselt number vary much if the particles move such as in a fluidized bed of particles. The PR-DNS results in Chapters 2–4 show that the mean fluid temperature can vary significantly over a few particle diameter, and it might be expected that particle motion in this mean temperature gradient can result in a change in the statistical quantities such as average Nusselt number. Therefore, heat transfer in a freely evolving suspension of gas–solid flow is compared with that in fixed bed of particles in Chapter 5.

In addition, the average heat transfer models are proposed using the PR-DNS data that assume all particles to be the isothermal particles in Chapter 3 which means that the particle temperature is independent of time and space. However, in reality, the isothermal particles assumption may not hold if the particle temperature experiences high heating rates as formed

in biomass fast pyrolysis. It is necessary to validate heat transfer models by studying transient heat transfer on particles, which considers the variation of the particle temperature in time. In Chapter 9, a preliminary study of transient heat transfer in a steady gas-solid flow past a sphere in a duct using inflow/outflow boundary condition is performed using the FFD PR-DNS approach. This is a test case for verifying the capability of FFD PR-DNS to simulate transient heat transfer since the full-developed flow formulation of PS PR-DNS is not suitable for simulating variation of the particle temperature. In this transient heat transfer problem, the solid temperature of the sphere is assumed to be uniform but dependent of time. In addition to solving the gas-phase energy equation, the solid temperature evolves by solving the solid-phase energy equation. It is worth noting that in order to validate heat transfer models in EE TF CFD simulations, the transient heat transfer problem in a fixed bed of particles in gas–solid flow need to be studied over a wide range of Reynolds number and solid volume fraction in the future work.

1.4 Accomplishments

The tasks completed thus far to achieve the above research objectives are listed in Table 1.2-1.4. The details of these accomplishments are discussed in the following chapters.

1.5 Outline

The description of the scalar solver of PS PR-DNS formulation and validation of its performance are described in Chapter 2. Quantification and model development for the unclosed terms in average fluid temperature equation are discussed in Chapters 3 and 4. Using the PS PR-DNS data, the assumption of scale separation in multiphase flow theories is valid in Chapter 5. The transported PDF approach is introduced to study scalar fluctuation and its unclosed terms are identified in Chapter 6. In Chapter 7, the hydrodynamic and scalar solvers of FFD PR-DNS that accounts for wall effect of heat and mass transfer in gas-solid flow are developed and validated. The FFD PR-DNS methodology to perform simulations of a duct flow without or with particles is presented in Chapter 7. A detailed comparison of FFD PR-DNS data and

experimental data for flow past a train of particles is report in Chapter 8. A transient heat transfer study from a sphere in a duct is also given using FFD PR-DNS in Chapter 9. In Chapter 10, the FFD PR-DNS scalar solver is extended to account for mass transfer on a sphere with a first-order surface chemical reaction, and the PR-DNS data are compared with 2D analytical solutions. The summary of the findings and future works are presented in Chapters 11 and 12.

Table 1.2: (i) Accomplishments corresponding to research objectives.

Tools/Methods	Results	Conclusions (in Chapters)
Pseudo-spectral (PS) PR-DNS	1. Developed the scalar solver of PS PR-DNS and validated the scalar solver by using several test cases 2. Simulated flow past a fixed homogeneous particle assembly with heat transfer for a few Reynolds numbers and solid volume fractions	Developed and validated the scalar solver of PS PR-DNS to account for heat transfer in gas–solid flow (Chapter 2)
	Simulated a flow past a fixed homogeneous particle assembly with heat transfer over a range of Reynolds numbers and solid volume fractions in gas–solid flow	Established the PR-DNS dataset using PS PR-DNS approach (Chapters 3 and 4)
	1. Extended the scalar solver of FFD PR-DNS to account for particle motion in the acceleration frame 2. Performed a simulation of a freely evolving suspension of particles at particle-gas density ratio of 100	Extended the scalar solver of FFD PR-DNS to account for particle motion (Chapter 5)
Fully finite-difference (FFD) PR-DNS	1. Developed and parallelized the hydrodynamic and scalar solvers of FFD PR-DNS to simulate wall-bounded flow that allows for various boundary conditions 2. Validated the hydrodynamic and scalar solvers of the FFD PR-DNS in a suite of test cases by comparing analytical solutions, experimental and numerical data 3. Simulated a flow past a fixed homogeneous particle assembly with heat transfer in a square duct	Developed and validated the FFD PR-DNS approach to simulate wall-bounded flow with particles (Chapter 7)
Extended scalar solver of FFD PR-DNS	1. Extended the scalar solver of FFD PR-DNS to account for the first-order chemical reaction on the particle surface 2. Simulated mass transfer in a fixed sphere for low and high particle Reynolds number in a reacting gas-solid flow 2. Validate the PR-DNS results with 1D and 2D analytical solutions of mass transfer in a sphere at low Reynolds number	Extended the scalar solver of FFD PR-DNS to account for mass transfer with a first-order surface chemical reaction (Chapter 10)

Table 1.3: (ii) Accomplishments corresponding to research objectives.

Theory/ Modeling	Results	Conclusions
Flow physics	Found that even velocity field is homogeneous in the case of flow past a fixed homogeneous particle assembly, the temperature field is inhomogeneous along axial location	Explored the behaviors of the inhomogeneous temperature field in a fixed particle assembly (Chapter 2)
	1. Obtained a characteristic length scale from the bulk fluid temperature field using PS PR-DNS data of homogeneous fixed assemblies and freely evolving suspension of particles 2. Compared bulk fluid temperature and average Nusselt number obtained from the case of flow past the fixed assembly and freely evolving suspension of particles 3. Proposed a criterion for scale separation in the gas-solid heat transfer problem	Developed a criterion for scale separation (Chapter 5)
	1. Derived the transport equation for scalar variance 2. Derived the phase-conditional single-point velocity-composition PDF transport equation 3. Quantified the scalar variance and mixing time scale for different solid volume fractions at high speed flow in gas-solid heat transfer	Studied scalar fluctuation by flow past a fixed assembly of particles (Chapter 6)
	1. Compared the results of FFD PR-DNS data with experimental data obtained from the same experimental setup in a duct for the cases of laminar pure duct flow, flow past a sphere and a train of five spheres 2. Found the effect of the separation distance on the wall boundary layer growth and the wake behind spheres	Validated both experimental and PR-DNS approaches and studied the wake behind the spheres (Chapter 8)
	1. Investigated wall effect on drag force and heat transfer of a single particle in a square duct by varying the distance between the particle and duct wall 2. Simulated flow past a fixed particle assembly in a square duct with heat transfer	Investigated wall effect on velocity (or drag force) and heat transfer of a single particle and particle beds in a square duct using FFD PR-DNS (Chapter 7)

Table 1.4: (iii) Accomplishments corresponding to research objectives.

Theory/ Modeling	Results	Conclusions
	1. Performed simulations of flow past a fixed sphere with accounting for variation of the sphere temperature in time 2. Studied the effect of the finite particle-fluid thermal inertia ratio on the quantities such as Nusselt number 3. Found that Nusselt number become steady-state in a small time scale	Studied the variation of the particle temperature in time (Chapter 9)
Flow physics	1. Studied the dependence of mass transfer at particle surface on chemical reaction rate constant and species diffusion coefficient 2. Investigated mass transfer on a sphere at high Reynolds number (up to 100) in a reacting gas–solid flow 3. Compared the Sherwood number obtained from PR-DNS with the existing Sherwood number correlation with and without the surface chemical reaction	Studied the dependence of mass transfer on parametrized space using FFD PR-DNS (Chapter 10)
Model development	Quantified and modeled average gas–solid heat transfer	Developed closure models for average gas–solid heat transfer in the two–fluid equation (Chapter 3)
	1. Quantified and modeled velocity–temperature covariance term and fluid–phase axial conduction term in the average fluid temperature equation using PS PR-DNS data 2. Proposed correlations for effective thermal diffusivity using wake scaling analysis and implied model	Developed closure models for fluid–phase axial conduction and velocity–temperature covariance in the two–fluid equation (Chapter 4)
	1. Identified unclosed terms in the phase-conditioned single-point velocity-composition joint PDF transport equation 2. Discussed the possible closure models for the phase-conditioned single-point composition PDF transport equation 3. Propose a correlation for the PDF of fluid temperature by fitting the PS PR-DNS data 4. Quantified the mixing time scale for two-phase flow in the mixing model	Discussed the possible closure models for the composition PDF transport equation using PR-DNS data (Chapter 6)

CHAPTER 2. ROLE OF FLUID HEATING IN DENSE GAS–SOLID FLOW AS REVEALED BY PARTICLE–RESOLVED DIRECT NUMERICAL SIMULATION

This chapter is an article titled "Role of fluid heating in dense gas–solid flow as revealed by particle-resolved direct numerical simulation" published in International Journal of Heat and Mass transfer (Tenneti et al. (2013)). This article is authored by S. Tenneti, B. Sun, R. Garg and S. Subramaniam. My contribution is to perform the simulations of the flow past a fixed assembly of particles over a range of mean slip Reynold numbers and solid volume fractions and analyze the numerical data.

Heat transfer is important in gas–solid flows that are encountered in many industrial applications such as energy generation. Computational fluid dynamics (CFD) simulations of heat transfer in gas–solid flow are based on statistical theories that result in averaged equations (e.g., EE TF model). These averaged equations require accurate models for unclosed terms such as the average gas–solid heat flux. The average gas–solid or interphase heat flux is closed in terms of the Nusselt number Nu, which is specified as a function of the solid volume fraction ε_s, mean flow Reynolds number $\mathrm{Re_m}$ and Prandtl number Pr. In developing closure models for the average interphase heat flux it is assumed that the gas–solid flow is locally homogeneous i.e., the effect of fluid heating (or cooling) on the average fluid temperature is neglected. However, continuous heating (or cooling) of the fluid along the flow direction causes the average fluid temperature to become inhomogeneous. In this work we develop a particle–resolved direct numerical simulation (PR–DNS) methodology to study heat transfer in steady flow past statistically homogeneous random assemblies of stationary particles. By using an analogy with thermally fully developed flow in pipes, we develop a thermal similarity condition that ensures a statistically homogeneous Nusselt number, even though the average fluid temperature field

is inhomogeneous. From PR–DNS results we find that the effect of fluid heating cannot be neglected for gas–solid systems with high solid volume fractions and low mean flow Reynolds numbers. These results indicate that the assumption of scale separation implicit in two–fluid models is not always valid.

2.1 Introduction

Gas–solid flows occur in many industrial applications such as energy generation, food, chemical, and pharmaceutical processing. Carbon-neutral energy generation using biomass (Azar et al. (2006)) or chemical looping combustion (CLC) (Shen et al. (2008)), and CO_2 capture from flue gases using dry sorbents (Yi et al. (2007); Abanades et al. (2004)) are examples of emerging technologies (Wall (2007)) where an improved understanding of gas-solid heat transfer is crucial for process and component design. For instance, accurate prediction of the fluid–phase temperature field is very important for the CLC application because the reaction rates in combustion chemistry are highly temperature dependent. Similarly, in the CO_2 capture process using potassium–based dry sorbents the carbonation reaction is exothermic and the regeneration of the sorbent is endothermic (Yi et al. (2007)). Hence, gas–solid heat transfer is crucial for maximizing process efficiency. Both CLC and CO_2 capture technologies can be implemented using fluidized beds, and typical particle diameter values range from 50–150 μm. These particles are typically larger than the Kolmogorov length scale of turbulent dissipation η. Moreover, gas–solid flow in fluidized beds can have a solid volume fraction ranging from near close–packed (64% for random configurations of monodisperse spheres) to as low as 5% in the riser region. A fundamental understanding of heat transfer in fluid flow past finite sized particles ($D > \eta$) over a wide range of solid volume fraction and flow Reynolds number is therefore important for process design.

Computational fluid dynamics (CFD) simulations (Kashiwa and Gaffney (2003); Sun et al. (2007); Syamlal et al. (1993)) of gas–solid flow are increasingly being used as an efficient approach for design optimization because experiments are often costly and time-consuming. In two–fluid CFD simulations of gas–solid flow, the averaged equations governing mass, momentum, and energy conservation are solved. Figure 2.1 shows a schematic of the computational

domain in a CFD simulation of gas–solid flow. In every grid cell, governing equations for averaged quantities such as volume fraction, velocity and temperature are solved for both phases. Since these equations are obtained using a statistical averaging procedure (Drew and Passman (1998)), the average interaction terms corresponding to mass, momentum, and energy exchange between different phases need to be modeled. For example, two–fluid CFD formulations for heat transfer in gas–solid flow require closure of the average gas–solid heat transfer $\langle Q_{g-s} \rangle$. The average interphase heat flux $\langle Q_{g-s} \rangle$ is modeled in terms of an average Nusselt number and the difference between the average fluid and solid–phase temperature $\left\langle T^{(f)} \right\rangle - \left\langle T^{(s)} \right\rangle$. This Nusselt number is usually given by a correlation that depends on solid volume fraction ε_s, mean slip Reynolds number $\mathrm{Re_m}$ and the Prandtl number Pr.

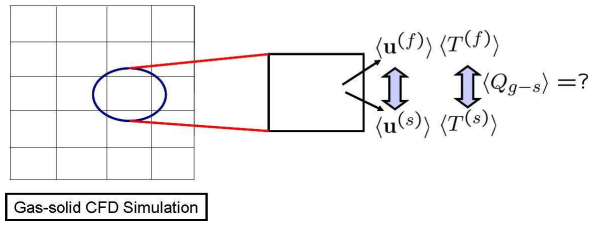

Figure 2.1: Schematic of a CFD simulation of gas–solid flow. In every computational grid cell, governing equations for the averaged quantities in both phases are solved. Here, $\mathbf{u}^{(f)}$ is the average fluid–phase velocity, $T^{(f)}$ is the average fluid–phase temperature, $\mathbf{u}^{(s)}$ is the average solid–phase velocity and $T^{(s)}$ is the average solid–phase temperature. In this schematic, Q_{g-s} denotes the average gas–solid interphase heat transfer.

Correlations for the Nusselt number corresponding to gas–solid heat transfer are typically obtained from a combination of experimental and theoretical studies. However, the experimental data from which these empirical correlations are deduced vary by orders of magnitude (Wakao and Kaguei (1982); Ronald and Christopher (2009)). Experimental measurement of heat transfer in gas–solid flow is challenging because of limited optical access and hence most measurements are intrusive. Theoretical studies of heat transfer in gas–solid systems are limited to creeping flow past ordered (Pfeffer and Happel (1964); Sorensen and Stewart (1974)) and random assemblies of spheres (Gunn (1978); Acrivos et al. (1980)). The randomness in particle positions and velocities together with the nonlinearity of the governing equations make the analytical treatment intractable at finite Reynolds numbers. Particle-resolved direct nu-

merical simulation (PR–DNS) of heat transfer in gas-solid flow is a first-principles, model-free simulation method that can used to gain better understanding of heat transfer in gas-solid flow. Furthermore, PR–DNS can be used to specify closure models for the unclosed average interphase interaction terms that arise in CFD simulations of gas–solid flow.

In applying closure models for the average interphase interaction terms such as the average interphase momentum transfer and interphase heat flux, it is assumed that the gas–solid flow is locally homogeneous. In other words, the average fluid and solid–phase velocities and temperatures are assumed to be uniform in the grid cell. Therefore, in order to specify closure models for the unclosed terms it is natural to simulate a statistically homogeneous gas–solid suspension using PR–DNS. Indeed, PR–DNS has been used successfully to solve the hydrodynamic problem and to provide a closure model for the average gas–solid momentum transfer. The closure for the average interphase momentum transfer is popularly known as a "drag law" and several researchers have extracted computational drag correlations for gas–solid flow by simulating steady flow past statistically homogeneous random assemblies of stationary spherical particles (Hill et al. (2001a,b); Van der Hoef et al. (2005); Beetstra et al. (2007a); Yin and Sundaresan (2009); Holloway et al. (2010); Tenneti et al. (2011)) in periodic domains. Tenneti et al. (2011) have rigorously shown that the evolution equation for the volume averaged fluid–phase momentum obtained from this setup is consistent with statistically homogeneous ensemble–averaged equations. This problem setup ensures that the flow field is statistically homogeneous and statistics such as the average interphase momentum transfer can be easily obtained by volume averaging.

In the heat transfer problem, the assumption of a statistically homogeneous average fluid temperature implies that the effect of heating (or cooling) by the particles does not change the average fluid temperature significantly. However, continuous heating (or cooling) of the fluid by the particles along the flow direction can cause the average fluid temperature to vary in that direction. The extent of this variation of the average fluid temperature depends on the solid volume fraction and mean flow Reynolds number. Although the hydrodynamic problem is *statistically homogeneous*, for some regimes of gas–solid flow it is conceivable that anisotropy in the fluid velocity results in a *statistically inhomogeneous* fluid temperature field. Therefore,

PR–DNS methodologies that are used to specify a closure model for the average Nusselt number in terms of the average solid volume fraction and mean flow Reynolds number must account for this inhomogeneity in the fluid temperature field. In this work we present a PR–DNS methodology to study heat transfer in statistically homogeneous gas–solid flow in periodic domains that accounts for the inhomogeneity in the temperature field. We use the analogy of flow in a fixed bed of particles with thermally fully developed flow in internal pipes to develop a thermal similarity condition that guarantees a statistically homogeneous Nusselt number. Using this new formulation we examine the regime of validity of the assumption of statistical homogeneity in the average fluid temperature field that is implicit in two–fluid CFD models.

We use the Particle–resolved Uncontaminated–fluid Reconcilable Immersed Boundary Method (PUReIBM) (Garg et al. (2010b); Tenneti et al. (2011, 2010)) to solve for heat transfer in gas–solid flow. We employ three–dimensional Cartesian grids to solve for the velocity, pressure, as well as the temperature fields. Dirichlet boundary conditions for both velocity and temperature at the surface of the particle are imposed via an immersed boundary (IB) forcing that is added to the momentum and temperature equations, respectively. The idea behind the extension of the IB method to the temperature equation is similar to the one used by Feng and Michaelides (2008) to study heat transfer in particle–laden flow with solid to fluid density ratio in the range 1.001–1.1.

The rest of the chapter is organized as follows. The problem description and the assumptions made to simplify the problem are described in section 2.2. The formulation of the heat transfer problem that is simulated in the particle–resolved DNS methodology is discussed in section 2.3. The governing equations are developed in section 2.4 and the numerical method used in our PR–DNS approach is described in section 2.5. The results obtained from PR–DNS of heat transfer in gas–solid flow are discussed in section 2.6 and finally the principal conclusions of this work are summarized in section 2.7.

2.2 Problem description

A schematic of the problem setup that is used in this work to study gas–solid heat transfer in a homogeneous suspension of randomly distributed spherical particles is shown in Fig. 2.2.

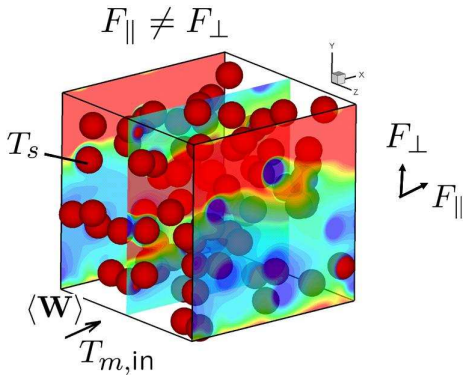

Figure 2.2: Schematic showing contours of steady temperature field in a flow through fixed bed of particles (solid volume fraction 0.1 and Reynolds number 20). In this schematic, $\langle \mathbf{W} \rangle$ is the mean slip velocity between the solid and the fluid–phase. The fluid enters the domain at a bulk temperature of $T_{m,in}$ and all the particles are held at a uniform constant temperature T_s.

The figure shows a random assembly of spherical particles in a unit cell, which repeats infinitely in all three directions. A steady flow is established by imposing a mean pressure gradient that corresponds to a mean flow Reynolds number that is defined based on the magnitude of mean slip velocity between the two phases as follows:

$$\mathrm{Re_m} = \frac{|\langle \mathbf{W} \rangle| \, (1 - \varepsilon_s) \, D}{\nu_f}. \tag{2.1}$$

Here $|\langle \mathbf{W} \rangle|$ is the magnitude of the mean slip velocity between the solid and fluid phases, which is in the direction shown in Fig. 2.2, D is the particle diameter and ν_f is the kinematic viscosity of the fluid. The bulk temperature of the fluid at the "inlet" of this unit cell is $T_{m,in}$ and all the particles are held at a uniform constant temperature of T_s. The bulk temperature of the fluid is the flux–weighted average temperature in a plane perpendicular to the direction of the mean slip velocity (see section 2.3 for a detailed definition). The difference in the bulk fluid temperature and the surface temperature of the particle drives gas–solid heat transfer. Here we consider only gas–solid flow so the Prandtl number is chosen to be 0.72. We neglect viscous heating, radiation and the effect of temperature change on the momentum equation due to density variation (free convection effects). The simplifying assumptions used in our problem setup are justified in Appendix A. We now develop a formulation that can be used to study the gas–solid flow heat transfer problem described in this section.

2.3 Formulation of the heat transfer problem

In order to use the problem setup shown in Fig. 2.2 to quantify the average Nusselt number, we must ensure that the heat transfer problem admits a statistically homogeneous Nusselt number. In other words, a thermally fully developed flow must be established in the fixed bed. Flow through a fixed bed of spheres is anisotropic due to finite mean slip velocity $\langle \mathbf{W} \rangle$ between the solid and fluid phases. This directionality in the flow implies that fluid downstream of a particle is heated up (or cooled down) by interphase heat transfer. This continuous heating of the fluid by the particles results in a mean fluid temperature that is inhomogeneous (Acrivos et al. (1980)) in the coordinate directed along the mean flow. However, since Nusselt number is a non-dimensional interphase heat flux, if the driving force (temperature difference between bulk fluid and particles) has the same variation as that of the interphase heat flux along the flow coordinate, it is possible to obtain a statistically homogeneous Nusselt number. In this section we develop a formulation that renders the Nusselt number statistically homogeneous, although the interphase heat flux and the mean fluid temperature are inhomogeneous.

In order to understand the heat transfer problem in statistically homogeneous suspensions we draw analogy from forced convection heat transfer in internal pipe flow. Statistically homogeneous gas–solid flow is analogous to fully developed pipe flow in two respects. Firstly, the flow field is statistically axisymmetric (Mehrabadi et al. (2015)), similar to the fully developed flow field in a pipe. Secondly, the *average* area occupied by the fluid (or the area fraction) in any plane perpendicular to the streamwise direction is constant in a statistically homogeneous suspension, and hence can be compared to a pipe with a constant area of cross section. Therefore, in an *average* sense we expect the heat transfer problem in statistically homogeneous gas–solid suspensions with isothermal particles to be similar to thermally fully developed flow in pipes with isothermal walls. For internal pipe flow, the flow is said to be thermally fully developed when the scaled temperature is not varying in the streamwise direction (Incropera et al. (2006)), i.e.,

$$\frac{\partial}{\partial x_{||}} \left(\frac{T(\mathbf{x}, t) - T_s}{T_m(x_{||}, t) - T_s} \right) = 0. \tag{2.2}$$

Without loss of generality we will assume that the flow direction is along the x–axis. In the

definition of the scaled temperature given above, T_s is the temperature of the isothermal pipe wall and T_m is called the "mixing–cup" or "bulk" temperature, which is defined as follows:

$$T_m(x_{||}) = \frac{\int_{A_f} (\mathbf{u}T) \cdot \mathbf{e}_{||} dA_f}{\int_{A_f} \mathbf{u} \cdot \mathbf{e}_{||} dA_f}, \tag{2.3}$$

where $\mathbf{e}_{||}$ is the unit vector along the streamwise direction and A_f is the area occupied by the fluid in a plane perpendicular to the streamwise direction. The thermally fully developed condition implies that for a pipe with constant cross–sectional area and isothermal walls, the local heat transfer coefficient at the wall (or Nusselt number) is independent of axial location (Incropera et al. (2006)). In other words, the local wall heat flux scaled by the temperature difference $\left(T_m(x_{||}) - T_s\right)$ is a constant. By using an analogy with pipe flow, the average Nusselt number in gas–solid flow will be statistically homogeneous if we ensure that the scaled temperature field θ, which is defined below is statistically homogeneous:

$$\theta(\mathbf{x}, t) = \frac{T(\mathbf{x}, t) - T_s}{\langle T_m \rangle (x_{||}, t) - T_s}. \tag{2.4}$$

In this definition, $\langle T_m \rangle (x_{||}, t)$ is the ensemble–averaged bulk temperature and T_s is the uniform temperature at which all the particles are maintained. In the next section we discuss the governing equations and boundary conditions for the problem of heat transfer past stationary isothermal particles in periodic domains that ensure that the normalized interphase heat flux is statistically homogeneous.

2.4 Governing Equations

The fluid temperature field T, in the absence of viscous heating, radiation and free convection effects, obeys the following convection–diffusion equation:

$$\frac{\partial T}{\partial t} + \frac{\partial (u_j T)}{\partial x_j} = \alpha_f \frac{\partial^2 T}{\partial x_j \partial x_j}, \tag{2.5}$$

where $\alpha_f = k_f / \rho_f c_{pf}$. Here k_f is the thermal conductivity, ρ_f is the thermodynamic density, and c_{pf} is the heat capacity of the fluid respectively. Equation 2.5 needs to be solved in the fluid together with the Dirichlet boundary condition of $T = T_s$ at the surface of the particles. At the boundaries of the computational domain, periodic boundary conditions are applied on

the *scaled temperature* θ (cf. Eq. 2.4). In the definition of θ for a random particle assembly, Eq. 2.3 gives an area–averaged estimate for the bulk temperature $\langle T_m \rangle$.

Since the boundary conditions at the domain boundaries are in terms of θ, it would appear to be easier to rewrite Eq. 2.5 in terms of θ and solve directly for θ. However, the evolution equation for θ contains additional terms that represent the evolution of the bulk temperature T_m. Therefore, in order to solve for θ we need to solve an additional equation for T_m. Moreover, solving for the evolution equation for T_m requires the computation of heat flux from every particle that intersects the plane perpendicular to the mean flow at each x location in the direction of the mean flow. Since there is a finite number of particles in the computational domain, the solution may suffer from statistical error. Therefore, it turns out to be easier to transform the periodic boundary conditions on θ to obtain similarity conditions on the temperature field $T(\mathbf{x}, t)$ and solve Eq. 2.5 for $T(\mathbf{x}, t)$.

In order to simplify the thermal similarity conditions and also to homogenize the boundary conditions on the particle surfaces we define a non-dimensional temperature field $\phi(\mathbf{x}, t)$as follows:

$$\phi(\mathbf{x}, t) = \frac{T(\mathbf{x}, t) - T_s}{T_{m,in} - T_s} \tag{2.6}$$

where, $T_{m,in}$ is the bulk temperature at $x = 0$. Using this definition of the non dimensional temperature, it is easy to see that the non dimensional bulk temperature $\phi_m(x_\parallel)$ has a similar definition:

$$\phi_m\left(x_\parallel, t\right) = \frac{T_m(x_\parallel, t) - T_s}{T_{m,in} - T_s}. \tag{2.7}$$

Substituting Eq. 2.6 in Eq. 2.5 gives the governing equation for the non dimensional temperature:

$$\frac{\partial \phi}{\partial t} + \frac{\partial (u_j \phi)}{\partial x_j} = \alpha_f \frac{\partial^2 \phi}{\partial x_j \partial x_j}. \tag{2.8}$$

The isothermal boundary conditions on the particle surface reduce to $\phi = 0$.

In order to understand the periodicity conditions and also for ease of implementation we introduce a quantity called the heat ratio r_h which is defined as:

$$r_h = \frac{T_{m,in} - T_s}{T_{m,out} - T_s}, \tag{2.9}$$

where $T_{m,out}$ is the bulk temperature at $x = L$ and L is the length of the box. The heat ratio is the ratio of the bulk temperature at the inlet ($x_\parallel = 0$) to the bulk temperature at the outlet ($x_\parallel = L$). In other words the heat ratio is simply the inverse of the non dimensional bulk temperature at $x_\parallel = L$ i.e.,

$$r_h = \frac{1}{\phi_{m,out}}. \tag{2.10}$$

The heat ratio quantifies by how much a *fluid* particle heats up when it leaves the box and so this quantity depends solely on the flow structure and the interphase heat transfer in the domain. A control volume analysis of the governing equation for ϕ reveals the following relation for the heat ratio:

$$r_h = \frac{T_m\left(x_\parallel\right) - T_s}{T_m\left(x_\parallel + L\right) - T_s} = \frac{T_m\left(x_\parallel \pm a\right) - T_s}{T_m\left(x_\parallel + L \pm a\right) - T_s}, \tag{2.11}$$

where a is any displacement in the streamwise direction. The periodic boundary conditions on ϕ now appear in a very simple form:

$$\begin{aligned} \phi(0, y, z) &= r_h \phi(L, y, z), \\ \phi(x_\parallel, 0, z) &= \phi(x_\parallel, L, z), \\ \phi(x_\parallel, y, 0) &= \phi(x_\parallel, y, L). \end{aligned} \tag{2.12}$$

An important point to be noted is that the heat ratio, or the amount by which the fluid gets heated up (or cooled down) when it reaches the end of the box, is an unknown quantity and it is part of the solution. In this formulation the thermal similarity conditions (cf. Eq. 2.12) are defined in terms of the heat ratio. So the heat transfer problem has to be solved iteratively until the heat ratio converges. In the next section we describe the immersed boundary methodology that is used to solve the heat transfer problem in statistically homogeneous suspensions.

2.5 Solution Approach

The complete details of the hydrodynamic PUReIBM solver are discussed elsewhere (Garg et al. (2010b); Tenneti et al. (2011)). Here the discussion is limited to the solution of the heat transfer problem in statistically homogeneous suspensions using PUReIBM. In PUReIBM, we employ Cartesian grids and solve the mass and momentum conservation equations at all the grid points

(including those lying inside the particles). Similarly the nondimensional temperature field is also solved at all grid points. The governing equation for ϕ that is solved in PUReIBM is

$$\frac{\partial \phi}{\partial t} + \frac{\partial (u_j \phi)}{\partial x_j} = -\frac{\partial q_j^{\phi}}{\partial x_j} + I_s f_{\phi}, \tag{2.13}$$

where $\mathbf{q}^{\phi} = \alpha_f \boldsymbol{\nabla} \phi$ is the heat flux, and f_{ϕ} is the additional immersed boundary (IB) forcing term that is nonzero only in the solid phase. The immersed boundary forcing f_{ϕ} accounts for the presence of the solid particles in the domain by ensuring that the isothermal boundary condition $\phi = 0$ is satisfied on the surface of the solid particles.

The surface of the solid particle is represented by a discrete number of points called boundary points. For spherical particles, the boundary points are specified by discretizing the sphere in spherical coordinates. In Fig. 2.3, a schematic describing the computation of the IB forcing is shown for the equatorial plane passing through the spherical particle. Another set of points called exterior points are generated by projecting these boundary points onto a sphere of radius $r + \Delta r$, where r is the radius of the particle (see exterior point represented by an open circle on the dashed line in figure 2.3). Similarly, the boundary points are projected onto a smaller sphere of radius $r - \Delta r$ and these points are called interior points. In our simulations Δr is taken to be same as the grid spacing. The IB forcing is computed only at the interior points. At these points the fluid temperature is forced in a manner similar to the ghost cell approach used in standard finite-difference/finite-volume based methods (Patankar (1980)). For the boundary condition $\phi = 0$ used in this work, the value of ϕ at the interior points is forced to be opposite in magnitude to the value of ϕ at the corresponding exterior points.

The distinctive feature of PUReIBM is that the forcing f_{ϕ} is computed only at points lying inside the solid particles. This ensures that the fluid–phase temperature field is not contaminated by the scalar IB forcing term f_{ϕ}, just as the fluid–phase velocity field is not contaminated by the hydrodynamic IB forcing. The consequences of fluid velocity contamination by IB forcing are discussed in detail by Tenneti et al. (2011). The computation of f_{ϕ} is similar to the computation of the IB forcing for the velocity field. The IB forcing term f_{ϕ}^{n+1} at the $(n+1)$th time–step is specified to cancel the remaining terms in the governing equation for ϕ and force

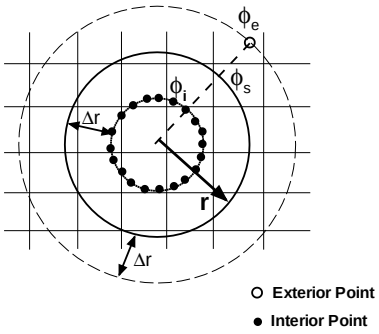

Figure 2.3: A schematic showing the computation of the immersed boundary forcing f_ϕ for an isothermal particle. The solid circle represents the surface of the particle at r. Open dot shows the location of one exterior point at $r + \Delta r$ (only one exterior point is shown for clarity, although there is one exterior point for each interior point) and filled dots show the location of interior points at $r - \Delta r$ where the immersed boundary forcing is computed. In the schematic, ϕ_e represents the temperature at the exterior point, ϕ_s is the surface temperature while ϕ_i is the temperature at the interior point.

the nondimensional temperature to its desired value ϕ^d at the interior points:

$$f_\phi^{n+1} = \frac{\phi^d - \phi^n}{\Delta t} + C_\phi^n - \left(\frac{\partial q_j^\phi}{\partial x_j} \right)^n \tag{2.14}$$

where C_ϕ^n is the convective term at the n time step.

The heat transfer equation (cf. Eq. 2.13) in PUReIBM is solved using a pseudo-spectral method, with a Crank–Nicolson scheme for the viscous terms, and an Adams-Bashforth scheme for the convective terms. The use of Fourier transforms in the cross stream directions and the Crank–Nicolson scheme in the streamwise direction results in an independent set of cyclic tridiagonal systems that are solved using the Sherman–Morrison formula. The coefficient matrices in the tridiagonal systems depend on the heat ratio r_h which is not known *a priori*. The temperature field is initialized with $r_h = 1$ and the simulation is performed iteratively till the value of the heat ratio converges. It must be noted that in this work we use the steady velocity field that is obtained from the hydrodynamic solver and the velocity field is not advanced during the solution of the heat transfer problem.

2.6 Results and Discussion

The hydrodynamic solver in the PUReIBM methodology has been extensively validated using a comprehensive suite of test cases (Tenneti et al. (2011)). In order to check the accuracy of the IB methodology for temperature and also to verify the thermal similarity boundary condition, we simulate convective heat transfer in a square duct. The no slip walls of the duct for the velocity field as well as the isothermal condition at the walls for the temperature field are generated using the IB methodology described in the previous section.

Using an analytical calculation, Shah and London (1978) found that the Nusselt number for a thermally fully developed laminar flow in a square duct is 2.976. We compare the Nusselt number obtained from PUReIBM simulations for three different Reynolds numbers with the analytical solution in table 2.1. We see that the results obtained from PUReIBM simulations agree very well with the analytical solution. The numerical convergence of Nusselt number with grid resolution for a Reynolds number of 100 is shown in Figure 2.4a.

Table 2.1: Comparison of Nusselt number obtained from PUReIBM simulation of duct flow for three different Reynolds numbers with the Nusselt number derived from an analytical calculation.

Reynolds number	PUReIBM	Analytical
20	3.013	2.976
50	3.029	2.976
100	3.033	2.976

In this figure we plot the relative error between the analytical and numerical solution. We see that the Nusselt number obtained from PUReIBM simulations converge to the analytical value given by Shah and London (1978). In figure 2.4b we plot the contours of the scaled temperature θ (cf. Eq. 2.4) along the flow direction. This plot verifies that the thermal similarity condition applied at the ends of the domain generates a thermally fully-developed flow. These tests confirm the accuracy and numerical convergence of the PUReIBM temperature solver and also the correctness of the application of the thermal similarity condition.

We now study heat transfer in statistically homogeneous gas–solid flow using PUReIBM PR-DNS of steady flow and heat transfer past stationary, isothermal particles in periodic domains.

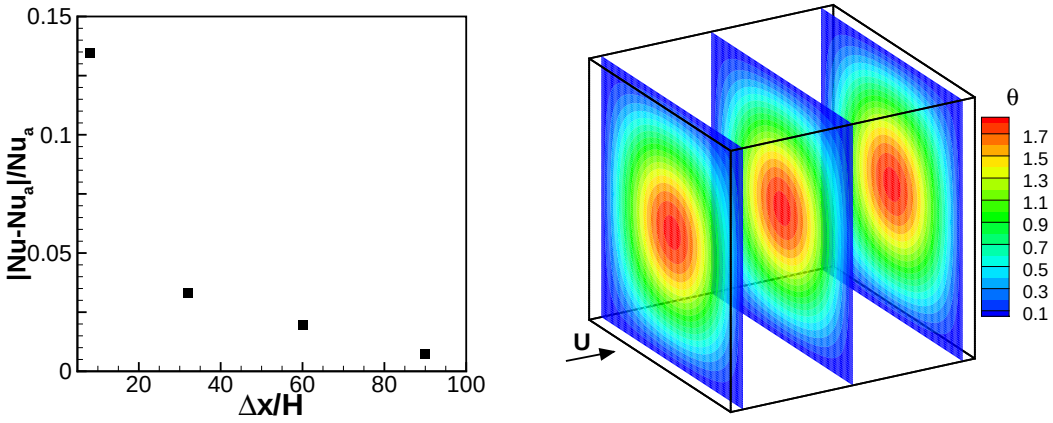

(a) (b)

Figure 2.4: 2.4a Convergence characteristics of Nusselt number with grid resolution for internal duct flow at a Reynolds number of 100 are shown in. In this plot Nu_a referes to the analytical value of the Nusselt number obtained by Shah and London (1978), Δx is the size of the grid cell and H is the channel height. 2.4b Contours of the scaled temperature θ are shown in three planes along the direction of the flow shown by the arrow.

Particle centers are initialized corresponding to a specified mean solid volume fraction ε_s. The particles are fixed in a random equilibrium configuration they attain following elastic collisions (in the absence of ambient fluid) starting from a lattice arrangement with a Maxwellian velocity distribution. The elastic collisions are simulated using a soft–sphere discrete element model (Cundall and Strack (1978); Garg et al. (2010a)). The pair correlation function at equilibrium specifies the particle configuration for random assemblies. Steady flow is established in the fixed bed by imposing a mean pressure gradient that corresponds to a mean flow Reynolds number. The hydrodynamic solver has been extensively validated in a comprehensive suite of tests (Tenneti et al. (2011)). The steady velocity field that is established in the fixed bed is used to evolve the temperature in pseudo–time until the heat ratio reaches a steady state.

The heat transfer problem is statistically inhomogeneous only in the direction of the mean flow and hence all statistics are estimated using area averages in planes perpendicular to the mean flow. Each random particle configuration is termed a realization of the gas–solid flow corresponding to a specified volume fraction and pair correlation function. The streamwise

variation of Nusselt number for the ω realization is defined as

$$\mathrm{Nu}\left(x_{\parallel};\omega\right)=\frac{q''\left(x_{\parallel};\omega\right)D}{k_f P\left(T_m\left(x_{\parallel};\omega\right)-T_s\right)}. \tag{2.15}$$

In this definition, $q''\left(x_{\parallel};\omega\right)$ is the interphase heat flux from the particles to the fluid that is averaged in the cross plane at the location x, and P is the perimeter formed by cutting the particles with the plane. The streamwise variation of Nusselt number obtained from a single realization is prone to statistical uncertainty due to finite number of particles in the computational domain. Therefore, the streamwise variation of Nusselt number from a single realization must be averaged over multiple independent simulations (MIS), each corresponding to a different realization of the particle configuration, to get a better estimate for the ensemble–averaged streamwise Nusselt number. If the streamwise Nusselt number obtained from averaging over several realizations is independent of the spatial location, we can say that the Nusselt number is statistically homogeneous. In that case volume averaging can also be used to improve this estimate.

From the PUReIBM heat transfer simulations we verify that the thermal similarity boundary condition produces a statistically homogeneous streamwise Nusselt number. Figure 2.5 shows the streamwise variation of Nusselt number (top panels) for a fixed bed with a solid volume fraction of 0.4 and mean flow Reynolds number of 100. In Fig. 2.5 we compare the local Nusselt number obtained from averaging over 50 MIS (Fig. 2.5a) with that obtained from averaging over 5 independent realizations (Fig. 2.5b). We see that the Nusselt number obtained from 50 MIS is constant along the flow direction. The Nusselt number from 5 MIS shows some variation along the axial direction. The finite size of the computational domain in the cross stream direction and also the small number of independent realizations are responsible for this streamwise variation in the Nusselt number. To see this more clearly, the variation of the area occupied by the fluid A_f along the flow direction is also shown in Fig. 2.5 (bottom panels). Recall that one of the conditions for statistical homogeneity of Nusselt number is that the area occupied by the fluid should be constant along the flow direction. The figures indicate that the estimate for the average area occupied by the fluid can vary along the flow direction and also at any given axial location there are fluctuations in the area across realizations (indicated by

error bars). The amplitude of the fluctuation in the area is found to be about 7% when the averaging is performed over 5 MIS. From convergence studies, we found that 50 realizations are required to reduce the amplitude in the fluctuation of the area to 2%. Similar requirements on the number of independent realizations were reported by Xu and Subramaniam (2010) in their study of particles in upstream turbulence. Figure 2.5a shows that the variation as well as the level of fluctuations in the Nusselt number and the area fraction are reduced when the averaging is performed over 50 MIS. We conclude that for statistically homogeneous assemblies, the formulation developed for the heat transfer problem ensures that the local Nusselt number is statistically homogeneous.

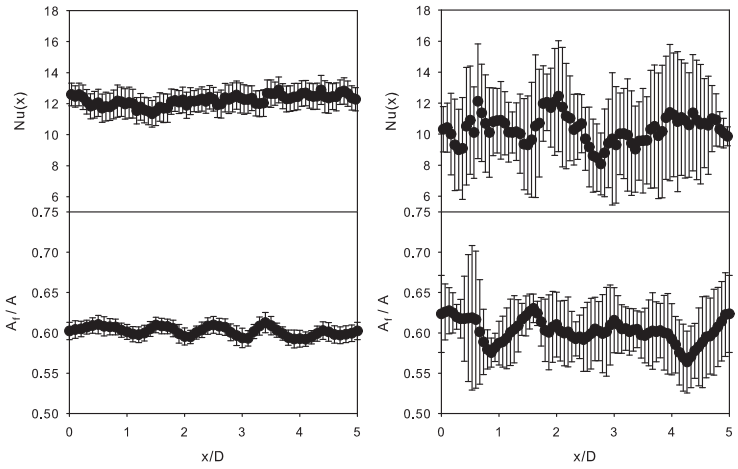

Figure 2.5: Variation of Nusselt number and the area occupied by the fluid–phase along the direction of the mean flow, obtained from PUReIBM simulations of heat transfer in a fixed bed at a volume fraction of 0.4 and mean flow Reynolds number of 100. The local Nusselt number is reported by averaging over 2.5a 50 and 2.5b 5 MIS.

Due to the statistical homogeneity of the Nusselt number in the streamwise direction, we can compute the average Nusselt number $\langle \mathrm{Nu} \rangle$ by averaging $\mathrm{Nu}(x_{\parallel})$ along the axial direction. Figure 2.6 shows compares the average Nusselt number obtained from PUReIBM simulations with the Nusselt number predicted by Gunn's correlation (Gunn (1978)). From the figure we see that the average Nusselt number increases with both solid volume fraction and mean flow Reynolds number and this behavior is consistent with the trend predicted by the correlation. It

must be noted that the Nusselt number correlation given by Gunn (1978) is a fit to experimental data obtained by several researchers for packed beds ($\varepsilon_s = 0.6$). Given that the experimental data itself has a wide variation, the agreement between the PUReIBM DNS and the correlation is excellent.

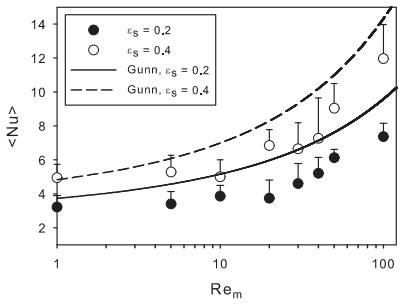

Figure 2.6: Behavior of the average Nusselt number $\langle \mathrm{Nu} \rangle$ with mean flow Reynolds number for two solid volume fractions. Symbols indicate data obtained from PUReIBM simulations while the solid lines are obtained from Gunn's correlation (Gunn (1978)).

In addition to the average Nusselt number, the nature of inhomogeneity of the fluid temperature field or fluid heating is important in modeling the average interphase heat transfer $\langle Q_{g-s} \rangle$. We plot the non-dimensional bulk temperature ϕ_m along the flow direction for two mean flow Reynolds numbers (1 and 100) and two solid volume fractions (0.2 and 0.4) in Fig. 2.7a. In this setup the particles are cooler than the incoming fluid and so the effect of the particles is to reduce the bulk fluid temperature. The results confirm the fact that the temperature field is not homogeneous in the flow direction. We see that the inhomogeneity in the nondimensional bulk temperature is especially apparent at high solid volume fraction and low Reynolds number. This spatial inhomogeneity is found to arise from the effect of fluid cooling, which is more pronounced at high solid volume fraction and low Reynolds number. This result is more easily evident when we consider the behavior of heat ratio r_h. Recall that the heat ratio gives a measure of the fluid cooling because $(1 - r_h)/r_h = (T_{m,out} - T_{m,in})/(T_{m,in} - T_s)$. Two limiting cases are of interest. If there is negligible fluid cooling, then $T_{m,out} \approx T_{m,in}$, and $r_h \approx 1$, in which case $(1 - r_h)/r_h \approx 0$. The other limiting case is of extreme cooling such that $T_{m,out} \approx T_s$, in which case $(1 - r_h)/r_h \approx -1$. Figure 2.7b shows a plot of this measure of fluid cooling, and we see that $(1 - r_h)/r_h$ is close to -1 at low mean slip Reynolds numbers and this

corresponds to near maximal cooling. As the Reynolds number increases the amount of cooling reduces and $(1 - r_h)/r_h$ departs from -1 towards zero.

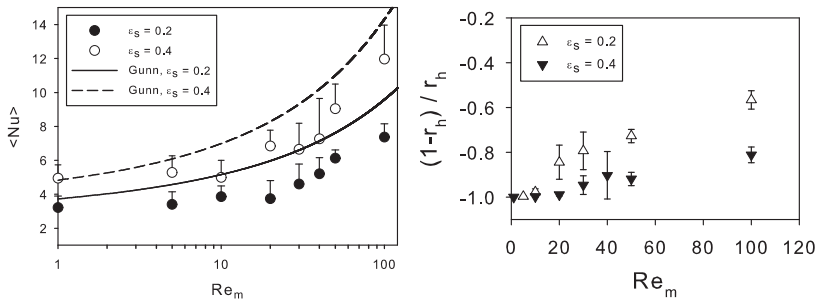

(a) (b)

Figure 2.7: 2.7a Variation of the nondimensional bulk fluid temperature along the axial direction for two mean flow Reynolds numbers (1 and 100) and two solid volume fractions (0.2 and 0.4). 2.7b Behavior of heat ratio with Reynolds number for two solid volume fractions (0.2 and 0.4).

The inhomogeneity in the mean fluid temperature has certain implications on modeling the average gas–solid heat transfer in two–fluid models. In treating the solid phase as a continuum in the two–fluid models there is an implicit assumption of separation of scales. It is assumed that the mean solid phase velocity and temperature vary on length scales that are much larger than the length scales over which the microstructure varies. And in turn, it requires the mean fluid temperature also to vary on similar length scales. However, the scale of variation of ϕ_m in Fig. 2.7a indicates that the mean fluid temperature can be inhomogeneous on the scale of the particle diameter. Therefore, the inhomogeneity of the average fluid–phase temperature cannot be neglected for all values of the solid volume fraction and mean slip Reynolds number in the CFD implementations of models for average gas–solid heat transfer. Consequently, these results indicate that in general a more sophisticated multiphase large-eddy simulation (LES) approach is necessary to properly account for the effects of fluid cooling (or heating) over all values of the solid volume fraction and mean slip Reynolds number.

2.7 Conclusions

In this work we present a particle–resolved direct numerical simulation methodology to study heat transfer in statistically homogeneous gas–solid flow. The Particle–resolved Uncontaminated–fluid Reconcilable Immersed Boundary Method (Tenneti et al. (2011)) (PUReIBM) has been extended to investigate heat transfer in fixed periodic assemblies of monodisperse spherical particles held at a constant uniform temperature. Periodic arrangement of particles induces a velocity field that is periodic in all three directions. Since the mean fluid velocity has a direction and all the particles are held at the same temperature, the resulting temperature field will not be periodic. In order to be consistent with the periodic arrangement of the particles, a thermal similarity boundary condition is applied on the temperature field by drawing analogy from thermally fully developed flow in pipes. The extension of PUReIBM to solve for the temperature field is validated by solving the heat transfer problem in a square duct. Numerical convergence and the validity of the thermal similarity condition in flow past random assemblies of spheres is verified. From PUReIBM PR–DNS of heat transfer in fixed particle assemblies, we establish that the formulation developed for heat transfer results in a statistically homogeneous average Nusselt number. We conclude that fluid heating (cooling) in gas–solid systems results in an inhomogeneous bulk fluid temperature. However, two–fluid CFD models that are used to solve for heat transfer in gas–solid systems employ the assumption of local homogneity of the bulk fluid temperature. Based on the PR–DNS results presented here, we conclude that for $\varepsilon_s < 0.4$ and $\mathrm{Re_m} > 10$, the bulk fluid temperature decays over a few particle diameters. The inhomogeneity of the bulk fluid temperature in these gas–solid flow systems can be accounted for in two–fluid CFD models by an appropriate choice of the grid size. However, for gas–solid flow systems with $\varepsilon_s > 0.4$ and $\mathrm{Re_m} < 10$ the bulk fluid temperature decays over a length scale that is on the order of a particle diameter. In such regimes, the assumption of separation of scales that is implicit in the underlying continuum formulation itself breaks down. Hence, more sophisticated subgrid models for the bulk fluid temperature are required for CFD of heat transfer in gas–solid systems of high solid volume fraction and low mean flow Reynolds number.

CHAPTER 3. MODELING GAS-SOLID HEAT TRANSFER USING PARTICLE RESOLVED DIRECT NUMERICAL SIMULATION: AVERAGE GAS-SOLID HEAT TRANSFER

This chapter is an article titled "Modeling average gas–solid heat transfer using particle-resolved direct numerical simulation" published in International Journal of Heat and Mass Transfer. This paper is authored by B. Sun, S. Tenneti and S. Subramaniam.

The purpose of this chapter is to develop gas–solid heat transfer models using Particle-resolved Direct Numerical Simulations (PR–DNS). Gas–solid heat transfer in steady flow through a homogeneous fixed assembly of monodisperse spherical particles is simulated using the Particle-resolved Uncontaminated-fluid Reconcilable Immersed Boundary Method (PUReIBM). PR–DNS results are obtained over a range of mean slip Reynolds number (1-100) and solid volume fraction (0.1-0.5). Fluid heating is important in gas–solid heat transfer, especially in dense low-speed flows, and the PUReIBM formulation accounts for this through a heat ratio which appears in the thermal self–similarity boundary condition that ensures thermally fully developed flow. The average volumetric interphase heat transfer rate (average gas–solid heat transfer) that appears in the average fluid temperature evolution equation is quantified and modeled using PR–DNS results. The Nusselt number corresponding to average gas–solid heat transfer is obtained from PR–DNS data, and compared with Gunn's Nusselt number correlation (Gunn (1978)). A new Nusselt number correlation is proposed that fits the PR–DNS data more closely and also captures the Reynolds number dependence more accurately. It is shown that the use of Nusselt number correlations based on the average bulk fluid temperature in the standard two–fluid model for gas–solid heat transfer is inconsistent, and results in up to 35% error in prediction of the average gas–solid heat transfer. Using PR–DNS data, a consistent two–fluid model is proposed that improves the predicted average gas–solid heat transfer.

3.1 Introduction

Gas–solid heat transfer is important in many emerging technologies such as carbon-neutral energy generation using biomass (Azar et al. (2006)), chemical looping combustion (Shen et al. (2008)), and CO_2 capture (Abanades et al. (2004); Yi et al. (2007); Miller et al. (2012)). An improved understanding of gas–solid heat transfer is crucial for process and component design in the development of these technologies. CFD simulations (Syamlal et al. (1993); Kashiwa and Gaffney (2003); Sun et al. (2007)) of multiphase flow are increasingly being used as an efficient alternative to experiments for process and design optimization, because experiments are often costly and time-consuming. Since the averaged equations governing mass, momentum, and energy that are solved in multiphase CFD simulations are obtained by using a statistical averaging procedure (Anderson and Jackson (1967); Drew and Passman (1998)), terms such as the average interphase transfer of momentum and energy between different phases need to be modeled.

Specifically, in the absence of mass transfer between phases the average fluid temperature equation from two–fluid theory (Syamlal et al. (1993); Garg (2009)) reads as follows:

$$\underbrace{\frac{\partial}{\partial t}\left\{\rho_f \varepsilon_f c_{pf} \langle T^{(f)} \rangle\right\}}_{\text{unsteady term}} + \underbrace{\frac{\partial}{\partial x_j}\left\{\rho_f \varepsilon_f c_{pf} \langle u_j^{(f)} \rangle \langle T^{(f)} \rangle\right\}}_{\text{mean flow convection}} = \underbrace{\left\langle \frac{\partial I_f}{\partial x_j} q_j \right\rangle}_{\substack{\text{(1) average gas–solid} \\ \text{heat transfer}}} \underbrace{- \frac{\partial}{\partial x_j}\langle I_f q_j \rangle}_{\substack{\text{(2) average conduction} \\ \text{in the fluid phase}}} \underbrace{- \frac{\partial}{\partial x_j}\left\{\rho_f c_{pf} \langle I_f u_j''^{(f)} T''^{(f)} \rangle\right\}}_{\substack{\text{(3) transport of temperature-} \\ \text{velocity covariance}}}, \tag{3.1}$$

and it contains the following unclosed terms: 1) average gas–solid heat transfer, 2) average conduction in the fluid phase, and 3) transport of temperature-velocity covariance. In Eq. 3.1, ρ_f and c_{pf} are the density and specific heat of the fluid phase, respectively, $q_j = -k_f \partial T / \partial x_j$ is the heat flux vector and $\varepsilon_f = \langle I_f \rangle$ is the volume fraction of the fluid phase, where $I_f(\mathbf{x}, t)$ is the fluid-phase indicator function that is unity if the point $\mathbf{x}$ lies on the fluid-phase at time t, and zero otherwise. If $\psi(\mathbf{x}, t)$ is any field (velocity or temperature), then its phasic average

$\langle \psi^{(f)} \rangle (\mathbf{x}, t)$ (average fluid velocity $\langle u_j^{(f)} \rangle$ and average fluid temperature $\langle T^{(f)} \rangle$) is its average value conditional on being in the fluid phase, which is defined as:

$$\left\langle \psi^{(f)} \right\rangle (\mathbf{x}, t) = \frac{\langle I_f(\mathbf{x}, t) \psi(\mathbf{x}, t) \rangle}{\langle I_f(\mathbf{x}, t) \rangle}. \tag{3.2}$$

We use angle brackets to denote ensemble–averaging of random fields over all particle configurations, and an overbar to indicate spatial averages[1] Using the phasic average, the fluctuating components of the fluid velocity and temperature in Eq. 3.1 are defined as $u_j''^{(f)} = u_j - \langle u_j^{(f)} \rangle$ and $T''^{(f)} = T - \left\langle T^{(f)} \right\rangle$, where these fluctuations depend on spatial location and time, although for brevity this dependence is not explicitly shown. The average fluid velocity is obtained by solving the averaged momentum and mass conservation equations. In order to solve Eq. 3.1 for the average fluid temperature, closure models are needed for terms (1)–(3). In a typical two–fluid simulation of gas–solid flow, this equation is coupled to a similar averaged temperature equation for the solid phase (Hrenya and Morris (2014)), but this work only focuses on models for average gas–solid heat transfer term in the average fluid temperature equation.

Although there has been theoretical analysis and experimental measurements of gas–solid heat transfer, it is difficult to develop models for the unclosed terms that are valid over a wide range of solid volume fraction and mean slip Reynolds number using these approaches. For instance, theoretical studies of heat transfer in gas–solid flow are limited to creeping flow past an isolated sphere (Clift et al. (1978)), ordered spheres (Sorensen and Stewart (1974); Pfeffer and Happel (1964)), or moderate flow past random assemblies of spheres (Gunn (1978); Acrivos et al. (1980)). At finite Reynolds number, the nonlinearity of the governing equations and the randomness in particle positions and velocities pose significant obstacles to theoretical analysis. Experimental measurement of gas–solid heat transfer is also challenging because of limited optical access. Various experimental techniques, such as axial heat conduction (Kunii and Smith (1961)), step response (Handley and Heggs (1968)), frequency response (Littman et al. (1968); Gunn and Desouza (1974)), and shot response (Wakao et al. (1977); Shen et al. (1981)) have been used to study heat transfer in gas–solid fixed-bed reactors over the last several decades (Wakao and Kaguei (1982)). However, these experimental studies

[1]For this problem these spatial averages appear as either a cross-sectional average of a random field that still depends on the particle configuration, or as a streamwise average of an inhomogeneous ensemble–averaged field.

report values for the Nusselt number in packed beds ($\varepsilon_s \approx 0.6$) that differ by three or four orders of magnitude (Wakao and Kaguei (1982)). Since most experimental measurements of heat transfer in gas–solid flow are intrusive, the flow disturbance caused by the probes is also a source of uncertainty. Furthermore, the gas–solid heat transfer rate is inferred from point-wise temperature measurements using simplified one–dimensional models of heat transfer that are based on assumptions such as the neglect of axial conduction in the fluid phase. Therefore, the validity of the assumptions implicit in these simplified one–dimensional models used in the inferential procedure is also a source of uncertainty.

This motivates us to use particle–resolved direct numerical simulation (PR–DNS), which is a first-principles, model-free simulation method that solves for the instantaneous three–dimensional velocity and temperature fields representing the flow and heat transfer around each particle. PR–DNS can be used to quantify the unclosed terms in Eq. 3.1, since these terms can be directly calculated from the instantaneous three–dimensional velocity and temperature fields. Indeed, several researchers have successfully extracted correlations for the average interphase *momentum* transfer in gas–solid flow by simulating steady flow past statistically homogeneous fixed assemblies of spherical particles (Hill et al. (2001a,b); Van der Hoef et al. (2005); Beetstra et al. (2007a); Yin and Sundaresan (2009); Tenneti et al. (2011)) in periodic domains. In recent years, researchers have also used PR–DNS to investigate heat transfer in gas–solid flow. Two-dimensional PR–DNS studies (Yu et al. (2006); Feng and Michaelides (2009)) on simulating gas–solid flow in an infinite channel with an isothermal particle have been reported. Haeri and Shrimpton (Haeri and Shrimpton (2013)) set up a staggered tube bank to study convective heat transfer in gas-solid flow with inflow and outflow boundary conditions. Massol and Simonin (Massol et al. (2004)) studied heat transfer in a fixed array of monodisperse spheres using three-dimensional PR–DNS. However, their formulation uses a source/sink term that is strictly valid only for those cases where fluid heating is negligible during the time it takes the flow to transit the computational domain. This restriction holds only for dilute suspensions at high Reynolds number (Acrivos et al. (1980)). Deen et al. (2012, 2014) and Tavassoli et al. (2013) used three-dimensional PR–DNS with inflow and outflow boundary conditions to compute the gas–solid heat transfer coefficient and Nusselt number that are

compared with Gunn's correlation (Gunn (1978)). Feng and Musong (2014) found that the entrance effect of heat transfer on particles in the fluidized bed is to produce high heat transfer rate on particles. However, these studies did not quantify all the unclosed terms in the average fluid temperature equation (Eq. 3.1).

Recently, Tenneti et al. (2013) have shown that fluid heating can be accounted for in three-dimensional PR–DNS of thermally fully–developed flow in periodic domains using a thermal self–similarity condition. In that work, the role of fluid heating and the Nusselt number for gas–solid heat transfer was reported for a limited range of Reynolds number $\mathrm{Re_m}$ and volume fraction ε_s. This study builds on the work of Tenneti et al. (2013) to comprehensively characterize the dependence of Nusselt number on solid volume fraction and mean slip Reynolds number, and to quantify and model the average gas–solid heat transfer.

Gunn (1978) developed a Nusselt number correlation for average gas–solid heat transfer that is a fit to experimental data from many sources that vary by several orders of magnitude (Wakao and Kaguei (1982)). Gunn's Nusselt number correlation can be used to compute the average gas–solid heat transfer, and it is widely used to model the first unclosed term of the right-hand side (RHS) of Eq. 3.1 (average gas–solid heat transfer) in CFD simulation of gas–solid heat transfer (Benyahia et al. (2012)). Tavassoli et al. (2013) and Tenneti et al. (2013) have used PR–DNS to quantify the average Nusselt number to compare with Gunn's correlation over a limited range of Reynolds number and volume fraction. However, the performance of Gunn's correlation needs to be assessed over a wide range of these parameters using PR–DNS. Additionally, the Nusselt number is computed in terms of the average bulk fluid temperature in Gunn's correlation (Gunn (1978)) and in the PR–DNS by Tenneti et al. (2013) and Tavassoli et al. (2013). However, in the two–fluid model, the difference between average fluid temperature (instead of the average bulk fluid temperature) and average solid temperature is used to compute the average gas–solid heat transfer. We address the question whether using the average fluid temperature in the two–fluid model is consistent with the Nusselt number definition, and whether this model is appropriate to accurately compute the gas–solid heat transfer.

The rest of the paper is organized as follows. In Section 3.2, we describe the heat transfer

problem in a fixed particle assembly and discuss the assumptions needed to simplify this problem. In Section 3.3, the PR–DNS approach that is used to solve this heat transfer problem is briefly described. The computation of the unclosed average gas–solid heat transfer term in the two–fluid model from PR–DNS data is then described. In Section 3.4, numerical convergence and the choice of numerical parameters are discussed. In Section 3.5 we compute the average Nusselt number and propose an new Nusselt number correlation for gas–solid heat transfer using PR–DNS data. We evaluate the accuracy of a standard two–fluid model for the average gas–solid heat transfer rate by comparison with PR–DNS data and propose an improved model in Section 3.6 . Finally, Section 3.7 discusses the applicability of the results and in Section 3.8 we summarize the principal findings of this work.

3.2 Gas–solid heat transfer in flow past a fixed assembly of particles

We consider gas–solid heat transfer in a steady flow past a homogeneous fixed assembly of monodisperse spherical particles as Fig. 3.1 shows.Although the hydrodynamic problem is statistically homogeneous, the mean fluid velocity is anisotropic. This directionality in the flow implies that fluid that is downstream of a particle is heated up (or cooled down) by interphase heat transfer, relative to fluid that is upstream of the particle. In other words, when we have forced convection heat transfer in a fixed assembly of particles with finite mean slip velocity $\langle \mathbf{W} \rangle = \left\langle \mathbf{u}^{(f)} \right\rangle - \left\langle \mathbf{u}^{(s)} \right\rangle$, where $\left\langle \mathbf{u}^{(f)} \right\rangle$ and $\left\langle \mathbf{u}^{(s)} \right\rangle$ are the average velocities in the fluid phase and solid phase, the fluid temperature varies with streamwise location in the particle assembly, and the average fluid temperature cannot be assumed to be uniform. With this heating or cooling of fluid by particles, the thermal problem becomes statistically inhomogeneous in the streamwise direction. This feature of heat transfer in gas–solid flows is well established (Acrivos et al. (1980)).

The inhomogeneity of the fluid temperature in a fixed particle assembly implies that in order to model unclosed terms in the average fluid temperature equation (Eq. 3.1), the average gas–solid heat transfer needs to be extracted from spatially varying surface statistics. However, spatially varying surface statistics converge slowly (Xu and Subramaniam (2010)) even with a large number of realizations, where each realization corresponds to a different particle configura-

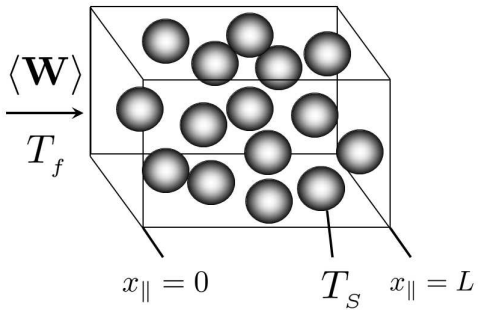

Figure 3.1: Schematic of steady flow with mean slip velocity $\langle \mathbf{W} \rangle$ through a fixed assembly of isothermal particles. The temperatures in the fluid phase and solid phase are $T_f(\mathbf{x}, t)$ and T_s, respectively. The inlet and outlet of the domain are at $x_\| = 0$ and $x_\| = L$, respectively.

tion with the same solid volume fraction and pair correlation function. However, Tenneti et al. (2013) showed that if the flow is thermally fully–developed, then the Nusselt number is statistically homogeneous even though the average fluid temperature varies in the streamwise direction. Therefore, in a thermally fully–developed flow, the average Nusselt number can be computed by volume–averaging using fewer realizations. Tenneti et al. (2013) developed a thermal self-similarity condition for gas–solid heat transfer in steady flow past a statistically homogeneous fixed assembly of particles that results in a thermally fully–developed flow. The same boundary condition has also been used by Tyagi and Acharya (2005) for simulating heat transfer in duct flow. We briefly summarize Tenneti et al. (2013) formulation of thermally fully–developed gas–solid flow here for completeness.

The assumptions made to simplify this heat transfer problem are the same as in Tenneti et al. (2013); Tenneti and Subramaniam (2014), namely: (i) isothermal particles with a single spatially uniform temperature for all particles that is constant in time, and (ii) neglect of radiation and free convection. A detailed justification for these assumptions can be found in Tenneti et al. (2013). Constant gas properties are also assumed for simplicity of the computation. The fluid temperature field $T(\mathbf{x}, t)$, in the absence of viscous heating, radiation and free convection effects,

obeys the following convection–diffusion equation:

$$\frac{\partial T}{\partial t} + \frac{\partial (u_j T)}{\partial x_j} = \alpha_f \frac{\partial^2 T}{\partial x_j \partial x_j}, \tag{3.3}$$

where $\alpha_f = k_f/\rho_f c_{Pf}$ is the thermal diffusivity in the fluid phase , and k_f is the thermal conductivity in the fluid phase. Equation (3.3) needs to be solved in the fluid with the Dirichlet boundary condition of $T = T_s$ at the surface of the particles, where T_s is the uniform temperature at which all the particles are maintained. As noted earlier, the average fluid temperature varies in the streamwise direction due to fluid heating (or cooling) by the particles. Since interphase heat transfer is driven by the difference between the temperatures in the solid and fluid phases, this results in an average interphase heat flux that also varies along the streamwise direction. The ratio of the response (average heat flux) to the driving force (average temperature difference) determines the Nusselt number, that in general also varies along the streamwise direction. However, if the flow is thermally fully–developed (as in internal pipe flow, see Incropera et al. (2006) for example), then the *locally scaled excess fluid temperature* field [2] θ, defined as:

$$\theta(\mathbf{x}, t) = \frac{T(\mathbf{x}, t) - T_s}{\langle T_m \rangle (x_{||}, t) - T_s}, \tag{3.4}$$

is statistically homogeneous at steady state and does not vary in the streamwise or axial direction $x_{||}$ (Tenneti et al. (2013)), i.e.,

$$\frac{\partial \theta}{\partial x_{||}} = \frac{\partial}{\partial x_{||}} \left(\frac{T(\mathbf{x}) - T_s}{\langle T_m \rangle (x_{||}) - T_s} \right) = 0. \tag{3.5}$$

In the above definition, $\langle T_m \rangle (x_{||}, t)$ is the ensemble–averaged bulk fluid temperature or "mixing–cup" temperature, which is defined as the average of the bulk fluid temperature on each realization ω (corresponding to a particle configuration, which occurs with probability dP_ω), such that

$$\langle T_m \rangle (x_{||}, t) = \int_{\omega \in \Omega} T_m(x_{||}, t; \omega)\, dP_\omega, \tag{3.6}$$

where the bulk fluid temperature on each realization is

$$T_m(x_{||}, t; \omega) = \frac{\int_{A_f} (\mathbf{u}T) \cdot \mathbf{e}_{\|} dA_f}{\int_{A_f} \mathbf{u} \cdot \mathbf{e}_{\|} dA_f}, \tag{3.7}$$

[2] For simplicity this quantity is later referred to as simply the scaled fluid temperature.

where $\mathbf{e}_{||}$ is the unit vector along the streamwise direction and A_f is the area occupied by the fluid in a plane perpendicular to the streamwise direction. In general for any function $Q(x_{||}, t; \omega)$ that is defined for a realization ω, we define the ensemble-average as

$$\langle Q \rangle (x_{||}, t) = \int_{\omega \in \Omega} Q(x_{||}, t; \omega)\, dP_\omega. \tag{3.8}$$

The thermally fully–developed condition implies that at steady state the local wall heat flux scaled by the temperature difference $\left(\langle T_m \rangle (x_{||}) - T_s \right)$ is a constant. In other words, the spatial variation of interphase heat flux in response to the temperature difference occurs in such a way that the heat transfer coefficient (or the Nusselt number) at each axial location remains the same throughout the bed. The advantage of establishing a thermally fully–developed flow is that there are no entrance length effects and the average Nusselt number can be calculated by averaging over all the particles in the bed, rather than accounting for its variation in the streamwise direction. This is accomplished by implementing a thermal self–similarity condition, which requires periodic boundary conditions on the scaled fluid temperature (Tenneti et al. (2013)).

For reasons detailed in Tenneti et al. (2013), it is easier to transform the periodic boundary conditions on θ to obtain similarity conditions on the temperature field $T(\mathbf{x}, t)$ and solve Eq. 3.3 for $T(\mathbf{x}, t)$. Simplification of the thermal similarity conditions and homogenization of the boundary conditions on the particle surfaces is accomplished by defining a non–dimensional excess temperature field [3] $\phi(\mathbf{x}, t)$ as follows:

$$\phi(\mathbf{x}, t) = \frac{T(\mathbf{x}, t) - T_s}{\langle T_{m,in} \rangle - T_s}, \tag{3.9}$$

where $\langle T_{m,in} \rangle$ is the average inlet bulk fluid temperature that is defined by Eq. 3.6 in terms of the inlet bulk fluid temperature $T_{m,in}$, which is given by Eq. 3.7 evaluated at $x_{||} = 0$. Using this definition of the non–dimensional temperature, it is easy to see that the average non–dimensional bulk fluid temperature $\langle \phi_m \rangle$ has a similar definition:

$$\langle \phi_m \rangle (x_{||}, t) = \frac{\langle T_m \rangle (x_{||}, t) - T_s}{\langle T_{m,in} \rangle - T_s}. \tag{3.10}$$

[3] For simplicity this quantity is referred to as the non–dimensional temperature.

Substituting Eq. 3.9 in Eq. 3.3 gives the governing equation for the non–dimensional temperature:

$$\frac{\partial \phi}{\partial t} + \frac{\partial (u_j \phi)}{\partial x_j} = \alpha_f \frac{\partial^2 \phi}{\partial x_j^2}. \tag{3.11}$$

The isothermal boundary conditions on the particle surface reduce to $\phi = 0$. The periodic boundary conditions on ϕ now appear in a very simple form:

$$\begin{aligned} \phi(0, y, z) &= r_h \phi(L, y, z), \\ \phi(x_\parallel, 0, z) &= \phi(x_\parallel, L, z), \\ \phi(x_\parallel, y, 0) &= \phi(x_\parallel, y, L), \end{aligned} \tag{3.12}$$

where r_h is the heat ratio, which is defined as:

$$r_h = \frac{\langle T_{m,in} \rangle - T_s}{\langle T_{m,out} \rangle - T_s}. \tag{3.13}$$

In this definition of the heat ratio $\langle T_{m,out} \rangle$ is the average bulk fluid temperature at $x_\parallel = L$, and L is the length of the box. The heat ratio is the ratio of the excess bulk fluid temperature at the inlet ($x_\parallel = 0$) to the excess bulk fluid temperature at the outlet ($x_\parallel = L$). In other words, the heat ratio is simply the inverse of the average non–dimensional bulk fluid temperature at $x_\parallel = L$ i.e.,

$$r_h = \frac{1}{\langle \phi_m \rangle_{out}}. \tag{3.14}$$

The heat ratio quantifies by how much a *fluid* particle heats up when it leaves the box and so this quantity depends solely on the flow structure and the interphase heat transfer in the domain. Note that the heat ratio, or the amount by which the fluid gets heated up (or cooled down) when it reaches the end of the box, is an unknown quantity and is obtained as a part of the solution.

There is a useful relation that shows that the non–dimensional temperature (Eq. 3.9) is simply the product of the scaled temperature (Eq. 3.4) and the average non–dimensional bulk fluid temperature (Eq. 3.10):

$$\phi(\mathbf{x}, t) = \left(\frac{T(\mathbf{x}, t) - T_s}{\langle T_m \rangle (x_{||}, t) - T_s} \right) \left(\frac{\langle T_m \rangle (x_{||}, t) - T_s}{\langle T_{m,in} \rangle - T_s} \right) = \theta(\mathbf{x}, t) \langle \phi_m \rangle (x_{||}, t). \tag{3.15}$$

Multiplying the above equation by the fluid indicator function I_f, taking the expectation (see Eq. 3.8), and using the definition in Eq. 3.2 leads to the corresponding relation between the phase–averaged counterparts:

$$\langle \phi^{(f)} \rangle (\mathbf{x}, t) = \langle \theta^{(f)} \rangle (\mathbf{x}, t) \langle \phi_m \rangle (x_{||}, t), \tag{3.16}$$

Also noting that the θ field is statistically homogeneous at steady state reveals that the inhomogeneity in the steady average fluid temperature field arises solely from the inhomogeneity in the bulk fluid temperature:

$$\langle \phi^{(f)} \rangle (x_{||}) = \langle \theta^{(f)} \rangle \langle \phi_m (x_{||}) \rangle. \tag{3.17}$$

In the next section we describe the numerical method that is used to solve the heat transfer problem and extract unclosed terms.

3.3 Numerical method

The gas–solid heat transfer problem described in Sec. 2 can be solved using our PR–DNS approach, which is called the Particle-resolved Uncontaminated-fluid Reconcilable Immersed Boundary Method (PUReIBM) (Tenneti et al. (2011); Tenneti and Subramaniam (2014); Tenneti (2013)).

3.3.1 PUReIBM formulation

Complete details of the PUReIBM hydrodynamic solver are discussed by Tenneti et al. (Tenneti et al. (2011); Tenneti (2013); Tenneti et al. (2010)) and Garg et al. (2010b). The extension of the PUReIBM hydrodynamic solver to account for the temperature equation in gas–solid heat transfer is described in Tenneti et al. (2013). Here we briefly review the numerical approach to solve the gas–solid heat transfer problem in a fixed assembly of isothermal particles.

It is worth noting that the equations in Section 3.2 are formulated in terms of the ensemble–averaged bulk fluid temperature (see Eqs. 3.9 and 3.13). The solution to these equations can be accomplished by simultaneously solving Eq. 3.11 in parallel for several different particle configurations subject to the boundary conditions is Eqs. 3.12 and 3.14 on a parallel computer.

In this setup each particle configuration and corresponding fluid temperature field is stored on a node, and the ensemble–averaged bulk fluid temperature is communicated to all nodes at the end of each time step. However, it turns out that the statistical variability of the bulk fluid temperature and heating ratio in different particle configurations is small, provided the computational domains are sufficiently large. Therefore, our approach has been to replace the ensemble–averaged bulk fluid temperature with the bulk fluid temperature in that realization. In this case the scaled fluid temperature for each realization is rewritten as follows,

$$\theta(\mathbf{x},t;\omega) = \frac{T(\mathbf{x},t;\omega) - T_s}{T_m(x_{||},t;\omega) - T_s}, \tag{3.18}$$

and the non–dimensional fluid temperature is rewritten as

$$\phi(\mathbf{x},t;\omega) = \frac{T(\mathbf{x},t;\omega) - T_s}{T_{m,in}(\omega) - T_s}. \tag{3.19}$$

This effectively decouples the temperature solution in different particle configurations and allows the solution in each realization to proceed independently. Ensemble-averaged quantities are computed from the individual steady temperature fields corresponding to each realization, as described in the next section. The small statistical variability in the bulk fluid temperature and heating ratio from one realization to another justify this decoupling approach. We can use Eqs. 3.18 and 3.19 at steady state to infer the following useful relation between the non–dimensional, scaled and bulk fluid temperature fields from each realization, which is the analog of Eq. 3.15:

$$\phi(\mathbf{x};\omega) = \left(\frac{T(\mathbf{x};\omega) - T_s}{T_m(x_{||};\omega) - T_s}\right)\left(\frac{T_m(x_{||};\omega) - T_s}{T_{m,in}(\omega) - T_s}\right) = \theta(\mathbf{x};\omega)\phi_m(x_{||};\omega). \tag{3.20}$$

In PUReIBM (see Chapter 2), the following non–dimensional fluid temperature equation is solved at all grid nodes

$$\rho_f c_{pf}\left[\frac{\partial\phi}{\partial t} + \frac{\partial(u_j\phi)}{\partial x_j}\right] = -\frac{\partial q_j^{\phi}}{\partial x_j} + I_s f_{\phi}, \tag{3.21}$$

where $q_j^{\phi} = -k_f \partial\phi/\partial x_j$ is the heat flux per unit temperature difference, I_s is the solid-phase indicator function, and f_{ϕ} is the scalar Immersed Boundary (IB) direct forcing in the solid phase. The immersed boundary forcing accounts for the presence of the solid particles in the domain by ensuring that the isothermal boundary condition $\phi = 0$ is satisfied on the surface

of each solid particle. The surface of the solid particle is represented by a discrete number of points called boundary points. For spherical particles, the boundary points are specified by discretizing the sphere in spherical coordinates. Another set of points called exterior points are generated by projecting these boundary points onto a sphere of radius $r + \Delta r$, where r is the radius of the particle. Similarly, the boundary points are projected onto a smaller sphere of radius $r - \Delta r$ and these points are called interior points. In our simulations Δr is taken to be same as the grid spacing. The IB forcing is computed only at the interior points. At these points the fluid temperature is forced in a manner similar to the ghost cell approach used in standard finite-difference/finite-volume based methods (Patankar (1980)). For the boundary condition $\phi = 0$ used in this work, the value of ϕ at the interior points is forced to be opposite in magnitude to the value of ϕ at the corresponding exterior points.

A distinctive feature of PUReIBM is that the scalar IB forcing f_ϕ is computed only at points lying inside the solid particles. This ensures that the fluid–phase temperature field is not contaminated by the scalar IB forcing term f_ϕ, just as the fluid–phase velocity field is not contaminated by the hydrodynamic IB forcing. The consequences of fluid velocity contamination by IB forcing are discussed in detail by Tenneti et al. (2011). The computation of f_ϕ is similar to the computation of the IB forcing for the velocity field. The scalar IB forcing at the $(n+1)$th time-step f_ϕ^{n+1} is specified to cancel the remaining terms in the governing equation and forces the non–dimensional temperature ϕ^n to its desired value ϕ^d at the particle surface:

$$f_\phi^{n+1} = \rho_f c_{pf} \frac{\phi^d - \phi^n}{\Delta t} + \rho_f c_{pf} C_\phi^n + \left(\frac{\partial q_j^\phi}{\partial x_j} \right)^n \tag{3.22}$$

where $C_\phi^n = [\partial(u_j \phi)/\partial x_j]^n$ is the convective term at the nth time-step. The non–dimensional fluid temperature equation (Eq. 3.21) is solved using a pseudo-spectral method, with the Crank-Nicolson scheme for the viscous terms, and an Adams-Bashforth scheme for the convective terms. Fourier transforms are used in the cross-stream directions and a finite–difference scheme is used in the streamwise direction (Yusof (1996)). Implementation of the periodic boundary conditions in Eq. 3.12 results in an independent set of cyclic tridiagonal systems that are solved using the Sherman-Morrison formula (Tenneti (2013)). Details on the numerical method can be found elsewhere (Tenneti et al. (2011, 2013); Tenneti (2013); Garg et al. (2010b)). A

noteworthy feature of this approach is that the heat ratio r_h in Eq. 3.12 is an unknown quantity and is solved iteratively. The temperature field is initialized with $r_h = 1$ and the simulation is marched in pseudo time until the value of the heat ratio converges.

3.3.2 Relation of PR–DNS data to unclosed terms

In order to quantify the unclosed terms in the average fluid temperature equation in Eq. 3.1 from PR–DNS data, the correspondence between PR–DNS data and the unclosed terms needs to be established. The thermal fully–developed condition guarantees that terms like the Nusselt number and the scaled fluid temperature θ are statistically independent of the streamwise direction as shown by Tenneti et al. (2013). Therefore, we use volume-averaging over the fluid domain to compute those terms. However, since the average fluid temperature varies along the streamwise direction, terms like the average gas–solid heat transfer are not statistically homogeneous and they depend on the streamwise direction. For such terms we use a cross-sectional average, for instance, the average gas–solid heat transfer is computed from the local volumetric interphase heat transfer rate. In order to define the local volumetric gas–solid heat transfer rate $q_\phi'''(x_{||};\omega)$ (see Eq. B.8), the PR–DNS instantaneous fluid temperature equation (Eq. 3.1) is integrated over the cross-sectional area of fluid region A_f in the $y-z$ plane perpendicular to the streamwise direction $x_{||}$ (see details in Appendix B). Cross-sectionally averaged terms such as the local volumetric interphase heat transfer rate $q_\phi'''(x_{||};\omega)$ only depend on the streamwise coordinate.

For cross-sectionally averaged terms such as the local volumetric interphase heat transfer rate, the numerical value from PR–DNS data for every realization ω would equal the corresponding average in the limit that the cross-sectional area of the domain tends to infinity. In practice, acceptable convergence can be obtained with large domain sizes, but the domain size is limited by computer memory. However, even domains that are large enough such that two–point correlations decay to zero may not provide good particle statistics especially at low solid volume fraction. However, the statistical variability in the PR–DNS estimate of the unclosed terms arising from finite number of particles in each domain can be reduced by averaging over multiple independent simulations (MIS) or realizations. For instance, the average gas–solid

heat transfer term is estimated from PR–DNS data as

$$\left\langle \frac{\partial I_f}{\partial x_j} q_j^{\phi} \right\rangle (x_{||}) \approx \frac{1}{M} \sum_{\omega=1}^{M} \left\{ q_{\phi}^{'''}(x_{||};\omega) \right\}, \tag{3.23}$$

where $q_{\phi}^{'''}(x_{||};\omega)$ is given by Eq. B.8 (see Appendix B for details) and M is the number of realizations. The choice of number of MIS depends on the statistic being estimated. We find that mean values and second moments converge fairly quickly within 4 or 5 realizations. Higher–order statistics would require a larger number of realizations to reduce statistical variability.

3.4 Simulation Results and Numerical Convergence

We have performed PR–DNS simulations over a range of mean slip Reynolds number $\mathrm{Re_m}$ = 1-100 and solid volume fraction ε_s = 0.1-0.5 in gas–solid flow with Prandtl number of 0.7, as summarized in Table 3.1. Before discussing the results, we establish numerical convergence of the simulation method for steady gas–solid heat transfer in a fixed particle assembly.

Table 3.1: Parameters for simulation of heat transfer in steady flow past random fixed assemblies of particles. The physical parameters are the solid volume fraction ε_s and the mean slip Reynolds number $\mathrm{Re_m}$. The numerical parameters are the ratio of the box length to the particle diameter L/D and the grid resolution $D_m = D/\Delta x$. The number of particles N_p is determined by ε_s and L. Five independent simulations of each case are simulated to reduce statistical variability.

ε_s	Re_m	L/D	N_p	D_m
0.1	1, 5, 10, 20, 30, 40, 50, 100	7.5	80	20
0.2	1, 5, 10, 20, 30, 40, 50, 100	7.5	161	20
0.3	1, 5, 10, 20, 30, 40, 50, 100	5	71	30
0.4	1, 5, 10, 20, 30, 40, 50, 100	5	95	30
0.5	1, 5, 10, 20, 30, 40, 50, 100	4	61	40

3.4.1 Numerical convergence

Numerical convergence and accuracy of the scalar solver in PUReIBM have been established in Tenneti et al. (2013). The principal numerical parameters relevant to this study are the grid resolution $D_m = D/\Delta x$, domain size L/D and the number of independent simulations. Since these are steady calculations, the time-marching is done in pseudo–time. The Courant-Friedrich-Lewy (CFL) number based on mean slip velocity and grid size is always less than 0.5.

In a previous study (Garg et al. (2010b)) we have shown that the code is stable for this choice of CFL number, and yields convergent solutions with this choice of pseudo–time step.

3.4.2 Grid resolution

Tenneti et al. (2013) compared PUReIBM simulations of steady heat transfer in a duct with an analytical result and showed that the simulation results converge accurately to the analytical value with increasing grid resolution. Here we demonstrate numerical convergence of the Nusselt number for steady heat transfer in flow past random assemblies of monodisperse spherical particles.

Figure 3.2(a) shows the convergence characteristics of the volumetric mean Nusselt number (see Eq. B.18 in Appendix B) with respect to grid resolution $D_m = D/\Delta x$, where D is the particle diameter and Δx is the grid spacing. We choose the box length to be $L/D = 4$ so that different grid resolutions can be tested within available computational resources. Elsewhere we have used the decay of scaled fluid temperature autocorrelation to justify the choice of box length. All simulations here are repeated with the same random particle configuration. The relative error in the volumetric mean Nusselt number between the coarsest grid $D_m = 20$ and the finest grid $D_m = 70$ is about 11%. The volumetric mean Nusselt number at $\varepsilon_s = 0.4$ and $\mathrm{Re_m} = 20$ also converges to an asymptotic value of 7.8 with increasing grid resolution.

3.4.3 Number of realizations

Besides the grid resolution, the statistical variability arising from finite number of particles can be an issue as discussed in Section 3.3.2. In order to obtain good statistics, we need to reduce the statistical variability in the PR–DNS estimate of the unclosed terms arising from finite number of particles by averaging over MIS corresponding to independent particle configurations. The choice of the number of MIS depends on the convergence of statistics as Figure 3.2(b) shows. This figure shows the convergence of average Nusselt number with increasing number of MIS at $\varepsilon_s = 0.4$ and $\mathrm{Re_m} = 20$, along with the 95% confidence intervals corresponding to each set of MIS. We conclude that we can estimate the true average (obtained with 70 realizations) using 5 realizations, while recognizing that the 95% confidence intervals

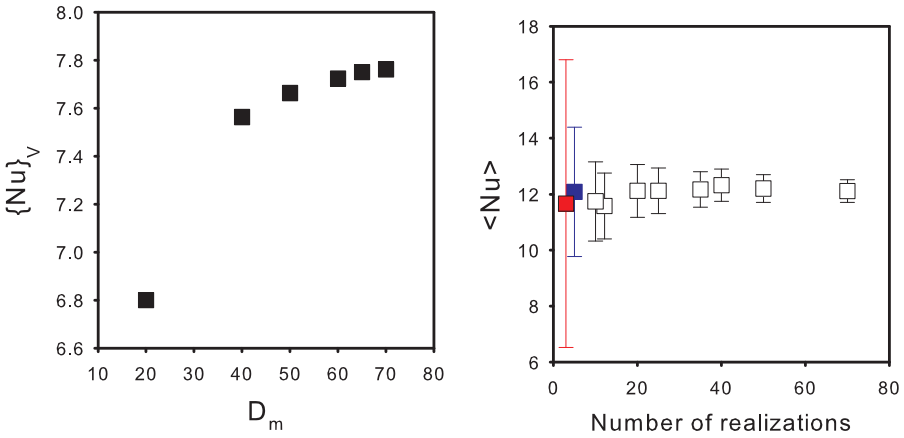

(a) (b)

Figure 3.2: (a) Convergence characteristics of the volumetric mean Nusselt number (see Eq. B.18) with grid resolution $D_m = D/\triangle x$ for heat transfer in a random assembly of spheres at $\mathrm{Re_m} = 20$ and $\varepsilon_s = 0.4$. The same random particle configuration with $L/D = 4$ is used for all grid resolution values. (b) Dependence of average Nusselt number on number of MIS or realizations at $\mathrm{Re_m} = 20$ and $\varepsilon_s = 0.4$. Symbols indicate average Nusselt number and error bars indicate 95% confidence intervals. The red and blue filled symbol represent the average Nusselt number obtained using 2 and 5 realizations, respectively.

with 5 realizations correspond to about 15% of the true average value. Hence, we use 5 MIS for all simulations to obtain the average Nusselt number over a range of Reynolds number and volume fraction.

3.4.4 Choice of numerical parameters

In addition to the grid resolution and number of realizations, the box length is also a numerical parameter, and we have discussed its choice elsewhere. In that work it is shown that the scaled temperature autocorrelation decays within a box of length $5D$ for a solid volume fraction of 0.4 and Reynolds number 100 (lower Reynolds number cases decay to zero within shorter separation distances). Based on this comprehensive study of the dependence of our PR–DNS heat transfer results on the principal numerical parameters, we have chosen values for grid resolution and number of independent simulations that minimize numerical error within the available computational resources (see Table 3.1). However, since we have explored a wide parameter range, each of these choices does incur some numerical error, and we estimate that

in the worst case scenario where all the errors add cumulatively, the maximum numerical error in the average Nusselt number would be 15–20%.

We can estimate the maximum numerical error using an error model similar to that Garg et al. (2007) and Xu and Pope (1999) used. The total numerical error in the average Nusselt number is defined as

$$\epsilon_{\mathrm{Nu}} = \{\mathrm{Nu}\}_{V,D_m} - \langle \mathrm{Nu} \rangle \,, \tag{3.24}$$

where $\{\mathrm{Nu}\}_{V,D_m}$ is the numerical estimate. This total numerical error contains contributions from grid resolution and finite number of particles. In order to calculate the total numerical error in the average Nusselt number, the total numerical error ϵ_{Nu} can be decomposed as

$$\epsilon_{\mathrm{Nu}} = \Sigma_{\mathrm{Nu}} + D_{\mathrm{Nu}} = \Sigma_{\mathrm{Nu}} + B_{\mathrm{Nu}} + S_{\mathrm{Nu}}, \tag{3.25}$$

where Σ_{Nu} is the statistical error, and D_{Nu} is the deterministic error and is further decomposed into bias error B_{Nu} and discretization error S_{Nu}. Note that it is infeasible to determine these coefficients for the entire parameter range of solid volume fraction and Reynolds number with current computational resources. Therefore, we construct the error model based on available PR-DNS data and apply it to find the maximum error in the worst case scenario that corresponds to the lowest grid resolution. Based on this error model, the total numerical error for the worst case scenario with grid resolution $D_m = 20$ is 18.5%, with the major contribution of 12% coming from the discretization error (statistical error contributes 4.5% and bias error contributes only 2%). Of all the simulations, only two cases corresponding to $\varepsilon_s = 0.1$ and $\varepsilon_s = 0.2$ use a grid resolution $D_m = 20$. All the other cases simulated use higher grid resolution $D_m \geq 30$ and therefore incur less discretization error, and consequently less total error. Note that the difference between existing correlations such as Gunn's correlation and the measured data (see Figure 3.3) is several orders of magnitude larger than this error. It is also worth noting that the total numerical error that we have estimated in our "worst case" scenario with $D_m = 20$ is still low compared to the usual error associated with convection heat transfer correlations that is estimated at about 25% (see Chapter 7.2.6 in Incropera et al. (2006)).

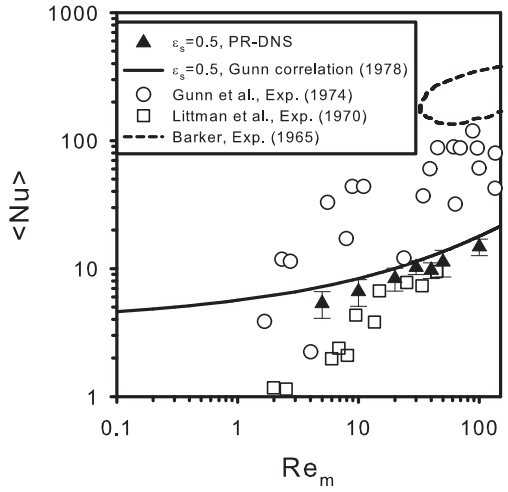

Figure 3.3: Comparison of Nusselt number from experimental data in packed beds with Gunn's correlation and PR-DNS data at $\varepsilon_s = 0.5$. The triangles represent PR-DNS data with 95% confidence and the solid line represents Gunn's correlation (1978) at $\varepsilon_s = 0.5$ that is close to a packed bed. The open circles represent the experimental data from Gunn and Desouza (1974), the open squares represent experimental data from Littman and Sliva (1970), and the range inside dashed line represents Barker's experimental data (Barker (1965)) in a packed bed.

3.5 Nusselt number corresponding to average gas–solid heat transfer

We now compare our PR–DNS data with Gunn's Nusselt number correlation (Gunn (1978)) for gas–solid heat transfer that is widely used in two–fluid CFD models. We propose a new Nusselt number correlation for gas–solid flow that more closely matches our PR–DNS data and that also captures the Reynolds number dependence more accurately. The Nusselt number data obtained from our PUReIBM simulations are also compared with another gas–solid heat transfer PR–DNS reported by Tavassoli et al. (2013). We also compute the average gas–solid heat transfer in the two–fluid model using the Nusselt number from PR–DNS and compare it with the average gas–solid heat transfer extracted directly from PR–DNS. We find discrepancies that we are able to explain and reduce by proposing an improved model for average gas–solid heat transfer that is based on our model for the average bulk fluid temperature.

3.5.1 Computation of Nusselt number from PR–DNS

For gas–solid heat transfer, Gunn's Nusselt number correlation (Gunn (1978)) of experimental data is used to compute the average gas–solid heat transfer in Eq. 3.28. Gunn's correlation (Gunn (1978)) is written as the following function of Reynolds number Re, bed porosity ε_b, and Prandtl number Pr:

$$\mathrm{Nu} = (7 - 10\varepsilon_b + 5\varepsilon_b^2)(1 + 0.7\mathrm{Re}^{0.2}\mathrm{Pr}^{1/3}) + (1.33 - 2.4\varepsilon_b + 1.2\varepsilon_b^2)\mathrm{Re}^{0.7}\mathrm{Pr}^{1/3}. \tag{3.26}$$

This correlation is valid in the bed porosity range $0.35 \leq \varepsilon_b = 1 - \varepsilon_s \leq 1.0$ and $1 \leq \mathrm{Re} \leq 10^5$. We extend Tenneti et al. (2013) comparison of Nusselt number obtained from PR–DNS with Gunn's correlation to comprehensively compare Nusselt number over the range of Reynolds number Re_m and volume fraction ε_s given in Table 3.1. Figure 3.4 shows the dependence of average Nusselt number on Reynolds number at low and high solid volume fractions.The lines in Fig. 3.4(a) (line with symbols in Fig. 3.4(b)) are the Nusselt number obtained from Gunn's correlation (Gunn (1978)) that is a fit to a collection of experimental data obtained from many sources. As expected, at a given volume fraction the average Nusselt number increases with Reynolds number due to an increase in the magnitude of the convection term. While the overall trend of the Nusselt number dependence on Reynolds number is captured by Gunn's correlation, it predicts a higher value of Nusselt number with Reynolds number than seen in the PR–DNS data. Gunn's correlation is within 20% of the PR–DNS data, and there are slight differences in the dependence on Reynolds number.

In order to place this comparison in context it should be noted that Gunn's correlation is an inspired fit to experimental data that vary by several orders of magnitude (see Fig. 3.3). On this scale, the difference between PR-DNS and Gunn's correlation of 20% is infinitesimal in comparison to the discrepancy between the correlation and the measurements themselves. An estimate of the contribution of free convection shows that it contributes less than 13% of the average Nusselt number even in the cases where it is expected to be important (low Reynolds number). The differences between the PR-DNS data and the experiment are more likely to arise from (i) experimental uncertainties (note the wide variation among the experimental studies themselves), (ii) assumption of constant gas properties in the simulations, (iii) the model

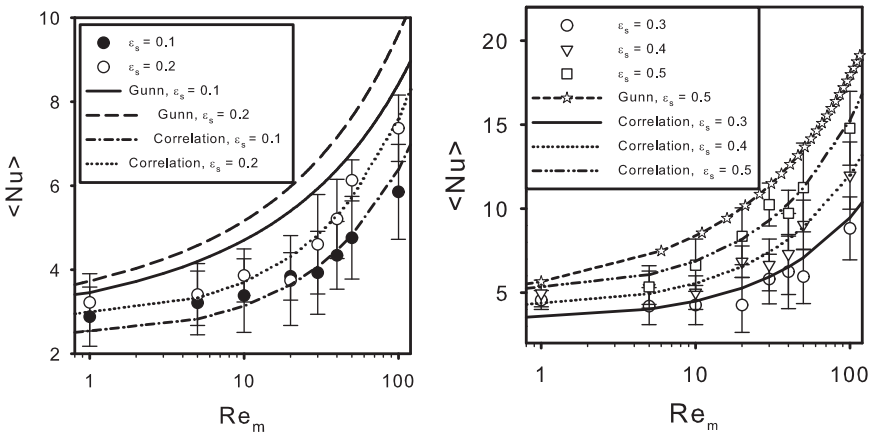

(a) (b)

Figure 3.4: Dependence of the average Nusselt number in random particle assemblies on mean slip Reynolds number $\mathrm{Re_m}$ for (a) low solid volume fraction ($\varepsilon_s \leq 0.2$), and (b) higher solid volume fraction ($\varepsilon_s \geq 0.3$) for gas–solid flow with Pr = 0.7. The symbols are the average Nusselt number from PR–DNS data and error bars indicate 95% confidence intervals using 5 MIS. The lines with symbols represent Gunn's correlation Gunn (1978). The lines without symbols represent the new PUReIBM Nusselt number correlation in Eq. 3.27.

assumption for axial conduction that is used to interpret the Nusselt number in the experimental reports, and (iv) at higher Reynolds number, the neglect of transport of temperature–velocity covariance in the 1-D model used to infer the Nusselt number in the experiments.

Figure 3.5 shows the dependence of the average Nusselt number on solid volume fraction for different Reynolds numbers. At a given Reynolds number, as the solid volume fraction increases so does the average Nusselt number. The dependence on solid volume fraction is explained on the basis that as the isothermal particle surfaces come closer, the temperature gradient in the fluid phase between them increases. In Fig. 3.5 we again see a systematic difference between Gunn's correlation and the PR–DNS data at a solid volume fraction of 0.5.

3.5.2 Nusselt number correlation from PR–DNS

In order to provide a correlation that better fits the PR–DNS data and to capture its dependence on Reynolds number more accurately, the following Nusselt number correlation for

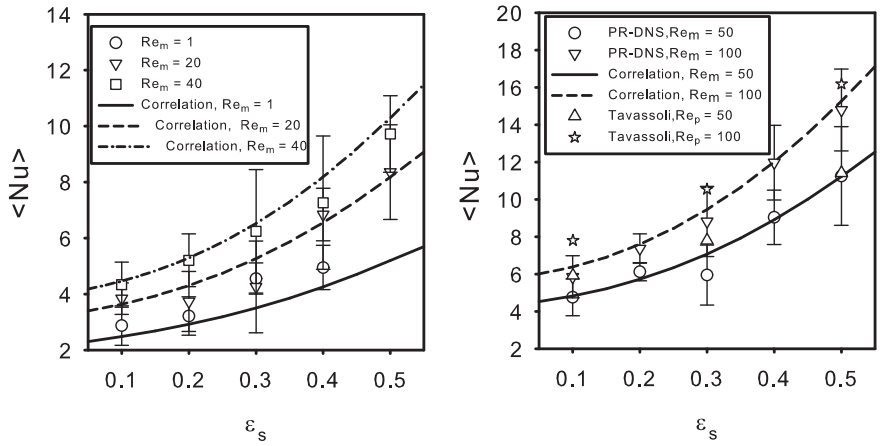

(a) (b)

Figure 3.5: Dependence of the average Nusselt number in random particle assembly on solid volume fraction ε_s (a) at low Reynolds number: $\mathrm{Re_m} = 1$, 20 and 40, and (b) higher Reynolds number: $\mathrm{Re_m} = 50$ and 100, for gas–solid flow with $\mathrm{Pr} = 0.7$. The symbols (open circle, open square, and downward triangle) are the average Nusselt number from PR–DNS data and error bars indicate 95% confidence intervals using 5 MIS. The other symbols (upward triangle and star) at $\varepsilon_s = 0.1$, 0.3, and 0.5 are the data from Tavassoli et al. (2013). The lines represent the PR–DNS Nusselt number correlation.

gas–solid flow is proposed by fitting our PR–DNS data:

$$\mathrm{Nu} = (-0.46 + 1.77\varepsilon_b + 0.69\varepsilon_b^2)/\varepsilon_b^3 + (1.37 - 2.4\varepsilon_b + 1.2\varepsilon_b^2)\mathrm{Re}^{0.7}\mathrm{Pr}^{1/3}. \tag{3.27}$$

For simplicity of notation we drop the angle bracket notation in the expression for this correlation of average Nusselt number. This correlation is valid in the bed porosity range $0.5 \leq \varepsilon_b \leq 1.0$ and $1 \leq \mathrm{Re} \leq 100$. The first term in the new correlation accounts for the dependence of the Nusselt number on volume fraction. It is developed using the same ε_b^3 dependence as Tenneti et al. (2011) employed to propose their PUReIBM drag correlation. This confirms in a limited sense the existence of a Reynolds analogy between drag and heat transfer in gas–solid flows. The second part of the PUReIBM correlation is the same as Gunn's correlation (see Eq. 3.26), and it completely represents the dependence of Nusselt number on Reynolds number. Note that in Gunn's correlation the first term also has a dependence on Reynolds number. As the Reynolds number and solid volume fraction tend to zero ($\varepsilon_b \to 1$), this new PUReIBM correlation also yields the limiting value for the Nusselt number of 2, corresponding to conduction from a

sphere.

In Fig. 3.5 the lines without symbols represent the PUReIBM Nusselt number correlation from PR–DNS data. The average difference between PR–DNS data and the PUReIBM correlation is about 7% for the range of Reynolds numbers considered. Fig. 3.5 also shows that the PUReIBM correlation closely fits most of the PR–DNS data except at low Reynolds number $\mathrm{Re_m} = 1$.

Figure 3.5(b) shows that our PR–DNS data compare with the average Nusselt number from Tavassoli et al. (2013). They also reported that the differences between their selected PR–DNS results and Gunn's correlation are about 20%. Their average Nusselt number values are always larger than those from our PR–DNS data. One possible explanation for this difference could be the difference in the setup of the gas–solid heat transfer problem in the two studies. In the Tavassoli et al. (2013) study the flow domain includes both a thermally developing entrance region and a thermally fully–developed region, whereas in our setup there is only a thermal fully–developed region. Therefore, it is possible that Tavassoli et al. (2013) obtained a higher value of the heat transfer coefficient (and Nusselt number) since the local heat transfer coefficient in the thermally developing entrance region for gas–solid flow is much higher than that in the thermal fully–developed region.

An important point to note is that the Nusselt number in Gunn's correlation as well as in our PR–DNS is computed in terms of the difference between the *bulk* fluid temperature (as shown in Fig. 3.6(a)) and the particle temperature. However, the two–fluid model (cf. Eq. 3.1) calculates the average gas–solid heat transfer in terms of the difference between the average fluid temperature (as shown in Fig. 3.6(b)) and the particle temperature. In Fig. 3.6(a), the average non–dimensional bulk fluid temperature from PR-DNS data denoted by open symbols decays rapidly due to fluid cooling in the streamwise direction. The same trend is also observed in the average non–dimensional fluid temperature as shown in Fig. 3.6(b). However, since the average non–dimensional bulk fluid includes the effect of the local velocity (cf. Eq. 3.6), we show in the following that it is inconsistent to use the Nusselt number defined in terms of the difference between the bulk fluid temperature and the particle temperature in the two–fluid model for average gas–solid heat transfer. Computational results quantify the magnitude

of discrepancy arising from this inconsistency, and we then propose an improved model that reduces the discrepancy.

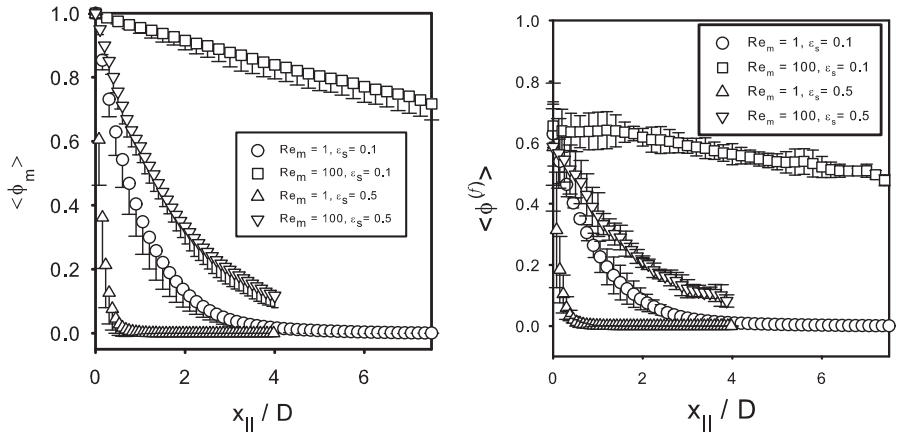

(a) (b)

Figure 3.6: Axial variation of average non–dimensional bulk fluid temperature in Eq. 3.10 and cross-sectional average non–dimensional fluid temperature (Eq. 3.17) from PR–DNS data for $\varepsilon_s = 0.1$ and 0.5 at mean slip Reynolds number of 1 and 100. Error bars in both panels (shown only below the symbols in (a) for clarity) represent 95% confidence intervals inferred from 5 MIS.

3.6 Improved two–fluid model for average gas–solid heat transfer

A widely used two–fluid model (Benyahia et al. (2012)) for the average gas–solid heat transfer rate $\langle q_j \partial I_f / \partial x_j \rangle$ (cf. Eq. 3.1) is written in terms of the difference between average fluid temperature $\left\langle T^{(f)} \right\rangle$ and average solid temperature $\left\langle T^{(s)} \right\rangle$ as

$$q'''_{TF} = \frac{6 k_f \varepsilon_s \mathrm{Nu_m}}{D^2} \left(\left\langle T^{(s)} \right\rangle - \left\langle T^{(f)} \right\rangle \right), \tag{3.28}$$

where ε_s is the solid volume fraction, and $\mathrm{Nu_m}$ is a model for the Nusselt number that is usually taken from a correlation to experimental data. This expression for the average volumetric gas–solid heat transfer rate q'''_{TF} is valid for steady heat transfer in a homogeneous assembly of fixed monodisperse spherical particles, and is derived in Appendix C.

In order to verify the performance of this two–fluid model for average gas–solid heat transfer, we compute the average volumetric interphase heat transfer rate q'''_{TF} from the two–fluid model

as

$$q'''_{TF} = \frac{6\varepsilon_s k_f \mathrm{Nu}}{D^2}\left(\left\langle T^{(s)}\right\rangle - \overline{\langle T^{(f)}\rangle}\right)$$

(see Eq. D.11 in Appendix D) where the PR–DNS data for average Nusselt number in Figs. 3.4 and 3.5 are used. Note that since $\langle T^{(f)}\rangle$ varies significantly along $x_{||}$ in many cases, the two–fluid definition of $\langle T^{(f)}\rangle$ in Eq. 3.28 is appropriately modified as

$$\overline{\langle T^{(f)}\rangle} = \frac{1}{L}\int_0^L \langle T^{(f)}\rangle(x_{||})\, dx_{||}$$

(see Eq. D.10 in Appendix D) when it is used in the two–fluid model.

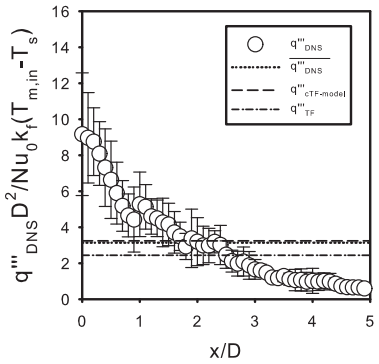

Figure 3.7: Variation of the normalized average volumetric heat transfer rate q'''_{DNS} (cf. Eq. D.12) with axial location $x_{||}$ at $\mathrm{Re_m} = 50$ and $\varepsilon_s = 0.4$. The symbols represent the normalized average volumetric heat transfer rate q'''_{DNS} and error bars indicate 95% confidence intervals using 5 MIS. q'''_{DNS} is normalized by $h_0(T_{m,in} - T_s)/D$, where h_0 is the heat transfer coefficient from the limiting value of Nusselt number $\mathrm{Nu}_0 = h_0 D/k_f = 2$ (at $\mathrm{Re_m} \to 0$ and $\varepsilon_s \to 0$). The dotted line, dashed line, and dot-dashed line represent $\overline{q'''_{DNS}}$ in Eq. D.12, $q'''_{cTF-model}$ in Eq. D.8, and q'''_{TF} in Eq. D.11, respectively.

We also directly compute the average volumetric interphase heat transfer rate $\overline{q'''_{DNS}}$ from PR–DNS data that is a statistical estimate of $\langle q'''_\phi\rangle$ (see Eq. D.12 in Appendix D). Figure 3.7 shows a comparison of the normalized average volumetric interphase heat transfer rate from the two–fluid model and PR–DNS at $\mathrm{Re_m} = 50$ and $\varepsilon_s = 0.4$. The magnitude of the normalized average volumetric interphase heat transfer rate q'''_{DNS} has a large drop from 9.1 to 0.65 over the length of the particle bed. This decay of q'''_{DNS} with axial location $x_{||}$ indicates that the gas–solid heat transfer is not homogeneous over $L = 5D$. The normalized difference between $\overline{q'''_{DNS}}$ and q'''_{TF} is about 19%. Fig. 3.9(a) shows that the normalized difference between $\overline{q'''_{DNS}}$

and q'''_{TF} ranges from 5% to 36% over a range of Reynolds number and solid volume fraction, and increases with increasing solid volume fraction, with the maximum value occurring at $\varepsilon_s = 0.5$. The average volumetric interphase heat transfer rate predicted by the two–fluid model q'''_{TF} is considerably different from $\overline{q'''_{DNS}}$, even though the Nusselt number is taken from PR–DNS data. One reason for this difference is because of the inconsistency in using a Nusselt number based on the difference between bulk fluid temperature and the particle surface temperature in conjunction with a temperature difference based on the average fluid temperature in Eq. 3.28 to obtain the two–fluid model for the average volumetric interphase heat transfer rate q'''_{TF}. As noted earlier, the average Nusselt number in a fixed assembly of particles from PR–DNS is obtained in terms of the difference between the bulk fluid temperature and solid temperature as Eq. B.14, and not the difference between the average fluid temperature and solid temperature. Thus, the difference between the two average volumetric interphase heat transfer rates results from using the average fluid temperature in the two–fluid model. Using a temperature difference based on the bulk fluid temperature is the correct way to compute the average volumetric interphase heat transfer rate in the two–fluid model, but the bulk fluid temperature is not solved as a field variable in the two–fluid model.

Our approach to remedy this problem is to express the average fluid temperature in the two–fluid model expression (Eq. 3.28) in terms of the bulk fluid temperature. In Appendix D, we use the relation between the average bulk fluid temperature and cross-sectional average fluid temperature in Eq. 3.17 to propose the following consistent two–fluid model for the average volumetric interphase heat transfer rate:

$$q'''_{cTF-model} = \frac{6\pi\varepsilon_s k_f \mathrm{Nu}}{4D^2 \left\langle \theta^{(f)} \right\rangle} \left(\left\langle T^{(s)} \right\rangle - \left\langle T^{(f)} \right\rangle \right), \tag{3.29}$$

where the average scaled fluid temperature $\langle \theta^{(f)} \rangle$ can be extracted from PR–DNS data. In fact, since the scaled fluid temperature θ is statistically homogeneous we can legitimately use volume averaging and subsequent ensemble–averaging over different particle configurations to compute $\langle \theta^{(f)} \rangle$ as $\left\langle \theta^{(f)} \right\rangle \cong 1/M \sum_{\omega=1}^{M} \left\{ \theta^{(f)} \right\}(\omega)$, where $\left\{ \theta^{(f)} \right\}(\omega) = \int_{V_f} \theta(\mathbf{x};\omega) dV/V_f$. Figure 3.8 shows the variation of the average scaled fluid temperature $\langle \theta^{(f)} \rangle$ with Reynolds number and volume fraction. For a given Reynolds number, the average scaled fluid temperature increases

with increasing volume fraction. We also observe that the average scaled fluid temperature is only weakly dependent on Reynolds number. Based on this PR–DNS data we propose the following correlation for the average scaled fluid temperature

$$\left\langle \theta^{(f)} \right\rangle = 1 - 1.6\varepsilon_s(1-\varepsilon_s) - 3\varepsilon_s(1-\varepsilon_s)^4 \exp(-\mathrm{Re}_\mathrm{m}^{0.4}\varepsilon_s) \tag{3.30}$$

that fits PR–DNS data with an average error of 5%. This correlation is a function of solid volume fraction and Reynolds number, and can be used to relate the mean fluid temperature to the bulk fluid temperature. In the limiting case of infinite dilution (i.e. solid volume fraction $\varepsilon_s \to 0$), the average scaled fluid temperature $\left\langle \theta^{(f)} \right\rangle$ is equal to one. This limiting value is consistent with the fact that for flow without particles the temperature field is uniform.

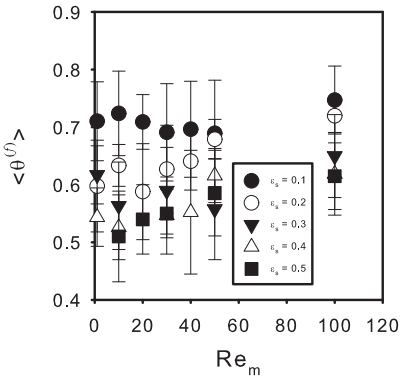

Figure 3.8: Variation of the average scaled fluid temperature $\left\langle \theta^{(f)} \right\rangle$ over Reynolds number of $1-100$ and volume fraction of $0.1-0.5$. Error bars represent 95% confidence intervals inferred from 5 MIS.

Using the expressions for average volumetric interphase heat transfer rate in Appendix D, Fig. 3.7 shows that the difference between $q'''_{cTF-model}$ (see Eq. D.8) and $\overline{q'''_{DNS}}$ (see Eq. D.12) is about 8% and less than the difference between q'''_{TF} and $\overline{q'''_{DNS}}$ at a solid volume fraction of 0.4. Thus, although q'''_{DNS} is inhomogeneous along the axial location, $q'''_{cTF-model}$ is still close to the PR–DNS data. Figure 3.9(b) compares the average volumetric interphase heat transfer rate from this consistent two–fluid model and PR–DNS data over a wide range of Reynolds number and solid volume fraction. The maximum value of the difference between $\overline{q'''_{DNS}}$ and $q'''_{cTF-model}$ is about 12%. For the cases where scale separation holds (ε_s =0.1, $\mathrm{Re}_m \geq 20$) we find that the difference is very low (the maximum of the difference is about 7%). Therefore, for the scale

separated cases the consistent two–fluid model that uses the bulk fluid temperature difference is very accurate. Thus, the consistent model that uses the bulk fluid temperature difference with the Nusselt number correlation based on the bulk fluid temperature results in significant improvement of the predicted average gas–solid heat transfer rate.

For the rest of the cases the error most probably arises from the spatial inhomogeneity of the average fluid temperature in the domain (cf. Eq. D.10 and Fig. 3.7). Even so, for most of the cases the difference between $\overline{q'''_{DNS}}$ and $q'''_{cTF-model}$ is below 12%, whereas as noted earlier the difference between $\overline{q'''_{DNS}}$ and q'''_{TF} (see Fig. 3.9(a)) are in the range of 5-36%. However, these errors should be interpreted cautiously since they relied on having the spatial variation of the average fluid temperature from the PR–DNS, which would not be the case in practical application of the two–fluid model. Nevertheless, this improved consistent two–fluid model (see Eq. 3.29) for the average volumetric interphase heat transfer rate that uses the average scaled fluid temperature $\left\langle \theta^{(f)} \right\rangle$ correlation (see Eq. 3.30) can be directly used in existing multiphase CFD codes that are based on the two–fluid model.

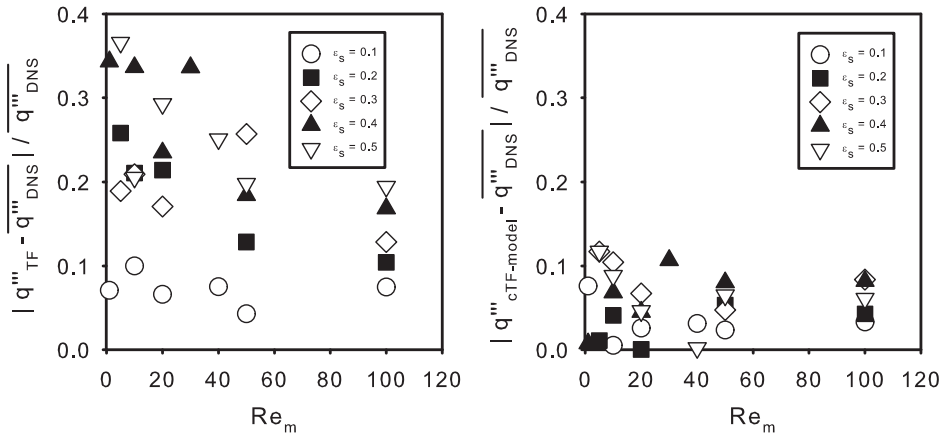

Figure 3.9: Comparison of average volumetric interphase heat transfer rate over a range of solid volume fraction and mean slip Reynolds number with $\overline{q'''_{DNS}}$ (see Eq. D.12) from PR–DNS data: (a) the standard two–fluid model (see Eq. D.11), and (b) the newly improved consistent two–fluid (cTF) model (see Eq. D.8). The average Nusselt number and average fluid temperature in both models are taken from PR–DNS.

3.7 Discussion

The results for gas–solid heat transfer presented here have been obtained under certain simplifying assumptions. Here we discuss the applicability of the results and identify areas for future work that would extend these results. As noted earlier, the principal assumptions in this work are: (i) isothermal particles with a single spatially uniform temperature for all particles that is constant in time, and (ii) neglect of radiation and free convection. Clearly the Nusselt number correlation can depend on the temperature boundary condition at the particle surface. A more faithful description would involve a coupled solution of the conduction problem inside each sphere. Such computations would certainly be more computationally expensive but are not out of reach for future studies. An intermediate simpler approach would be to assume a uniform temperature inside each solid particle (infinite conductance limit that can be characterized by the Biot number) and yet allow each particle's temperature to vary in time. Table 3.2 shows the Biot number for typical particles encountered in the applications that motivate this study. In each of these applications it seems that a uniform particle temperature is a reasonable assumption for small particle diameters, and only in the biomass application with large particle diameters is spatial temperature inhomogeneity inside the particle likely to be important. Smaller particle diameters also more closely satisfy the neglect of free convection, as discussed in detail in Tenneti et al. (2013).

It is also useful to estimate the validity of the assumption of a constant particle temperature that is not varying in time. Table 3.2 also shows the ratio of the particle thermal response time to the mean flow through time over a particle diameter. This shows that the particle thermal response time is usually much larger than the flow through time with the ratio ranging from 10 to 3895. The typical box size in the PR-DNS simulations is at most $8D$ and therefore only in the case of biomass particles do we expect the particle temperature to change on a time scale comparable to the transit time for the flow through the domain. In future studies it would be relatively simple to use a lumped capacitance model and allow particle temperatures to vary in time.

Since the Nusselt number correlation inferred from PR–DNS in this study is obtained using

Table 3.2: Typical particle properties and non–dimensional parameters such as the Biot number and the time scale ratio τ_{Lc}/τ_{flow} that are encountered in gas–solid heat transfer applications such as CO_2 capture (Yi et al. (2007)), chemical looping combustion (CLC) (Shen et al. (2008)), and biomass pyrolysis (Xue et al. (2011, 2012)). In CO_2 capture the gas phase is CO_2 and the solid phase is $NaCO_3$; in CLC the gas phase is CO and the solid phase is $CaSO_4$; in biomass pyrolyisis the gas phase is N_2 and the solid phase is bagasse. The Biot number is defined as $\mathrm{Bi} = hD/k_s$, where the heat transfer coefficent is computed by $h = \mathrm{Nu}k_f/D$, and the Nusselt number is in the range $2-20$ from our simulations. The particle thermal response time for a sphere is defined as $\tau_{Lc} = \rho_s c_{p,s} V/A_s h = \rho_s c_{p,s} D/6h$, and the flow through time is $\tau_{flow} = D/|\langle \mathbf{W} \rangle|$.

	D (μm)	ρ_s (kg/m^3)	$c_{p,s}$ (kJ/kg·K)	ρ_f (kg/m^3)	$c_{p,f}$ (kJ/kg·K)	$\rho_s c_{p,s}/\rho_f c_{p,f}$	k_s (W/m·K)	k_f (W/m·K)	Bi	τ_{Lc}/τ_{flow}
CO_2 capture	401	2394	3.93	1.77	0.85	6254	0.5	0.017	0.06-0.7	36-1897
CLC	100	2960	2.1	0.44	1.1	12843	0.9	0.052	0.11-1.2	74-3895
Biomass	500	400	2.27	0.42	1.22	1772	0.6	0.054	0.18-1.8	10-537

data from heat transfer in fixed beds (in fact, so is Gunn's correlation), care should be taken when applying it to fluidized beds. The results from this study show that the mean fluid temperature can vary significantly over a few particle diameters, and it might be expected that particle motion in this mean temperature gradient can result in a change in the Nusselt number. Note that in the hydrodynamic problem there is no mean velocity gradient because the velocity field is homogeneous. Therefore, in the hydrodynamic problem the drag force and pseudo–turbulent kinetic energy for high Stokes number particles in freely evolving suspension are well approximated by fixed–bed computations (see Tenneti (2013) and Mehrabadi et al. (2015)). Heat transfer in freely evolving suspension of gas–solid flow should be performed for a complete verification but these are outside the scope of this study.

Although simulating a thermally fully developed flow allows us to propose Nusselt number correlations with relatively low statistical variability, this study does not account for entrance length effects. Now that we have the thermally fully developed results in hand, we plan to investigate the effect of entrance length on the heat transfer problem by using inflow/outflow boundary conditions in future reports.

The Nusselt number correlation proposed in this work is restricted to gas–solid flow. Simulation of heat transfer in liquid-solid flow requires considerably higher grid resolution to resolve the thermal boundary layers that correspond to high Prandtl number. It is of interest to consider whether the Nusselt number correlation proposed in this work can also be used to compute the Sherwood number in a mass transfer problem on the basis of the Reynolds analogy. However, if mass transfer is strongly coupled to heat transfer, as is often the case in gas-solid flows, then the Sherwood number will depend not only on the Reynolds number and Schmidt number, but also on the Lewis number. The validity of the Reynolds heat/mass transfer analogy in gas-solid flows is a worthwhile topic for future study. Finally, it should be noted that these results are applicable to steady heat transfer and they do not account for the effect of unsteady mean temperature effects on the Nusselt number in gas–solid flow.

3.8 Conclusions

PR–DNS simulations of gas–solid heat transfer in steady flow through a homogeneous fixed assembly of particles is used to verify the assumptions underlying the continuum formulation of averaged equations, and to quantify the average gas–solid heat transfer term in the average fluid temperature equation over a range of mean slip Reynolds numbers (1-100) and volume fractions (0.1-0.5). PR–DNS data for the Nusselt number as a function of Reynolds number $\mathrm{Re_m}$ and volume fraction ε_s is compared with Gunn's correlation (Gunn (1978)). The average Nusselt number computed from PR–DNS data is close to Gunn's correlation with an average difference of 20%. A new PUReIBM Nusselt number correlation is proposed using PR–DNS data with an average difference of 7% that captures the Reynolds number dependence more accurately. This correlation is valid in a range of $0.5 \leq \varepsilon_b \leq 1.0$ and $1 \leq \mathrm{Re} \leq 100$.

The average gas–solid heat transfer in the two–fluid model is computed based on the average Nusselt number and the difference between average particle temperature and average fluid temperature, which can result in 5% to 36% difference when compared with the average gas–solid heat transfer obtained directly from PR–DNS data. These results indicate that rather than the average fluid temperature, it is the bulk fluid temperature that is the correct choice to compute average gas–solid heat transfer in gas–solid flow. Using a relation between the

average bulk fluid temperature and average fluid temperature, an improved model for the average gas–solid heat transfer is developed in terms of average scaled fluid temperature $\left\langle \theta^{(f)} \right\rangle$, average Nusselt number $\langle \mathrm{Nu} \rangle$, volume fraction ε_s, and the difference between the average fluid temperature $\left\langle T^{(f)} \right\rangle$ and average solid temperature $\left\langle T^{(s)} \right\rangle$. This model can be directly used for computing the average gas–solid heat transfer in two–fluid computations.

CHAPTER 4. PSEUDO-TURBULENT HEAT FLUX AND AVERAGE GAS-PHASE CONDUCTION DURING GAS-SOLID HEAT TRANSFER

This chapter is an article titled "Pseudo-turbulent heat flux and average gas-phase conduction during gas-solid heat transfer: flow past random fixed particle assemblies" that has been published in Journal of Fluid Mechanics. This article is authored by B. Sun, S. Tenneti, S. Subramaniam, D. L. Koch.

Fluctuations in the gas-phase velocity can contribute significantly to the total gas-phase kinetic energy even in laminar gas-solid flows (Mehrabadi et al. (2015)), and these pseudo–turbulent fluctuations can also enhance heat transfer in gas-solid flow. In this work, the pseudo–turbulent heat flux arising from temperature-velocity covariance, and average fluid-phase conduction during convective heat transfer in a gas-solid flow are quantified and modeled over a wide range of mean slip Reynolds number and solid volume fraction using Particle-resolved Direct Numerical Simulations (PR-DNS) of steady flow through a random assembly of fixed isothermal monodisperse spherical particles. A thermal self-similarity condition on the local excess temperature is used to guarantee thermally fully-developed flow (Tenneti et al. (2013)). The average gas-solid heat transfer rate for this flow has been reported elsewhere (Sun et al. (2015)). Although the mean velocity field is homogeneous, the mean temperature field in this thermally fully-developed flow is inhomogeneous in the streamwise coordinate. An exponential decay model for the average bulk fluid temperature is proposed. The pseudo–turbulent heat flux that is usually neglected in two-fluid models of the average fluid temperature equation is computed using PR-DNS data. It is found that the transport term in the average fluid temperature equation corresponding to the pseudo–turbulent heat flux is significant when compared to the average gas-solid heat transfer over a significant range of solid volume fraction and mean slip Reynolds number that was simulated. For this flow setup a gradient-diffusion model for

the pseudo–turbulent heat flux is found to perform well. The Péclet number dependence of the effective thermal diffusivity implied by this model is explained using a scaling analysis. Axial conduction in the fluid phase, which is often neglected in existing one-dimensional models, is also quantified. As expected, it is found to be important only for low Péclet number flows. Using the exponential decay model for the average bulk fluid temperature, a model for average axial conduction is developed that verifies standard assumptions in the literature. These models can be used in two-fluid simulations of heat transfer in fixed beds. A budget analysis of the mean fluid temperature equation provides insight into the variation of the relative magnitude of the various terms over the parameter space.

4.1 Introduction

An improved understanding of gas-solid heat transfer is crucial for design and scale-up of process equipment in many industries, such as biomass fast pyrolysis (Brown (2011)), chemical looping combustion (Shen et al. (2008)), and CO_2 capture (Abanades et al. (2004); Yi et al. (2007)). Instead of conducting expensive experiments, multiphase computational fluid dynamics (CFD) (Syamlal et al. (1993); Kashiwa and Gaffney (2003); Sun et al. (2007)) are increasingly being used for reactor scale-up from laboratory to pilot and full-scale plants, and also for evaluation of different design options (Halvorsen et al. (2003)). Device-scale multiphase CFD simulations are usually based on the Eulerian-Eulerian two-fluid model (Anderson and Jackson (1967); Drew and Passman (1998)) in which averaged equations for conservation of mass, momentum, energy are given for each phase, with coupling terms representing the interphase interactions. These equations contain unclosed terms that need to be modeled accurately, since the predictive capability of multiphase CFD simulations depends on the accuracy of models for interphase exchange of species, momentum, and heat.

In the absence of mass transfer between phases, the average fluid temperature equation

from two-fluid theory (Syamlal et al. (1993); Garg (2009)) reads as follows:

$$\underbrace{\frac{\partial}{\partial t}\left\{\rho_f \varepsilon_f c_{pf} \langle T^{(f)} \rangle\right\}}_{\text{unsteady term}} + \underbrace{\frac{\partial}{\partial x_j}\left\{\rho_f \varepsilon_f c_{pf} \langle u_j^{(f)} \rangle \langle T^{(f)} \rangle\right\}}_{\text{mean flow convection}} = \underbrace{\left\langle \frac{\partial I_f}{\partial x_j} q_j \right\rangle}_{\substack{\text{(1) average gas–solid} \\ \text{heat transfer}}} \underbrace{- \frac{\partial}{\partial x_j} \langle I_f q_j \rangle}_{\substack{\text{(2) average conduction} \\ \text{in the fluid phase}}} \underbrace{- \frac{\partial}{\partial x_j}\left\{\rho_f c_{pf} \langle I_f u_j''^{(f)} T''^{(f)} \rangle\right\}}_{\substack{\text{(3) pseudo–turbulent} \\ \text{heat flux term}}}, \tag{4.1}$$

and it contains the following unclosed terms: 1) average gas-solid heat transfer, 2) average conduction in the fluid phase, and transport term involving the pseudo–turbulent heat flux $\rho_f c_{pf} \langle I_f u_j''^{(f)} T''^{(f)} \rangle$ arising from temperature-velocity covariance. In Eq. 4.1, ρ_f and c_{pf} are the density and specific heat of the fluid phase, respectively, $q_j = -k_f \partial T / \partial x_j$ is the heat flux vector and $\varepsilon_f = \langle I_f \rangle$ is the volume fraction of the fluid phase, where $I_f(\mathbf{x}, t)$ is the fluid-phase indicator function that is unity if the point $\mathbf{x}$ lies on the fluid-phase at time t, and zero otherwise. If $\psi(\mathbf{x}, t)$ is any field (velocity or temperature), then its phasic average $\langle \psi^{(f)} \rangle(\mathbf{x}, t)$ (average fluid velocity $\langle u_j^{(f)} \rangle$ and average fluid temperature $\langle T^{(f)} \rangle$) is its average value conditional on being in the fluid phase, which is defined as:

$$\left\langle \psi^{(f)} \right\rangle (\mathbf{x}, t) = \frac{\langle I_f(\mathbf{x}, t) \psi(\mathbf{x}, t) \rangle}{\langle I_f(\mathbf{x}, t) \rangle}. \tag{4.2}$$

We use angle brackets to denote ensemble-averaging of random fields over all particle configurations, and an overbar to indicate spatial averages (in this problem these spatial averages appear either as a cross-sectional average of a random field that depends on the particle configuration, or as a streamwise average of an inhomogeneous ensemble-averaged field). Using the phasic average, the fluctuating components of the fluid velocity and temperature in Eq. 4.1 are defined as $u_j''^{(f)} = u_j - \langle u_j^{(f)} \rangle$ and $T''^{(f)} = T - \left\langle T^{(f)} \right\rangle$, where these fluctuations depend on spatial location and time, although for brevity this dependence is not explicitly shown. The average fluid velocity is obtained by solving the averaged momentum and mass conservation equations. In order to solve Eq. 4.1 for the average fluid temperature, closure models are needed for terms (1)–(3). In a typical two-fluid simulation of gas-solid flow, this equation is coupled to a similar

averaged temperature equation for the solid phase (Hrenya and Morris (2014)), but this work only focuses on models for the unclosed terms in the average fluid temperature equation. In a recent study (Sun et al. (2015)) the average gas-solid heat transfer term was quantified and modeled. This study focuses on quantification and modeling of the pseudo–turbulent heat flux that arises from the temperature-velocity covariance, and average conduction in the fluid phase.

The transport term (3) in the average fluid temperature equation (Eq. 4.1) arises from correlation of gas-phase velocity and temperature fluctuations that result in a pseudo–turbulent heat flux, and it is typically neglected in CFD simulations. These gas-phase velocity fluctuations can arise from turbulence inherent in the gas-phase, or they can be generated by wakes resulting from the interaction of particles with the mean slip velocity between the gas and solid phases. The second mechanism can generate gas-phase velocity fluctuations even in laminar gas-solid flow and these are termed pseudo-turbulent velocity fluctuations. They arise due to spatio-temporal fluctuations in the fluid velocity, and in steady flows their primary contribution is from the spatial variation of fluid velocity due to the presence of particles in a flow with a nonzero mean slip velocity. The kinetic energy associated with these fluctuations is called the pseudo-turbulent kinetic energy (PTKE). Tenneti (2013) and Mehrabadi et al. (2015) have quantified PTKE in fixed particle assemblies and freely evolving suspensions, and have shown that the level of PTKE is a significant fraction of the kinetic energy associated with the mean slip velocity. Similarly, the temperature-velocity covariance results in a pseudo-turbulent heat flux (PTHF), which needs to be quantified in non-isothermal gas-solid flow.

The study of pseudo–turbulent heat flux in fixed bed heat transfer is closely related to the mass transfer problem of a solute dispersing in a porous medium or a bed of particles. Together these may be termed the passive scalar transport problem provided the effects of free convection can be neglected. There are several theoretical studies related to hydrodynamic dispersion in a random fixed bed of particles (Koch and Brady (1985, 1987a,b)) or a periodic porous medium (Brenner and Gaydos (1977); Brenner (1980); Edwards et al. (1991)) in Stokes or low Reynolds number flow. Koch and Brady (1985) solved the convection-diffusion equation for mass transfer in Stokes flow through fixed beds using an asymptotic analysis that is valid in the dilute limit (low solid volume fraction). In their analysis, Koch and Brady (1985) assumed

a linear concentration profile that varies slowly (on the length scale of the one–particle problem) in the axial direction. Koch and Brady (1985) decompose the mean flux as the sum of a mean convective term and an effective diffusive flux, which includes the covariance of concentration and velocity (the analog of PTHF). They obtained the dependence of the effective diffusivity D_{eff} on the Péclet number ($P = Ua/D_f$), which characterizes the ratio of convective effects to diffusive effects. Here U is the superficial fluid velocity, a is the particle diameter and D_f is the molecular diffusivity of the solute. At low Péclet number ($P = Ua/D_f < 1$) they obtained a P^2 dependence, whereas at high Péclet number they obtained terms proportional to P and $P\ln(P)$. The linear dependence is attributed to the mechanical dispersion mechanism while the $P\ln(P)$ dependency is attributed to a non–mechanical dispersion mechanism that arises from the no–slip boundary condition (obtained from a boundary layer analysis). Koch's work provides early evidence that in fixed particle beds the presence of bulk convective motion induces fluid velocity fluctuations (mechanical dispersion) because of the presence of particles, and this is an important factor affecting macrotransport.

Hydrodynamic dispersion as described by Brenner and others treats the dispersion of solute particles through periodic porous media (Brenner (1980); Lowe and Frenkel (1996); Manz et al. (1999); Capuani et al. (2003); Mostaghimi et al. (2012)) or randomly placed particles (Maier et al. (2000, 2003)). Brenner (1980) showed that by considering the evolution equation of the transition probability density $P(\mathbf{R}, t|\mathbf{R}', t = 0)$ for the spatial position of solute molecules, one can formally arrive at the convection–diffusion equation governing the instantaneous concentration $c(\mathbf{R}, t)$ (or solute number density) field, which is nothing but the unnormalized probability density of solute molecule position $P(\mathbf{R}, t)$. It has been established by several authors (Brenner (1980); Pope (1998)) that the mean squared displacement of solute molecules, which Brenner showed can be obtained from moments of the transition probability density of the solute particles, is related to the effective diffusivity. The moments of the transition probability density lead to the B–field in periodic porous media.

Thermal dispersion in fixed beds or porous media defined by Kaviany (2012) and Whitaker (1999) based on temperature-velocity covariance and a gradient-diffusion model were studied experimentally (Yagi et al. (1960); Özgümüş et al. (2013)) and numerically (Kuwahara et al.

(1996); Pedras and de Lemos (2008); Jeong and Choi (2011)). In the above experimental and numerical works, local thermal equilibrium between solid and fluid phases is assumed to be valid and solid surface temperature evolves with the fluid temperature in time. Several numerical studies (Kuwahara et al. (1996); Pedras and de Lemos (2008); Jeong and Choi (2011)) that simulated flow past a 2D or 3D ordered array of objects with interphase heat transfer in a periodic media at high Péclet number found a Pe^n scaling of the thermal dispersion, which n was close to 2. Different from the studies on thermal dispersion, Acrivos et al. (1980) theoretically analyzed Stokes flow past a fixed bed of spheres with interphase heat transfer and studied the case of arbitrary conductivities in the fluid and solid phases without assuming local thermal equilibrium. They considered interphase heat transfer at low Reynolds number and low Péclet number and found that it is important to account for the effect of heat transfer on the mean temperature field. Assuming a locally linear mean temperature field they only focused on the analysis of mean temperature conditional on particle location for Péclet number number far less than unity.

The present study considers a similar scalar transport problem as Koch and Brady (1985), but for heat transfer in flow through a random arrangement of isothermal particles over a wide range of Reynolds number and solid volume fraction. The assumption of isothermal particles with nonzero interphase transfer precludes a direct comparison with the findings of Koch and Brady (1985), even if the scaling of effective diffusivity with Péclet number were to hold outside the Stokes flow regime. The problem in our study is formulated in an Eulerian frame and the pseudo–turbulent heat flux is directly obtained by statistically averaging the product of the instantaneous Eulerian velocity and concentration/temperature fields. Our formulation accounts for the finite size of particles and resolves the fluid–particle interface, without resorting to drag models as in White and Nepf (2003). Essentially we generate the microtransport fields in the presence of interphase transfer, which when averaged manifest as macrotransport. We also do not assume the spatial variation of the mean fluid temperature field. In fact, we show that the need to account for fluid heating (Acrivos et al. (1980)) automatically results in a mean fluid temperature variation that is naturally obtained as part of the solution by assuming a thermally fully-developed flow. This fluid heating resulting from the

interphase heat transfer is also absent in the studies of Brenner and others who assumed a linear concentration gradient with zero interphase mass transfer (Brenner (1980); Lowe and Frenkel (1996); Manz et al. (1999); Maier et al. (2000, 2003); Capuani et al. (2003); Mostaghimi et al. (2012)). The effect of the interphase transfer on transport can be quantified by the product of Damkohler number and Péclet number (Bekri et al. (1995)) which is the Nusselt number in our setup.

The term corresponding to average conduction in the fluid phase in the average fluid temperature equation is often neglected, or modeled using one-dimensional models. These one-dimensional models for axial conduction are in fact used to interpret experimental data (Littman et al. (1968); Gunn and Desouza (1974); Wakao et al. (1979); Wakao and Kaguei (1982)). In these one-dimensional models (Littman et al. (1968); Gunn and Desouza (1974); Wakao et al. (1979); Wakao and Kaguei (1982)), axial conduction in the fluid phase (average conduction is denoted axial conduction in the one-dimensional context) is calculated in terms of the second derivative of the average fluid temperature, and the axial (fluid) thermal dispersion coefficient which is obtained from experimental measurements. Although it is to be expected that relative magnitude of average conduction in the fluid phase compared to interphase gas-solid heat transfer will decrease with increasing Péclet number ($\mathrm{Pe_D} = \mathrm{Re_m Pr} = \mid \langle \mathbf{W} \rangle \mid D/\alpha_f$,where the Reynolds number is based on the mean slip velocity between the phases and particle diameter D, with α_f being the thermal diffusivity in the fluid phase), there is lack of quantitative data on average conduction in the fluid phase in flow through fixed or fluidized beds, and its variation with Reynolds number and volume fraction. Owing to this lack of quantitative data, the one-dimensional model for axial conduction has also not been verified.

Although theoretical analyses and experimental measurements have been used to study dispersion in fixed beds, it is difficult to develop models for the unclosed terms corresponding to the PTHF and average fluid–phase conduction that are valid over a wide range of solid volume fraction and mean slip Reynolds number using these approaches. At finite Reynolds number, the nonlinearity of the governing equations and the randomness in particle positions and velocities pose significant obstacles to theoretical analysis. Experimental measurement of gas-solid heat or mass transfer is also challenging because of limited optical access. Various ex-

perimental techniques such as frequency response or a pulse input that are reviewed by Delgado (2006) have been used to measure longitudinal (axial) dispersion in porous media for gas-solid flow. Early experimental measurements of gas–solid heat transfer (Kunii and Smith (1961); Handley and Heggs (1968); Littman et al. (1968); Gunn and Desouza (1974); Shen et al. (1981); Wakao et al. (1977)) used point-wise temperature measurements using simplified one-dimensional models of heat transfer that are based on assumptions such as the neglect of axial conduction in the fluid phase. Therefore, such measurements cannot be used to quantify the average axial conduction. Measurement of the temperature-velocity covariance requires simultaneous field measurements of velocity and temperature in a gas-solid flow. While such planar measurements are possible using laser-based techniques such as simultaneous particle image velocimetry (PIV) (Adrian (1991, 2005)) and planar laser-induced fluorescence (PLIF) (Van Cruyningen et al. (1990); Crimaldi (2008)), these are difficult to deploy in dense gas-solid flow.

In order to overcome these difficulties in theoretical analysis and experimental measurements of gas-solid heat transfer, we use a particle-resolved direct numerical simulation (PR-DNS) approach to quantify unclosed terms and develop models for them. The PR-DNS methodology can be used to accurately quantify the unclosed terms in Eq. 4.1, since these unclosed terms can be directly calculated from the instantaneous three-dimensional velocity and temperature fields. In recent years, the average interphase *momentum* transfer in gas-solid flow has been quantified by simulating steady flow past statistically homogeneous fixed assemblies of spherical particles (Hill et al. (2001a,b); Van der Hoef et al. (2005); Beetstra et al. (2007a); Yin and Sundaresan (2009); Tenneti et al. (2011)) using PR-DNS. More recently, heat transfer in gas-solid flow (Yu et al. (2006); Feng and Michaelides (2009); Deen et al. (2012); Tavassoli et al. (2013); Haeri and Shrimpton (2013); Deen and Kuipers (2014)) has also been reported using PR-DNS approaches. However, these studies did not quantify all the unclosed terms in the average fluid temperature equation (Eq. 4.1).

In order to quantify and model unclosed terms in the two-fluid model, Tenneti et al. (2013) have developed three-dimensional PR-DNS of thermally fully-developed flow in periodic domains using a thermal self-similarity condition that accounts for fluid heating by the particles. The role of fluid heating by particles and the Nusselt number for gas-solid heat transfer were

reported for a limited range of Reynolds number $\mathrm{Re_m}$ and volume fraction ε_s. Sun et al. (2015) used the same PR-DNS of thermally fully-developed flow past fixed particle of assemblies to develop an improved model for the average gas-solid heat transfer rate (see the term (1) in Eq. 4.1). In that work, a new Nusselt number correlation corresponding to average gas-solid heat transfer was proposed over a range of Reynolds number $1 \leq \mathrm{Re_m} \leq 100$ and volume fraction $0.1 \leq \varepsilon_s \leq 0.5$. Following the same methodology of Tenneti et al. (2013) and Sun et al. (2015), we consider gas-solid heat transfer in steady flow past a homogeneous fixed assembly of monodisperse spherical particles to quantify and model the pseudo–turbulent heat flux and average conduction in the fluid phase in Eq. 4.1.

The rest of the paper is organized as follows. In Section 4.2, we describe the heat transfer problem in a fixed particle assembly and discuss the assumptions used to simplify this problem. In Section 4.3, the PR-DNS approach that is used to solve this heat transfer problem is briefly described. In Section 4.4, we quantify and model the axial variation of the mean fluid temperature using PR-DNS data. In Section 4.5, the PTHF arising from temperature-velocity covariance is quantified and a model for the PTHF is proposed. In Section 4.6, we quantify the average fluid-phase conduction term from PR-DNS data and verify its model. We also perform a budget analysis of the average fluid temperature equation (Eq. 4.1) and discuss the relative magnitude of terms at steady state as a function of solid volume fraction and mean slip Reynolds number in Section 4.7. Finally, the principal findings of this work are summarized in Section 4.8.

4.2 Problem description

A canonical problem that is useful for understanding the physical mechanisms in heat transfer as well as for developing models for the unclosed terms is steady flow past a homogeneous assembly of monodisperse spherical particles. As Fig. 4.1 shows, in this gas-solid heat transfer setup the fluid is heated up or cooled down by the difference between the solid- and gas-phase temperature. The directional nature of the flow (the mean fluid velocity is anisotropic) implies that although the hydrodynamic problem is homogeneous, the average fluid temperature cannot be assumed to be uniform. Due to this heating or cooling of fluid by particles, the thermal

problem becomes statistically inhomogeneous in the streamwise direction. This feature of heat transfer in gas-solid flows is well established (Acrivos et al. (1980)).

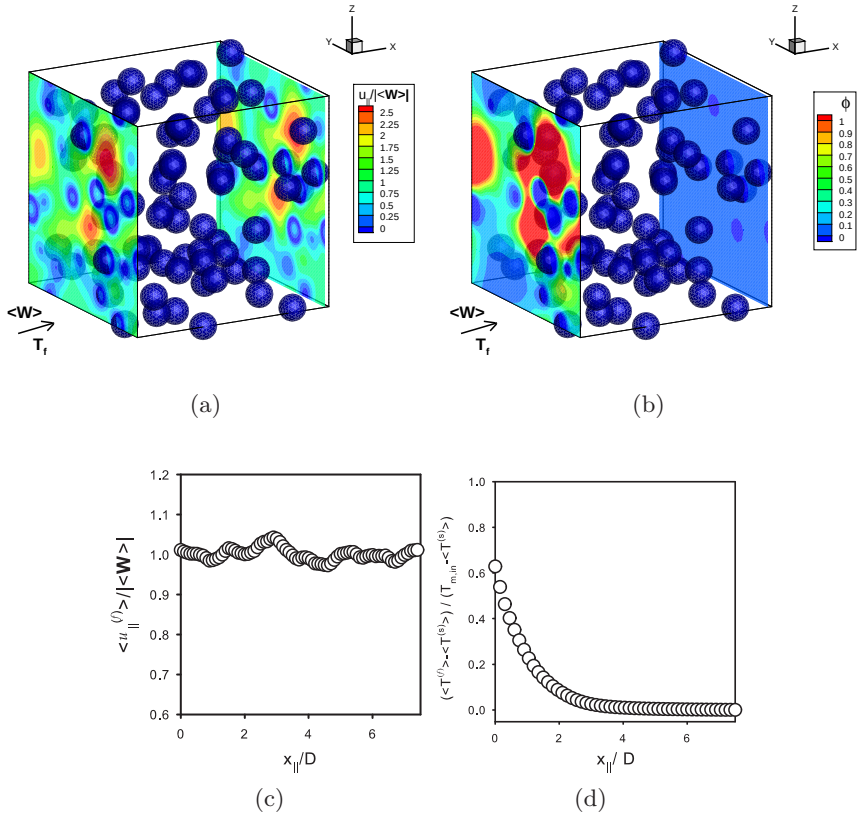

Figure 4.1: Contours of the steady (a) axial velocity and (b) temperature field in flow past a fixed particle assembly. The corresponding (c) average axial fluid velocity (see Eq. 4.2) and (d) average non-dimensional fluid temperature along the axial location $x_{\parallel}$ (see Eqs. 4.2 and 4.7) are shown in the bottom panel. In this figure $\langle \mathbf{W} \rangle$ is the mean slip velocity between the solid and fluid phase, T_f is the fluid temperature, $\left\langle u_{\parallel}^{(f)} \right\rangle$ is the average axial fluid velocity, $\left\langle T^{(f)} \right\rangle$ is the average fluid temperature in the axial location, $\left\langle T^{(s)} \right\rangle$ is the average solid temperature, and $T_{m,in}$ is the inlet bulk fluid temperature. At particle surfaces the no-slip and no-penetration boundary conditions are imposed on the fluid velocity, and the isothermal boundary condition is imposed on the fluid temperature. Periodic boundary conditions are imposed on the fluctuating velocity and pressure fields at domain boundaries, and the self-similarity boundary condition is used for the fluid temperature (see Eq. 4.13).

The inhomogeneity of the fluid temperature in a fixed particle assembly has implications for the quantification of unclosed terms in the average fluid temperature equation (Eq. 4.1). Specifically, if statistics calculated at the gas-solid interface, such as the average gas-solid heat transfer, vary along the streamwise coordinate, then these need to be extracted from spatially

varying surface statistics. Xu and Subramaniam (2010) noted that spatially varying surface statistics converge slowly even with a large number of realizations, where each realization corresponds to a different particle configuration with the same solid volume fraction and pair correlation function. However, Tenneti et al. (2013) and Sun et al. (2015) showed that if the flow is thermally fully-developed, then the Nusselt number is statistically homogeneous even though the average fluid temperature and average gas-solid heat transfer varies in the streamwise direction. A statistically homogeneous Nusselt number can be computed by volume averaging that yields fast convergence with even a few realizations. For this reason, Tenneti et al. (2013) developed a thermal self-similarity condition for gas-solid heat transfer in steady flow past a statistically homogeneous fixed assembly of particles that results in a thermally fully-developed flow. The same boundary condition has also been used by Tyagi and Acharya (2005) for simulating heat transfer in duct flow. We briefly summarize Tenneti et al. (2013) formulation of thermally fully-developed gas-solid flow here.

The following assumptions are used to simplify this heat transfer problem. Particles are assumed to be isothermal with a single spatially uniform temperature for all particles that is constant in time. Radiation and free convection effects are neglected. A detailed justification for these assumptions can be found in Tenneti et al. (2013). Under these conditions, the fluid temperature field $T(\mathbf{x},t)$ obeys the following convection-diffusion equation:

$$\frac{\partial T}{\partial t}+\frac{\partial\left(u_j T\right)}{\partial x_j}=\alpha_f\frac{\partial^2 T}{\partial x_j \partial x_j}, \tag{4.3}$$

where $\alpha_f = k_f/\rho_f c_{Pf}$ is the thermal diffusivity in the fluid phase, and k_f is the thermal conductivity in the fluid phase. Note that the above gas properties are assumed to be constant for this heat transfer problem. This equation needs to be solved in conjunction with the Dirichlet boundary condition $T = T_s$ at the surface of the particles, where T_s is the uniform temperature for all the particles. If the flow is thermally fully-developed (as in internal pipe flow, see Incropera et al. (2006) for example), then the *locally scaled excess fluid temperature* field θ, defined as:

$$\theta(\mathbf{x},t)=\frac{T(\mathbf{x},t)-T_s}{\langle T_m\rangle\left(x_{||},t\right)-T_s}, \tag{4.4}$$

does not vary in the streamwise or axial direction $x_{||}$ at steady state (Tenneti et al. (2013)),

i.e.,

$$\frac{\partial \theta}{\partial x_{||}} = \frac{\partial}{\partial x_{||}} \left(\frac{T(\mathbf{x}) - T_s}{\langle T_m \rangle (x_{||}) - T_s} \right) = 0. \tag{4.5}$$

This thermal self-similarity condition also ensures that the θ field is statistically homogeneous at steady state. For simplicity θ is later referred to as simply the *scaled fluid temperature*. In the above definition, $\langle T_m \rangle (x_{||}, t)$ is the ensemble-averaged bulk fluid temperature, which is defined as the average of the bulk fluid temperature on each realization ω (corresponding to a particle configuration, which occurs with probability dP_ω), such that

$$\langle T_m \rangle (x_{||}, t) = \int_{\omega \in \Omega} T_m(x_{||}, t; \omega)\, dP_\omega, \tag{4.6}$$

where the bulk fluid temperature on each realization is

$$T_m(x_{||}, t; \omega) = \frac{\int_{A_f} (\mathbf{u}T) \cdot \mathbf{e}_{\|} dA}{\int_{A_f} \mathbf{u} \cdot \mathbf{e}_{\|} dA}, \tag{4.7}$$

where $\mathbf{e}_{\|}$ is the unit vector along the streamwise direction and A_f is the area occupied by the fluid in a plane perpendicular to the streamwise direction. In general for any function $Q(x_{||}, t; \omega)$ that is defined for a realization ω, we define the ensemble-average as

$$\langle Q \rangle (x_{||}, t) = \int_{\omega \in \Omega} Q(x_{||}, t; \omega)\, dP_\omega. \tag{4.8}$$

The thermally fully-developed condition implies that at steady state the local wall heat flux scaled by the temperature difference $\left(\langle T_m \rangle (x_{||}) - T_s \right)$ is a constant. The advantage of establishing a thermally fully-developed flow is that there are no entrance length effects. Note that the entrance length region can contribute very high Nusselt number values that can contaminate the true Nusselt number in a gas-solid flow. Thermally fully-developed flow is accomplished by implementing the thermal self-similarity condition (cf. Eq. 4.5), which requires periodic boundary conditions on the scaled fluid temperature (Tenneti et al. (2013)).

For reasons detailed in Tenneti et al. (2013), it is easier to transform the periodic boundary conditions on θ to obtain similarity conditions on the temperature field $T(\mathbf{x}, t)$ and solve Eq. 4.3 for $T(\mathbf{x}, t)$. Simplification of the thermal similarity conditions and homogenization of the boundary conditions on the particle surfaces is accomplished by defining a non-dimensional excess temperature field (for simplicity this quantity is referred to as the non-dimensional

temperature) $\phi(\mathbf{x}, t)$ as follows:

$$\phi(\mathbf{x}, t) = \frac{T(\mathbf{x}, t) - T_s}{\langle T_{m,in} \rangle - T_s}, \tag{4.9}$$

where $\langle T_{m,in} \rangle$ is the average inlet bulk fluid temperature that is defined by Eq. 4.6 in terms of the inlet bulk fluid temperature $T_{m,in}$, which is given by Eq. 4.7 evaluated at $x_{||} = 0$. Using this definition of the non-dimensional temperature, the non-dimensional bulk fluid temperature $\phi_m(x_{||}, t; \omega)$ on a realization ω is defined as,

$$\phi_m(x_{||}, t; \omega) = \frac{T_m(x_{||}, t; \omega) - T_s}{\langle T_{m,in} \rangle - T_s}, \tag{4.10}$$

and the average non-dimensional bulk fluid temperature $\langle \phi_m \rangle$ has a similar definition:

$$\langle \phi_m \rangle(x_{||}, t) = \frac{\langle T_m \rangle(x_{||}, t) - T_s}{\langle T_{m,in} \rangle - T_s}. \tag{4.11}$$

We solve the governing equation for the non-dimensional temperature derived by substituting Eq. 4.9 in Eq. 4.3 as:

$$\frac{\partial \phi}{\partial t} + \frac{\partial (u_j \phi)}{\partial x_j} = \alpha_f \frac{\partial^2 \phi}{\partial x_j^2}. \tag{4.12}$$

In this non-dimensional temperature equation, the isothermal boundary conditions on the particle surface reduce to $\phi = 0$. The periodic boundary conditions on ϕ appear in a very simple form:

$$\begin{aligned} \phi(0, y, z) &= r_h \phi(L, y, z), \\ \phi(x_{\|}, 0, z) &= \phi(x_{\|}, L, z), \\ \phi(x_{\|}, y, 0) &= \phi(x_{\|}, y, L), \end{aligned} \tag{4.13}$$

where r_h is the heat ratio, which is defined as:

$$r_h = \frac{\langle T_{m,in} \rangle - T_s}{\langle T_{m,out} \rangle - T_s}. \tag{4.14}$$

In the definition of the heat ratio, $\langle T_{m,out} \rangle$ is the average bulk fluid temperature at $x_{\|} = L$, and L is the length of the box. The heat ratio quantifies by how much a *fluid* particle heats up when it leaves the box and so this quantity depends solely on the flow structure and the interphase heat transfer in the domain. Note that the heat ratio, or the amount by which the fluid gets heated up (or cooled down) when it reaches the end of the box, is an unknown quantity and is obtained as a part of the solution.

4.3 Numerical method

The gas-solid heat transfer problem described in Section 4.2 can be solved using our PR-DNS approach, which is called the Particle-resolved Uncontaminated-fluid Reconcilable Immersed Boundary Method (PUReIBM) (Garg et al. (2010b); Tenneti et al. (2011); Tenneti (2013); Tenneti and Subramaniam (2014)). The gas–phase velocity and pressure fields in the gas-solid heat transfer problem are solved using the following conservation equations for mass and momentum:

$$\frac{\partial u_i}{\partial x_i} = 0, \tag{4.15}$$

$$\frac{\partial u_i}{\partial t} + \frac{\partial \left(u_i u_j\right)}{\partial x_j} = -\frac{1}{\rho_f} g_i + \nu_f \frac{\partial^2 u_i}{\partial x_j \partial x_j} + I_s f_{u,i}, \tag{4.16}$$

where ν_f is the fluid-phase kinetic viscosity, g_i represents the pressure gradient, and $f_{u,i}$ is the additional immersed boundary (IB) direct forcing term. Complete details of the PUReIBM hydrodynamic solver are discussed by Garg et al. (2010b) and Tenneti *et al.* (Tenneti et al. (2011); Tenneti (2013); Tenneti et al. (2010)), while the scalar solver is discussed in Tenneti et al. (2013). Here we briefly review the numerical approach to solve the gas-solid heat transfer problem for steady flow past a fixed assembly of isothermal spherical particles.

It is worth noting that the equations in Section 4.2 are formulated in terms of the ensemble-averaged bulk fluid temperature (see Eqs. 4.9 and 4.14). The solution to these equations can be accomplished by simultaneously solving Eq. 4.12 in parallel for several different particle configurations subject to the boundary condition in Eq. 4.13 on a parallel computer. In this setup each particle configuration and corresponding fluid temperature field is stored on a node, and the ensemble-averaged bulk fluid temperature is communicated to all nodes at the end of each time step. However, it turns out that the statistical variability of the bulk fluid temperature and heating ratio in different particle configurations is small, provided the computational domains are sufficiently large. Therefore, the ensemble-averaged bulk fluid temperature is replaced by the bulk fluid temperature in that realization in our approach. In this case the scaled fluid temperature for each realization is rewritten as

$$\theta(\mathbf{x}, t; \omega) = \frac{T(\mathbf{x}, t; \omega) - T_s}{T_m(x_{||}, t; \omega) - T_s}, \tag{4.17}$$

and the non-dimensional temperature is rewritten as

$$\phi(\mathbf{x},t;\omega) = \frac{T(\mathbf{x},t;\omega) - T_s}{T_{m,in}(\omega) - T_s}. \tag{4.18}$$

This effectively decouples the temperature solution in different particle configurations and allows the solution in each realization to proceed independently. Ensemble-averaged quantities (see Eq. 4.8) are computed from the individual steady temperature fields corresponding to each realization, as described in Sections 4.5 and 4.6. The small statistical variability in the bulk fluid temperature from one realization to another justifies this decoupling approach (Tenneti et al. (2013)).

In PUReIBM the following non-dimensional fluid temperature equation is solved at all grid nodes

$$\rho_f c_{pf}\left[\frac{\partial \phi}{\partial t} + \frac{\partial (u_j \phi)}{\partial x_j}\right] = -\frac{\partial q_j^{\phi}}{\partial x_j} + I_s f_{\phi}, \tag{4.19}$$

where $q_j^{\phi} = -k_f \partial\phi/\partial x_j$ is the heat flux per unit temperature difference, I_s is the solid-phase indicator function, and f_ϕ is the scalar Immersed Boundary (IB) direct forcing in the solid phase (Tenneti et al. (2013)). The scalar IB forcing f_ϕ is computed only at grid points located inside the solid particles. This ensures that the fluid temperature field is not contaminated by the scalar IB forcing f_ϕ. The scalar IB forcing at the $(n+1)$th time-step f_ϕ^{n+1} is specified to cancel the remaining terms in the governing equation and forces the non-dimensional temperature ϕ^n to its desired value ϕ^d at the particle surface:

$$f_\phi^{n+1} = \rho_f c_{pf}\frac{\phi^d - \phi^n}{\Delta t} + \rho_f c_{pf} C_\phi^n + \left(\frac{\partial q_j^{\phi}}{\partial x_j}\right)^n. \tag{4.20}$$

In the above equation $C_\phi^n = [\partial(u_j\phi)/\partial x_j]^n$ is the convective term at the nth time-step. Details of the numerical method and validation tests for the hydrodynamic solution (Garg et al. (2010b); Tenneti et al. (2011); Tenneti (2013)) as well as the temperature calculation (Tenneti et al. (2013); Tenneti (2013); Sun et al. (2015)) appear elsewhere.

Using the PUReIBM approach we have performed PR-DNS simulations over a wide range of mean slip Reynolds number $\mathrm{Re_m}$ = 1-100 and solid volume fraction ε_s = 0.1-0.5 in homogeneous fixed particle assemblies with Prandtl number of 0.7, as summarized in table 4.1. In order to access a range of Péclet number ($\mathrm{Pe_D} = \mathrm{Re_m Pr} = |\langle \mathbf{W} \rangle| D/\alpha_f$, where α_f being the thermal

Table 4.1: Parameters for simulation of heat transfer in steady flow past random fixed assemblies of particles. The physical parameters are the solid volume fraction ε_s and the mean slip Reynolds number $\mathrm{Re_m}$. The numerical parameters are the ratio of the box length to the particle diameter L/D and the grid resolution $D_m = D/\Delta x$. The number of particles N_p is determined by ε_s and L. Five independent simulations of each case are simulated to reduce statistical variability.

ε_s	Re_m	L/D	N_p	D_m
0.1	1, 5, 10, 20, 30, 40, 50, 100	7.5	80	20
0.2	1, 5, 10, 20, 30, 40, 50, 100	7.5	161	20
0.3	1, 5, 10, 20, 30, 40, 50, 100	5	71	30
0.4	1, 5, 10, 20, 30, 40, 50, 100	5	95	30
0.5	1, 5, 10, 20, 30, 40, 50, 100	4	61	40

diffusivity in the fluid phase) and thereby deduce scaling behavior, a few simulations are also presented for Prandtl numbers of 0.01, 0.1, 0.7 and 1 at $\mathrm{Re_m} = 1$ and 100 and $\varepsilon_s = 0.1$. The convergence of relevant heat transfer characteristics such as the Nusselt number with numerical parameters has been established previously (Sun et al. (2015)). The choice of grid resolution and the number of realizations for these simulations is based on those findings. PR-DNS data from these simulations are now analyzed to quantify and model the PTHF and average fluid-phase conduction.

4.4 Inhomogeneity of fluid temperature in a fixed particle assembly

A key feature of this gas-solid flow is the variation of mean fluid temperature in the streamwise direction which arises from fluid heating or cooling by the particles. Note that this mean field variation is often assumed in analytical treatments. Here we have obtained it as part of the solution by imposing the thermally fully developed condition at the inlet and outlet domain boundaries. Since it plays an important role in both the PTHF transport term and average fluid-phase conduction, we first quantify and characterize its behavior.

In Section 4.2 we noted that this gas-solid heat transfer problem for steady flow through a fixed homogeneous assembly of particles is analogous *in an average sense* to internal forced convection in a pipe. For the case of constant pipe wall temperature, the bulk fluid temperature

in thermally fully-developed internal pipe flow (Incropera et al. (2006)) can be expressed as

$$\frac{dT_m(x_{||})}{dx_{||}} = \frac{d(T_m(x_{||}) - T_s)}{dx_{||}} = -\frac{Ph}{\dot{m}c_{pf}}(T_m(x_{||}) - T_s), \tag{4.21}$$

where h is the local heat transfer coefficient that is independent of $x_{||}$ in thermally fully-developed flow, $\dot{m}$ is the mass flow rate, and P is the perimeter of the pipe cross section. Integrating Eq. 4.21, the following expression for the non-dimensional bulk fluid temperature $\phi_m = (T_m(x_{||}) - T_s)/(T_{m,in} - T_s)$ can be obtained in terms of the Nusselt number $\mathrm{Nu} = hD/k_f$:

$$\phi_m(x_{||}) = \exp\left(-\frac{P\mathrm{Nu}k_f}{\dot{m}c_{pf}D}x_{||}\right). \tag{4.22}$$

For our case of a statistically homogeneous fixed random assembly of particles, the analogous expression for the axial variation of $\phi_m(x_{\|};\omega)$ at steady state for one realization is

$$\frac{d\phi_m(x_{\|};\omega)}{dx_{\|}} = -\frac{P(x_{||};\omega)\mathrm{Nu}(x_{||};\omega)k_f}{\dot{m}c_{pf}D}\phi_m(x_{\|};\omega), \tag{4.23}$$

where the steady flow rate through the homogeneous fixed assembly of particles is $\dot{m} = A\rho_f |\langle \mathbf{W} \rangle| \varepsilon_f$ and $P(x_{||};\omega)$ is the perimeter of spheres intersecting the plane at $x_{||}$ on realization ω (see Fig. D.1 in Appendix D). Taking the ensemble-average of Eq. 4.23 results in

$$\frac{d\langle \phi_m \rangle (x_{\|})}{dx_{\|}} = -\frac{\left\langle P(x_{\|})\mathrm{Nu}(x_{\|})\phi_m(x_{\|})\right\rangle k_f}{\dot{m}c_{pf}D} = -\frac{\left\langle P(x_{\|})\right\rangle \left\langle \mathrm{Nu}(x_{\|})\right\rangle \left\langle \phi_m(x_{\|})\right\rangle k_f}{\dot{m}c_{pf}D}. \tag{4.24}$$

Note that in general the average of a product of random variables is not equal to the product of the averages. Here we are not assuming that the variables $\phi_m(x_{\|})$, $\mathrm{Nu}(x_{\|})$ and $P(x_{\|})$ are uncorrelated, but that any dependence of $\phi_m(x_{\|})$ and $\mathrm{Nu}(x_{\|})$ on $P(x_{\|})$ is captured in the definition of the average heat transfer coefficient (see Eq. D.2 in Appendix D and following discussion). Thus, the expression for the average non-dimensional bulk fluid temperature is written as

$$\langle \phi_m \rangle (x_{||}) = \exp\left(-\frac{\left\langle P(x_{||})\right\rangle \left\langle \mathrm{Nu}(x_{||})\right\rangle k_f}{\dot{m}c_{pf}D}x_{||}\right). \tag{4.25}$$

For the average bulk fluid temperature in thermally fully-developed gas-solid flow represented by Eq. 4.25, we replace $\mathrm{Nu}(x_{||})$ with the average Nusselt number $\langle \mathrm{Nu} \rangle$ (see Eqs. B.15 and B.17) and $P(x_{||})$ with the average perimeter $\langle P \rangle$, (see Appendix D) , to obtain

$$\langle \phi_m \rangle (x_{||}) = \exp\left(-\frac{6\pi\varepsilon_s}{4}\frac{\langle \mathrm{Nu} \rangle}{\mathrm{Re_m Pr}}\frac{x_{||}}{D}\right) = \exp\left(-\lambda\frac{x_{||}}{D}\right), \tag{4.26}$$

where the mean slip Reynolds number $\mathrm{Re_m} = |\langle \mathbf{W} \rangle| D(1-\varepsilon_s)/\nu_f$, the Prandtl number $\mathrm{Pr} = \nu_f/\alpha_f = (\mu_f/\rho_f)/(k_f/\rho_f c_{pf})$, and the ratio $\langle P \rangle / A = 6\pi\varepsilon_s/(4D)$ (cf. Eq. D.5) have been substituted. The non-dimensional coefficient λ given by

$$\lambda = \frac{6\pi\varepsilon_s \langle \mathrm{Nu} \rangle}{4\mathrm{Re_m Pr}}, \tag{4.27}$$

determines the rate of decay of the bulk temperature with axial distance. The PR-DNS data for $\langle \phi_m \rangle$ as a function of axial distance shown in Fig. 4.2(a) indicate an exponential decay. We find that the following exponentially decaying model

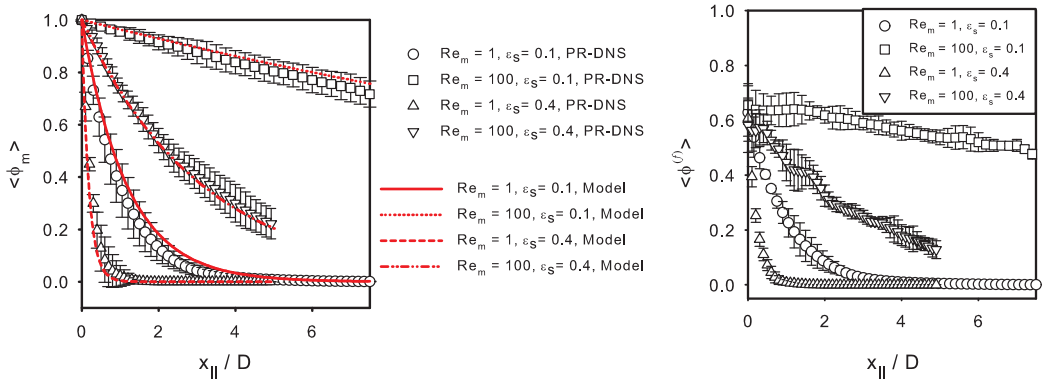

(a) (b)

Figure 4.2: Axial variation of average non-dimensional bulk fluid temperature and average non-dimensional fluid temperature from PR-DNS: (a) Comparison of the exponential decay model (lines) for the average non-dimensional bulk fluid temperature (see Eq. 4.28) with PR-DNS data (open symbols). (b) Cross-sectionally average of non-dimensional fluid temperature (see Eq. 4.34) from PR-DNS data for $\varepsilon_s = 0.1$ and 0.4 at two different Reynolds numbers (open symbols). Error bars in both panels represent 95% confidence intervals inferred from 5 MIS.

$$\langle \phi_m \rangle (x_{||}) = e^{-\lambda_m x_{||}/D}, \tag{4.28}$$

with the non-dimensional decay coefficient λ_m given by

$$\lambda_m = \frac{6\pi\varepsilon_s \langle \mathrm{Nu} \rangle}{4(\mathrm{Re_m} + 1.4)\mathrm{Pr}}, \tag{4.29}$$

fits the PR-DNS data for axial variation of non-dimensional bulk fluid temperature shown in Fig. 4.2(a). This model for $\langle \phi_m \rangle$ is similar to Eq. 4.27 with a minor difference arising from fitting the data. The average Nusselt number $\langle \mathrm{Nu} \rangle$ in λ_m is taken from PR-DNS data corresponding

to the $\mathrm{Re_m}$, Pr and ε_s values for each case. Figure 4.2(a) compares this exponential decay model for the average non-dimensional bulk fluid temperature with PR-DNS data for two different volume fractions. The average error is 2.4% at $\varepsilon_s = 0.1$ and 3.8% at $\varepsilon_s = 0.4$ for a Reynolds number of $\mathrm{Re_m} = 100$. While in analytical treatments (Acrivos et al. (1980)) this variation is assumed to be linear, an important finding from our study is that the imposition of thermal self–similarity conditions at the inlet and outlet boundaries results in a thermally fully developed flow with an exponential decay of the mean fluid temperature. As we show later, this has important implications for the pseudo–turbulent (effective) thermal diffusivity that is inferred from the data.

There is a useful relation that shows that the non-dimensional fluid temperature (Eq. 4.9) is simply the product of the scaled fluid temperature (Eq. 4.4) and the average non-dimensional bulk fluid temperature (Eq. 4.11):

$$\phi(\mathbf{x},t) = \left(\frac{T(\mathbf{x},t) - T_s}{\langle T_m\rangle(x_{||},t) - T_s}\right)\left(\frac{\langle T_m\rangle(x_{||},t) - T_s}{\langle T_{m,in}\rangle - T_s}\right) = \theta(\mathbf{x},t)\langle\phi_m\rangle(x_{||},t). \tag{4.30}$$

Multiplying the above equation by the fluid indicator function I_f, taking the expectation (see Eq. 4.8), and using the definition in Eq. 4.2 leads to the corresponding relation between the phase-averaged counterparts:

$$\langle\phi^{(f)}\rangle(\mathbf{x},t) = \langle\theta^{(f)}\rangle(\mathbf{x},t)\langle\phi_m\rangle(x_{||},t), \tag{4.31}$$

Also noting that the θ field is statistically homogeneous at steady state reveals that the inhomogeneity in the steady average fluid temperature field arises solely from the inhomogeneity in the bulk fluid temperature:

$$\langle\phi^{(f)}\rangle(x_{||}) = \langle\theta^{(f)}\rangle\langle\phi_m(x_{||})\rangle. \tag{4.32}$$

The above relation implies $\langle\phi^{(f)}\rangle \sim \exp\left(-\lambda x_{||}/D\right)$ since the average scaled fluid temperature $\left\langle\theta^{(f)}\right\rangle$ is statistically homogeneous and does not depend on the axial location (it is only a function of Reynolds number and solid volume fraction).

Figure 4.2(b) shows the average non-dimensional fluid temperature $\langle\phi^{(f)}\rangle$ that is computed by ensemble-averaging the cross-sectional average of the non-dimensional fluid temperature

$\left\{\phi^{(f)}\right\}_{cs}$, given by

$$\left\{\phi^{(f)}\right\}_{cs}(x_{||};\omega) = \frac{1}{A_f}\int_{A_f}\phi(\mathbf{x};\omega)dA, \tag{4.33}$$

to obtain

$$\langle\phi^{(f)}\rangle(x_{||}) \approx \frac{1}{M}\sum_{\omega=1}^{M}\left\{\phi^{(f)}\right\}_{cs}(x_{||};\omega). \tag{4.34}$$

The average non-dimensional bulk fluid temperature from PR-DNS data is denoted by symbols in Fig. 4.2(a), and it decays exponentially due to fluid cooling in the streamwise direction. The effect of fluid cooling (or heating) by particles is significant at high solid volume fraction and low Reynolds number, and it occurs over progressively shorter length scales as solid volume fraction increases and Reynolds number decreases. The variation of $\left\langle\phi^{(f)}\right\rangle$ in Fig. 4.2(b) indicates that the average non-dimensional fluid temperature can be inhomogeneous on the scale of a few particle diameters. With this understanding and exponential decay model for the average bulk temperature and average fluid temperature in hand, we now turn to quantification and modeling of the PTHF and average conduction in the fluid phase.

4.5 Pseudo-turbulent heat flux

In TF CFD simulations the PTHF term is typically neglected. Since Tenneti (2013) and Mehrabadi et al. (2015) have reported that PTKE is an significant fraction of the kinetic energy associated with the mean slip velocity in fixed particle assemblies, this suggests that the PTHF could also be significant in the gas-solid heat transfer problem. The finding in the previous section that the average fluid temperature decays exponentially in the streamwise direction has several important implications for the PTHF term. In single-phase flows it is well known that scalar fluctuations cannot be sustained in the absence of mean temperature gradients. However, if a linear mean temperature gradient is imposed, then the resulting fluctuating temperature field is homogeneous (Sirivat and Warhaft (1983); Subramaniam and Pope (1998)). Sirivat and Warhaft (1983) performed a fundamental scalar mixing experiment by imposing a linear cross-stream temperature gradient and studying the correlation between temperature and velocity fluctuations. The gas-solid heat transfer problem that we describe in

this paper is interesting because it offers a similar setup wherein temperature fluctuations are sustained due to an exponentially decaying streamwise mean temperature gradient.

Another interesting feature of this flow relates to the transport term involving the PTHF. Note that in statistically homogeneous flow this transport term is zero. Indeed in the case of the statistically homogeneous hydrodynamic problem where the mean fluid velocity is homogeneous there is no fluid–phase Reynolds stress transport term (Mehrabadi et al. (2015)). Therefore, although the magnitude of the Reynolds stress in that case was reported by Mehrabadi et al. (2015) as the PTKE, its transport could not be quantified or modeled. On the other hand, the inhomogeneous mean temperature field in this corresponding gas-solid heat transfer problem gives us the opportunity to quantify and model the transport term involving the PTHF.

We now deduce an important property of the PTHF in our problem setup. We show that for this flow setup the inhomogeneity in the temperature-velocity covariance arises solely from inhomogeneity in the non-dimensional bulk temperature. This observation is later used to propose a gradient-diffusion model for the pseudo-turbulent heat flux. Substituting the definition of the non-dimensional fluid temperature fluctuation $\phi''^{(f)}(\mathbf{x}) = \phi(\mathbf{x}) - \langle\phi^{(f)}\rangle\left(x_{\parallel}\right)$ into the expression for the ensemble-averaged PTHF $\left\langle I_f u_i''^{(f)}\phi''^{(f)}\right\rangle\left(x_{\parallel}\right)$, noting that the average of the fluctuating fluid velocity $\left\langle I_f u_i''^{(f)}\right\rangle$ is zero due to statistical homogeneity of the velocity field, and using the relation $\phi = \langle\phi_m\rangle\,\theta$ between the non-dimensional bulk fluid temperature ϕ_m and the scaled fluid temperature θ (see Eq. 4.30), results in the following simplification of the ensemble-averaged PTHF:

$$\left\langle I_f u_i''^{(f)}\phi''^{(f)}\right\rangle\left(x_{\parallel}\right) = \left\langle I_f u_i''^{(f)}\theta\right\rangle\langle\phi_m\rangle\left(x_{\parallel}\right). \tag{4.35}$$

Note that although $\left\langle I_f u_i''^{(f)}\phi''^{(f)}\right\rangle$ is inhomogeneous in $x_{\parallel}$, the covariance of velocity and scaled temperature $\left\langle I_f u_i''^{(f)}\theta\right\rangle$ is expected to be statistically homogeneous, since both the fluid velocity field u_i and the scaled fluid temperature field θ are statistically homogeneous. Interestingly, in this particular thermally fully-developed steady gas-solid heat transfer problem, the inhomogeneity in the temperature-velocity covariance arises solely from inhomogeneity of the non-dimensional bulk temperature. It should be noted that in general the initial condition of the fluctuating temperature field will not permit this simplification. Nevertheless, this sim-

plification provides a strong justification for the gradient-diffusion model that we later use to model the PTHF.

The results reported in this study correspond to the simulation of the unsteady temperature equation (see Eq. 4.19) with a steady velocity field that is a converged hydrodynamic solution to flow past the particle configuration. This solution approach is valid because temperature is a passive scalar in the regime of gas-solid heat transfer considered in this study. We have also simulated a case with fully coupled instantaneous velocity and temperature fields to account for any unsteady effects as shown in Fig. 4.3. We do not find significant differences in the PTHF between the steady results of the fully coupled simulation and that obtained from coupling with the steady velocity field. This is because the primary contribution to the PTHF arises from spatial fluctuations of velocity and temperature that are adequately captured by our averaging procedure. Here we provide the first report of PTHF data in gas-solid flow from PR-DNS.

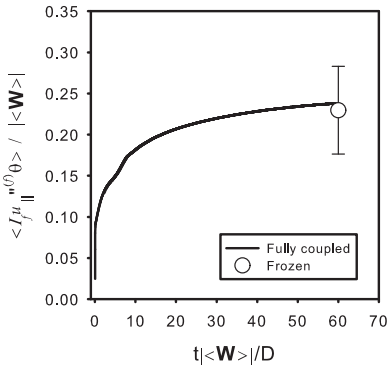

Figure 4.3: Variation of $\left\langle I_f u_{\|}^{\prime\prime(f)} \theta \right\rangle$ with non-dimensional time for the case with mean slip Reynolds number of 100 and solid volume fraction of 0.1. The solid line represents the evolution of $\left\langle I_f u_{\|}^{\prime\prime(f)} \theta \right\rangle$ for a computation where the scalar solver is coupled to the instantaneous velocity field. The open circle represents the value of $\left\langle I_f u_{\|}^{\prime\prime(f)} \theta \right\rangle$ obtained with the scalar solver using a frozen velocity field, and the error bars are obtained from 5 realizations.

4.5.1 Computation of PTHF

First we describe the computation of the PTHF from our PR-DNS setup, and then the computation of the corresponding transport term. In our thermal fully-developed gas-solid flow, the fluid velocity is statistically homogeneous whereas the fluid temperature is inhomogeneous

along the axial location $x_{\parallel}$. Therefore, any average involving fluid temperature has to be computed over a cross-sectional plane at a given axial location. Here the PTHF is computed from PR-DNS data using cross-sectional averages over M realizations as

$$\left\langle I_f u_i^{\prime\prime(f)} \phi^{\prime\prime(f)} \right\rangle \left(x_{\parallel} \right) \approx \frac{1}{M} \sum_{\omega=1}^{M} \left\{ \frac{1}{A} \int_A I_f u_i^{\prime\prime(f)} \phi^{\prime\prime(f)} \left(\mathbf{x}; \omega \right) dA \right\}, \tag{4.36}$$

where the fluid velocity fluctuation for each realization is defined as

$$u_i^{\prime\prime(f)} \left(\mathbf{x}; \omega \right) = u_i \left(\mathbf{x}; \omega \right) - \left\{ u_i^{(f)} \right\}_V \left(\omega \right), \tag{4.37}$$

and where $\left\{ u_i^{(f)} \right\}_V$ is the volumetric mean fluid velocity that is computed as

$$\left\{ u_i^{(f)} \right\}_V \left(\omega \right) = \frac{\frac{1}{V} \int_V I_f \left(\mathbf{x}; \omega \right) u_i \left(\mathbf{x}; \omega \right) dV}{\frac{1}{V} \int_V I_f \left(\mathbf{x}; \omega \right) dV} = \frac{1}{V_f} \int_V I_f u_i dV. \tag{4.38}$$

The non-dimensional temperature fluctuation $\phi^{\prime\prime} \left(\mathbf{x}; \omega \right)$ for each realization is defined as

$$\phi^{\prime\prime} \left(\mathbf{x}; \omega \right) = \phi \left(\mathbf{x}; \omega \right) - \left\{ \phi^{(f)} \right\}_{cs} \left(x_{\parallel}; \omega \right), \tag{4.39}$$

where $\left\{ \phi^{(f)} \right\}_{cs}$ is the cross-sectional average of the non-dimensional temperature along axial location (see Eq. 4.33). Note that in our problem setup due to the periodicity in the y and z directions only the PTHF along the axial coordinate $\left\langle I_f u_{\parallel}^{\prime\prime(f)} \phi^{\prime\prime(f)} \right\rangle$ is non-zero. Therefore, we only discuss the axial component of the PTHF in the following.

Since the PTHF is computed using the cross-sectional average in Eq. 4.36 (unlike the Nusselt number, which is computed using a volume average since it is statistically homogeneous), it is susceptible to higher statistical variability than the Nusselt number. Figure 4.4 shows the axial variation of the ensemble-averaged PTHF $\left\langle I_f u_{\parallel}^{\prime\prime(f)} \phi^{\prime\prime(f)} \right\rangle$ for $\mathrm{Re_m} = 100$ and $\varepsilon_s = 0.4$. The square symbols are the ensemble-average from 5 MIS while the downward triangles are the ensemble-average from 50 MIS. Both averages are very close, indicating convergence. However, as expected, the one-sided error bars from 5 MIS (denoted below the square symbols) are larger than the error bars from 50 MIS (above the downward triangles). Since the ensemble-averaged PTHF obtained from 50 MIS is within the range of the error bars of $\left\langle I_f u_{\parallel}^{\prime\prime(f)} \phi^{\prime\prime(f)} \right\rangle$ obtained from 5 MIS, we use 5 MIS to quantify the PTHF over a range of mean slip Reynolds numbers and solid volume fractions.

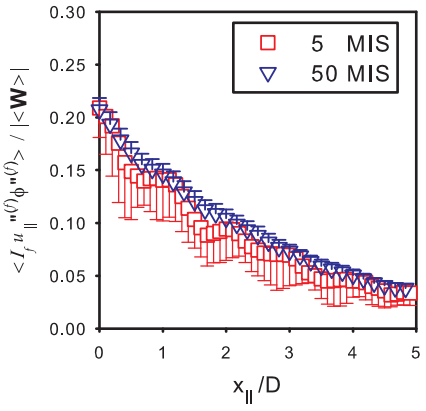

Figure 4.4: Variation of the ensemble-averaged PTHF normalized by the magnitude of mean slip velocity $|\langle \mathbf{W} \rangle|$ along axial location $x_\parallel$ over 5 and 50 MIS at $\mathrm{Re_m} = 100$ and $\varepsilon_s = 0.4$. The square and triangle symbols represent the PTHF obtained using 5 and 50 MIS, respectively. One-sided error bars indicate 95% confidence intervals.

Figure 4.4 also shows that the PTHF decays along the axial coordinate. In the hydrodynamic solution of this gas-solid flow, the PTKE $\left\langle I_f u_i''^{(f)} u_i''^{(f)} \right\rangle /2$ does not change with axial location since the velocity field is statistically homogeneous. However, in the heat transfer problem, the fluid temperature variance $\left\langle I_f \phi''^{(f)} \phi''^{(f)} \right\rangle$ decays (result not shown here) because the mean temperature gradient decays along the axial coordinate. Correspondingly, the covariance of temperature and velocity also decays. This corresponds to the decay of $\langle \phi_m \rangle$ (see Fig 4.2(a)) that is shown to be the sole source of inhomogeneity in the PTHF (see Eq. 4.35).

As shown in Eq. 4.35, another way to compute the PTHF is to obtain $\left\langle I_f u_i''^{(f)} \theta \right\rangle$, and then multiply it by the average non-dimensional bulk fluid temperature $\langle \phi_m \rangle$. Since the scaled temperature field θ is homogeneous, we also expect $\left\langle I_f u_i''^{(f)} \theta \right\rangle$ to be statistically homogeneous along the axial coordinate. Figure 4.5 shows the ensemble-averaged axial value of $\left\langle I_f u_i''^{(f)} \theta \right\rangle$ (only the magnitude of $\left\langle I_f u_\parallel''^{(f)} \theta \right\rangle$ is non-zero due to the periodicity in the y and z directions), which is computed by

$$\left\langle I_f u_i''^{(f)} \theta \right\rangle \approx \frac{1}{M} \sum_{\omega=1}^{M} \left\{ I_f u_i''^{(f)} \theta \right\} \left(x_\parallel ; \omega \right), \tag{4.40}$$

for 5 and 50 MIS. Again the two ensemble-averaged values are reasonably close to each other, with higher MIS yielding smaller error bars, as expected. The ensemble-average using 50 MIS clearly shows that $\left\langle I_f u_\parallel''^{(f)} \theta \right\rangle$ is statistically homogeneous. Therefore, $\left\langle I_f u_\parallel''^{(f)} \theta \right\rangle$ can be

computed using a volume average. For $\mathrm{Re_m} = 100$ and $\varepsilon_s = 0.4$, the volume-averaged value of $\left\langle I_f u_{\parallel}^{\prime\prime(f)} \theta \right\rangle$ (i.e. $\overline{\left\langle I_f u_{\parallel}^{\prime\prime(f)} \theta \right\rangle} = \frac{1}{L}\int_0^L \left\langle I_f u_{\parallel}^{\prime\prime(f)} \theta \right\rangle \left(x_{\parallel}\right) dx_{\parallel}$, for convenience we drop the overbar later) is about 0.22 from five MIS and 0.20 from 50 MIS. This indicates that the volume-averaged value with fewer realizations is close to the one from 50 MIS. Therefore, $\left\langle I_f u_{\parallel}^{\prime\prime(f)} \theta \right\rangle$ can be calculated as a volume average from five realizations and only depends on mean slip Reynolds number and solid volume fraction.

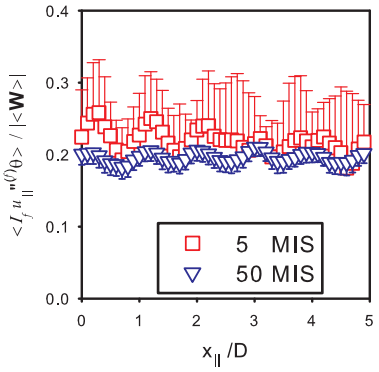

Figure 4.5: Variation of $\left\langle I_f u_{\parallel}^{\prime\prime(f)} \theta \right\rangle$ normalized by mean slip velocity $|\langle \mathbf{W} \rangle|$ along axial location $x_{\parallel}$ at $\mathrm{Re_m} = 100$ and $\varepsilon_s = 0.4$. The red and blue symbols represent the PTHF obtained using 5 and 50 realizations, respectively. One-sided error bars indicate 95% confidence intervals.

In order to develop a model for the PTHF, we characterize the dependence of $\left\langle I_f u_{\parallel}^{\prime\prime(f)} \theta \right\rangle$ on mean slip Reynolds number and solid volume fraction as shown in Fig. 4.6. Since θ is non-dimensional, we expect $\left\langle I_f u_{\parallel}^{\prime\prime(f)} \theta \right\rangle$ to scale with $|\langle \mathbf{W} \rangle|$ and therefore increase with mean slip Reynolds number ($\mathrm{Re_m} = (1-\varepsilon_s)|\langle \mathbf{W} \rangle| D/\nu_f$) for a fixed solid volume fraction. For a fixed solid volume fraction (see Fig. 4.6(a)), the volume average of $\left\langle I_f u_{\parallel}^{\prime\prime(f)} \theta \right\rangle$ normalized by the magnitude of the mean slip velocity $|\langle \mathbf{W} \rangle|$ is not constant but decreases slightly with increasing mean slip Reynolds number, indicating that the dependence of $\left\langle I_f u_{\parallel}^{\prime\prime(f)} \theta \right\rangle$ on $|\langle \mathbf{W} \rangle|$ is not exactly linear. The mean value of $\left\langle I_f u_{\parallel}^{\prime\prime(f)} \theta \right\rangle$ is not very sensitive to mean slip Reynolds number but lies in the range 0.2-0.34 for $1 \leq \mathrm{Re_m} \leq 100$. Figure 4.6(b) shows that for a fixed Reynolds number $\left\langle I_f u_{\parallel}^{\prime\prime(f)} \theta \right\rangle / |\langle \mathbf{W} \rangle|$ first increases with increasing solid volume fraction up to $\varepsilon_s = 0.2$, and then decreases for $\varepsilon_s > 0.2$. In order to develop a PTHF model in Sec. 4.5.3, a correlation for $\left\langle I_f u_{\parallel}^{\prime\prime(f)} \theta \right\rangle$ is given by fitting PR-DNS data:

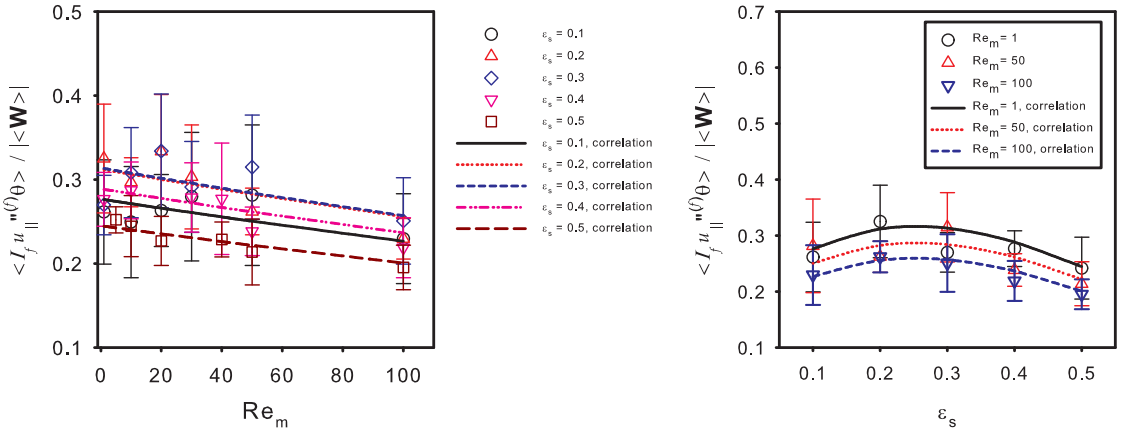

(a) (b)

Figure 4.6: Dependence of $\left\langle I_f u_{\parallel}^{\prime\prime(f)} \theta \right\rangle$ on (a) mean slip Reynolds number at $\varepsilon_{\rm s} = 0.1 - 0.5$, and (b) solid volume fraction at $\mathrm{Re_m} = 1$, 50 and 100. The symbols are $\left\langle I_f u_{\parallel}^{\prime\prime(f)} \theta \right\rangle$ from PR-DNS data and the lines are the correlation by fitting PR-DNS data in Eq. 4.41. Error bars indicate 95% confidence intervals using 5 MIS.

$$\left\langle I_f u_{\parallel}^{\prime\prime(f)} \theta \right\rangle = (1-\varepsilon_s)\left(0.2 + 1.2\varepsilon_s - 1.24\varepsilon_s^2\right) \exp\left(-0.002\mathrm{Re_m}\right) |\left\langle \mathbf{W} \right\rangle|. \tag{4.41}$$

This correlation shown by the lines in Fig. 4.6 fits the data with an average deviation of 8%. It is valid in the range of $0.1 \leq \varepsilon_s \leq 0.5$ and $1 \leq \mathrm{Re_m} \leq 100$. Note that the homogeneity of $\left\langle I_f u_{\parallel}^{\prime\prime(f)} \theta \right\rangle$ in Eq. 4.35 also implies that, in thermally fully-developed homogeneous flow the source of inhomogeneity in PTHF arises solely from the average bulk fluid temperature. More importantly, inhomogeneity of PTHF implies that the transport term corresponding to the PTHF in Eq. 4.1 is non-zero.

In the following, we first quantify the magnitude of PTHF relative to convective mean flux and then propose a model for it in Sec. 4.5.3. In Sec. 4.5.4 the Péclet number dependence of the effective thermal diffusivity is explained using a wake scaling analysis. In Sec. 4.5.5 we quantify the magnitude of the transport term involving the PTHF relative to the average gas-solid heat transfer term in Eq. 4.1.

4.5.2 Relative importance of the PTHF to convective mean flux

In order to verify the importance of PTHF, we compare the PTHF with the convective mean flux $\varepsilon_f \langle u_i^{(f)} \rangle \langle \phi^{(f)} \rangle$ that appears in Eq. 4.1. Based on the expression for the PTHF in Eq. 4.35 and the relation for $\left\langle \phi^{(f)} \right\rangle$ in Eq. 4.32, the ratio of the PTHF to the convective mean flux can be written as

$$\frac{\left\langle I_f u_i''^{(f)} \phi'' \right\rangle \left(x_\parallel \right)}{\varepsilon_f \left\langle u_i^{(f)} \right\rangle \langle \phi^{(f)} \rangle \left(x_\parallel \right)} = \frac{\left\langle I_f u_i''^{(f)} \theta \right\rangle \langle \phi_m \rangle}{\varepsilon_f \left\langle u_i^{(f)} \right\rangle \langle \phi^{(f)} \rangle} = \frac{\left\langle I_f u_i''^{(f)} \theta \right\rangle}{\varepsilon_f \left\langle u_i^{(f)} \right\rangle \langle \theta^{(f)} \rangle}. \tag{4.42}$$

Since all the terms in the last expression of the above equation are homogeneous, the ratio of the PTHF to the convective mean flux is independent of axial location. Since $\left\langle I_f u_i''^{(f)} \theta \right\rangle$, $\left\langle u_i^{(f)} \right\rangle$ and $\left\langle \theta^{(f)} \right\rangle$ are functions of mean slip Reynolds number and volume fraction, this ratio also depends only on mean slip Reynolds number and solid volume fraction.

It can be shown that the ratio of PTHF to the convective mean flux is independent of axial location. The reason for this homogeneity lies in the important property of the PTHF that we deduce in the paragraph preceding equation (4.35). There we used the relation $\phi = \langle \phi_m \rangle \theta$ to show in equation (4.35) that the spatial inhomogeneity in the PTHF $\left\langle I_f \mathbf{u}''^{(f)} \phi''^{(f)} \right\rangle \left(x_\parallel \right)$ arises solely from the inhomogeneity of the non-dimensional bulk temperature $\langle \phi_m \rangle$. When the PTHF is divided by the convective mean flux, the only spatially inhomogeneous terms appear as a ratio $\langle \phi_m \rangle / \left\langle \phi^{(f)} \right\rangle$. However, by virtue of equation (4.32) this ratio is simply $1/\left\langle \theta^{(f)} \right\rangle$, which is statistically homogeneous because the locally scaled excess fluid temperature field θ is statistically homogeneous. In order to verify this independence of the ratio of the PTHF to the convective mean flux on axial location, Figure 4.7(a) shows the axial variation of this ratio using 5 and 50 realizations. Although the ratio obtained from 5 realizations has more statistical variability than the one from 50 MIS, neither shows any systematic dependence on axial location. This finding confirms the statistical homogeneity of this ratio in Eq. 4.42.

Figure 4.7(b) shows a comparison of the axial PTHF with the convective mean flux $\varepsilon_f \langle u_\parallel^{(f)} \rangle \langle \phi^{(f)} \rangle$ over a range of mean slip Reynolds numbers and solid volume fractions. Note that again due to the periodicity in the y and z directions, we only compare the axial value $\left\langle I_f u_\parallel''^{(f)} \theta \right\rangle$ with $\varepsilon_f \langle u_\parallel^{(f)} \rangle \langle \phi^{(f)} \rangle$. The symbols denote the ratio of the PTHF to the convective mean flux. For a fixed Reynolds number, the ratio increases with increasing solid volume fraction in most cases.

For $\mathrm{Re_m} = 100$, the PTHF is about 40% of the convective mean flux at $\varepsilon_s = 0.1$ but about 70% of the convective mean flux at $\varepsilon_s = 0.5$. The increase in the magnitude of the PTHF results from higher fluctuations at higher solid volume fraction. For a fixed solid volume fraction, the ratio of the PTHF to the convective mean flux tends to decrease slightly with increasing mean slip Reynolds number. Overall, the magnitude of PTHF is in the range 40% to 100% of the convective mean flux. Therefore, the PTHF is a significant fraction of the total convective flux even at low solid volume fraction.

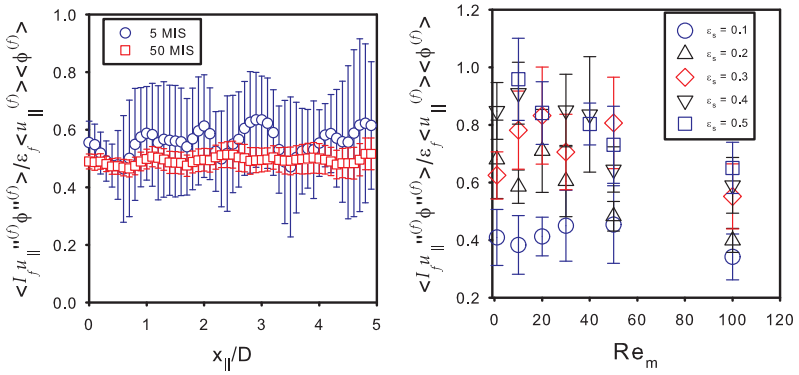

(a) (b)

Figure 4.7: (a) Axial variation of the ratio of the PTHF to the convective mean flux at $\mathrm{Re_m} = 100$ and $\varepsilon_s = 0.4$. The open circles and the squares represent the ratio obtained from 5 MIS and 50 MIS, respectively. Error bars indicate 95% confidence intervals from 5 MIS (blue) and 50 MIS (red). (b) Comparison of the PTHF with convective mean flux $\varepsilon_f \langle u_{\parallel}^{(f)} \rangle \langle \phi^{(f)} \rangle$ in the range $1 \leq \mathrm{Re_m} \leq 100$ and $0.1 \leq \varepsilon_s \leq 0.5$. The open symbols represent the ratio of the PTHF and $\varepsilon_f \langle u_{\parallel}^{(f)} \rangle \langle \phi^{(f)} \rangle$ obtained from PR-DNS data. Error bars indicate 95% confidence intervals from 5 MIS.

4.5.3 Model for pseudo-turbulent heat flux

Since the PTHF is found to be significant for gas-solid heat transfer, the transport term involving the PTHF needs to be modeled in CFD simulations based on the two-fluid model (see Eq. 4.1). In order to develop a model for the PTHF, we introduce a gradient-diffusion model by analogy with turbulent scalar flux models in single-phase flow (Fox (2003)):

$$R_{\mathbf{u}\phi} = \frac{\left\langle I_f u_j^{\prime\prime(f)} \phi^{\prime\prime(f)} \right\rangle \left(x_{\parallel} \right)}{\langle I_f \rangle} = -\alpha_{jk,PT} \frac{\partial \left\langle \phi^{(f)} \right\rangle}{\partial x_k}, \tag{4.43}$$

where $\alpha_{jk,PT}$ is the pseudo-turbulent thermal diffusivity. Note that in general the thermal diffusivity is a tensor rather than a scalar. However, in our gas-solid heat transfer problem, the only non-zero component of the PTHF is the axial component which is aligned with the gradient of the mean fluid temperature. Therefore, we can only deduce one component $\alpha_{||,||}$ of the pseudo-turbulent thermal diffusivity tensor from the PR-DNS data, as follows:

$$R_{u_\parallel \phi} = \frac{\left\langle I_f u_\parallel''^{(f)} \phi''^{(f)} \right\rangle \left(x_\parallel\right)}{\langle I_f \rangle} = -\alpha_{PT} \frac{\partial \left\langle \phi^{(f)} \right\rangle}{\partial x_\parallel}, \tag{4.44}$$

where $\alpha_{PT} = \alpha_{||,||}$.

Once the pseudo-turbulent thermal diffusivity α_{PT} is computed, the transport term involving the PTHF at a given axial location can be obtained in terms of the pseudo-turbulent thermal diffusivity α_{PT} and average non-dimensional fluid temperature $\left\langle \phi^{(f)} \right\rangle$ as:

$$\frac{\partial}{\partial x_{||}} \left\{ \rho_f c_{pf} \left\langle I_f u_\parallel''^{(f)} \phi''^{(f)} \right\rangle \left(x_\parallel\right) \right\} = \frac{\partial}{\partial x_{||}} \left(-\varepsilon_f \rho_f c_{pf} \alpha_{PT} \frac{\partial \left\langle \phi^{(f)} \right\rangle}{\partial x_{||}} \right). \tag{4.45}$$

A model for the pseudo-turbulent thermal diffusivity α_{PT} can be derived by substituting the relation $\left\langle \phi^{(f)} \right\rangle = \left\langle \theta^{(f)} \right\rangle \langle \phi_m \rangle$ in Eq. 4.32, then substituting Eq. 4.35 into Eq. 4.44, and replacing $\langle \phi_m \rangle$ with the exponential decay model $\langle \phi_m \rangle = \exp\left(-\lambda x_\parallel / D\right)$ (see Eq. 4.28) to obtain:

$$\alpha_{PT} = -\frac{\left\langle I_f u_\parallel''^{(f)} \theta \right\rangle \exp\left(-\lambda x_\parallel / D\right)}{-\varepsilon_f \left\langle \theta^{(f)} \right\rangle \frac{\lambda}{D} \exp\left(-\lambda x_\parallel / D\right)} = \frac{D}{\lambda} \frac{\left\langle I_f u_\parallel''^{(f)} \theta \right\rangle}{(1-\varepsilon_s) \left\langle \theta^{(f)} \right\rangle}. \tag{4.46}$$

Using the correlation for $\left\langle I_f u_\parallel''^{(f)} \theta \right\rangle$ given in Eq. 4.41, the expressions for λ given in Eq. 4.29 and the average scaled fluid temperature $\left\langle \theta^{(f)} \right\rangle$ from Sun et al. (2015), the final expression for α_{PT} is

$$\alpha_{PT} = \frac{4D\left(\mathrm{Re_m} + 1.4\right)\mathrm{Pr}}{6\pi\varepsilon_s \langle \mathrm{Nu} \rangle} \frac{\left(0.2 + 1.2\varepsilon_s - 1.24\varepsilon_s^2\right) \exp\left(-0.002\mathrm{Re_m}\right) |\langle \mathbf{W} \rangle|}{\left[1 - 1.6\varepsilon_s(1-\varepsilon_s) - 3\varepsilon_s(1-\varepsilon_s)^4 \exp(-\mathrm{Re_m^{0.4}}\varepsilon_s)\right]}, \tag{4.47}$$

It is noteworthy that in this model α_{PT} scales as $D|\langle \mathbf{W} \rangle|$. Also as expected α_{PT} is independent of axial location and depends only on $\mathrm{Re_m}$, ε_s, and Pr (note that $\langle \mathrm{Nu} \rangle$ is also a function of $\mathrm{Re_m}$, ε_s, and Pr (cf. Eq. 27 in Sun et al. (2015)).

In order to evaluate the performance of this model for the pseudo-turbulent thermal diffusivity α_{PT}, we compare α_{PT} obtained from direct quantification of the PTHF $\left\langle I_f u_\parallel''^{(f)} \phi''^{(f)} \right\rangle$

using PR-DNS data in Eq. 4.44 with the model expression given by Eq. 4.47. Figure 4.8 shows the dependence of the ratio α_{PT}/α_f (α_f is the constant molecular thermal diffusivity that is equal to ν_f/Pr) on mean slip Reynolds number and solid volume fraction.

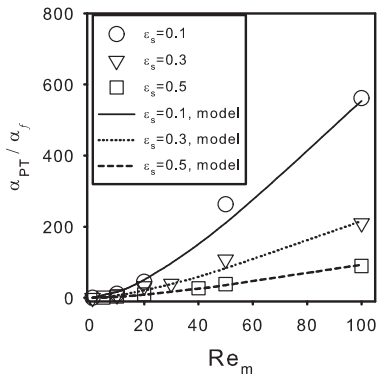

Figure 4.8: Dependence of the pseudo-turbulent thermal diffusivity normalized by the molecular thermal diffusivity in the fluid phase α_f for gas-solid flow on mean slip Reynolds number and solid volume fraction. The symbols represent the average values from PR-DNS data using 5 MIS. The lines represent the model for the pseudo-turbulent thermal diffusivity for $\varepsilon_s = 0.1$, 0.3 and 0.5.

The symbols denote the values of α_{PT}/α_f extracted from PR-DNS data which show that the pseudo-turbulent thermal diffusivity is two orders of magnitude larger than its molecular counterpart. In Fig. 4.8 the pseudo-turbulent thermal diffusivity α_{PT} increases with increasing mean slip Reynolds number for a fixed solid volume fraction. This increase is due to the increase in the magnitude of $\mathbf{u}''^{(f)}$ with increasing Reynolds number.

For a fixed Reynolds number, Fig. 4.8 shows that as the solid volume fraction increases the pseudo-turbulent thermal diffusivity decreases. Since the pseudo-turbulent thermal diffusivity α_{PT} can be conceived as arising from the product of a velocity scale $\mathbf{u}''^{(f)}$ (or equivalently the velocity scale $|\langle \mathbf{W} \rangle|$, since the two are related by a correlation for k_f given in Mehrabadi et al. (2015)), and a length scale ℓ, the dependence for fixed Reynolds number must arise from a change in the length scale associated with α_{PT}. Looking at the expression for α_{PT} in Eq. 4.46, we can see that such a length scale dependence on solid volume fraction can arise from $D/\lambda\,(1-\varepsilon_s)$, $\left\langle \theta^{(f)} \right\rangle$ or $\left\langle I_f u_{\parallel}''^{(f)} \phi''^{(f)} \right\rangle$. Since the velocity field and the scaled temperature field θ are statistically homogeneous, the Eulerian two-point correlation corresponding to $\left\langle I_f u_{\parallel}''^{(f)} \theta \right\rangle$

is:

$$\rho_{u_{\parallel}\theta}(\mathbf{r}) = \frac{\left\langle I_f(\mathbf{x})\theta''^{(f)}(\mathbf{x}) \cdot I_f(\mathbf{x}+\mathbf{r})u_{\parallel}''^{(f)}(\mathbf{x}+\mathbf{r})\right\rangle}{\left\langle I_f(\mathbf{x})\theta''^{(f)}(\mathbf{x}) \cdot I_f(\mathbf{x})u_{\parallel}''^{(f)}(\mathbf{x})\right\rangle}, \tag{4.48}$$

and it can be computed to infer a length scale associated with $\left\langle I_f u_{\parallel}''^{(f)}\phi''^{(f)}\right\rangle$. Note that in the above equation $\left\langle I_f u_{\parallel}''^{(f)}\theta''^{(f)}\right\rangle$ is equal to $\left\langle I_f u_{\parallel}''^{(f)}\theta\right\rangle$ because $\theta = \left\langle\theta^{(f)}\right\rangle + \theta''^{(f)}$ and $\left\langle I_f u_{\parallel}''^{(f)}\right\rangle = 0$.

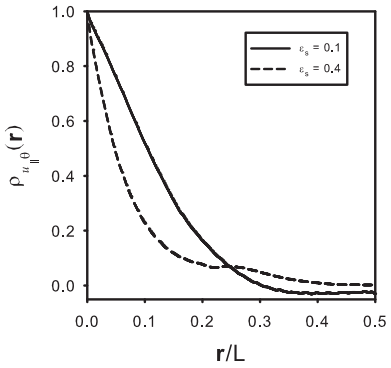

Figure 4.9: Decay of the scaled fluid temperature-velocity fluctuation cross correlation functions with separation distance $\mathbf{r}$ obtained from steady flow past a random configuration of spheres at a solid volume fraction of 0.1 and 0.4, and mean slip Reynolds numbers of 100. The box length is $L = 7.5D$ for solid volume fraction of 0.1 and $L = 5D$ for for solid volume fraction of 0.4, respectively.

Figure 4.9 shows the Eulerian two-point cross-correlation corresponding to scaled temperature-velocity for solid volume fractions of 0.1 and 0.4.The decay of the cross-correlation to zero within the computational domain establishes the adequacy of the domain size. In dispersion without interphase heat transfer, the temperature fluctuations are only driven by velocity fluctuations. Since the temperature-velocity correlation would be arising from the velocity-velocity correlation, the velocity-velocity correlation length (which is related to the Brinkman length for Stokes flow) is the important length scale for hydrodynamic dispersion (Koch and Brady (1985)). However, for the present study with interphase heat transfer, the temperature fluctuations arise from both the velocity fluctuation and the interphase heat transfer. The fluctuations from the interphase heat transfer may not scale with the velocity fluctuation. Therefore, this temperature-velocity cross-correlation is the relevant important correlation for our problem rather than the velocity-velocity correlation. The cross-correlation curves in Fig. 4.9 for the

two volume fractions have comparable length scales. The length scale ($L_{u_\parallel\theta} = \int_0^\infty \rho_{u_\parallel\theta}(\mathbf{r})\mathrm{d}\mathbf{r}$) for the case with a solid volume fraction of 0.1 is 0.114, while for a solid volume fraction of 0.4 it is 0.078. While this is a 46% increase, it alone cannot explain the 230% increase in α_{PT} that is seen in Fig. 4.9. This implies that the length scale in the θ field is only weakly sensitive to solid volume fraction. Thus, $\left\langle I_f u_\parallel''^{(f)}\theta \right\rangle$ is not solely responsible for the change in length scale with solid volume fractions that is observed in α_{PT}. Also the scaled fluid temperature $\left\langle \theta^{(f)} \right\rangle$ varies only slightly with Reynolds number and solid volume fraction (see Sun et al. (2015), Fig. 8). Clearly, only the length scale $D/\lambda\,(1-\varepsilon_s)$ is important in determining the magnitude of the pseudo-turbulent thermal diffusivity α_{PT}. According to the expression for λ (see Eq. 4.27), with increasing solid volume fraction, the length scale $D/\lambda\,(1-\varepsilon_s)$ decreases. This explains the decrease of the pseudo-turbulent thermal diffusivity α_{PT} with solid volume fraction in Fig. 4.8.

Figure 4.8 also compares the model for the pseudo-turbulent thermal diffusivity (see Eq. 4.47) with the PR-DNS data. The lines represent the model for α_{PT} given by Eq. 4.47 at selected solid volume fractions. This figure shows that the model has a good agreement with PR-DNS data with an average difference of 18%. Therefore, this model for the pseudo-turbulent thermal diffusivity can be used to compute the transport term involving the PTHF in the average fluid temperature equation (Eq. 4.1) if we assume a simpler isotropic form of the pseudo-turbulent diffusivity tensor given in Eq. 4.43.

4.5.4 Scaling of pseudo-turbulent thermal diffusivity with Péclet number

Theoretical studies on hydrodynamic dispersion in fixed beds for Stokes/low Reynolds number flow predict the dependence of the effective diffusivity on the Péclet number (Brenner (1980); Carbonell and Whitaker (1983); Eidsath et al. (1983)). Koch and Brady (1985) derived linear and $\mathrm{Pe}\ln(\mathrm{Pe})$ dependencies in the effective diffusivity by solving the convection-diffusion equation for mass transfer with no source or sink of mass within the particles in Stokes flow using an asymptotic analysis that is valid in the dilute limit (low solid volume fraction). The analysis of Koch and Brady (1985) is for the case with no source or sink of mass within the particles, which is an important distinction from the present work. Here the Péclet number

is defined as $\mathrm{Pe} = Ua/D_f$, where U is the average velocity through the bed, a is the particle radius and D_f is the molecular diffusivity of the scalar. The linear dependence is attributed to the mechanical dispersion mechanism while the $\mathrm{Pe}\ln(\mathrm{Pe})$ dependency is attributed to a non–mechanical dispersion mechanism that arises from the no–slip boundary condition (obtained from a boundary layer analysis).

While the Koch and Brady (1985) analysis is valid for Stokes flow at dilute solid volume fraction, the results of the present study span a range of Reynolds number from 1 to 100 and solid volume fraction values from 0.1 to 0.5. Furthermore, since in our heat transfer problem we impose the isothermal boundary condition on particle surfaces, we cannot compare directly with the results of Koch and Brady (1985). Acrivos et al. (1980) analyzed Stokes flow past a fixed bed with heat transfer at low Péclet number when the local mean temperature profile is approximately linear, rather than exponential, corresponding to the decay length of the mean temperature being larger than the Brinkman screening length. However, the cases studied here correspond to $\mathrm{Pe} \geq 1$. Here we deduce the scaling of the effective thermal diffusivity with Péclet number in two ways. The first is based on correlations developed from the PR-DNS data for the average bulk fluid temperature and Nusselt number. We then present a scaling analysis similar to that described in Koch (1993) which is appropriate for $Re_a \gg 1$, where $Re_a = U_{\|}a/\nu_f$ is the Reynolds number based on the radii of particle, $U_{\|}$ is the mean fluid velocity (which is the mean slip velocity for fixed particles considered in this study).

In Appendix E we derive a model for the effective thermal diffusivity based on the correlations developed for the average bulk fluid temperature and Nusselt number. This reveals the scaling of the effective thermal diffusivity with Péclet number as:

$$\frac{\alpha_{PT} + \alpha_f}{\alpha_f} = \frac{C_1 C_3}{C_2\left(C_4 + C_5 \mathrm{Re_m^{0.7}Pr^{1/3}}\right)}\mathrm{Pe_D^2} + 1, \tag{4.49}$$

where the coefficients C_1 through C_5 are functions of only the solid volume fraction. In figure 4.10, we compare this model evaluated at $\mathrm{Pr} = 0.7$ for a fixed solid volume fraction ($\varepsilon_s = 0.1$) with PR-DNS data. This derived model (represented by the red solid line) is very close to our PR-DNS data that are obtained for cases with different Prandtl number values. For these values the factor preceding the square of the Péclet number is approximately constant. This

good agreement with the PR-DNS data shows that the effective thermal diffusivity has a $\mathrm{Pe_D^2}$ scaling (see also the match with the blue dashed line representing $1 + 0.25\mathrm{Pe_D^2}$).

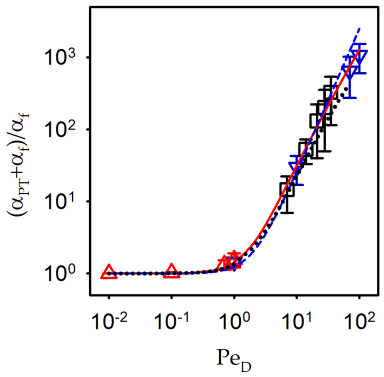

Figure 4.10: Variation of $(\alpha_{PT} + \alpha_f)/\alpha_f$ with Péclet number $\mathrm{Pe_D} = |\langle \mathbf{W} \rangle| D/\alpha_f$ at $\mathrm{Re_m} = 1$ (up-triangle), $\mathrm{Re_m} = 100$ (down-triangle) with $\mathrm{Pr} = 0.01$, 0.1, 0.7 and 1, and $\mathrm{Re_m} = 10 - 50$ at $\mathrm{Pr} = 0.7$ (square) for solid volume fraction of 0.1. The dashed line represents the $1 + 0.25\mathrm{Pe^2}$ scaling and the solid line represents the model in Eq. 4.49. The dotted line represents the $0.065\mathrm{Pe_D^2}\left[\ln(1/\mathrm{Pr}) + 1\right] + 1$ scaling at $\mathrm{Re_m} = 100$ for different Prandtl numbers ($0.01 \leq \mathrm{Pr} \leq 0.7$) in Eq. F.11.

The dependence of effective thermal diffusivity on Péclet number can also be explained on the basis of scaling arguments in the hydrodynamic and and thermal wakes behind a particle. The wake structure can be deduced from the conditionally averaged fluid velocity $\left\langle I_f U_{\parallel} \right\rangle_c (\mathbf{r} = \mathbf{X} - \mathbf{X}_p | \mathbf{X}_p)$ and conditionally averaged scaled fluid temperature

$$\langle I_f (T - T_s) / (\langle T_m \rangle - T_s) \rangle_c (\mathbf{r} = \mathbf{X} - \mathbf{X}_p | \mathbf{X}_p),$$

where $\mathbf{X}_p$ and $\mathbf{r}$ are the particle position and the relative separation between the particle and field point in the fluid, respectively. These conditional averages correspond to averaging the fluid velocity or temperature field over members of an ensemble where each particle's center has been translated to the origin.

Figure 4.11 shows that for dilute flow there exists a distinct hydrodynamic wake at Re_m=100, and a distinct thermal wake behind the particle at both large and small Péclet number. It is observed in Fig. 4.11(b) and (c) that the thermal wake is longer and thinner at higher Péclet (or higher Prandtl number) than at lower Péclet number. The distance over which wake can

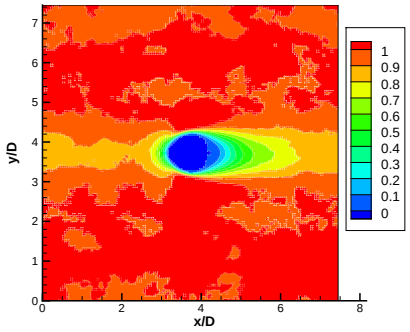

(a) $\mathrm{Re_m} = 100$: Velocity field

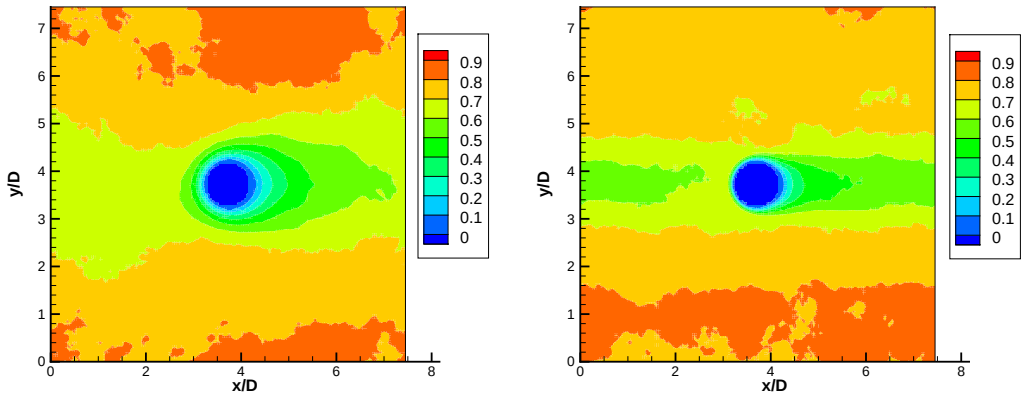

(b) Pr=0.01

(c) Pr=1

Figure 4.11: Contour plot of (a) the conditionally averaged fluid velocity that is defined as $\left\langle I_f U_\parallel \right\rangle_c / |\langle \mathbf{W} \rangle|$, (b)-(c) the conditionally averaged scaled fluid temperature that is defined as $\langle I_f (T - T_s) / (\langle T_m \rangle - T_s) \rangle_c$ based on $\langle T_m \rangle$ for solid volume fraction of 0.1 and mean slip Reynolds number of 100 (a). The conditional average is obtained from 5 MIS.

diffuse due to the viscous diffusion in the cross-stream direction over the time it takes for the fluid to convect a distance $x_\parallel$ in the streamwise direction is $\sqrt{\left(\nu_f x_\parallel / U_\parallel\right)}$. We can identify the width of the hydrodynamic wake r_{WM} in the near-wake and far-wake regions as follows. For $x_\parallel < aRe_a$, the diffusion of momentum in the near-wake region occurs over a smaller distance than the $O(a)$ size of the region disturbed by the particle. For $x_\parallel > aRe_a$ in the far-wake region

the wake thickness is larger than the particle size leading to:

$$r_{WM} = \begin{cases} \sim O(a), & x_\parallel < aRe_a \\ \left(\frac{\nu_f x_\parallel}{U_\parallel}\right)^{1/2} = a\left(\frac{x_\parallel}{aRe_a}\right)^{1/2}, & x_\parallel > aRe_a \end{cases}. \tag{4.50}$$

The velocity fluctuation can be derived from the momentum balance equation $\pi r_{WM}^2 \rho_f U_\parallel u_\parallel'' = F$ leading to

$$\frac{u_\parallel''}{U_\parallel} = C_D \frac{a^2}{r_{WM}^2} = C_D \frac{a\,Re_a}{x_\parallel} = \begin{cases} \sim O(C_D), & x_\parallel < aRe_a \\ C_D \frac{a\,Re_a}{x_\parallel}, & x_\parallel > aRe_a \end{cases}, \tag{4.51}$$

where $F = C_D \rho_f U_\parallel^2 \pi a^2$ is the drag force and C_D is the drag coefficient corresponding to a fixed particle bed. Essentially this says that in the near-wake region the fluid velocity does not vary much ($u_\parallel'' - U_\parallel = O\left(U_\parallel\right)$) whereas in the far-wake region the fluctuation is far less than the mean velocity ($u_\parallel'' = u - U_\parallel \ll U_\parallel$).

Similarly, the width of the thermal wake r_{WH} can be estimated on the basis of thermal diffusivity as

$$r_{WH} = \begin{cases} \sim O(a) & x_\parallel < aPe_a \\ a\left(\frac{x_\parallel}{aPe_a}\right)^{1/2} & x_\parallel > aPe_a \end{cases}, \tag{4.52}$$

and the temperature fluctuation can be derived from the energy balance equation

$$\pi r_{WH}^2 \rho_f c_{pf} U_\parallel T'' = Q_{pf} = 4\pi a^2 h \left(T_s - \langle T_m \rangle\right)$$

as

$$\frac{T''}{(T_s - \langle T_m \rangle)} = \frac{4h}{\rho_f c_{pf} U_\parallel} \frac{a^2}{r_{WH}^2} = \frac{4h}{\rho_f c_{pf} U_\parallel} \frac{aPe_a}{x_\parallel} = \begin{cases} \sim O\left(\frac{4h}{\rho_f c_{pf} U_\parallel}\right), & x_\parallel < aPe_a \\ \frac{4h}{\rho_f c_{pf} U_\parallel} \frac{aPe_a}{x_\parallel}, & x_\parallel > aPe_a \end{cases} \tag{4.53}$$

where $Pe_a = U_\parallel a/\alpha_f$ is the Péclet number based on the radius of the particle, and r_{WH} is the width of the thermal wake. The thermal wake for $x_\parallel < aPe_a$ depends on whether the temperature field is disturbed throughout on $O(a)$ region at the back of the particle or only

in a thinner region where the thermal boundary layer separates from the particle. We assume that it is an $O(a)$ region and this assumption is verified by the thermal wakes in Fig. 4.11(b) and (c).

The unconditional ensemble-averaged PTHF $\left\langle I_f u_\parallel''^{(f)} T''^{(f)} \right\rangle$ is calculated from the wake scaling analysis as the particle number density n_p times an integral over the probability density function (pdf) of the conditionally averaged particle position f:

$$\left\langle I_f u_\parallel''^{(f)} T''^{(f)} \right\rangle = n_p \int_0^{L_w} \int\int f dx_\parallel dy dz, \tag{4.54}$$

where n_p is the particle number density defined as the ratio of the average number of particles to the volume of the domain, and L_w is the length of the wake that represents the velocity contour surrounding the particle where the value of the conditionally ensemble-averaged velocity reaches $|\langle \mathbf{W} \rangle|$ (note that since the particles are stationary, the mean slip velocity is equal to the unconditionally averaged fluid velocity). Note that the full length of the far wake is not attained in the computational domain as shown in Fig. 4.11(a) due to hydrodynamic interactions with neighbor particles (note that the two-point velocity correlation has decayed to zero within the computational domain, indicating that the domain is large enough for this to not be an artifact of periodicity). In this study we have $\mathrm{Pr} \leq 1$, and the thermal far-wake and hydrodynamic near-wake region overlap in the interval $aPe_a < x_\parallel < aRe_a$. By inserting Eqs. 4.50-4.53, and integrating over the near-wake, intermediate, and far-wake regions, the PTHF yields

$$\left\langle I_f u_\parallel''^{(f)} T''^{(f)} \right\rangle = Pe_a \left[k_2 \ln\left(\frac{1}{\mathrm{Pr}}\right) + k_3 \ln\left(\frac{L_w}{aRe_a}\right) + k_1 \right], \tag{4.55}$$

where k_1, k_2, and k_3 are undetermined coefficients arising from the scaling estimates and uncertainty in the limits of the integral (see Appendix F). In the above expression, the $\ln(1/\mathrm{Pr})$ term comes from the intermediate region and the constant term comes from the near wake. Note that since hydrodynamic interactions with neighbor particles cause the velocity to decay before achieving a far-wake behavior, $\ln(L_w/aRe_a)$ is not present in practice. The detailed derivation can be found in Appendix F. Substituting this expression for the PTHF into the expression for the pseudo-turbulent thermal diffusivity:

$$\alpha_{PT} = -\frac{\left\langle I_f u_\parallel''^{(f)} T''^{(f)} \right\rangle \left(x_\parallel\right)}{\dfrac{\partial \langle I_f T \rangle}{\partial x_\parallel}} \sim \frac{\left\langle I_f u_\parallel''^{(f)} T''^{(f)} \right\rangle \left(x_\parallel\right)}{\dfrac{\partial \left(T_s - \langle T_m \rangle\right)}{\partial x_\parallel}}, \tag{4.56}$$

and using the decay length scale of the bulk and mean fluid temperature D/λ to write the gradient as $\left(T_s - \langle T_m \rangle\right)/(D/\lambda)$ results in

$$\frac{\alpha_{PT} + \alpha_f}{\alpha_f} = \frac{C_D Pe_D^2}{\pi^2}\left[B_2 \ln\left(\frac{1}{\mathrm{Pr}}\right) + B_3 \ln\left(\frac{L_w}{aRe_a}\right) + B_1\right] + 1, \tag{4.57}$$

where $B_1 - B_3$ are again undetermined coefficients. Note that using the correct length scale based on the mean temperature gradient is crucial to recovering the scaling observed in PR–DNS.

The wake analysis of the scaling of the effective thermal diffusivity with Péclet number is compared with PR-DNS data in Fig. 4.10. The results obtained from the wake scaling analysis (the dotted line) agree well with the PR-DNS data (the symbols) at Re_m=100 for $\mathrm{Pr} < 1$. The Pe_D^2 scaling itself comes from there being a wake and from realizing that decay length is the scaling to use for mean temperature gradient. Therefore, this analysis of the hydrodynamic and thermal wakes behind the particle gives a physical explanation for the existence of a Pe_D^2 scaling in effective thermal diffusivity in the regime of high Reynolds number and low Prandtl number.

4.5.5 Relative importance of the PTHF in gas-solid heat transfer

We have found that the PTHF is significant when compared with the convective mean flux, especially for high solid volume fraction. In order to quantify the importance of the transport term involving the PTHF

$$\langle T_{\mathbf{u}\phi} \rangle \left(x_{||}\right) \equiv \nabla \cdot \left\{ \rho_f c_{pf} \left\langle I_f \mathbf{u}''^{(f)} \phi''^{(f)} \right\rangle \right\}, \tag{4.58}$$

we need to compute the streamwise derivative of $\left\langle I_f \mathbf{u}''^{(f)} \phi''^{(f)} \right\rangle$ since the PTHF is only statistically inhomogeneous along the axial coordinate. However, as shown in Fig. 4.4, given that the ensemble-averaged statistical estimate in Eq. 4.36 has statistical variability, this can yield noisy results. In order to circumvent this difficulty, we integrate the transport term over the computational domain to express the mean value of the transport term involving the PTHF in

the domain in terms of boundary values of the PTHF as follows:

$$\overline{\langle T_{\mathbf{u}\phi}\rangle} = \overline{\left\langle T_{u_\parallel \phi}\right\rangle} = \frac{1}{L}\int_L \frac{\partial}{\partial x_{||}}\left\{\rho_f c_{pf}\left\langle I_f u_{||}^{\prime\prime(f)}\phi^{\prime\prime(f)}\right\rangle\right\}\left(x_\parallel\right)dx_\parallel = \frac{1}{L}\left(\left[\rho_f c_{pf}\left\langle I_f u_{||}^{\prime\prime(f)}\phi^{\prime\prime(f)}\right\rangle\right]_{out} - \left[\rho_f c_{pf}\left\langle I_f u_{||}^{\prime\prime(f)}\phi^{\prime\prime(f)}\right\rangle\right]_{in}\right), \quad (4.59)$$

where L is the length of the domain, $[\cdot]_{in}$ and $[\cdot]_{out}$ are obtained at the inlet and outlet of the computational domain, respectively. Note that due to periodic boundary conditions in the y and z directions the flux term in those directions is zero.

In the two-fluid equation (see Eq. 4.1), since the gas-solid heat transfer is considered as a significant term, the importance of the transport term involving the PTHF can be quantified by comparing it with the average gas-solid heat transfer term (see Eq. 4.64). Figure 4.12 shows a comparison of the transport term involving the PTHF scaled by the average gas-solid heat transfer over a range of mean slip Reynolds numbers and solid volume fractions. The color symbols represent the ratio of the transport term involving the PTHF to the average gas-solid heat transfer.For a fixed Reynolds number beyond $\mathrm{Re_m} = 10$, the transport term involving the PTHF is about 50% of the average gas-solid heat transfer at $\varepsilon_s = 0.5$, and it drops to about 30% of the average gas-solid heat transfer at $\varepsilon_s = 0.1$. This increase in the transport term involving the PTHF with increasing solid volume fraction is similar to the findings of Tenneti (2013) and Mehrabadi et al. (2015) for PTKE in a fixed particle assembly. For a fixed solid volume fraction, the ratio of transport term involving the PTHF to the average gas-solid heat transfer does not vary significantly beyond $\mathrm{Re_m} = 10$, but reduces to $15\% - 20\%$ at $\mathrm{Re_m} = 1$. Therefore, we conclude that the transport term involving the PTHF is important compared to average gas-solid heat transfer for high solid volume fraction, and it cannot be neglected in CFD simulations based on the two-fluid model.

Note that for low Reynolds number ($\mathrm{Re_m} = 1$) Fig. 4.12 shows that the ratio of PTHF to gas-solid heat transfer reduces. This results from the fact that the total convective term (mean convective heat flux and PTHF) needs to balance axial conduction in the fluid phase and average gas-solid heat transfer in the average temperature equation in the steady flow (see Eq. 4.1). A budget analysis of these terms that is described later in this paper illustrates this point.

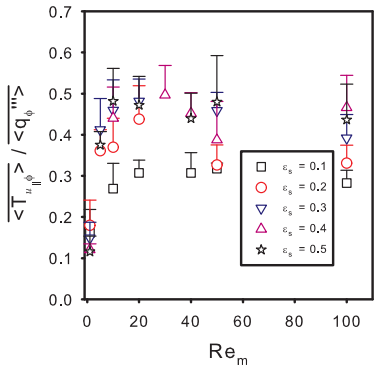

Figure 4.12: Comparison of transport term involving the PTHF (see Eq. 4.59) with the average gas-solid heat transfer (see Eq. B.11) in the range $1 \leq \mathrm{Re_m} \leq 100$ and $0.1 \leq \varepsilon_s \leq 0.5$. The symbols represent the transport term involving the PTHF obtained from PR-DNS data. Error bars indicate 95% confidence intervals from 5 MIS. For clarity, only half error bars for the circles are shown in this figure.

4.6 Average conduction in the fluid phase and its model

Average conduction in the fluid phase represents the divergence of the average heat flux in the fluid phase. Since the velocity and temperature fields are statistically homogeneous in cross-stream planes in our gas-solid flow problem that is described in Sec. 4.2, there is no average conduction in the cross-stream directions. We now establish the correspondence between PR-DNS data and the unclosed axial fluid-phase conduction term in Eq. 4.1.

Average axial conduction in the fluid phase is calculated from the PR-DNS temperature field (see Eq. B.10 in Appendix B and details leading up to it) by

$$\frac{\partial}{\partial x_j}\left\langle I_f q_j^{\phi}\right\rangle\left(x_{\|}\right) \approx \frac{1}{M}\sum_{\omega=1}^{M}\left\{\frac{1}{A}\int_A \frac{\partial I_f q_{||}^{\phi}(\mathbf{x},t;\omega)}{\partial x_{||}} dA\right\}, \tag{4.60}$$

where $q_j^{\phi} = -k_f \partial\phi/\partial x_j$ is heat flux vector based on the non-dimensional temperature field $\phi(\mathbf{x},t) = \left(T(\mathbf{x},t) - T_s\right)/\left(T_{m,in} - T_s\right)$ ($T_{m,in}$ is the inlet bulk fluid temperature), k_f is the thermal conductivity in the fluid phase, and $\omega = 1, \ldots M$ on the right hand side represents M realizations of the particle configuration from which the expression in curly braces is computed and subsequently averaged over. The integrand on the right hand side of Eq. 4.60 represents the sole nonzero contribution to average conduction that arises from $I_f q_{||}^{\phi}(\mathbf{x},t;\omega)$, the axial component of the non-dimensional heat flux in the fluid phase on a realization ω. The axial

conduction term from a particular particle configuration is averaged over the cross-sectional plane with area A that is located at $x_{||}$. Since the non-dimensional fluid temperature decays exponentially in the axial coordinate, both the non-dimensional heat flux and the average axial conduction term vary along the axial coordinate. More details regarding the computation of the axial conduction term can be found in Appendix B.

Figure 4.13 shows the ensemble-averaged PR-DNS values (the open circles) for the normalized axial conduction in the fluid phase at a mean slip Reynolds number $\mathrm{Re_m} = 5$ for two different solid volume fraction values of 0.1 and 0.4. The reference scale for the axial

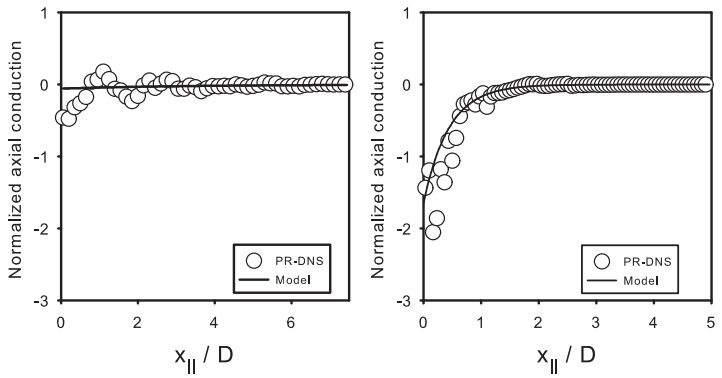

(a) $\varepsilon_s = 0.1$ (b) $\varepsilon_s = 0.4$

Figure 4.13: Normalized axial conduction in the fluid phase $\dfrac{\partial}{\partial x_{||}} \left\langle I_f q_{||}^{\phi} \right\rangle \left(x_{\|} \right) \dfrac{D^2}{k_f}$ at $\mathrm{Re_m} = 5$ for solid volume fraction of 0.1 and 0.4. The open circles are the PR-DNS data averaged over 5 MIS and the solid line represents the model.

conduction term based on the non-dimensional temperature ϕ is k_f/D^2, where D is the particle diameter. Note that this corresponds to a normalization of $k_f(T_{m,in} - T_s)/D^2$ for the axial conduction term in the dimensional average fluid temperature equation (Eq. 4.1). As shown in Fig. 4.2(b), the average non-dimensional fluid temperature $\left\langle \phi^{(f)} \right\rangle$ decays exponentially along the axial direction because the fluid is progressively cooled as it passes over the particles. For low Reynolds number the average fluid temperature decays to zero within $4D$ for the case with a solid volume fraction of 0.1, and within less than D for a solid volume fraction of 0.4 (cf. Fig. 4.2(b)). The axial conduction term shown in Fig. 4.13 is negative because the average non-dimensional fluid temperature decays exponentially with axial location

$\left\langle \phi^{(f)} \right\rangle \sim \exp\left(-\lambda x_{\|}/D\right)$, and therefore for a statistical homogeneous particle assembly (where $\varepsilon_f = 1 - \varepsilon_s$ is independent of $\mathbf{x}$), we have

$$\frac{\partial}{\partial x_{\|}} \left\langle I_f q_{\|}^{\phi} \right\rangle = -k_f \varepsilon_f \frac{\partial^2 \left\langle \phi^{(f)} \right\rangle}{\partial x_{\|} \partial x_{\|}} \sim -k_f \varepsilon_f \left(\lambda/D\right)^2 \exp(-\lambda x_{\|}/D) \tag{4.61}$$

(details of the derivation are shown in Appendix G).

Figure 4.14 shows contours of the magnitude of the heat flux vector $\left|I_f \mathbf{q}^{\phi}\right|$ normalized by the reference scale k_f/D^2 for the same cases in Fig. 4.13 with mean slip Reynolds number $\mathrm{Re_m} = 5$ for solid volume fraction values of 0.1 and 0.4.As we go deeper into the bed the heat flux in the fluid phase also goes to zero because the fluid temperature becomes relatively uniform. Only for small values of the axial location $x_{||}/D$ do we see nonzero heat flux values, and the dependence of the heat flux contours with solid volume fraction is consistent with the average fluid temperature plots shown in Fig. 4.2. Therefore, axial conduction becomes progressively smaller along the axial coordinate, and this drop is more pronounced for higher volume fraction. This indicates that the magnitude of the average axial conduction term that is the second derivative of the average fluid temperature is higher for higher solid volume fraction because of the rapid decay of the average fluid temperature (cf. Eq. 4.61), with higher λ values encountered for higher solid volume fractions (see the model for the non-dimensional decay coefficient λ_m in Sec. 4.4).

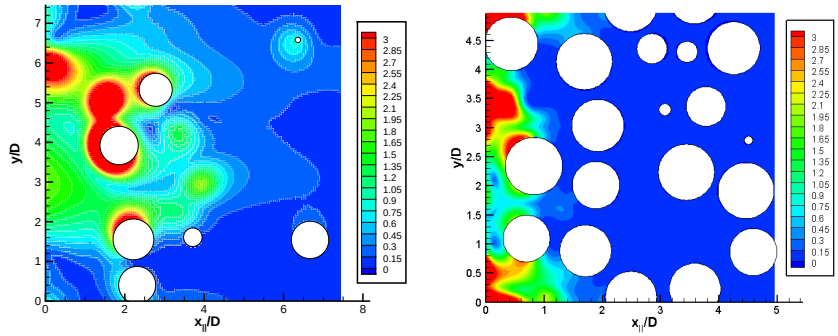

(a) $\varepsilon_s = 0.1$ (b) $\varepsilon_s = 0.4$

Figure 4.14: Contours of the magnitude of the heat flux vector $\left|I_f \mathbf{q}^{\phi}\right|$ normalized by the reference scale k_f/D^2 at $\mathrm{Re_m} = 5$ for solid volume fraction of 0.1 and 0.4.

4.6.1 Verification of the fluid-phase axial conduction model

Since average axial conduction in the fluid phase is modeled in terms of the second derivative of $\left\langle \phi^{(f)} \right\rangle$, a model for axial conduction in the fluid phase can be developed by using the expression for $\left\langle \phi^{(f)} \right\rangle$ ($\langle \phi^{(f)} \rangle \sim \exp\left(-\lambda x_{||}/D\right)$) and Eq. 4.32 given in Sec 4.4. Using these relations, the model for axial conduction in the fluid phase is:

$$\frac{\partial}{\partial x_{\parallel}} \left\langle I_f q_{\parallel}^{\phi} \right\rangle = -k_f \varepsilon_f \frac{\partial^2 \left\langle \phi^{(f)} \right\rangle}{\partial x_{\parallel} \partial x_{\parallel}} \approx -k_f \varepsilon_f \left\langle \theta^{(f)} \right\rangle (\lambda/D)^2 \exp(-\lambda x_{\parallel}/D). \tag{4.62}$$

A comparison of the average axial conduction in the fluid phase from PR-DNS data and the above model is shown in Fig. 4.13. For the case of solid volume fraction of 0.1 in Fig. 4.13(a), the normalized axial conduction in the fluid phase (normalized by the reference scale k_f/D^2) obtained from PR-DNS data shows some scatter about the model prediction in Eq. 4.62, although the average trend is captured by the model. The scatter in the PR-DNS data is because of the finite number of realizations and statistical variability in $\left\langle \phi^{(f)} \right\rangle$, and should reduce with more realizations. Computational resources limit these results to five realizations of the particle configuration. Nevertheless, the model does a fairly good job of capturing the trend in the PR-DNS data. For the case with solid volume fraction $\varepsilon_s = 0.4$ shown in Fig. 4.13(b), the PR-DNS data shows scatter within the length $L = 2D$, but the model still captures the trend of axial conduction in the fluid phase. This results from the fact that at the same Reynolds number, the fluid temperature at high solid volume fraction (0.4) decays faster to approach the particle surface temperature than the one at low solid volume fraction (0.1) (see Fig. 4.2).

4.6.2 Relative importance of fluid-phase axial conduction in average gas-solid heat transfer

We now quantify the relative importance of the fluid-phase axial conduction $\partial \left\langle I_f q_{\parallel}^{\phi} \right\rangle / \partial x_{\parallel}$ with respect to average gas-solid heat transfer $\left\langle q_{\phi}''' \right\rangle$ (see Eq. B.11) over the range of solid volume fraction and mean slip Reynolds number considered in this work. Since both of terms are spatially inhomogeneous and vary with axial location $x_{\parallel}$, it is convenient to define volumetric averages of these quantities. We quantify the average volumetric axial conduction in the fluid phase by spatially averaging axial conduction in the fluid phase over the domain length L to

obtain:

$$\overline{\langle q'''_{cond} \rangle} = \frac{1}{L} \int_0^L \frac{\partial}{\partial x_{\parallel}} \left\langle I_f q^{\phi}_{\parallel} \right\rangle \left(x_{\parallel} \right) \, dx_{||}. \tag{4.63}$$

In order to validate the assumption of neglecting axial conduction in the fluid phase in one-dimensional models that are used to interpret experimental data, we compare this term with average gas-solid heat transfer that is

$$\overline{\left\langle q'''_{\phi} \right\rangle} = \frac{1}{L} \int_0^L \left\langle q'''_{\phi} \right\rangle \left(x_{\parallel} \right) \, dx_{||}, \tag{4.64}$$

where $\left\langle q'''_{\phi} \right\rangle$ is the local average interphase heat transfer rate (see Eq. B.11). Figure 4.15 compares the average volumetric axial conduction in the fluid phase $\overline{\langle q'''_{cond} \rangle}$ with the average gas-solid heat transfer $\overline{\left\langle q'''_{\phi} \right\rangle}$ at selected volume fractions over a range of Reynolds number values.For a fixed solid volume fraction, the ratio $\overline{\langle q'''_{cond} \rangle} / \overline{\left\langle q'''_{\phi} \right\rangle}$ decreases rapidly with increasing mean slip Reynolds number and goes to almost zero at high mean slip Reynolds number of 100. The scaled average volumetric axial conduction also increases with solid volume fraction at each Reynolds number. This results from higher temperature gradients (and heat flux) due to increase in the proximity of particle surfaces at high solid volume fraction. For the case of solid volume fraction of 0.4, the average volumetric axial conduction in the fluid phase $\overline{\langle q'''_{cond} \rangle}$ is about 84% of the average gas-solid heat transfer $\overline{\left\langle q'''_{\phi} \right\rangle}$ at $\mathrm{Re_m} = 1$ but only 3% at $\mathrm{Re_m} = 20$.

These findings imply that in the low Reynolds number regime, there are high gradients of heat flux in the fluid phase. It is clear that the average volumetric axial conduction in the fluid phase $\overline{\langle q'''_{cond} \rangle}$ is important only for $\mathrm{Re_m} < 20$ (when compared to average gas-solid heat transfer). Therefore, the neglect of axial conduction in one-dimensional models that are used to infer the Nusselt number corresponding to average gas-solid heat transfer from inlet/outlet temperature measurements is justified for $\mathrm{Re_m} > 20$. In the low Reynolds number regime $\mathrm{Re_m} < 20$ (or low Péclet number since in gas-solid flow Prandtl number can be less than the order of one) this assumption is not justified. Now in order to understand the balance of various terms in Eq. 4.1 we perform a budget analysis in the following section.

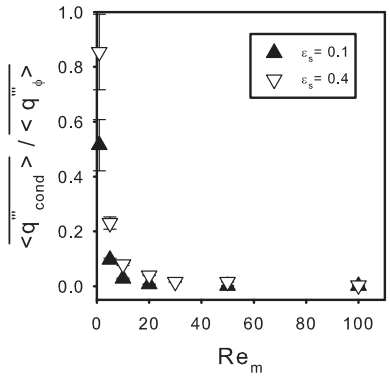

Figure 4.15: Dependence of the ratio of average volumetric axial conduction in the fluid phase to average gas-solid heat transfer $\overline{\langle q'''_{cond}\rangle}/\overline{\langle q'''_{\phi}\rangle}$ on mean slip Reynolds number at solid volume fraction $\varepsilon_s = 0.1$ and 0.4. The symbols are the values of the ratio from PR-DNS data and error bars indicate 95% confidence intervals from 5 MIS.

4.7 Budget analysis and relative magnitude of terms

Figure 4.16 shows a budget analysis of the two-fluid equation (Eq. 4.1) at steady state for selected values in the parameter space of Reynolds number and solid volume fraction. At steady state, the remaining terms in Eq. 4.1, viz. fluid-phase axial conduction, transport term involving the PTHF, and mean convection, are compared with the average gas-solid heat transfer term $\overline{\langle q'''_{\phi}\rangle}$ in the following form:

$$\underbrace{\frac{\partial}{\partial x_j}\left\{\rho_f \varepsilon_f c_{pf}\langle u_j^{(f)}\rangle\langle T^{(f)}\rangle\right\}}_{\text{mean flow convection}} + \underbrace{\frac{\partial}{\partial x_j}\left\{\rho_f c_{pf}\langle I_f u_j''^{(f)} T''^{(f)}\rangle\right\}}_{\substack{\text{pseudo–turbulent}\\ \text{heat flux}}} + \underbrace{\frac{\partial}{\partial x_j}\langle I_f q_j\rangle}_{\substack{\text{average conduction}\\ \text{in the fluid phase}}} = \underbrace{\left\langle \frac{\partial I_f}{\partial x_j} q_j \right\rangle}_{\substack{\text{average gas-solid}\\ \text{heat transfer}}}, \quad (4.65)$$

In the above equation the average gas-solid heat transfer on the right hand side is negative (fluid loses heat to cold particles), and each term on the left hand side is also negative (mean fluid temperature and temperature-velocity covariance decay with axial distance into the bed). The absolute value of the terms on the left hand side normalized by absolute value of the

average gas-solid heat transfer sum to unity. In Fig. 4.16, the average axial conduction in the fluid phase is denoted by the blue bars. It is highest at $\varepsilon_s = 0.5$ and for all volume fraction values it decreases with increasing mean slip Reynolds number. It is about 80% of the average gas-solid heat transfer at $\varepsilon_s = 0.5$ and $\mathrm{Re_m} = 1$ but less than 1% of the average gas-solid heat transfer at $\mathrm{Re_m} = 100$.

The normalized transport term involving the PTHF is denoted by the green bars in Fig. 4.16. This term is about 10-20% of the average gas-solid heat transfer at $\mathrm{Re_m} = 1$ and increases with Reynolds number to about 50% of the average gas-solid heat transfer at $\mathrm{Re_m} = 100$. The dependence of the normalized transport term involving the PTHF on solid volume fraction shows a moderate increase for $\mathrm{Re_m} = 10$ and 100, but there is slight decrease with solid volume fraction at $\mathrm{Re_m} = 1$ as observed in Fig. 4.12.

Fig. 4.16 also shows the relative magnitude of the mean convection term in the parameter space of mean slip Reynolds number and solid volume fraction. For a fixed solid volume fraction, the relative magnitude of mean convection is less than 30% for low Reynolds number $\mathrm{Re_m} = 1$, but greater than 50% for high Reynolds number $\mathrm{Re_m} = 100$. Therefore, for high Reynolds number $\mathrm{Re_m} > 10$, the average gas-solid heat transfer, mean flow convection, and PTHF dominate the mean fluid energy balance. This budget analysis of the two-fluid equation in Eq. 4.65 gives insight into the relative importance of each of the terms in the gas-solid heat transfer problem.

4.8 Conclusions

PR-DNS simulations of gas-solid heat transfer in steady flow through a homogeneous fixed assembly of particles are used to quantify the pseudo–turbulent heat flux arising from correlation of temperature and velocity fluctuations, and the average fluid-phase conduction terms that appear in the average fluid temperature equation. These simulations are performed over a range of mean slip Reynolds numbers $(1-100)$ and volume fractions $(0.1-0.5)$ for a Prandtl number of 0.7. A few cases are also presented using different Prandtl numbers in the range $0.01 \leq \mathrm{Pr} \leq 1$ to access a range of Péclet number. PR-DNS results reveal that the average bulk fluid temperature and the average fluid temperature decay exponentially due to fluid cooling

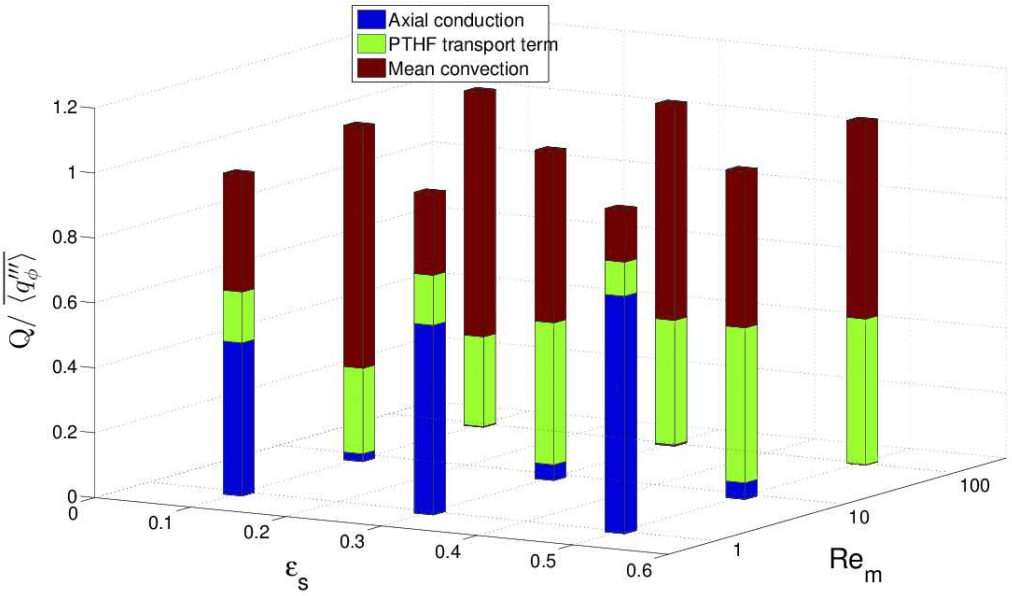

Figure 4.16: Budget of average fluid temperature equation in Eq. 4.1: the normalized axial conduction in the fluid phase, transport term involving the PTHF, and mean convection by the average gas-solid heat transfer $\overline{\langle q_\phi''' \rangle}$ for $\mathrm{Re_m} = 1$, 10, 100, and $\varepsilon_s = 0.1$, 0.3, and 0.5 using 5 MIS. Q represents absolute magnitude of these terms. The color columns represent axial conduction in the fluid phase (blue, on the bottom of the bar), the transport term involving the PTHF (green, on the middle of the bar), and mean convection (red, on the top of the bar), respectively.

by the particles. An exponential decay model for the average bulk fluid temperature is proposed with a decay lengthscale that depends on the problem parameters. The non-uniformity in the mean fluid temperature generates fluctuations in the temperature field that correlate with velocity fluctuations.

PR-DNS data show that the pseudo-turbulent heat flux (PTHF) transport is a significant contributor to the evolution of the average fluid temperature in gas-solid heat transfer. The term arising correlation of fluctuations in velocity and temperature cannot be neglected because the transport term involving the PTHF is about 10% of the average gas-solid heat transfer. A gradient-diffusion model for the PTHF is proposed in terms of the average fluid temperature gradient and a pseudo-turbulent thermal diffusivity. It is found that the qualitative features of the dependence of effective diffusivity on Péclet number are captured by a wake analysis

that is applicable to high Reynolds number flows (Koch (1993)). The PTHF model can be implemented in current CFD simulations of gas-solid heat transfer using the two-fluid model.

PR-DNS results also show that axial conduction in the fluid phase can be significant for $Re_m < 20$. These results shows that the neglect of axial conduction in one-dimensional models that are used to infer the Nusselt number corresponding to average gas-solid heat transfer from inlet/outlet temperature measurements is not justified for $Re_m < 20$. Based on the exponential decay model for the bulk fluid temperature, a simple model for average axial conduction in the fluid phase is proposed. This model captures the trends of average axial conduction in the fluid phase with mean slip Reynolds number and solid volume fraction in fixed particle assemblies.

A budget analysis of the two-fluid equation also indicates that average gas-solid heat transfer, mean convection, and PTHF terms are the dominant contributions for $Re_m > 10$ in a flow through homogeneous fixed particle assemblies. Using PR-DNS we have developed models for the PTHF and average conduction in the fluid phase.

CHAPTER 5. VALIDITY OF LOCAL CLOSURE MODELS BASED ON THE SCALE SEPARATION ASSUMPTION IN CONTINUUM THEORIES OF MULTIPHASE FLOW

This chapter is a manuscript titled "Validity of local closure models based on the scale separation assumption in continuum theories of multiphase flow: need for fluctuation hydrodynamics" that is prepared to submit to Journal of Fluid Mechanics-Rapids.

Scale separation between macroscales and microscales in continuum theories of multiphase flow is assumed on the basis that the characteristic length scale of macroscopic quantities is larger than that of organized mesoscale structures (higher order statistics such as two-point correlations), and this forms the basis for local closure models. The aim of this chapter is to validate the assumption of scale separation implied in continuum theories of multiphase flow by using particle-resolved direct numerical simulation (PR-DNS) results of gas-solid heat transfer in freely evolving suspensions and fixed bed of particles. The key feature of this gas-solid heat transfer problem is the inhomogeneous variation of mean and bulk fluid temperature in the streamwise direction. Using a characteristic length scale obtained from the inhomogeneous mean fluid temperature field, a criterion for scale separation in the gas-solid heat transfer problem is proposed. In many cases, the scale separation assumption is not valid and it is found that this assumption is only valid in dilute flow. Therefore, the local closure models that are frequently used based on scale separation assumption in the continuum theories of multiphase flow such as Eulerian-Eulerian two-fluid theory are not always valid in gas-solid flow. A non-local closure model developed for this gas-solid heat transfer problem in Sun et al. (2015) can overcome the failure of local closure models even though the scale separation assumption is not valid.

5.1 Introduction

A full description of multiphase flow provides far more information than practical applications need. Instead, statistical descriptions of multiphase flow are widely used to provide information on macroscopic average quantities that are practical to engineers and designers. Statistical approaches of multiphase flow (Drew and Passman (1998); Pai and Subramaniam (2009)) resulting in continuum theories can be categorized based on (a) whether each phase is represented using a random field (RF) or stochastic point process (SPP) description, (b) whether each phase is represented in an Eulerian or Lagrangian reference frame, and (c) the level of closure in the statistical theory (Subramaniam (2013)). The RF approach leads to the widely used Eulerian-Eulerian two-fluid (TF) theory in its ensemble-averaged (Drew (1983); Drew and Passman (1998)) or volume-averaged form (Anderson and Jackson (1967)), while the SPP approach leads to the kinetic theory of multiphase flow (Brilliantov and Pöschel (2010); Koch (1990)), Chapman-Enskog expansions (Chapman and Cowling (1953)), and other moment methods such as quadrature-based moment methods (Fox et al. (2008)).

The equations resulting from there continuum theories contain unclosed terms such as average interphase momentum or heat transfer that need to be modeled. These unclosed terms denoted generically as $\langle \mathcal{U} \rangle (\mathbf{x}, t)$ at a space-time location $(\mathbf{x}, t)$ are modeled in terms of known flow statistics at the same space-time location generically denoted as $\langle Q \rangle (\mathbf{x}, t)$ (in general, $\langle \mathcal{U} \rangle (\mathbf{x}, t) = f(\langle Q \rangle (\mathbf{x}, t)))$. For instance, the mean drag $\langle F \rangle (\mathbf{x}, t)$ is modeled as a function $f\left(\left\langle \mathbf{u}^{(f)} \right\rangle (\mathbf{x}, t), \left\langle \mathbf{u}^{(s)} \right\rangle (\mathbf{x}, t), ...\right)$ in terms of local mean fluid velocity $\left\langle \mathbf{u}^{(f)} \right\rangle$ and local mean particle velocity $\left\langle \mathbf{u}^{(s)} \right\rangle$. These local closure models rely on the assumption of scale separation. This scale separation assumption is analogous to the continuum hypothesis in single phase (Batchelor (2000)) where the macroscale variation of hydrodynamic variables such as bulk density appears on scales far larger than the microscale (molecular size) or mesoscale (range of interaction of molecules such as mean free path) (Subramaniam (2013)). In the RF approach, the length scale of mean fields (macroscale) is assumed to be larger than the length scale of higher order statistics such as the two-point density-density correlation $\langle I_\beta (\mathbf{x}) I_\beta (\mathbf{x} + \mathbf{r}) \rangle$ (Sundaram and Collins (1999)), where $I_\beta (\mathbf{x})$ is an indicator function.ă In

the SPP approach, the length scale of variation of the hydrodynamic variables such as the average number density or the average particle velocity are assumed to be larger than the length scale of higher order statistics such as particle pair correlation (Subramaniam (2013); Stoyan et al. (1995); Stoyan and Stoyan (1995)).

Since local closure models form the basis of widely used multiphase flow simulation techniques such as computational fluid dynamics (CFD) of two-fluid model (TFM) (Syamlal et al. (1993)), CFD–discrete element method (DEM) (Zhou et al. (2010)), large eddy simulations (LES)–DEM (Fox (2012)) etc, there are far-reaching implications of these scale separation assumptions to the local closure models that are used in these simulation techniques. The breakdown of scale separation in the multiphase flow context also implies that fluctuating hydrodynamics are important. Note that these fluctuations are not the same as turbulent fluctuations, which are a continuum phenomenon. The rigorous treatment of fluctuating hydrodynamics requires the solution of the density of these fluctuation that manifest in the pair separation space.

Anderson and Jackson (1967)'s assumption that there exists a length scale over which is much larger than individual particles averaging can be done is widely used in TFM. Similarly, in the CFD–DEM simulations (Zhou et al. (2010)), local average used in CFD implies that the average quantities such as fluid velocity in a computational grid cell is larger than a few particle diameters. In multiphase flow models, the idea of local homogeneity of the mean fields is used for instance in the local model for average heat transfer in the two-fluid context (Syamlal et al. (1993)) which is $\langle Q_{pf} \rangle (\mathbf{x}, t) = f\left(\left\langle T^{(f)} \right\rangle (\mathbf{x}, t), \left\langle T^{(s)} \right\rangle (\mathbf{x}, t), ...\right)$.

These assumptions on local closure models based on scale separation implicit in continuum theories of multiphase flow have not been validated. Existing experiments and numerical simulations do not conclusively address the question of the validity of scale separation although the formation of clusters in fluidized beds arising due to particle-fluid (hydrodynamic) and particle-particle interactions indicate that scale separation may not exist. Capecelatro et al. (2014, 2015) showed that clusters on the order of $10 - 100$ particle diameters can form in LES-DEM simulations of fully-developed fluidized bed. The evidence from other experiments such as Cocco et al. (2010) support Capecelatro et al. (2014, 2015)'s findings by observing clustering

formation with mean number of particles in a cluster over a range of $10 - 30$ in fluidized bed risers using high-speed particle imaging. This formation of clustering indicates that density-density correlations or pair correlations have length scales on the order of cluster scales rather than a few particle diameters.

The validity of these assumptions on scale separation can be ascertained by direct numerical simulations such as PR-DNS approach (Tenneti and Subramaniam (2014)). In terms of extending local closure models to account for nonlocal effects, Koch and Brady (1987b,a) found that microscale transport (microscale mixing) affects the average scalar quantities (mesoscale or macroscale) over short time scales, whereas this microscopic effect disappears after a sufficiently long time has elapsed. They analytically solved the ensemble-averaged scalar transport equation by imposing a constant average scalar gradient (Koch and Brady (1985)) and adding point source/sink terms (Koch and Brady (1987a,b)). This finding implies that the scale separation assumption strongly depends on the microscale transport process. However, these works cannot verify scale separation. Therefore, the PR-DNS is used to capture detailed information at the microscale (particle diameter) around particles. The information at the macroscale or mesoscale (a few or more particle diameters) can be obtained from microscopic PR-DNS data (Tenneti and Subramaniam (2014)). For instance, the macroscopic average quantities such as average bulk (mixing-cup) fluid temperature obtained from PR-DNS results of flow past a fixed bed of particles (Deen et al. (2012); Tenneti et al. (2013); Tenneti and Subramaniam (2014); Tavassoli et al. (2013); Sun et al. (2015)) indicated that heating up or cooling down the fluid by particles can occur on scale of a particle diameter in certain parameter ranges, thereby precluding the separation of scales needed for local closure models based on the continuum assumption in TFM or CFD-DEM.

The remainder of this paper is organized as follows. We give a brief description of physical problems to validate the scale separation assumption in § 5.2 and the numerical method in § 5.3. In § 5.4 we analyze PR-DNS results and propose a criterion for ascertaining the validity of the assumption. The solution for the failure of the scale separation assumption is discussed. We summarize our findings and conclude in § 5.5.

5.2 Problem description

In order to validate the scale separation assumption, we first choose a canonical heat transfer problem of a freely evolving suspension of monodisperse spherical particles in a gas-solid flow. Then we develop a criteria over a range of the parameter space by performing fixed bed calculations in a gas-solid flow, which yield results that are close to freely evolving suspensions for isothermal high Stokes number particles, but at considerably less computational cost. The reason to choose this heat transfer problem is that in this gas-solid heat transfer setup the fluid is heated up or cooled down by particles results in a non-uniform average fluid temperature field, although the hydrodynamic problem is homogeneous (Tenneti et al. (2013); Tenneti and Subramaniam (2014); Mehrabadi et al. (2015); Sun et al. (2015)). The heat transfer problem is statistically inhomogeneous in the streamwise direction. Therefore, scale separation can be verified by comparing the characteristic length scale of variation of mean quantities such as average bulk fluid temperature (see Fig. 5.1(a)) with a characteristic length scale from higher order statistics such as particle pair correlation or Eulerian two-point correlation of temperature and velocity (see Sun et al. (2016)). A summary of the characteristic length scales that are normally used in gas-solid heat transfer is listed in Table 5.1. In this work, we only discuss the validity of the scale separation assumption by using the scales in fluid phase. The other scales such as the particle pair correlation $\ell_{g(r)}$ are discussed in somewhere else (Mehrabadi et al. (2015)).

Table 5.1: The characteristic length scale used for heat transfer in gas-solid flow. $\ell_{\langle\phi_m\rangle}$ and $\ell_{\langle\phi^{(f)}\rangle}$ represent the characteristic length scale of mean fluid temperature and bulk fluid temperature, respectively. $\ell_{u\phi}$ and $\ell_{u\theta}$ represent the characteristic length scale of the cross-correlation of fluid velocity and fluid temperature, and the cross-correlation of fluid velocity and scaled fluid temperature, respectively. $\ell_{\langle\phi^{(s)}\rangle}$ represents the characteristic length scale of mean solid temperature and $\ell_{g(r)}$ represents the characteristic length scale of the particle pair correlation.

	Fluid phase	Solid phase
Mean quantities scales	$\ell_{\langle\phi_m\rangle}$ or $\ell_{\langle\phi^{(f)}\rangle}$	$\ell_{\langle\phi^{(s)}\rangle}$
Two-point correlation scales	$\ell_{u\phi}$ or $\ell_{u\theta}$	$\ell_{g(r)}$

The continuity, momentum and fluid temperature equations governing this gas-solid heat

transfer problem in the absence of free-convection and radiation are

$$\frac{\partial u_i}{\partial x_i} = 0, \tag{5.1}$$

$$\frac{\partial u_i}{\partial t} + u_j \frac{\partial u_i}{\partial x_j} = -\frac{1}{\rho_f} g_i + \nu_f \frac{\partial^2 u_i}{\partial x_j^2}, \tag{5.2}$$

and

$$\rho_f c_{pf} \left[\frac{\partial T}{\partial t} + u_j \frac{\partial T}{\partial x_j} \right] = k_f \frac{\partial^2 T}{\partial x_j^2}, \tag{5.3}$$

respectively, where ν_f is the fluid-phase viscosity, g_i is the pressure gradient, k_f is the fluid thermal conductivity, ρ_f is the fluid-phase density, c_{pf} is the specific heat capacity in the fluid phase. For a freely evolving suspension, the particles move under the influence of hydrodynamic and collisional forces, and are represented in a Lagrangian frame of reference at time t by $\{\mathbf{X}^{(i)}(t),\ \mathbf{V}^{(i)}(t),\ i = 1...N_p\}$, with $\mathbf{X}^{(i)}(t)$ and $\mathbf{V}^{(i)}(t)$ being the position and velocity of the ith particle, respectively, and N_p being the total number of particles. The position and translational velocity of the ith particle evolve according to Newton's second law as

$$\frac{d\mathbf{X}^{(i)}(t)}{dt} = \mathbf{V}^{(i)}(t), \tag{5.4}$$

$$m\frac{d\mathbf{V}^{(i)}(t)}{dt} = \mathbf{B} + \mathbf{F}_h^{(i)}(t) + \sum_{\substack{j=1 \\ j\neq i}}^{N_p} \mathbf{F}_{ij}^{(c)}(t), \tag{5.5}$$

where $\mathbf{B}$ is any external body force that is zero in this case, $\mathbf{F}_h^{(i)}$ is the hydrodynamic force (calculated from the velocity and pressure fields at the particle surface) and $\mathbf{F}_{ij}^{(c)}$ is the contact force on the ith particle as a result of collision with jth particle. More details about PR-DNS of freely evolving suspension of particles using the PUReIBM approach can be found in Tenneti et al. (2010) and Mehrabadi et al. (2015).

5.3 PR-DNS approach

The gas-solid heat transfer problems described in Section 5.2 can be solved using our PR-DNS approach, which is called the Particle-resolved Uncontaminated-fluid Reconcilable Immersed Boundary Method (PUReIBM) (Garg et al. (2010b); Tenneti et al. (2010, 2011, 2013);

Tenneti and Subramaniam (2014)). Complete details about solving governing equations and implementing boundary conditions by PUReIBM for a fixed bed simulation can be found in Tenneti et al. (2011, 2013). For a freely evolving suspension simulation in a gas-solid flow, Tenneti et al. (2010) developed a different simulation setup that performs the PR-DNS in an accelerating reference frame to overcome a difficulty in simulating a freely evolving suspension in the laboratory frame with periodic boundary conditions. The equations of motion in Eqs. 5.4 and 5.5 are solved in an accelerating frame of reference that moves with the mean velocity of the particles. The advantage of this setup is that the desired mean flow Reynolds number is specified as an input parameter so that we are able to solve the problem with reasonable time steps that resolve the flow. Here, we briefly show the formulation for the gas-solid heat transfer in a freely evolving suspension.

Since the particles are accelerating in the laboratory frame E, the new reference frame $\overline{E}$ moving with the mean particle velocity is a non-inertial frame of reference. Let the velocity and acceleration of with $\overline{E}$ respect to the laboratory frame E be $\mathbf{V}(t)$ and $\mathrm{A}(t)$, respectively. The transformation rules between the two frames are:

$$\overline{\mathbf{X}}(\bar{t}) = \mathbf{X}(t) - \int_0^t \mathbf{V}(t')dt', \tag{5.6}$$

for position vectors (such as particle center location), and

$$\overline{\mathbf{U}}(\bar{\mathbf{x}}, \bar{t}) = \mathbf{U}(\mathbf{x}, t) - \mathbf{V}(t), \tag{5.7}$$

for the fluid velocity field, and

$$\overline{\phi}(\bar{\mathbf{x}}, \bar{t}) = \phi(\mathbf{x}, t), \tag{5.8}$$

for the scalar field (Pope (2000)). Then the governing equations in PR-DNS approach for the mass, momentum and scalar transport in the accelerating frame are

$$\frac{\partial \overline{u}_i}{\partial x_i} = 0, \tag{5.9}$$

$$\frac{\partial \overline{u}_i}{\partial t} + \overline{u}_j \frac{\partial \overline{u}_i}{\partial \overline{x}_j} = -\frac{1}{\rho_f}\overline{g}_i + \nu_f \frac{\partial^2 \overline{u}_i}{\partial \overline{x}_j^2} - A_i + I_s f_{u_i}, \tag{5.10}$$

and

$$\rho_f c_{pf} \left[\frac{\partial \overline{\phi}}{\partial \overline{t}} + \overline{u_j} \frac{\partial \overline{\phi}}{\partial \overline{x}_j} \right] = k_f \frac{\partial^2 \overline{\phi}}{\partial \overline{x}_j^2} + I_s f_\phi, \tag{5.11}$$

where f_{u_i} and f_ϕ are the immersed boundary (IB) forcing terms for the velocity and scalar field, respectively (Tenneti et al. (2011, 2010)), and ϕ is the non-dimensional fluid temperature as

$$\phi(\mathbf{x}, t; \omega) = \frac{T(\mathbf{x}, t; \omega) - T_s}{\langle T_{m,in} \rangle - T_s}. \tag{5.12}$$

where T_s is the solid temperature, $\langle T_{m,in} \rangle$ is the ensemble-averaged inlet bulk fluid temperature that is obtained at axial location $x_{||} = 0$ in terms of the bulk fluid temperature

$$T_m(x_{||}, t; \omega) = \frac{\int_{A_f} (\mathbf{u}T) \cdot \mathbf{e}_{||} dA}{\int_{A_f} \mathbf{u} \cdot \mathbf{e}_{||} dA}, \tag{5.13}$$

$\mathbf{e}_{||}$ is the unit vector along the streamwise direction, A_f is the area occupied by the fluid in a plane perpendicular to the streamwise direction, and the ensemble-averaged quantities $\langle Q \rangle$ is obtained from $\langle Q \rangle (x_{||}, t) = \int_{\omega \in \Omega} Q(x_{||}, t; \omega)\, dP_\omega$, P_ω is the probability of a particle configuration ω occurring. The momentum equation in Eq. 5.10 in the accelerating frame has an acceleration term compared to the original momentum equation in Eq. 5.2. However, the formulation of the scalar equation in Eq. 5.11 for a freely evolving suspension is the same as that in fixed particle assembly simulation in Eq. 5.3. Note that in the accelerating frame, the velocity in the convection term is the relative velocity between the accelerating frame and fluid obtained from Eq. 5.10. Therefore, we straightforwardly use the same method for the fixed particle assembly simulation to solve the fluid temperature equation in Eq. 5.11 without revising the formulation in Tenneti et al. (2013).

In order to solve the above fluid-phase equations in Eqs. 5.10 and 5.11, the same boundary conditions are imposed as those used in the fixed bed simulations (Tenneti et al. (2011, 2013)). The no-slip and no-penetration boundary conditions are used for the particle velocity, and the isothermal boundary condition (constant particle temperature) is used for the particle

temperature. A thermal self-similarity boundary condition is imposed at the domain boundary to ensure that the flow is thermally fully-developed (Tenneti et al. (2013)). In order to solve the equations of motion in Eqs. 5.4 and 5.5, particle-particle interactions are treated using a soft-sphere model in a DEM solver (Tenneti et al. (2010)).

5.4 Results and discussions

Recalling the setups in § 5.2, a key feature of the gas-solid flow with heat transfer in freely evolving suspension is the variation or inhomogeneity of mean fluid temperature in the streamwise direction which arises from fluid heating or cooling by the particles. The inhomogeneous fluid temperature field is solved by imposing thermal self-similarity boundary conditions in the PR-DNS approach (Tenneti et al. (2013)). Since the macroscopic average quantities are computed from the PR-DNS results of the temperature field in the microscale, the scale separation assumption can be verified. Note that under certain conditions (Pai and Subramaniam (2009)) there is an equivalence between the corresponding levels of closure in the RF and SPP approaches such that Pai and Subramaniam (2009) established the relations between the RF and SPP descriptions at the single-point probability density function (PDF) level of closure. Therefore, in the following discussions we only focus on the validation of the scale separation assumption in the Eulerian-Eulerian TF theory of the RF approach in its ensemble-averaged sense.

5.4.1 Length scale for average bulk fluid temperature

We first perform a simulation of freely evolving suspension of particles at a mean slip Reynolds number of 20 and solid volume fraction of 0.1 with the solid/fluid density ratio of 100. We initialize the velocity field, particle velocities and locations from a hydrodynamic solution of the freely evolving suspension in which the hydrodynamic quantities such as drag and granular temperature have reached steady-state (Mehrabadi et al. (2015)). The velocity and temperature solutions are fully coupled in the freely evolving suspension simulation.

Figure 5.1(a) shows the variation of the ensemble-averaged non-dimensional bulk fluid temperature obtained by averaging over time along axial location. The ensemble-averaged non-

dimensional bulk fluid temperature is a key variable to quantify the inhomogeneous variation of fluid temperature field (instead of the mean fluid temperature due to less variation of bulk fluid temperature (see Sun et al. (2015))). The ensemble-averaged non-dimensional bulk fluid temperature $\langle \phi_m \rangle$ is obtained based on the non-dimensional bulk fluid temperature along the axial direction $x_{||}$ is

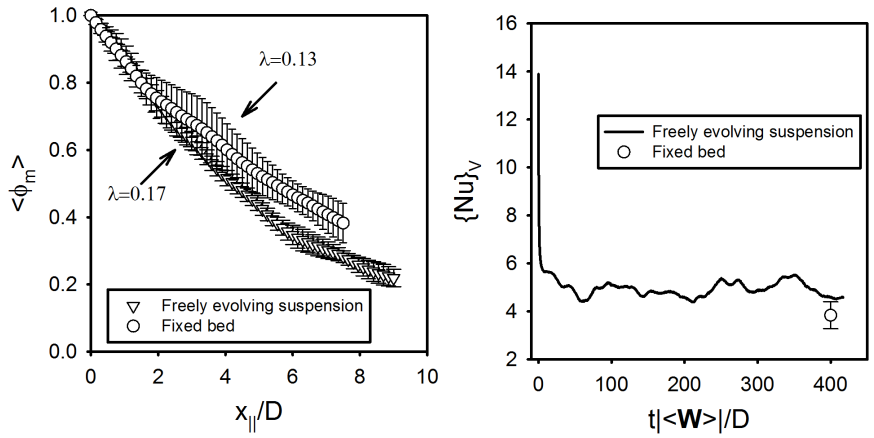

(a) (b)

Figure 5.1: (a) Variation of average non-dimensional fluid temperature $\langle \phi_m \rangle$ with non-dimensional axial location $x_{\|}/D$ at $\mathrm{Re_m} = 20$ and $\varepsilon_s = 0.1$. The triangles represent the average fluid temperature obtained from 5 snapshots in freely evolving suspension chosen at different times. The circles represent the average fluid temperature obtained in a fixed bed of particles. The error bars represent the 95% confidence over five realizations or snapshots of particle configurations. (b) Time history of average Nusselt number $\{\mathrm{Nu}\}_V$ in time (non-dimensional time $\hat{t} = t\,|\langle \mathbf{W} \rangle|\,/D$, where $|\langle \mathbf{W} \rangle|$ is the mean slip velocity) at $\mathrm{Re_m} = 20$ and $\varepsilon_s = 0.1$ in a freely evolving suspension of particles. The solid line represents the volume-averaged Nusselt number obtained in freely evolving suspension. The symbol represents the average Nusselt number obtained in a fixed bed of particles and the error bar represents the 95% confidence over five realizations of particle configurations.

$$\phi_m(x_{||}, t; \omega) = \frac{T_m(x_{||}, t; \omega) - T_s}{\langle T_{m,in} \rangle - T_s}. \tag{5.14}$$

Note that we name the ensemble-averaged non-dimensional bulk fluid temperature as the average bulk fluid temperature for short. For the freely evolving suspension simulation five snapshots are chosen at different times (for non-dimensional time is greater than 80 in Fig. 5.1(b)) and then averaged to obtain $\langle \phi_m \rangle$. As Fig. 5.1(a) shows, the average bulk fluid temper-

ature in the freely evolving suspension simulation decays rapidly with axial location. Within a length of $9D$, $\langle\phi_m\rangle$ decreases to about 20% of its inlet value. The decay rate of $\langle\phi_m\rangle$ can be obtained by an exponential decay model for average bulk fluid temperature (see Chapters 3 and 4) expressed as

$$\langle\phi_m\rangle\left(x_{||}\right) = \exp\left(-\lambda x_{||}/D\right), \tag{5.15}$$

where the coefficient λ determines the rate of decay of the average bulk fluid temperature with non-dimensional axial distance $x_{||}/D$. By fitting the PR-DNS data, the decay rate is obtained about $\lambda = 0.17$ in this dilute flow. Based on the decay rate, we can define a characteristic length scale $\ell_{\langle\phi_m\rangle} = D/\lambda$ that characterizes the variation of macroscopic average quantities such as average bulk fluid temperature (also see Table 5.1).

In order to quantify this characteristic length scale over a range of a parameter space, a parametric study for this length scale can be performed easily in fixed particle bed simulations (Tenneti et al. (2013); Sun et al. (2015)) instead of the freely evolving suspension simulations. Therefore, we compare the results obtained from freely evolving suspension simulation with that of a fixed bed simulation for the same Reynolds number and solid volume fraction to see if fixed bed simulations are the good approximation to the freely evolving suspension simulations. Fig. 5.1(a) shows that the moving particles (freely evolving suspension) result in a slight smaller length scale $D/\lambda = 1/0.17$ compared with the fixed particles cases $D/\lambda = 1/0.13$. This finding indicates that moving particles result in a faster decay of the average bulk fluid temperature field in the streamwise direction, which is physically reasonable. This could be because the motion of particles results in more mixing that is more effective in cooling down the fluid. It is also possible that particles that are colder than fluid move around to cool down the nearby fluid in the freely evolving suspension, relative to the fixed bed. We note that this small difference that is seen for isothermal particles could be significantly increased if the particles have lower thermal inertia and if their temperature changes significantly with time. In addition, analogous to the drag force in the hydrodynamic problem (Tenneti et al. (2010); Mehrabadi et al. (2015)), the average Nusselt number that is an important output to quantify heat transfer in gas-solid flow (Sun et al. (2015)) is also computed in both simulations. Fig. 5.1(b) shows the time history of the volume-averaged Nusselt number $\{\mathrm{Nu}\}_V(t) = \frac{1}{L}\int_0^L \mathrm{Nu}(x_{||}, t)dx_{||}$, where L is the length

of the computational box, $\mathrm{Nu}(x_{||}, t)$ is the cross-sectional average Nusselt number (Sun et al. (2015)). The volume-averaged Nusselt number decays very quickly at early time and then smoothly tends to a steady value. The difference in the average Nusselt number between the fixed particle assembly (the circle) and freely evolving suspension simulations (the solid line) is about 10%.

Based on these results from PR-DNS simulations of freely evolving suspension, we find that the statistics of the velocity field and temperature field obtained from freely evolving suspension are not very different from the fixed bed simulation results. It is plausible that a fixed assembly of isothermal particles is a good approximation to freely evolving suspensions with isothermal high-Stokes number particles. Therefore, we use the data obtained from fixed bed simulations to present the length scale $\ell_{\langle\phi_m\rangle} = D/\lambda$ as below and develop a criterion for scale separation in the next section.

Figure 5.2(a) shows the decay rate λ obtained from the PR-DNS data over a range of mean slip Reynolds numbers $\mathrm{Re_m}$ $(1 - 100)$ and solid volume fractions ε_s $(0.1 - 0.5)$ for a Prandtl number of 0.7. It indicates that for a fixed solid volume fraction, the characteristic length scale $\ell_{\langle\phi_m\rangle} = D/\lambda$ increases with increasing Reynolds numbers. For a fixed Reynolds number, the length scale reduces more in a dense flow than in a dilute flow. This is because the heat transfer between particle and fluid phases increases with higher solid volume fraction. Using this characteristic length scale $\ell_{\langle\phi_m\rangle}$, we can collapse of the PR-DNS data for average bulk fluid temperature $\langle\phi_m\rangle$ with scaled axial distance $\lambda x_{||}/D$ for selected mean slip Reynolds number and solid volume fraction values as shown in Figure 5.3. All the values of $\langle\phi_m\rangle$ over the entire range of $\mathrm{Re_m}$ and ε_s simulated lie in the range between the symbols for the cases $(\mathrm{Re}_m, \varepsilon_s) = (1,\ 0.3)$ and $(5,\ 0.5)$. For values of scaled axial distance $\lambda x_{||}/D \leq 4$ from the inlet plane, the average bulk fluid temperature collapses perfectly on to the straight line in the log-linear plot, indicating that the PR-DNS data verifies exponential decay of $\langle\phi_m\rangle$. Therefore, although the fluid cools down at different rates (depending on the solid volume fraction and mean slip Reynolds number), as one proceeds down the particle assembly in the streamwise direction, this exponential decay law allows us to develop a criterion for departure from local homogeneity of the average bulk fluid temperature using the characteristic length scale $\ell_{\langle\phi_m\rangle}$.

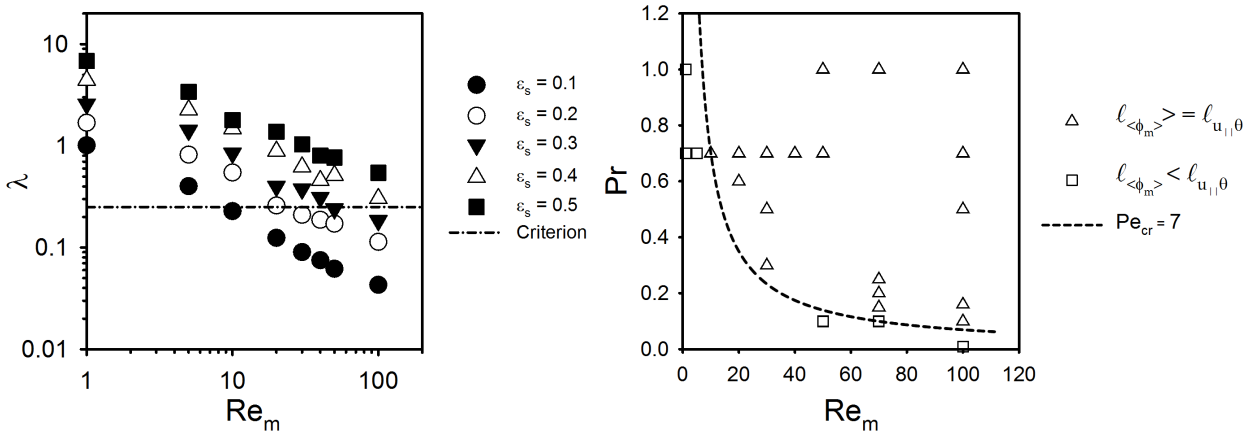

(a) (b)

Figure 5.2: (a) The decay rate λ obtained with PR-DNS data for a range of solid volume fraction and mean slip Reynolds number. Symbols are averages from PR-DNS data using 5 independent realizations. The horizontal short dash-dot line at $\lambda = 0.25$ indicates the boundary that separates the cases satisfying the assumption of local homogeneity ($\lambda < 0.25$ below the line) from those that do not ($\lambda > 0.25$ above the line). (b) Dependence of the characteristic length scale for average bulk fluid temperature $\ell_{\langle\phi_m\rangle}$ on mean slip Reynolds number $\mathrm{Re_m}$ and Prandtl number Pr for a solid volume fraction of 0.1 based on the criterion $\ell_{\langle\phi_m\rangle} > \ell_{u_{\parallel}\theta} = 4D$. The triangle symbols represent the cases with $\ell_{\langle\phi_m\rangle} > \ell_{u_{\parallel}\theta} = 4D$ and the square symbols represent the cases with $\ell_{\langle\phi_m\rangle} > \ell_{u_{\parallel}\theta} = 4D$. The dashed line represents the critical Péclet number $\mathrm{Pe_{cr}} = 7$ defined based on the particle diameter.

5.4.2 Criterion for validity of scale separation assumption

In the EE TF theory, the mean fluid temperature as well as the mean solid temperature are assumed to be spatially uniform or locally homogeneous. This assumption underlying the continuum formulation of the TFM is valid if there exists a scale separation between macroscales and microscales. A macroscopic length scale ℓ_{macro} can be defined as the characteristic length scale of variation of the mean fluid temperature by $\ell_{macro} = \langle T^{(f)}\rangle / \left|\nabla\langle T^{(f)}\rangle\right|$ (Tenneti and Subramaniam (2014)), where $\left\langle T^{(f)}\right\rangle = \langle I_f(\mathbf{x},t)T(\mathbf{x},t)\rangle \,/\, \langle I_f(\mathbf{x},t)\rangle$ is the ensemble-averaged fluid temperature. A characteristic length scale for the microscopic variation denoted

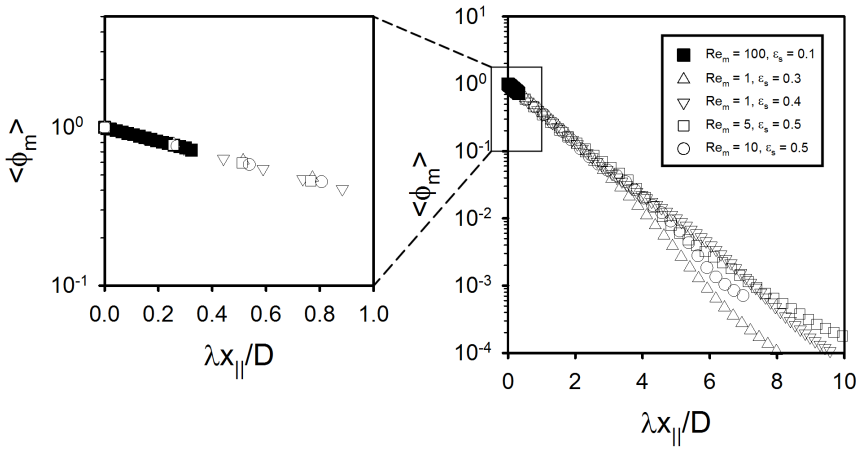

Figure 5.3: Variation of average bulk fluid temperature along scaled axial distance for selected Reynolds numbers and volume fractions with 5 independent realizations. The other cases lie within the limits of the symbols in this figure and are not shown for clarity.

by the Eulerian two-point cross-correlation length scale $\ell_{u_{||}\theta}$[1] (see Table 5.1) corresponds to $\left\langle I_f u''_{||}(\mathbf{x})\theta''(\mathbf{x}+\mathbf{r})\right\rangle$, where $u_{||}$ is the streamwise velocity and $\theta'' = \theta - \left\langle\theta^{(f)}\right\rangle$ is the scaled temperature fluctuation in Chapter 4. Note that in an inhomogeneous temperature field, a scaled fluid temperature θ that is scaled by the bulk fluid temperature T_m is used to calculate the cross-correlation instead of fluid temperature itself (Sun et al. (2015)). This is because the θ field is homogeneous and provides the data of the entire computational domain for statistical estimate instead of computing $\ell_{u_{||}\phi}$ from less data of cross-sectional plane of the computational domain. From PR-DNS of flow past a fixed bed of particles in Sun et al. (2015), it is found that $\ell_{u_{||}\theta} \sim 3-4D$. In other words, if $\ell_{macro} \gg \ell_{u_{||}\theta}$, then the length scale ℓ_{macro} of variation of macroscale quantities such as mean fluid temperature is significantly greater than the characteristic microscale associated with the characteristic length scale $\ell_{u_{||}\theta}$. Note that in TF CFD simulations (Syamlal et al. (1993)) the mean fluid temperature is used to represent the mean value in a computational grid cell whose characteristic length is at least a few particle diameters. Therefore, if scale separation holds and the mean temperatures are locally homogeneous then local closure models such as model for gas-solid heat transfer (Syamlal et al. (1993)), are valid in the TF theory and the CFD simulations should converge for grid sizes on the order of

[1]Other definitions could include the length scale $\ell_{\theta\theta}$ of the scaled temperature auto-covariance and this yields similar estimates.

a few particle diameters.

In the heat transfer problems of freely evolving suspension and fixed bed of particles, the macroscale length scale ℓ_{macro} can be represented by the characteristic length scale $\ell_{\langle\phi_m\rangle}$. The magnitude of the length scale $\ell_{\langle\phi_m\rangle}$ relative to $\ell_{u_\parallel\theta}$ determines whether the scale separation assumption is valid, or not. Note that the length scale $\ell_{u_\parallel\theta}$ corresponding to the temperature-velocity two-point correlation is the physically relevant length scale which determines whether there is scale separation, and it is independent of the length of the bed. As noted earlier, $\ell_{u_\parallel\theta}$ denotes the length scale over which the average fluid temperature is required to be uniform or homogeneous. Then it is clear that in the TF theory if the uniform length scale $\ell_{\langle\phi_m\rangle} = D/\lambda \geq \ell_{u_\parallel\theta} = 4D$ then the assumption of locally homogeneous mean fluid temperature or scale separation is valid, whereas if $\ell_{\langle\phi_m\rangle} < \ell_{u_\parallel\theta}$ then it is not.

Based on this criterion $\ell_{\langle\phi_m\rangle} \geq \ell_{u_\parallel\theta} = 4D$, one can identify the region in the parameter space of solid volume fraction and Reynolds number (or Péclet number) that satisfies the assumption of local homogeneity in Fig. 5.2(a). The horizontal line corresponding to $\lambda = 0.25$ in Fig. 5.2(a) demarcates the region where scale separation holds ($\lambda < 0.25$, below the line), and the region where it does not hold ($\lambda > 0.25$, above the line). Only the cases with low solid volume fraction and high Reynolds number ($\varepsilon_s = 0.1$ and $\mathrm{Re_m} \geq 7$, $\varepsilon_s = 0.2$ and $\mathrm{Re_m} \geq 20$, $\varepsilon_s = 0.3$ and $\mathrm{Re_m} \geq 50$) satisfy the criterion of local homogeneity of the average bulk fluid temperature or scale separation. For these cases, local closure models in the TF theory are valid. However, with increasing solid volume fraction and decreasing Reynolds number, λ increases beyond the threshold value as shown in Fig. 5.2(a). For these cases, the average bulk fluid temperature is inhomogeneous on the length scale $\ell_{u_\parallel\theta} \approx 3 - 4D$ and drops much more than 60% that is corresponding to $\langle\phi_m\rangle$ for non-dimensional axial location $\lambda x_\parallel/D > 1$ in the inset of Fig. 5.3. In these cases there is no scale separation between the macroscopic variation of the average bulk fluid temperature and the microscopic variation on the scale $\ell_{u_\parallel\theta}$.

For a fixed solid volume fraction we can also differentiate scale separation cases from non-scale separation ones. Fig. 5.2(b) shows the variation of the length scale of average bulk fluid temperature $\ell_{\langle\phi_m\rangle}$ for a solid volume fraction of 0.1 for different mean slip Reynolds number and Prandtl number values. Naturally from the evolution equation for the mean fluid temperature

we expect its decay length scale to only depend on the Péclet number, and not on the Reynolds and Prandtl numbers independently. The triangles represent cases with $\ell_{\langle\phi_m\rangle} \geq \ell_{u_\parallel\theta} = 4D$ and the squares represent the cases with $\ell_{\langle\phi_m\rangle} < \ell_{u_\parallel\theta} = 4D$. The dashed curve represents a constant critical Péclet number $\mathrm{Pe}_{\mathrm{cr}} = 7$, confirming our expectation that it is only the Péclet number that determines the length scale. For $\mathrm{Pe}_{\mathrm{m}} < \mathrm{Pe}_{\mathrm{cr}} = 7$ ($\mathrm{Pe}_{\mathrm{m}} = \mathrm{Re}_{\mathrm{m}}\mathrm{Pr}$) the average fluid temperature decays dramatically over $\ell_{u_\parallel\theta} = 4D$ and no scale separation assumption can be hold. Therefore, the parametric study again confirms that there exists a criterion for scale separation.

In the absence of scale separation, fluctuations become important and the equations of fluctuating hydrodynamics need to be considered. In other words, due to high fluid cooling (or heating) the bulk fluid temperature can vary significantly over the length scale $\ell_{u_\parallel\theta} \approx 3 - 4D$, and consequently local closure models cease to be valid. The existing TF model for average gas-solid heat transfer will need to be modified to account for the variation in the bulk fluid temperature on such small scales.

5.4.3 Nonlocal closure model

Since local closure models such as existing TF model for average gas-solid heat transfer are not valid in dense flow, one has to develop nonlocal closure models (analogous to Koch and Brady (1987b,a)) to account for the significant variation of mean quantities over small scales. In the inhomogeneous fluid temperature field of gas-solid heat transfer, the existing TF model for average gas-solid heat transfer (Syamlal et al. (1993)) that can be derived using volume-averaging (see Sun et al. (2015) for details) as

$$q'''_{TF} = \frac{6k_f\varepsilon_s\langle \mathrm{Nu}\rangle}{D^2}\left(\left\langle T^{(s)}\right\rangle - \overline{\left\langle T^{(f)}\right\rangle}\right) \tag{5.16}$$

($\langle \mathrm{Nu}\rangle$ is the average Nusselt number) assumes the homogeneity of the fluid temperature field over the characteristic length scale $\ell_{u_\parallel\theta}$. The expression $\overline{\left\langle T^{(f)}\right\rangle} = \frac{1}{V}\int_V \left\langle T^{(f)}\right\rangle(\mathbf{x})\,\mathrm{d}V$ (V is the control volume) in Eq. 5.16 does not consider the local large variation of mean fluid temperature along the streamwise direction in which the mean fluid temperature $\left\langle T^{(f)}\right\rangle(\mathbf{x})$ is statistically inhomogeneous (see Section 5.2). Sun et al. (2015) has resolved this issue by adding up local

gas-solid heat transfer over a length in the streamwise direction. Based on the same setup in Section 5.2, Sun et al. (2015) has proposed an consistent TF (cTF) closure model for average gas-solid heat transfer as

$$q'''_{cTF} = \frac{6\pi\varepsilon_s k_f \langle \mathrm{Nu} \rangle}{4D^2 \left\langle \theta^{(f)} \right\rangle} \left(\left\langle T^{(s)} \right\rangle - \overline{\left\langle T^{(f)} \right\rangle} \right). \tag{5.17}$$

The difference between TF model and cTF model is that the cTF model is derived by integrating the local gas-solid heat transfer expression in the cross-sectional plane over a length as

$$\left\langle q'''_{\phi} \right\rangle \left(x_{||} \right) = \frac{6\pi\varepsilon_s k_f \langle \mathrm{Nu} \rangle}{4D^2} \frac{\langle \phi^{(f)} \rangle \left(x_{||} \right)}{\left\langle \theta^{(f)} \right\rangle} \tag{5.18}$$

instead of volume-averaging of the fluid temperature. Note that $\left\langle \theta^{(f)} \right\rangle$ is only a function of the Reynolds number and solid volume fraction due to the homogeneity of the θ field. The detailed derivation of Eq. 5.17 can be found in Sun et al. (2015).

The effect of the scale separation assumption on the closure models can be seen by the comparison of the TF model and the cTF model as shown in Figure 5.4. This figure shows the comparison of the average volumetric interphase heat transfer rate from this TF model and cTF model with the PR-DNS data over the decay rate or the characteristic length scale $\ell_{\langle \phi_m \rangle} = D/\lambda$ for two solid volume fractions. In dilute flow ($\varepsilon_s = 0.1$), the maximum value of the difference between the average volumetric interphase heat transfer rate from PR-DNS $\overline{q'''_{DNS}}$ (see Sun et al. (2015)) and q'''_{TF} is about 10% whereas the maximum value of the difference between $\overline{q'''_{DNS}}$ and q'''_{cTF} is about 4%. It is worth noting that the maximum value of the difference using TF model is in the region that the scale separation assumption is not valid. Over a range of the length scale $\ell_{\langle \phi_m \rangle}$, we find that the difference between the cTF model and the PR-DNS data is small compared to the difference between the TF model and the PR-DNS data. In dense flow ($\varepsilon_s = 0.5$), the similar behavior has been observed. With increasing the length scale or decreasing the decay rate λ, the difference between $\overline{q'''_{DNS}}$ and q'''_{TF} decreases even thought the scale separation assumption does not hold for all the cases. The maximum of the difference, which is about 11% in cTF model, is far smaller than that in TF model. This implies that for all the cases the cTF closure model that uses the bulk fluid temperature difference is more

accurate than the TF model. This cTF model can be used in TF CFD simulations even though the assumption of the scale separation does not hold.

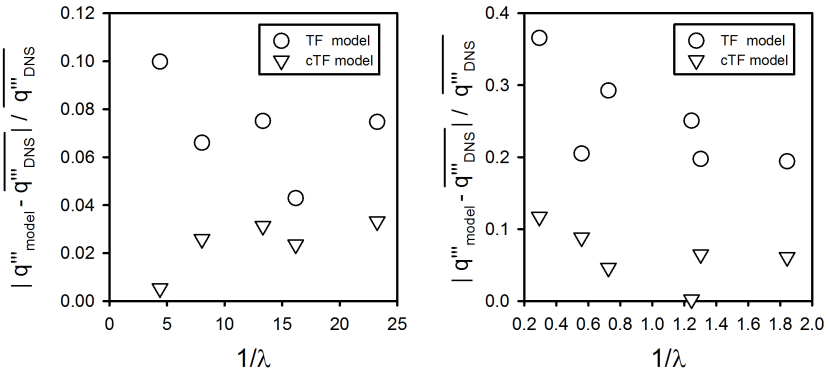

Figure 5.4: Comparison of the average volumetric interphase heat transfer rate from the TF model and the cTF model with PR-DNS data over the decay rate or the characteristic length scale $\ell_{\langle\phi_m\rangle}$ for the solid volume fraction of (a) $\varepsilon_s = 0.1$ and (b) $\varepsilon_s = 0.5$. The circles represent the data obtained from the TF model and the triangles represent the data from the cTF model.

5.5 Conclusion

We revisit the scale separation assumption in continuum theories of multiphase flow that underlies the validity of local closure models and point out that this assumption needs to be validated. Using high fidelity PR-DNS, gas-solid heat transfer in a freely evolving suspension of particles is chosen to verify the scale separation assumption. Fixed bed simulations, whose results are very close to those of freely evolving suspensions for isothermal high Stokes number particles, are used to perform parametric studies develop a criteria for scale separation. The average bulk fluid temperature from PR-DNS data decays exponentially over a characteristic length scale D/λ, where λ is the decay rate of the average bulk fluid temperature. An exponential decay model for the average bulk fluid temperature is used to verify the assumption of scale separation implicit in the continuum formulation of two-fluid equations by checking the local homogeneity of the average bulk fluid temperature at the microscale (on the order of $3-4$ particle diameters). The length scale D/λ defines the scale of inhomogeneity of the average bulk fluid temperature and is used to develop a criterion that ensures the validity of the local

homogeneity assumption or scale separation in the TF theory, model or CFD simulation. For ($\mathrm{Pe_m} \geq 7, \varepsilon_s = 0.1$), ($\mathrm{Re_m} \geq 20, \varepsilon_s = 0.2$) and ($\mathrm{Re_m} \geq 50, \varepsilon_s = 0.3$), the length scale over which the average bulk fluid temperature decays is greater than $3 \sim 4$ particle diameters, and the scale separation assumption underlying local closure models in the TF theory are valid. The criterion for the validity of scale separation also holds for freely evolving suspensions since the fixed assembly of isothermal particles is a good approximation to freely evolving suspensions with isothermal high-Stokes number particles. An consistent TF model for average gas-solid heat transfer has been proposed to resolve the situation that scale separation does not hold. Accurate prediction of gas-solid flows where scale separation does not hold requires consideration of fluctuation hydrodynamics and the development of closure models.

CHAPTER 6. TEMPERATURE FLUCTUATIONS IN GAS-SOLID FLOW

This chapter is a manuscript titled "Temperature fluctuations in gas-solid flow" that is under preparation.

In gas-solid flows, mixing of chemical species and their reactions both in the gas phase and at particle surfaces are important in industrial applications. Current computational fluid dynamics (CFD) closure models represent only the mean species mass fraction and mean gas-phase temperature that are used to determine Arrhenius-type reaction rates that are highly non-linear in terms of temperature. However, it is well known from the studies of single-phase turbulent reacting flow that the reaction rate evaluated at the mean temperature is a poor model for the average reaction rate in Arrhenius-type reactions due to the high level of temperature fluctuations resulting from turbulence. Therefore, transport of the probability density function (PDF) of composition (species mass fraction and temperature) is effectively used to model such turbulent reacting flows (Pope (1985); Haworth (2010)).

The purpose of this chapter is to study gas-phase temperature fluctuations (relevant to mixing) in gas-solid flow using the PDF transported approach and PR-DNS approach. The temperature variance is used to quantify the level of the temperature fluctuations in gas-solid flow. The transport equation for temperature variance is derived and its unclosed terms are identified. Then PR-DNS of a steady flow past a homogeneous fixed bed of particles with heat transfer is used to quantify the temperature variance in gas-solid heat transfer. The mixing time scale used in closure models for the average temperature dissipation rate is quantified using PR-DNS data. Since the single-point PDF of fluid temperature provides closure of the mean reaction rate in gas phase in reacting gas-solid flow, the PDF of fluid temperature is extracted from PR-DNS data. The phase-conditioned single-point velocity-composition PDF

transport equation that can be used to obtain the temperature PDF is derived, and its unclosed terms are identified. Modeling efforts for gas-solid reacting flow are discussed. Further model development is needed to model the interphase transfer terms in the velocity-composition PDF transport equation and validate closure models for gas-solid reacting flow.

6.1 Introduction

Mixing of chemical species and their reactions both in the gas phase and at the particle surfaces is important in many gas-solid flow applications such as biomass fast pyrolysis that also involves gas-phase reactions. Multiphase computational fluid dynamics (CFD), in which averaged equations for conservation of mass, momentum, energy are given for each phase with coupling terms representing the interphase interactions, are increasingly being used for simulations of these reacting gas-solid flow (Halvorsen et al. (2003)). Generally, the average chemical reaction source term in the averaged energy equation is simply assumed to be $\langle S_{\phi_\alpha}(\boldsymbol{\phi})\rangle = S_{\phi_\alpha}(\langle\boldsymbol{\phi}\rangle)$ for modeling reacting flow in CFD simulations (Fox (2003)), where the composition $\boldsymbol{\phi}$ represents the species mass fraction (Y_α) or enthalpy ($c_P T$) (Syamlal et al. (1993)), and S_{ϕ_α} is the chemical reaction source term that is a function of reaction rate vector that is formed by reaction rate constants. However, it is well known from single-phase reactive turbulence that the reaction rate evaluated at the mean temperature is a poor model for the average reaction rate in Arrhenius-type reactions due to the high level of temperature fluctuations resulting from turbulence.

The level of the mixing of scalars (chemical species) also depends on the intensity of scalar fluctuations. Scalar fluctuations arise from velocity fluctuations that in turn arise from different mechanisms in gas-solid flow. In single-phase turbulence, the level of velocity fluctuations results from the intensity of turbulence (Pope (2000)). However, in gas-solid flow the gas-phase velocity fluctuations can arise from turbulence inherent in the gas-phase, or they can be generated by wakes resulting from the interaction of particles with the mean slip velocity between the gas and solid phases. The second mechanism can generate gas-phase velocity fluctuations even in laminar gas-solid flow and these have been termed pseudo-turbulent velocity fluctuations in Mehrabadi et al. (2015).

In gas-solid flow, the studies of the pseudo-turbulent velocity fluctuations in fixed particle beds and freely evolving suspensions (Mehrabadi et al. (2015)) have shown that the level of these fluctuations is a significant fraction of the kinetic energy associated with the mean slip velocity. Similarly, in a gas-solid flow with heat or mass transfer, the cross correlation between temperature and velocity fluctuations (see Chapter 4) cannot be neglected, especially in dense flows. Thus, pseudo-turbulent velocity fluctuations enhance mixing and heat/mass transfer (see Chapters 3 and 4).

Scalar fluctuations have been quantified by the scalar variance that is used to identify the mixing time scale in single-phase turbulence (Pope (2000); Fox (2003)). As in single-phase turbulence, the time scale for scalar mixing is defined as $\tau_\phi = k_\phi/\varepsilon_\phi$, where k_ϕ and ε_ϕ represent the scalar variance and the scalar dissipation, respectively. The scalar mixing time scale τ_ϕ is proportional to the turbulence time scale, such as $\tau_\phi = \tau/C_\phi$, where $\tau = k_e/\varepsilon_e$ and C_ϕ is a constant. Here k_e represents the turbulent kinetic-energy velocity fluctuation and ε_e is the dissipation rate of k_e in Pope (2000) and Fox (2003). Different values of C_ϕ have been reported in the literature reviewed by Haworth (2010). However, in a gas-solid flow, the mixing time scale has not been reported. In this work, the mixing time scale in gas-solid flow is quantified for the case of steady flow past a fixed bed of particles with heat transfer. It is worth noting that due to the presence of the solid phase, there exist other time scales related to the characteristic length scale of the solid phase. For instance, in gas-solid heat transfer, the molecular time scale $\tau_{\phi_{mol}} \sim D/\alpha_f$ (where D is the particle diameter, and α_f is the thermal diffusivity) is used to determine the importance of thermal diffusion in gas-solid flow. These time scales are expected to be used to develop mixing models in gas-solid flow as those in single-phase turbulence (Haworth (2010); Fox (2003); Celis and da Silva (2015)).

Although the scalar variance charaterizes scalar fluctuations in reacting flows, the mean chemical reaction rate is not closed at this level. However, if the single-point scalar probably density function (PDF) is known then the mean chemical reaction rate in the gas phase is closed. The scalar variance that is used to compute the mixing time scale can be computed from PDF as a second moment, since the scalar PDF contains statistical information of all moments such as in single-phase turbulence (Pope (2000); Haworth (2010)). Recent studies

by several authors (Pozorski and Minier (1999); Zhu et al. (2000); Minier and Peirano (2001); Peirano and Minier (2002); Carrara and DesJardin (2006, 2008); Vegendla et al. (2009)) have extended the transported PDF approach to two-phase flows. Analogous to the derivation of Pope (1985) for the single-point velocity-composition PDF transport equation in single-phase turbulence, Pai and Subramaniam (2009) derived the phase-conditioned single-point velocity PDF transport equation in two-phase flow.

Unlike the phase-conditioned PDF of velocity-composition in two-phase flow, the single-phase velocity-composition PDF is well studied (Pope (1985); Fox (2003)). In single-phase flow, mixing and fluid acceleration terms in the single-point velocity-composition PDF transport equation need closure models. However, in two-phase flow, due to the existence of phase interfaces, there are interphase transfer terms of mass, momentum and energy that also appear in the phase-conditioned PDF transport equation (Minier and Peirano (2001); Carrara and DesJardin (2006, 2008); Zhu et al. (2000); Pai and Subramaniam (2009)). These interphase terms also need closure models since the phase-conditioned PDF does not contain statistical information pertaining the interface. Just as in the case of the single-point PDF there is no length-scale information (Pope (1985); Fox (2003)), and in particular information concerning the characteristic length scale between two solid surfaces is absent. Although a two-point (both points represent the location) PDF contains statistical information of characteristic length scale, the two-point PDF is not the focus of this work.

To solve the PDF transport equation, closure models for unclosed terms that appear in the PDF transport equation (see Eq. 6.16) need to be given. In single-phase flow, the unclosed mixing and fluid acceleration terms in the composition PDF transport equation are normally modeled by the interaction by exchange with the mean (IEM) models (Fox (2003)) and a gradient-diffusion model that introduces a turbulent diffusion term (Carrara and DesJardin (2006, 2008)), respectively. However, in two-phase flow, in addition to the unclosed mixing and fluid acceleration terms, the interphase transfer term in the single-point phase-conditioned PDF transport equation (Pai and Subramaniam (2009)) also needs to be modeled. Vegendla et al. (2009) modeled interphase mass transfer term in the two-point composition PDF transport equation in terms of mass transfer coefficient and concentration difference between solid and

gas phases. Although single-phase closure models (Vegendla et al. (2009)) have been extended to model the unclosed terms of the PDF transport equation in gas-solid flow and provided the reasonable results, the extension of single-phase closure models needs to be validated.

In order to validate and improve the closure models for the PDF transport equation, direct numerical simulation (DNS) has been widely used to gain a better understanding of the dynamics and to provide reference data for test cases. Single-phase DNS is used to provide DNS data and compare with the results of the PDF approaches (Pope (2000); Haworth (2010)). Similar to single-phase DNS, particle-resolved DNS (PR-DNS) for two-phase flow that fully resolves the droplet or particle by imposing boundary conditions at each particle or droplet's surface can be also used to develop closure models. In this work, we will extract the temperature PDF in gas-solid flow from PR-DNS data to understand the behavior of the temperature PDF in dilute and dense flows.

The rest of the chapter is organized as follows. In Section 6.2, we derive the temperature variance transport equation and quantify the temperature variance in a gas-solid heat transfer problem and mixing time scale that is used in closure models for gas-solid flow is quantified using the PR-DNS data. In Section 6.3, we extract the PDF of fluid temperature from PR-DNS data for different solid volume fractions. In Section 6.4, the phase-conditioned single-point velocity-composition PDF transport equation is derived and its unclosed terms are identified. The modeling efforts for these unclosed terms in the PDF transport equation are discussed. Finally, the principal findings are summarized in Section 6.5.

6.2 Temperature variance

6.2.1 Temperature variance equation

Since the scalar variance characterizes scalar fluctuations, the transport equation for scalar variance in two-phase flow is important to understand the evolution of scalar fluctuations. We first derive the transport equation for scalar variance in the Eulerian-Eulerian (EE) frame and then compare the scalar-variance transport equation for two-phase flow with that for single-phase flow. In a gas-solid heat transfer problem, a scalar represents the enthalpy that is in terms

of fluid temperature and the scalar variance transport equation becomes fluid temperature variance transport equation. The quantification of the temperature variance in the transport equation is provided.

The scalar variance can be defined by the Favre-averaged scalar variance

$$\widetilde{\Phi_{\alpha\alpha}^{(\beta)}} = \frac{\left\langle \rho I_\beta \phi_\alpha^{\prime\prime(\beta)} \phi_\alpha^{\prime\prime(\beta)} \right\rangle}{\langle \rho I_\beta \rangle}, \tag{6.1}$$

where $\langle\rangle$ represents the ensemble average, I_β is the indicator function in β phase, $\phi_\alpha^{(\beta)}$ is the mass fraction of species ($\phi_\alpha = Y_\alpha$) or the enthalpy ($\phi_\alpha = c_p T$) in phase β, $\rho = \rho(\boldsymbol{\phi})$ is the density that depends on the set of scalars $\boldsymbol{\phi}$, $\phi_\alpha^{\prime\prime(\beta)} = \phi_\alpha - \left\langle \widetilde{\phi_\alpha^{(\beta)}} \right\rangle$ is the scalar fluctuation, and $\left\langle \widetilde{Q^{(\beta)}} \right\rangle = \langle \rho I_\beta Q \rangle / \langle \rho I_\beta \rangle$ is the Favre-averaged of Q in phase β (see details in Appendix H). The transport equation for scalar variance can be derived from the scalar transport equation or the PDF transport equation (see Appendix L). The details of the derivation from the PDF transport equation is shown in Appendix L. Here, we only show the final expression for the scalar-variance transport equation, which reads:

$$\begin{aligned}
\frac{\partial}{\partial t}\left[\langle \rho I_\beta \rangle \widetilde{\Phi_{\alpha\alpha}^{(\beta)}}\right] \;+\; & \frac{\partial}{\partial x_k}\left[\langle \rho I_\beta \rangle \widetilde{\Phi_{\alpha\alpha}^{(\beta)}} \left\langle \widetilde{U_k^{(\beta)}} \right\rangle\right] \\
= \; & -2\left\langle \rho I_\beta u_k^{(\beta)} \phi_\alpha^{\prime\prime(\beta)} \right\rangle \frac{\partial \left\langle \widetilde{\phi_\alpha^{(\beta)}} \right\rangle}{\partial x_k} - \frac{\partial}{\partial x_k}\left\langle \rho I_\beta u_k^{(\beta)} \phi_\alpha^{\prime\prime(\beta)} \phi_\alpha^{\prime\prime(\beta)} \right\rangle \\
& + 2\left\langle -\phi_\alpha^{\prime\prime(\beta)} \frac{\partial \left(I_\beta J_k^\alpha\right)}{\partial x_k} \right\rangle + 2\left\langle \phi_\alpha^{\prime\prime(\beta)} J_k^\alpha \frac{\partial I_\beta}{\partial x_k} \right\rangle + \left\langle 2\rho I_\beta \phi_\alpha^{\prime\prime(\beta)} S_\alpha \right\rangle \\
& + \left\langle \phi_\alpha^{\prime\prime(\beta)} \phi_\alpha^{\prime\prime(\beta)} S_\rho^{(\beta)} \right\rangle,
\end{aligned} \tag{6.2}$$

where $u_k^{(\beta)} = U_k - \left\langle \widetilde{U_k^{(\beta)}} \right\rangle$ is the fluctuation of the velocity in phase β, J_k^α is the flux of the scalar α, S_α is the chemical reaction source/sink term, $S_\rho^{(\beta)}$ is the interphase mass transfer due to the velocity of the phasic interface in phase β. Assuming Fick's law, the flux of scalar α is defined as $J_k^\alpha = -\Gamma_\alpha \partial \phi_\alpha / \partial x_k$, where Γ_α is the molecular diffusivity of the scalar α. The description of each term in the above equation is as follows. The two terms on the left-hand side represent the unsteady and convective derivative of the phasic-Favre scalar variance. On the right-hand side, the first term represents the scalar-variance production, the second term represents scalar-variance flux term, the third term represents the diffusion of fluctuations, and the fourth term

represents the interphase transfer with scalar fluctuation. The fifth term represents the source or sink of scalar fluctuations due to chemical reaction. The final term represents the source in the transport equation due to mass transfer at the interface (the average of this term appears in the phasic mean mass conservation equation).

In this work, we focus on the quantification of fluid temperature variance in the transport equation in a non-reacting gas-solid flow. The non-reacting gas-solid flow we choose to study is the steady flow past a fixed homogeneous particle assembly with heat transfer that was described in Chapters 2-5. In this heat transfer problem the velocity field is homogeneous whereas the temperature field is inhomogeneous in the axial direction $x_{\|}$ due to particle heating (or cooling). The assumptions made for this heat transfer problem are (i) no chemical reaction source/sink S_α, (ii) neglect of radiation and free convection (iii) no mass transfer at the interface $S_\rho^{(\beta)}$, (iv) steady flow, and (v) constant density. Therefore, based on these assumptions, the scalar-variance transport equation in Eq. 6.2 can be simplified as

$$\begin{aligned}\left\langle \widetilde{U_k^{(\beta)}} \right\rangle \frac{\partial}{\partial x_k}\left[\rho \left\langle I_\beta \right\rangle \widetilde{\Phi_{\alpha\alpha}^{(\beta)}}\right] &= -2\rho \left\langle I_\beta u_k^{(\beta)} \phi_\alpha''^{(\beta)} \right\rangle \frac{\partial \left\langle \phi_\alpha^{(\beta)} \right\rangle}{\partial x_k} - \rho \frac{\partial}{\partial x_k}\left\langle I_\beta u_k^{(\beta)} \phi_\alpha''^{(\beta)} \phi_\alpha''^{(\beta)} \right\rangle \\ &\quad + \Gamma_\alpha^{(\beta)} \frac{\partial^2 \left\langle I_\beta \phi_\alpha''^{(\beta)} \phi_\alpha''^{(\beta)} \right\rangle}{\partial x_k \partial x_k} + \Gamma_\alpha^{(\beta)} \left\langle I_\beta \frac{\partial \phi_\alpha''^{(\beta)}}{\partial x_k} \frac{\partial \phi_\alpha''^{(\beta)}}{\partial x_k} \right\rangle \\ &\quad + 2\left\langle \phi_\alpha''^{(\beta)} J_k^\alpha \frac{\partial I_\beta}{\partial x_k} \right\rangle, \end{aligned} \tag{6.3}$$

where $\left\langle Q^{(\beta)} \right\rangle = \langle I_\beta Q \rangle / \langle I_\beta \rangle$ is the ensemble average of the variable, $\Gamma_\alpha^{(\beta)}$ is the molecular diffusivity of the scalar α in phase β. The details of the simplification can be found in Appendix L. Compared to the steady-state constant-density transport equation for scalar variance in single-phase turbulence (Fox (2003)), which reads:

$$\langle U_k \rangle \frac{\partial}{\partial x_k}\langle \phi_\alpha'' \phi_\alpha'' \rangle = -2\langle \rho u_k \phi_\alpha'' \rangle \frac{\partial \langle \phi_\alpha \rangle}{\partial x_k} - \frac{\partial}{\partial x_k}\langle \rho u_k \phi_\alpha'' \phi_\alpha'' \rangle + \Gamma_\alpha \frac{\partial^2 \langle \phi_\alpha'' \phi_\alpha'' \rangle}{\partial x_k \partial x_k} - 2\Gamma_\alpha \left\langle \frac{\partial \phi_\alpha''}{\partial x_k} \frac{\partial \phi_\alpha''}{\partial x_k} \right\rangle, \tag{6.4}$$

it is clear that the scalar-variance production term (the first term on the right-hand side of Eqs. 6.3 and 6.4), the scalar-variance flux term (the second term), and the scalar dissipation term (the fourth term) appear in both the transport equations. The first four terms on the

right-hand side of Eq. 6.4 in single-phase turbulence are identical to the first four terms on the right hand side of Eq. 6.3 in two-phase flow. Only the fifth term in Eq. 6.3 does not appear in Eq. 6.4 since there is no interphase transfer in single-phase flow.

In single-phase turbulence, the transport equation for scalar variance has three unclosed terms: (i) the scalar-variance production, (ii) the scalar-variance flux, and (iii) the scalar dissipation. For two-phase flow, there is another unclosed interphase transfer term (the fifth term on the RHS of Eq. 6.3) due to the presence of the interface between phases. In order to solve the transport equation for scalar variance, the unclosed terms in the transport equation have to be modeled. In single-phase turbulence, the scalar-variance production term is modeled by a gradient-diffusion model (Pope (2000); Fox (2003)). The scalar-variance flux term is also modeled by the gradient-diffusion model or modified gradient-diffusion model (Fox (2003)) as $\langle u_k \phi''_\alpha \phi''_\alpha \rangle \sim \langle u_k u_k \rangle \partial \langle \phi''_\alpha \phi''_\alpha \rangle / \partial x_k$. The scalar dissipation term is normally modeled by the equilibrium model (Spalding (1971)) that is in terms of k_e, ε_e, and $\langle \phi''_\alpha \phi''_\alpha \rangle$. Closure models for corresponding terms in gas-solid flow need to be developed and PR-DNS (Sun et al. (2015, 2016)) provides the data for such a study. In this work, we only provide the PR-DNS data for the scalar variance, and the validity of closure models for the scalar-variance transport equation in two-phase flow is deferred to future work. The same approach used for the average fluid temperature equation in Chapters 3 and 4 can be followed here also.

6.2.2 Quantification of temperature variance

The temperature variance in the gas-solid heat transfer problem can be quantified using PR-DNS data that have been generated in Chapters 2-5. Figure 6.1 shows the axial variation of non-dimensional fluid temperature variance $\langle I_f \phi''^{(f)} \phi''^{(f)} \rangle$ that is computed by ensemble-averaging the cross-sectional average of the the non-dimensional fluid temperature $\left\{ I_f \phi''^{(f)} \phi''^{(f)} \right\}_{cs}$, given by

$$\left\{ I_f \phi''^{(f)} \phi''^{(f)} \right\}_{cs} (x_{||}; \omega) = \frac{1}{A_f} \int_{A_f} \phi''^{(f)} \phi''^{(f)} dA, \tag{6.5}$$

to obtain

$$\langle I_f \phi''^{(f)} \phi''^{(f)} \rangle (x_{||}) \approx \frac{1}{M} \sum_{\omega=1}^{M} \left\{ I_f \phi''^{(f)} \phi''^{(f)} \right\}_{cs} (x_{||}; \omega), \tag{6.6}$$

where ω is one realization of the random particle configuration. Note that the non-dimensional fluid temperature is defined as $\phi = (T - \langle T_{m,in} \rangle) / (T_s - \langle T_{m,in} \rangle)$ in Chapter 2, where $\langle T_{m,in} \rangle$ is the bulk fluid temperature at the inlet of the computation domain, and T_s is the solid temperature. Since the average non-dimensional fluid temperature $\left\langle \phi^{(f)} \right\rangle$ is inhomogeneous in the axial direction, $\langle I_f \phi''^{(f)} \phi''^{(f)} \rangle$ is also inhomogeneous in the axial direction and decays with axial location due to fluid cooling as shown in Fig. 6.1 for both dilute and dense flows. Compared with the decay rate of $\langle I_f \phi''^{(f)} \phi''^{(f)} \rangle$ in dilute flow ($\varepsilon_s = 0.1$), $\langle I_f \phi''^{(f)} \phi''^{(f)} \rangle$ in dense flow ($\varepsilon_s = 0.4$) decays much faster for this high Reynolds number of 100. This results from the increase of velocity fluctuations with solid volume fraction as shown in Mehrabadi et al. (2015). It appears that the high velocity fluctuations result in high temperature fluctuations.

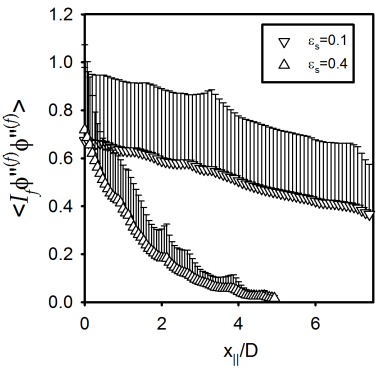

Figure 6.1: Variation of the temperature variance $\left\langle I_f \phi''^{(f)} \phi''^{(f)} \right\rangle$ with axial locations for solid volume fraction of 0.1 and 0.4 at mean slip Reynolds number of 100. The error bars above the symbols correspond to 5 realizations of random particle figuration. One-sided error bars indicate 95% confidence intervals.

Although $\langle I_f \phi''^{(f)} \phi''^{(f)} \rangle$ is statistically inhomogeneous along axial location, $\langle I_f \phi''^{(f)} \phi''^{(f)} \rangle$ can be split into a homogeneous piece and an inhomogeneous piece by using the scaled fluid temperature θ that was discussed through Chapters 2-4. Based on the relation $\langle \phi^{(f)} \rangle = \langle \phi_m \rangle \langle \theta^{(f)} \rangle$, $\langle I_f \phi''^{(f)} \phi''^{(f)} \rangle$ can be expressed as $\left\langle I_f \theta''^{(f)} \theta''^{(f)} \right\rangle \langle \phi_m \rangle^2$ in which $\left\langle I_f \theta''^{(f)} \theta''^{(f)} \right\rangle$ is statistically homogeneous due to the homogeneity of the θ field. Figure 6.2 shows the variation of $\left\langle I_f \theta''^{(f)} \theta''^{(f)} \right\rangle$ with axial locations for dilute and dense flows at mean slip Reynolds number of 100. As we expected, $\left\langle I_f \theta''^{(f)} \theta''^{(f)} \right\rangle$ is homogeneous along the axial location for both

dilute and dense flows. The value of $\left\langle I_f \theta''^{(f)} \theta''^{(f)} \right\rangle$ in dense flow is higher than that in dilute flow, which again confirms that higher temperature fluctuations exist in dense flow at this high speed (mean slip Reynolds number of 100). Due to the homogeneity of $\left\langle I_f \theta''^{(f)} \theta''^{(f)} \right\rangle$, the volume-average of $\left\langle I_f \theta''^{(f)} \theta''^{(f)} \right\rangle$ can be obtained as

$$\overline{\left\langle I_f \theta''^{(f)} \theta''^{(f)} \right\rangle} = \frac{1}{L} \int_0^L \left\langle I_f \theta''^{(f)} \theta''^{(f)} \right\rangle \left(x_\parallel \right) \mathrm{d}x_\parallel. \tag{6.7}$$

Note that for simplicity, we still use $\left\langle I_f \theta''^{(f)} \theta''^{(f)} \right\rangle$ as the volume-average of $\left\langle I_f \theta''^{(f)} \theta''^{(f)} \right\rangle$ instead of $\overline{\left\langle I_f \theta''^{(f)} \theta''^{(f)} \right\rangle}$. Therefore, the fluid temperature variance can be computed by using the $\left\langle I_f \theta''^{(f)} \theta''^{(f)} \right\rangle$. The normalized fluid temperature variance can be computed using this homogeneity of $\left\langle I_f \theta''^{(f)} \theta''^{(f)} \right\rangle$ as follows:

$$\frac{\left\langle I_f \phi''^{(f)} \phi''^{(f)} \right\rangle}{\left\langle \phi^{(f)} \right\rangle^2} = \frac{\left\langle I_f \theta''^{(f)} \theta''^{(f)} \right\rangle \left\langle \phi_m \right\rangle^2}{\left\langle \theta^{(f)} \right\rangle^2 \left\langle \phi_m \right\rangle^2} = \frac{\left\langle I_f \theta''^{(f)} \theta''^{(f)} \right\rangle}{\left\langle \theta^{(f)} \right\rangle^2}. \tag{6.8}$$

In the above equation, $\left\langle \theta^{(f)} \right\rangle$ is given in Chapter 3. Figure 6.3 shows the variation of the fluid temperature variance normalized by the square of average fluid temperature with solid volume fraction at the mean slip Reynolds number of 100. Compared with average fluid temperature, the fluid temperature variance becomes larger with solid volume fraction. If one knows the average fluid temperature, $\left\langle I_f \phi''^{(f)} \phi''^{(f)} \right\rangle$ can be computed in each cross-sectional plane.

6.2.3 Mixing time scale

Here, we would also like to use the PR-DNS data to extract the mixing time scale that is an important parameter for developing closure model for mixing. Figure 6.4 shows a preliminary results for the ratio of the mixing time scale $\tau_\phi = k_\phi / \varepsilon_\phi$ to the molecular time scale $\tau_{\phi_{mol}} = D/\alpha_f$ with solid volume fractions at mean slip Reynolds number of 100. Note that for the same Reynolds number cases, $\tau_{\phi_{mol}}$ does not change since α_f is constant for Prandtl number of 0.7 in gas-solid flow. The fluid temperature variance in gas-solid flow is defined as

$$k_\phi = 2 \left\langle I_f \phi''^2 \right\rangle, \tag{6.9}$$

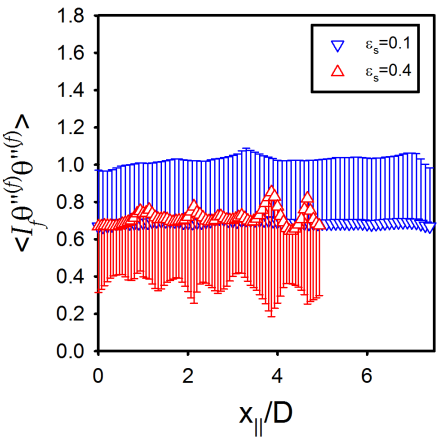

Figure 6.2: Variation of the scaled fluid temperature variance $\left\langle I_f \theta''^{(f)} \theta''^{(f)} \right\rangle$ for solid volume fraction values of 0.1 and 0.4 at mean slip Reynolds number of 100. One-sided error bars represent 95% confidence intervals inferred from five different realizations of random particle configuration.

and the dissipation of fluid temperature is defined as

$$\varepsilon_\phi = 2\alpha_f \left\langle I_f \frac{\partial \phi}{\partial x_i} \frac{\partial \phi}{\partial x_i} \right\rangle . \tag{6.10}$$

Fig. 6.4 shows that $\tau_\phi/\tau_{\phi_{mol}}$ decreases with increasing solid volume fraction. This reduction of the mixing time scale indicates that the mixing rate of the fluid temperature increases, due to pseudo-turbulent fluctuations. This behavior also confirms that velocity fluctuations (Mehrabadi et al. (2015)) enhance mixing of fluid temperature in pseudo-turbulent dense gas-solid heat transfer. It is also seen that the molecular time scale $\tau_{\phi_{mol}}$ is larger than τ_ϕ by more than one order of magnitude even in a dilute flow ($\varepsilon_s = 0.1$).

6.3 PDF of fluid temperature

Besides using the scalar-variance transport equation to obtain the scalar variance, the scalar variance can be also computed from the PDF of scalar. Based on the PR-DNS data of the case of a flow past a fixed particle beds with heat transfer, the PDF of fluid temperature can be extracted. Figure 6.5(a) shows the PDF of non-dimensional fluid temperature ϕ at different axial locations $x_{||}$. The peak in the PDF of the fluid temperature becomes steeper with increasing downstream distance $x_{||}$ ($x_{||}/D = 0$ represents the upstream). The shift of

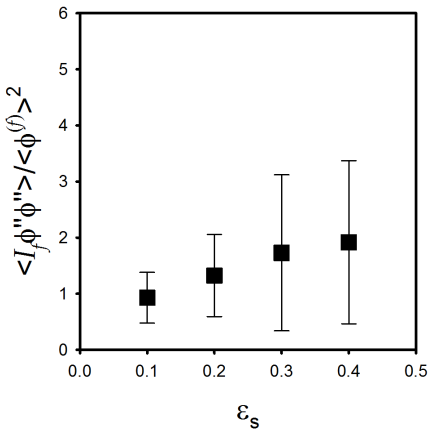

Figure 6.3: Variation of the non-dimensional fluid temperature variance that is defined as $\left\langle I_f \phi''^{(f)} \phi''^{(f)} \right\rangle$ (normalized by the average non-dimensional fluid temperature $\left\langle \phi^{(f)} \right\rangle^2$) for solid volume fraction values of $0.1 - 0.4$ at mean slip Reynolds number of 100. The error bars represent 95% confidence intervals inferred from five different realizations of the particle configuration.

the center of PDF of the fluid temperature towards $\psi = 0$ implies that the fluid temperature distribution at $x_{\|}/D = 4$ is much closer to the particle surface temperature.

Since the PDF of fluid temperature varies with axial location, it is not easy to develop a model or correlation for PDF of fluid temperature. Instead of fluid temperature, the PDF of scaled fluid temperature θ is a better choice, since the scaled fluid temperature is homogeneous and self-similar as discussed in Chapters 2-4. The cumulative distribution function (CDF) of the scaled fluid temperature F_θ can be computed as follows:

$$F_\phi(\psi) = P\{\phi < \psi\} = P\{\langle\phi_m\rangle\,\theta < \psi\} = P\left\{\theta(y,z) < \frac{\psi}{\langle\phi_m\rangle(x_{||})}\right\} = F_\theta\left(\frac{\psi}{\langle\phi_m\rangle(x_{||})}\right), \tag{6.11}$$

where $\langle\phi_m\rangle$ is the bulk fluid temperature (see Chapters 3 and 4) and only depends on the axial location. Then the PDF of scaled fluid temperature $f_\theta(\Theta)$ can be obtained by using the derivative of the CDF as

$$f_\phi(\psi) = \frac{\mathrm{d}F_\phi(\psi)}{\mathrm{d}\psi} = \frac{\mathrm{d}}{\mathrm{d}\psi}F_\theta\left[\frac{\psi}{\langle\phi_m\rangle\left(x_{||}\right)}\right] = \frac{1}{\langle\phi_m\rangle\left(x_{||}\right)}f_\theta(\Theta). \tag{6.12}$$

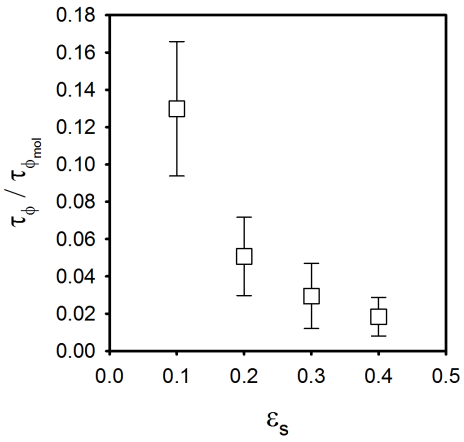

Figure 6.4: Variation of the mixing time scale for scalar variance $\tau_\phi = k_\phi/\varepsilon_\phi$ normalized by the molecular time scale $\tau_{\phi_{mol}}$ with solid volume fractions $(0.1 - 0.4)$ at mean slip Reynolds number of 100. The error bars represent the 95% confidence intervals from five realizations of the random particle configuration.

Therefore, the PDF of the fluid temperature at any location can be recovered from the PDF of the scaled fluid temperature by dividing $\langle \phi_m \rangle \left(x_{||} \right)$. Figure 6.5(b) shows the PDF of the scaled fluid temperature for different solid volume fractions. For the same mean slip Reynolds number of 100, the shape of PDF of the scaled fluid temperature becomes steeper with increasing solid volume fraction. The center of the PDF also moves towards $\Theta = 0$. The high solid volume fraction results in more heat transfer and cooling the flow much quicker. It is worth noting that in Fig. 6.5(b), the left tail of the PDF does not go to zero since the scaled fluid temperature is close to zero near the particle surface due to the isothermal boundary condition.

The shape of the PDF f_θ in two-phase flow is different from the shape of PDF of scalar in single-phase turbulence (Gaussian distribution) because of the interphase transfer term in two-phase flow. In other words, in two-phase flow, the shape of the PDF of scalar is determined not only by the mixing term in the PDF transport equation but also by the interphase transfer term. A correlation for the PDF of the scaled fluid temperature by fitting the PDF f_θ from PR-DNS data is being investigated. The correlation for the temperature PDF will give a candidate presumed PDF for use in presumed PDF approaches in two-phase flow. However, one concern is that the presumed PDF in two-phase flow is likely to depend on the temperature boundary condition at the particle surface. In single-phase flow a beta PDF or a set of delta functions

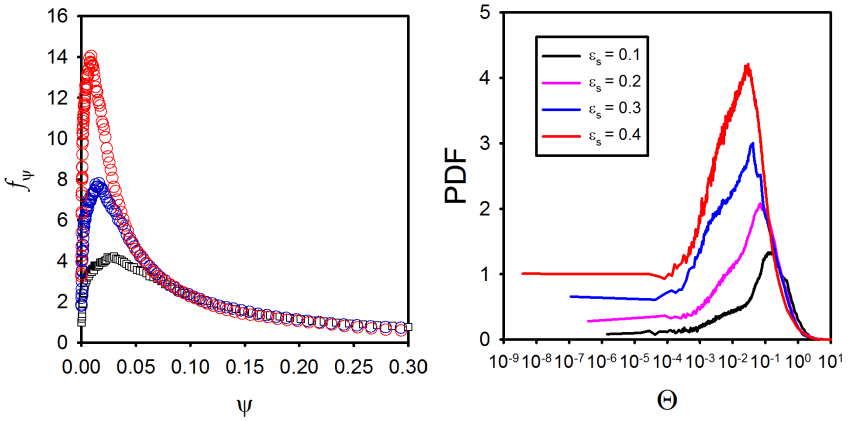

Figure 6.5: (a) The PDF of non-dimensional fluid temperature extracted in the cross section are located in axial location $x_{\|}/D = 0$ (black square), $x_{\|}/D = 2$ (blue circle), and $x_{\|}/D = 4$ (red circle) for solid volume fraction of 0.4 and mean slip Reynolds number of 100. (b) The variation of the PDF of scaled fluid temperature θ with solid volume fractions $(0.1 - 0.4)$ at mean slip Reynolds number of 100.

is normally used as presumed PDF (Fox (2003)). Compared to the presumed PDF approach that approximates the shape of the PDF, the transported PDF approach does not require any assumptions regarding prior shape of the PDF because the shape of the PDF is computed using the corresponding PDF transport equation. In the following section, the transported PDF approach is present.

6.4 Transported PDF approach

Based on the discussions in the previous sections, the scalar PDF is of importance because it contains statistical information of all moments and can compute average gas-phase reaction rate in closed form. Since the PR-DNS approach is time-consuming to obtain the scalar PDF and is not currently feasible for in device-scale simulations, the transported PDF approach can be used to obtain the scalar PDF in an efficient way, as is done in single-phase flows involving combustion or turbulent mixing (Haworth (2010)). In this section, the transport equation for the phase-conditioned single-point velocity-composition joint PDF is derived. We then discuss the unclosed terms that need to be modeled.

6.4.1 Phase-conditioned single-point velocity-composition joint PDF transport equation

Using the statistical representation of two-phase flow in Appendix H, the phase-conditioned single-point velocity-composition joint PDF transport equation can be derived. This derivation of PDF transport equation is given using two methods. One is the delta function method in Appendix I that is an extension of Pai and Subramaniam (2009)'s approach that derived the phase-conditioned single-point velocity PDF transport equation. The other is the test function method in Appendix J that is used to derive a single-phase velocity-composition single-point PDF transport equation by Pope (1985). Using the definition of phase-conditioned PDF in Appendix H, the phase-conditioned single-point velocity-composition joint PDF transport equation is derived using these two methods. Here, we briefly describe the final expression for the phase-conditioned single-point velocity-composition joint PDF transport equation.

With the continuity equation

$$\frac{\partial \rho}{\partial t} + \frac{\partial \rho U_j}{\partial x_j} = 0, \tag{6.13}$$

the momentum equation ($\boldsymbol{A}$ is the fluid acceleration)

$$\rho \frac{DU_k}{Dt} = \rho A_k, \tag{6.14}$$

and the composition equation ($\boldsymbol{\Theta}$ is the rate of change of composition that is composed of a diffusion and a reaction source term)

$$\rho \frac{D\phi_\alpha}{Dt} = \rho \Theta_\alpha, \tag{6.15}$$

the PDF transport equation for two-phase flow is obtained using the delta function method (Pope (1981)), in a manner similar to Pai and Subramaniam (2009) for phase-conditioned velocity PDF transport equation, as

$$\frac{\partial \mathcal{F}_{\mathbf{U}\boldsymbol{\phi}|I_\beta}}{\partial t} + V_k \frac{\partial \mathcal{F}_{\mathbf{U}\boldsymbol{\phi}|I_\beta}}{\partial x_k} = -\frac{\partial}{\partial V_k}\left[\langle \rho I_\beta A_k \,|\mathbf{V},\boldsymbol{\psi}\rangle \frac{\mathcal{F}_{\mathbf{U}\boldsymbol{\phi}|I_\beta}}{\langle \rho I_\beta \,|\mathbf{V},\boldsymbol{\psi}\rangle}\right] - \frac{\partial}{\partial \psi_\alpha}\left[\langle \rho I_\beta \Theta_\alpha \,|\mathbf{V},\boldsymbol{\psi}\rangle \frac{\mathcal{F}_{\mathbf{U}\boldsymbol{\phi}|I_\beta}}{\langle \rho I_\beta \,|\mathbf{V},\boldsymbol{\psi}\rangle}\right] + \left\langle \rho(U_k - U_k^{(I)}) \frac{\partial I_\beta}{\partial x_k} \middle| \mathbf{V},\boldsymbol{\psi}\right\rangle \frac{\mathcal{F}_{\mathbf{U}\boldsymbol{\phi}|I_\beta}}{\langle \rho I_\beta \,|\mathbf{V},\boldsymbol{\psi}\rangle}. \tag{6.16}$$

where $\mathcal{F}_{\mathbf{U}\boldsymbol{\phi}|I_\beta}(\mathbf{V},\boldsymbol{\psi},\mathbf{x},t) = \langle \rho(\boldsymbol{\phi}) I_\beta(\mathbf{x},t)\,\delta(\mathbf{U}(\mathbf{x},t)-\mathbf{V})\,\delta(\boldsymbol{\phi}(\mathbf{x},t)-\boldsymbol{\psi})\rangle$ is the Favre mass density conditional on phase β, $\mathbf{V}$ and $\boldsymbol{\psi}$ are the velocity and composition sample space variables, and $U_k^{(I)}$ is the velocity of the phasic interface. The description of each term in Eq. 6.16 is as follows. The two terms on the left-hand side represent the unsteady and convective derivative of the phasic Favre mass density. On the right-hand side, the first term represents the transport in velocity space due to fluid acceleration, the second term represents the transport in composition space due to mixing and reaction, and the third term represents a source in the transport equation due to mass transfer at the interface in the phasic mean mass conservation. Since Pai and Subramaniam (2009, 2012) have already discussed the first and third term on the right-hand side of Eq. 6.16, we will only focus on the second term related to the compositions on the right-hand side of Eq. 6.16 in the following sections.

6.4.2 Unclosed terms in the PDF transport equation

The conditional mean rate of change of composition term $\langle \rho I_\beta \Theta_\alpha \,|\boldsymbol{V},\boldsymbol{\psi}\rangle$ in the second term on the right-hand side of the PDF transport equation (see Eq. 6.16) can be expanded using the expression corresponding to diffusion flux and chemical reaction source/sink as:

$$\rho\Theta_\alpha(\boldsymbol{x},t) = -\frac{\partial J_i^\alpha}{\partial x_i} + \rho S_\alpha \tag{6.17}$$

as

$$\langle \rho I_\beta \Theta_\alpha \,|\mathbf{V},\boldsymbol{\psi}\rangle = \left\langle \left[-\frac{\partial (I_\beta J_i^\alpha)}{\partial x_i} + J_i^\alpha \frac{\partial I_\beta}{\partial x_i} + I_\beta \rho S_\alpha\right] \middle| \mathbf{V},\boldsymbol{\psi}\right\rangle. \tag{6.18}$$

where J_i^α is the flux of the scalar α. Assuming Fick's law, the scale flux $J_i^\alpha = -\Gamma_\alpha \partial\phi_\alpha/\partial x_i$, where Γ_α is the molecular diffusivity of the scalar α. Since we focus on the scalar PDF, the

phase-conditioned single-point composition PDF transport equation is obtained from Eq. 6.16 (see Appendix K) as

$$\frac{\partial \mathcal{F}_{\boldsymbol{\phi}|I_\beta}}{\partial t} + \frac{\partial \left[\left\langle \widetilde{U_k^{(\beta)}} \right\rangle \mathcal{F}_{\boldsymbol{\phi}|I_\beta} \right]}{\partial x_k} + \frac{\partial \left[\langle u_k \,|\boldsymbol{\psi}\rangle \, \mathcal{F}_{\boldsymbol{\phi}|I_\beta} \right]}{\partial x_k} = -\frac{\partial}{\partial \psi_\alpha} \left[\left\langle -\frac{\partial \left(I_\beta J_i^\alpha \right)}{\partial x_i} \middle| \boldsymbol{\psi} \right\rangle \frac{\mathcal{F}_{\boldsymbol{\phi}|I_\beta}}{\langle \rho I_\beta \,|\boldsymbol{\psi}\rangle} \right] - \frac{\partial}{\partial \psi_\alpha} \left[\left\langle J_i^\alpha \frac{\partial I_\beta}{\partial x_i} \middle| \boldsymbol{\psi} \right\rangle \frac{\mathcal{F}_{\boldsymbol{\phi}|I_\beta}}{\langle \rho I_\beta \,|\boldsymbol{\psi}\rangle} \right] - \frac{\partial}{\partial \psi_\alpha} \left[\langle I_\beta \rho S_\alpha \,|\boldsymbol{\psi}\rangle \frac{\mathcal{F}_{\boldsymbol{\phi}|I_\beta}}{\langle \rho I_\beta \,|\boldsymbol{\psi}\rangle} \right]. \quad (6.19)$$

Note that the above equation neglects the interphase mass transfer term (the third term on the right-hand side of Eq. 6.16). The first term on the right-hand side in Eq. 6.19 represents scalar diffusion in phyiscal space in phase β conditional on composition. The second term on the right-hand side is the interphase transfer term. The third term on the right-hand side represents the chemical reaction source/sink term in phase β. Since the PDF transport equation is a single-point description of the two-phase flow that lacks the length scale information such as gradient, the first term is an unclosed term that is evaluated at a single location in space-time coordinates. Since the phase-conditioned single-point velocity-composition joint PDF also lacks information about the phase interface, the second term is also unclosed. It is worth noting that the chemical reaction source/sink term in the *solid* phase (the counterpart of the third term in Eq. 6.19), also needs to be modeled, whereas chemical reaction source/sink term in the gas phase is treated exactly without approximation in the PDF transport equation. In addition, since the second term on the left-hand side of Eq. 6.19 contains the velocity conditional on composition, this term needs to be modeled. The closure models for these unclosed terms need to be given in order to solve the PDF transport equation. In the following section, candidate models for the unclosed interphase and diffusion terms of the PDF transport equation are discussed and the mixing time scale that is often used in mixing models (Fox (2003)) is computed from the PR-DNS data.

6.4.3 Model development

Unlike in two-phase flow, many closure models for the PDF transport equation in a single-phase turbulence have been proposed and used in turbulent mixing and combustion problems. The unclosed velocity fluctuation conditional on scalar, which is the third term in the left-hand side of Eq. 6.19 of the single-point composition PDF transport equation for single-phase turbulence, is closed by using a gradient-diffusion model (Raman et al. (2004)) that introduces a turbulent diffusion term. The unclosed diffusion them conditional on scalar (the first term in the right-hand side of Eq. 6.19) representing the micromixing term, can be closed by using different approaches. In the case of non-reacting single-phase turbulent flows, the micromixing model (Fox (2003)) must fulfill some constraints concerning the shape of the PDF: the mean values must be constant, the variance decay must be exponential, and the asymptotic shape of the PDF must be Gaussian. One widely used model for the micromixing term is the interaction by exchange with the mean (IEM) model (Fox (2003); Raman et al. (2004); Cassiani et al. (2005)). The IEM model assumes a linear relaxation of the scalar toward its mean value as

$$\left\langle \Gamma_\alpha \frac{\partial^2 \phi_\alpha}{\partial x_i \partial x_i} \left| \psi_\alpha \right. \right\rangle = \frac{1}{\tau_\phi} \left(\langle \phi_\alpha \rangle - \psi_\alpha \right). \tag{6.20}$$

Note that the mixing time scale is defined early as $\tau_\phi = k_\phi / \varepsilon_\phi$, where the scalar fluctuation is $k_\phi = 2 \left\langle \phi_\alpha''^2 \right\rangle$ and the scalar dissipation is $\varepsilon_\phi = 2\Gamma \left\langle (\partial \phi_\alpha / \partial x_i)^2 \right\rangle$.

However, closure models for two-phase flow has not yet been developed much, particularly with considering the interphase transfer between two phases. The single-phase closure models such as gradient-diffusion model and mixing model have been extended to modeling two-phase flow. The interphase transfer term is modeled by Vegendla et al. (2009); Prasad Vegendla et al. (2012) as a function of heat or mass transfer coefficient and the difference between the temperature or mass fraction in gas and solid phases. However, the interphase term $\langle -J_i^\alpha \partial I_\beta / \partial x_i \left| \boldsymbol{\psi} \right. \rangle$ in Eq. 6.19 is conditional on $\boldsymbol{\psi}$, but the current model (Vegendla et al. (2009); Prasad Vegendla et al. (2012)) does not account for this conditional effect in the interphase transfer model. These closure models need to be validated. Based on these closure models, the PDF transport equation for two-phase flow can be solved using a Monto-Carlo

type particle method (Pope (1994); Fox (2003)) that can be used to express the PDF transport equation in terms of equivalent stochastic differential equations (SDE) to simulate the evolution of the notional or computational particles (Vegendla et al. (2009); Prasad Vegendla et al. (2012); Popov and Pope (2014)). We note that the correct scalar PDF can be only obtained from this type particle method based on a adequately resolved velocity field. For instance, Popov and Pope (2014) performed a simulation of bluff body stabilized flame using large eddy simulation approach for the velocity field and the transported PDF approach for evolving scalar field.

6.5 Conclusion

Temperature variance in gas-solid flow is studied using the transported PDF and PR-DNS approaches. The transport equation for fluid temperature variance is derived using the single-point velocity-composition joint PDF transport equation for two-phase flow. The PR-DNS of a flow past a homogeneous fixed bed of particles with heat transfer is used to quantify the fluid temperature variance in gas-solid heat transfer. The mixing time scale in two-phase flow used in a IEM model is quantified. We found that in a dense flow, the mixing of fluid temperature is enhanced due to the high intensity of the velocity fluctuations. Since the scalar PDF can be used to compute scalar variance, PDF of fluid temperature is extracted from the PR-DNS data and the shape of PDF is closed to log-normal but is not equal to zero in the lower limit. The phase-conditioned single-point velocity-composition PDF transport equation is derived and its unclosed terms are identified. Modeling efforts for single-phase turbulence and two-phase flow are discussed. Further modeling efforts are needed to model the interphase transfer term in the PDF transport equation and the validity of closure models in two-phase flow are also needed.

CHAPTER 7. FULLY FINITE-DIFFERENCE PR-DNS METHOD: APPLICATION TO HYDRODYNAMICS AND HEAT TRANSFER ON PARTICLES IN A DUCT FLOW

This chapter is a manuscript titled "Application to hydrodynamics and heat transfer on particles in a duct flow using particle–resolved direct numerical simulation approach" that is under preparation.

In previous Chapters 2-6, the thermally fully-developed flow has been achieved using the PS PR-DNS approach in a periodic domain. In order to study wall-bounded flow with inflow/outflow boundary conditions, the PS PR-DNS approach does not work appropriately. The aim of the chapter is to develop a PR-DNS approach to account for wall-bounded flow with inflow/outflow boundary conditions. A fully finite-difference (FFD) scheme version of PR-DNS for hydrodynamic and scalar solver is developed based on the frame of PR-DNS of Tenneti *et al.* (Tenneti et al. (2011, 2013); Tenneti (2013)) and Garg et al. (2010b) who developed the PS scheme version of PR-DNS to simulate gas–solid flow by imposing periodic boundary conditions. The hydrodynamic and scalar solvers of the FFD PR-DNS are validated in a suite of test cases including fully–developed duct flow, flow past simple cubic and face centered cubic particle arrangements, and developing duct flow with and without a single particle. In the case of developing duct flow without or with a fixed sphere, the inflow/outflow boundary condition with traction boundary condition is used to simulate developing flow in a square duct. A flow past a fixed homogeneous particle assembly in a square duct with heat transfer is also simulated. The preliminary PR-DNS results obtained from this case show the duct wall effect on fluid velocity and temperature in gas–solid flow.

7.1 Introduction

Many industrial applications such as chemical looping combustion and fluidized beds are the system of wall-bounded gas–solid flows. In such a system, since solid particles and walls of the reactors affect velocity or temperature profiles, it results in intrinsically multiscale (Tenneti and Subramaniam (2014)). For instance, in a circulating fluidized bed (Lim et al. (1995)) statistical homogeneous velocity far from the walls of reactors is observed in the macroscale. However, near walls the velocity is non-linear because of the development of the momentum boundary layers and particle aggregations in the microscale (Lim et al. (1995)). In order to study such gas–solid flow in a wall-bounded system, experimental measurements and numerical simulations have been employed.

Experimental measurement of gas–solid flow is challenging because of limited optical access that result in the lack of resolution of the detailed flow. Experimental measurement techniques such as pressure drop signal (Ergun (1952); Mauret and Renaud (1997a,b)), electroresistivity probes (Park et al. (1969); Rigby et al. (1970)), photographing with ordinary cameras (Pyle and Harrison (1967); Godard and Richardson (1969)) have been used to measure the velocity and pressure in gas–solid fixed-bed reactors over the last several decades (Wakao and Kaguei (1982)). Since most experimental measurements of gas–solid flow are intrusive, flow disturbance caused by the probes is a source of uncertainty. Recently, non-intrusive laser optical measurement techniques such as Magnetic Resonance Imaging (MRI) (Gladden (1999)), particle image velocimetry (PIV), and planar laser-induced fluorescence (PLIF) are developed for research and diagnostics into flow and combustion processes. These techniques are capable of measuring an entire two-dimensional cross section of the flow field simultaneously with a high degree of accuracy. For instance, combination of PIV and PLIF allows us to visualize and measure the concentration and temperature field in fluid flow. With index of refraction matching to avoid the light refraction and resulting image distortions, the flow inside a bed of particles can be visualized, which cannot be measured using transitional experimental techniques.

However, these non-intrusive techniques such as PIV and PLIF have their limitations. For instance, regular PIV only gives two components of velocity in a two dimensional plane. Even

though stereoscopic PIV can be used for visualization of all three components of velocity field, this technique is still limited to measurement in a single two dimensional plane. For PLIF measurement of concentration, fluorescence can cause from other species, especially from hydrocarbons in high pressure reacting flows. Also, since the fluorescence of the dye is a function of the laser light intensity, temporal and spatial variation of laser light needs to accounted for.

The limitations of experimental measurements motivate researchers to employ numerical simulation as an alternative tool to study wall-bounded gas-solid flow. The continuum models such as a two–fluid model (Anderson and Jackson (1967); Drew (1983)) in which both the fluid phase and the solid phase are treated as continuous media or two–fluid DEM (Sun et al. (2007)) are used for macroscale industrial device-scale simulation. However, the TF CFD simulation needs closure models from microscale physics since particle-fluid and particle-particle interactions at the microscale affect the quantities at the macroscale. Recently, the microscale physics is addressed by particle-resolved direct numerical simulation (PR–DNS). This approach accounts for the solid-fluid interaction by solving the Navier-Stokes equation with the initial value problem for the motion of the particles simultaneously. At the microscale, PR–DNS provides an accurate and efficient numerical approximation to the evolution of such a complete description of gas–solid flow. The PR-DNS is a first-principles approach to develop accurate closure models for gas–solid flow. The review of existing PR-DNS approaches has been done elsewhere (Tenneti et al. (2011); Tenneti and Subramaniam (2014)).

Tenneti et al. (2011) and Garg et al. (2010b) have developed a PR-DNS approach that is a pseudo-spectral (PS) formulation of PR-DNS to solve and develop models in gas–solid flow. This approach has been successfully applied for simulations of fixed and freely evolving suspension of particles in a fully-developed region of gas–solid flow (Tenneti et al. (2011); Tenneti and Subramaniam (2014); Tenneti et al. (2010); Mehrabadi et al. (2015)). However, it has not yet accounted for wall-bounded flow with particles in these simulations. In this work, a fully finite-difference (FFD) formulation of PR-DNS base on the similar frame of PS PR-DNS is developed for accounting for wall effect and inflow/outflow boundary conditions.

In order to study wall effect on particles in gas–solid flow, the test case of a developing duct flow with particles is used to mimic flow past particles in a wall-bounded system. In

the simulations of developing duct flow, one has to deal with an outlet boundary condition that guarantees numerical condition should not disturb upstream flow. In order to overcome this issue (Tsynkov (1998)), different outlet boundary conditions such as non-reflecting outlet boundary condition derived from a wave equation (Orlanski (1976); Jin and Braza (1993); Forestier et al. (2000)) have been proposed. In this work, the open and traction boundary condition which is efficient for fluid-solid interactions (Liu (2009); Coutand and Shkoller (2005); Guermond et al. (2005)) is imposed as outlet boundary conditions. The open and traction boundary condition developed by Poux et al. (2011) has been successfully used to simulate incompressible flows with objects.

This chapter is organized as follows. In Section 7.2, the description of the duct flow with particles is given. A fully finite-difference scheme of the PR-DNS approach is developed to solve the above physical problem in Section 7.3. In Section 7.4, the hydrodynamic and scalar solvers of the FFD PR-DNS are parallelized and validated by a suite of test cases. Using this FFD PR-DNS, wall effect on a single particle and particle assembly are studied in gas–solid flow in Section 7.5. Finally, the principal findings of this chapter is summarized in Section 7.6.

7.2 Problem description

The purpose of this work is to study a flow past particles with heat transfer in a square duct as a setup in Fig. 7.1. The figure shows that a steady flow past a random assembly of spherical particles in a square duct with uniform velocity U_{in} and temperature $T_{f,in}$ along the axial location $x_{\|}$, where the walls are located in y and z directions. The mass, momentum conservation, and scalar equations to describe this above problem that has constant density wall-bounded flow with heat transfer are

$$\frac{\partial u_i}{\partial x_i} = 0 \tag{7.1}$$

and

$$\frac{\partial u_i}{\partial t} + S_i = -\frac{1}{\rho_f} g_i + \nu_f \frac{\partial^2 u_i}{\partial x_j^2}. \tag{7.2}$$

respectively. Where $S_i = \partial(u_i u_j)/\partial x_j$ is the convection, ρ_f is the fluid-phase density, ν_f is the kinetic viscosity, g represents body forces (e.g., hydrostatic pressure gradient or gravity). The scalar (fluid temperature in this work) equation in the absence of viscous heating, radiation and free convection effects is

$$\rho_f c_{pf} \left(\frac{\partial T}{\partial t} + S_T \right) = k_f \frac{\partial^2 T}{\partial x_j^2}, \tag{7.3}$$

where $T(\mathbf{x}, t)$ is the temperature field, $S_T = \partial(u_j T)/\partial x_j$ is the convection, k_f is the thermal conductivity in the fluid phase, c_{pf} is the constant pressure specific heat capacity in the fluid phase. No–slip and isothermal boundary conditions at the particle surface is imposed. Dirichlet boundary condition at $x = 0$ and Neumann boundary condition at $x = L$ are used for the domain boundary conditions. The isothemal wall boundary condition is also used for all walls in y and z directions.

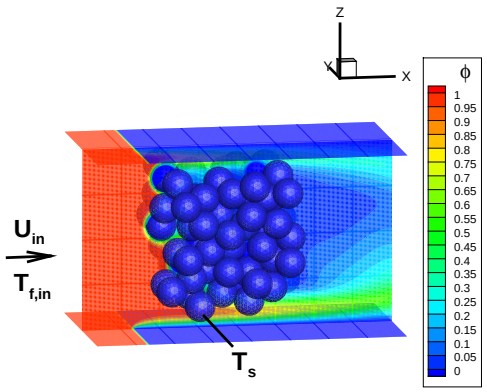

Figure 7.1: Schematic of the temperature contour of flow past a fixed assembly of spheres in a square duct. The temperature of the spheres is T_s. The uniform velocity U_{in} and temperature $T_{f,in}$ are specified at the inlet of the square duct, respectively. The non–dimensional fluid temperature ϕ is defined as $\phi = (T - T_s) / (T_{f,in} - T_s)$. At the surface, the non–dimensional fluid temperature ϕ is equal to zero in this case.

7.3 Solution approach

The above heat transfer problem can be solved using PR–DNS approach, which is called the Particle-resolved Uncontaminated-fluid Reconcilable Immersed Boundary Method (PUReIBM).

This PUReIBM has been developed based on pseudo–spectral (PS) scheme and used to study homogeneous suspensions of isothermal particles in gas–solid flow by Tenneti et al. (Tenneti et al. (2011, 2013); Tenneti and Subramaniam (2014)) and Garg et al. (2010b). However, this PS PR-DNS approach is restricted to study problems with periodic boundary condition. In order to simulate wall–bounded fluid–solid flows and impose various boundary conditions such as Dirichlet boundary condition or flux boundary condition, a fully finite-difference (FFD) scheme version of PR-DNS is developed to simulate the fluid–solid flow with heat or mass transfer in this chapter.

7.3.1 FFD PR-DNS approach

The fluid–solid flow with heat transfer problem is solved using Eq. 7.1-7.3 by introducing the indicator function

$$I_\beta = \begin{cases} 1 & \text{point } (\mathbf{x}, \mathrm{t}) \text{ lies in phase } \beta \\ 0 & \text{otherwise} \end{cases},$$

as

$$\frac{\partial u_i}{\partial t} + S_i = -\frac{1}{\rho_f} g_i + \nu_f \frac{\partial^2 u_i}{\partial x_j^2} + I_s f_u \tag{7.4}$$

and

$$\rho_f c_{pf} \left(\frac{\partial T}{\partial t} + S_T \right) = k_f \frac{\partial^2 T}{\partial x_j^2} + I_s f_T, \tag{7.5}$$

where f_u and f_T are the additional immersed boundary (IB) direct forcing terms that are nonzero only in the solid phase. The IB direct forcing accounts for the presence of the solid particles in the domain by ensuring that the no–slip and no–penetration, and isothermal boundary conditions are satisfied on each particle surface. Complete details about the IB forcing can be found in Tenneti et al. (2011) and Garg et al. (2010b).

The main difference between the PS and FFD PR-DNS is that in the FFD PR-DNS the equations Eqs. 7.1, 7.4 and 7.5 are solved using a fully finite–difference scheme in all directions,

instead of using Fourier transforms in the cross-stream directions. This allows us to implement various boundary conditions such as walls and inflow/outflow. With appropriate boundary conditions the governing equations in Eqs. 7.1, 7.4 and 7.5 are discretized on the uniform Cartesian grid and solved at each time step. The spatial discretization of the equations in Eqs. 7.1, 7.4 and 7.5 is performed by a second-order finite–difference scheme on a fully-staggered grid. On a fully-staggered grid, the velocity or momentum variables are located at the cell faces while the scalar variables such as pressure and scalar are stored at cell centers. We perform the time discretization of the momentum equation as :

$$\frac{u_i^{n+1} - u_i^n}{\triangle t} = -(\frac{3}{2}S_i^n - \frac{1}{2}S_i^{n-1}) - \frac{1}{\rho_f}\nabla q^{n+1} + \frac{\nu_f}{2}\nabla^2(u_i^n + u_i^{n+1}) + I_s f_{u,i}^{n+1}, \tag{7.6}$$

where the IB forcing is

$$f_{u,i}^{n+1} = \frac{u_i^d - u_i^n}{\triangle t} + S_i^n + \frac{1}{\rho_f}g_i^n - \nu_f\frac{\partial^2 u_i^n}{\partial x_j^2}. \tag{7.7}$$

For the temporal discretization of the momentum equation, the Adams-Bashforth scheme is used for the convective terms, and the Crank-Nicolson scheme is used for the viscous terms. In order to solve the discretized momentum equation (Eq. 7.6), a two-step fractional step method is used. The first step to obtain the intermediate velocity field u_i^* is computed from

$$\frac{u_i^* - u_i^n}{\triangle t} = -(\frac{3}{2}S_i^n - \frac{1}{2}S_i^{n-1}) - \frac{1}{\rho_f}\nabla q^n + \frac{\nu_f}{2}\nabla^2(u_i^n + u_i^*) + f_{u,i}^{n+1}. \tag{7.8}$$

Since the velocity in the $n+1$th step u_i^{n+1} is required to satisfy the divergence-free condition, the second step is to solve the Poisson equation (Eq. 7.9) to correct the velocity field based on the intermediate velocity field as shown in Eq. 7.10:

$$\frac{\triangle t}{\rho}\nabla^2\varphi = \nabla \cdot u_i^*, \tag{7.9}$$

and

$$u_i^{n+1} = u_i^* - \frac{\triangle t}{\rho}\nabla\varphi. \tag{7.10}$$

The pressure at the $n+1$th step is also updated based on the pressure at the previous step

$$p^{n+1} = p^n + \phi - \frac{\nu_f \triangle t}{2} \nabla^2 \phi. \tag{7.11}$$

The discretized temperature equation is also solved implicitly using the same temporal discretization for the solution of the momentum equation in Eq. 7.6:

$$\frac{T^{n+1} - T^n}{\triangle t} = -(\frac{3}{2} S_T^n - \frac{1}{2} S_T^{n-1}) + \frac{\alpha_f}{2} \nabla^2 (T^n + T^{n+1}) + f_T^n, \tag{7.12}$$

where the IB direct forcing term f is

$$f_T^{n+1} = \frac{T_i^d - T_i^n}{\triangle t} + S_T^n - k_f \frac{\partial^2 T^n}{\partial x_j^2}. \tag{7.13}$$

For the spatial discretization of the convection and diffusion terms of the above temperature equation, the same schemes to solve the momentum equations are used to solve these terms in discretized temperature equation (Eq. 7.12). The sparse matrices generated from Eqs. 7.6, 7.9 and 7.12 are solved using the open software Portable Extensible Toolkit for Scientific Computation (PETSc).

7.3.2 Boundary conditions

The above governing equations need to be solved with the appropriate boundary conditions. In Chapter 2, the thermal self-similarity boundary condition has been developed to simulate the thermal fully–developed flow using periodic boundary condition in PS PR-DNS approach. In PS PR-DNS, the boundary condition is restricted to periodic boundary condition whereas in FFD PR-DNS, various boundary conditions can be used to solve various problems. For instance, Neumann boundary condition at the exit of the computational domain such as zero velocity gradient is used to simulations of developing free flow or duct flow for outflow boundary condition. However, this kind of boundary conditions normally has the non-physical reflection at the exit (Jin and Braza (1993)). In order to reduce the effect at the exit of domain, open and traction boundary conditions can be imposed in the computational domain. Poux et al. (2011) used open and traction boundary conditions to avoid non-physical reflection and also achieve the higher rate of convergence in space and time. Following their implement of this

boundary condition, the open and traction boundary boundary condition for developing duct flow in FFD PR-DNS is described briefly as below.

For simplicity let Ω be a 3D bounded domain with $\mathbf{n}$ unit normal to the domain boundary $\Gamma = \partial\Omega$. The domain boundary Γ can be split into two part Γ_D and Γ_N that represent the Dirichlet boundary condition and Neumann boundary condition, respectively. Therefore, the velocity and pressure fields in the domain Ω satisfy

$$\mathbf{u} = \mathbf{f} \text{ on } \Gamma_D, \tag{7.14}$$

and

$$(\mu\nabla\mathbf{u} - p\mathbf{I}) \cdot \mathbf{n} = 0 \text{ on } \Gamma_N, \tag{7.15}$$

where $\mathbf{I}$ is the unit tensor, $\mathbf{f}$ is the boundary condition. In the case of developing duct flow with or without particles, $\mathbf{f} = \mathbf{0}$ for the wall boundary and $\mathbf{f}$ is uniform for the inlet velocity while the outlet boundary condition is imposed as Eq. 7.15. Details of the implement of open and traction boundary conditions can be found in Poux et al. (2011).

7.4 Numerical convergence and accuracy

The FFD PR-DNS approach has been developed and parallelized (see Appendix M). A suite of tests are used to validate the convergence and accuracy of the FFD PR-DNS approach in the following sections. The test cases includes fully–developed duct flow, flow past a simple cubic (SC) array of particles, and developing duct flow with and without a single sphere using inflow/outflow boundary condition.

7.4.1 Thermal fully–developed flow in a square duct

First, in order to investigate the accuracy of the FFD PR-DNS approach, we simulate a thermal fully-developed flow in a square duct. The numerical results from the FFD PR-DNS are compared with the analytical solution for the fully-developed flow in a square duct (Shah and London (1978)). The analytical solution for the streamwise velocity is

$$\frac{u}{u_m} = \frac{48}{\pi^3}\left[\sum_{n=1,3\ldots}^{\infty}\frac{1}{n^3}(-1)^{(n-1)/2}\left[1-\frac{\cosh(n\pi y/2a)}{\cosh(n\pi b/2a)}\right]\cos\left(\frac{n\pi z}{2a}\right)\right] \Big/ \left[1-\frac{192}{\pi^2}\left(\frac{a}{b}\right)\sum_{n=1,3\ldots}^{\infty}\frac{1}{n^5}\tanh\left(\frac{n\pi b}{2a}\right)\right] \tag{7.16}$$

where $2a$ and $2b$ are the height and width of the cross-section of a rectangle duct, respectively, and u_m is the mean velocity in the streamwise direction. In the case of a square duct, a is set equal to be b. Numerical results obtained from the FFD PR-DNS are also compared with those obtained from the PS PR-DNS. Note that in the PS PR-DNS, IB forcing is used to implement the wall of the square duct to satisfy no-slip and no-penetration, and isothermal boundary conditions.

Figure 7.2(a) shows that error of streamwise velocity profile between numerical results and analytical solution along the central line in the cross section of the square duct. It is clear that the error in the velocity profile obtained using the PS PR-DNS is higher than the one using the FFD PR-DNS. The error of streamwise velocity in the entire domain of the duct is also shown in Fig. 7.2(b) using the L2-norm of the error. The L2-norm of the error is defined as

$$\xi_{\|u\|_2} = \left[\frac{1}{N_y N_z}\sum_{j=1}^{N_y}\sum_{k=1}^{N_z}\left(\frac{u_{j,k}^{num}-u_{j,k}^{ana}}{u_m^{ana}}\right)^2\right]^{1/2}, \tag{7.17}$$

where N_y and N_z is the number of grid nodes in y and z direction. In Fig. 7.2 the spatial accuracy of the FFD PR-DNS is observed to be the second-order in the L2 norm, whereas the accuracy of the PS PR-DNS is only the first-order accurate. One hypothesis to explain the first-order accuracy in the PS PR-DNS is that only one layer of grid nodes is used to implement the IB forcing so that there are not enough points to represent the Eulerian IB forcing (see details in Tenneti et al. (2011)).

For heat transfer problem, Table 7.1 shows the Nusselt number obtained from the analytical solution and numerical results, as well as its relative error between them.The analytical solution for the Nusselt number in the case of the thermal fully–developed flow in a square duct is 2.976 (Shah and London (1978)). In the PS PR-DNS, the Nusselt number is 3.029, whereas the Nusselt number is 2.980 in the FFD PR-DNS. The relative error using the FFD PR-DNS is smaller than the one using PS PR-DNS. This results from the second-order accuracy in the

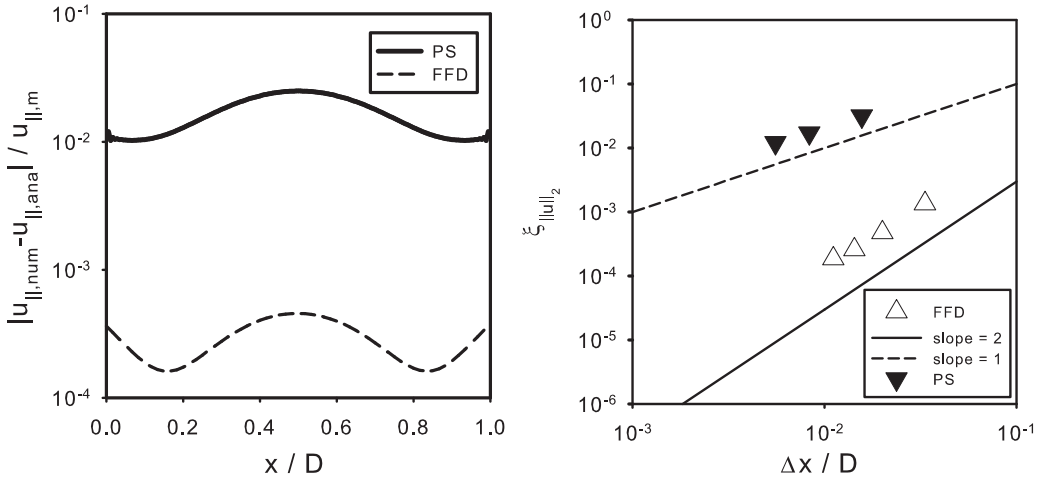

(a) (b)

Figure 7.2: (a) Error between numerical results ($D_m = D/\triangle x = 90$) and analytical solution along the central line in the cross section of the duct. The solid line represents the error of the velocity obtained from PS PR-DNS, and the dashed line represents the error of the velocity obtained from FFD PR-DNS. (b) Accuracy of PS and FFD PR-DNS in the duct flow using the L2-norm of the error. The symbols represent the L2-norm error using PS and FFD PR-DNS. The dashed line represents the line of slope of 1 and inidicates first-order convergence and the solid line represents the line of slope of 2 and inidicates second-order convergence.

FFD PR-DNS and the first-order accuracy in the PS PR-DNS.

Table 7.1: Comparison of Nusselt number between numerical results (PS and FFD PR-DNS) and the analytical solution (ANA) with grid resolution $D_m = 50$ at $\mathrm{Re_m} = 50$. The relative errors are calculated based on the analytical solution from Shah and London (1978).

	FFD	PS	ANA
Nusselt number	2.980	3.029	2.976
relative error	0.13%	1.78%	-

7.4.2 Flow past a SC array of particles

In order to ascertain the convergence characteristics of the FFD PR-DNS, a flow past a SC array of particles is considered. In this case, the simulation setup is the flow past a SC array of particles in a periodic domain. The drag force is defined by Tenneti et al. (2011) as

$$\{F_{i,d}\}_V^{\mu} = \frac{1}{N_p}\left\{ - \langle g_i \rangle_V \varepsilon_s V + \oint_{\partial V^{int}} \tau_{ji} n_i^{(s)} dA \right\}, \tag{7.18}$$

where N_p is the number of particles in the entire domain, and $\tau_{ji} = -p'\delta_{ji} + \mu_f(\partial u_i/\partial x_j + \partial u_j/\partial x_i)$ is the stress tensor, and

$$- \langle g_i \rangle_V = \rho_f \frac{\partial \langle u_i \rangle_V}{\partial t} + \frac{1}{(1-\varepsilon_s)V}\left\{ \oint_{\partial V^{int}} \tau_{ji} n_i^{(s)} dA \right\}, \tag{7.19}$$

is the mean pressure gradient (see details in Tenneti et al. (2011)). The above terms are normalized by the Stokes drag force $F_{St} = 3\pi\nu_f D\,(1-\varepsilon_s)\,|\langle \mathbf{W} \rangle|$ acting on an isolated sphere with a mean slip velocity $|\langle \mathbf{W} \rangle|$.

Convergence characteristics of the normalized drag force with grid resolution D_m is investigated as shown in Fig. 7.3. It shows that using the PS and the FFD PR-DNS, the normalized drag force converges beyond $D_m = 45$ for this SC case. Going to a finer grid reveals that the normalized drag force converges to a value of about 7.20 using the PS PR-DNS and about 7.15 using the FFD PR-DNS. The difference of the normalized drag force between FFD PR-DNS and PS PR-DNS results from the finite-difference scheme and pseudo-spectral scheme. The convergence test will be useful for the choice of numerical parameters for simulations later.

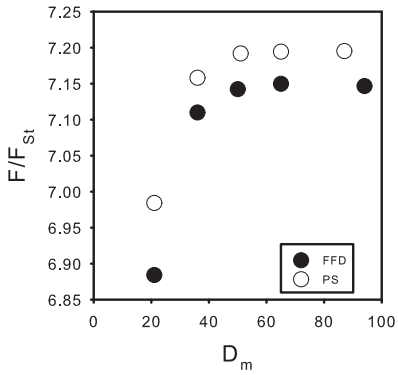

Figure 7.3: Convergence characteristics of the normalized drag force with grid resolution D_m (a) for a SC case of mean slip Reynolds number $\mathrm{Re_m} = 20$ (based on the mean slip velocity) and solid volume fraction $\varepsilon_s = 0.2$. F_{St} is the drag force of a sphere in Stokes flow. The open circles and the black circles represent the drag force obtained from FFD PR-DNS and PS PR-DNS, respectively.

7.4.3 Flow past a fixed sphere

The third test case is a flow past a fixed sphere in an open field, which is a benchmark test for the accuracy of any numerical simulation approach. Using the parallel FFD PR-DNS solver (see details in Appendix M) flow past a spherical particle in a large domain can be simulated in order to avoid the effect of boundary conditions on the sphere. Note that in the PS PR-DNS with periodic boundary conditions it is not possible to simulate flow past a fixed sphere in an open field because of the mirror images of the particle that appear due to periodic boundary conditions. In this case, steady flow past a sphere with a uniform velocity U_{in} in the inlet is simulated in a computational domain of dimensions $20D \times 20D \times 20D$, where D is the diameter of the sphere. Except for the inlet boundary condition, Neumann boundary conditions are imposed on all the domain boundaries. No-slip and no-penetration boundary conditions are imposed at the sphere surface. The Reynolds number is defined as $\mathrm{Re} = \rho_f D U_{in}/\mu_f$ and is varied from 20 to 140. The sphere is represented using 30 grid points on the diameter.

Figure 7.4 shows drag coefficient of the sphere in the case of flow past a sphere in the large domain. The drag coefficient is defined as $C_D = 2F_d/(\rho_f U_{in}^2 A)$, where F_d is the drag force, and $A = \pi D^2/4$ is the frontal area of the sphere. The drag coefficient from FFD PR-DNS shows an excellent agreement with existing numerical data (Pepiot and Desjardins (2010)) and experimental data (Clift et al. (1978)). It indicates that the parallel FFD PR-DNS has the capability to capture flow physics accurately.

7.4.4 Developing duct flow

In a real system, it is not easy to define a fully–developed flow region since the flow needs to be developed in association with the entrance length effect. In addition, the flow is often bounded by the walls of reactors. Wall effect on the flow and particles need to be considered in many cases. In order to study the entrance length effect and wall effect on particles and fluid flow, the simulation of developing duct flow with inflow/outflow boundary conditions is performed using FFD PR-DNS. Figure 7.5(a) shows the contour plot of axial velocity field for a developing laminar flow in a square duct. The extended inlet with free-slip boundary condition

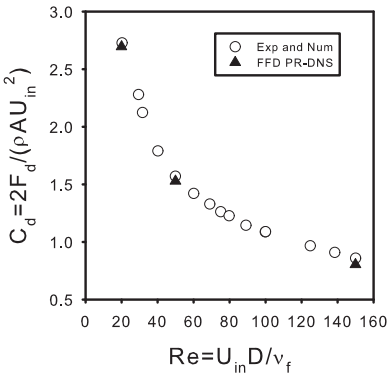

Figure 7.4: Drag coefficient C_D of the sphere in the case of flow past a fixed sphere with Reynolds numbers in a computational domain of 20Dx20Dx20D: the triangles represent the FFD PR-DNS results, and the circles represent the numerical results from Pepiot and Desjardins (2010) and standard drag coefficient of a sphere from Clift et al. (1978).

is introduced before the uniform flow enters the square duct. That is because Williams (1993) reported that the setup of the uniform velocity in the inlet of the duct for simulating developing laminar flow results in retarded growth of the wall boundary layer near the entrance of the duct. He found that the numerical result can match the experimental data with the extension of the upstream flow by adding a free-slip velocity boundary condition. However, he used only one extended length L_{ext} to simulate the developing duct flow. In this work, the effect of different lengths of the extended domain on the velocity along the center of the duct is studied as shown in Fig. 7.5(b). It is observed that the relative error between the experimental data (Goldstein and Kreid (1967)) and numerical results is about 18% for $L_{ext}/L = 1/40$ but 3.5% for $L_{ext}/L = 1/10$. This indicates that a slug flow still exists when using a small extended domain, whereas using a longer extended domain ($L_{ext}/L = 1/4$) the velocity in the center of the duct shows a good agreement with the experimental data.

Good agreement between numerical results using the FFD PR-DNS and experiments of Goldstein and Kreid (1967) can also be seen in Fig. 7.6. This figure shows that the velocity profile at the different axial locations of the square duct is developing along the streamwise direction. At the non–dimensional location $\hat{x} = x/D/\mathrm{Re} = 0.02$, the average difference between numerical data (denoted by lines) and experimental data (denoted by symbols) is only about 3%. At $\hat{x} = 0.1$,

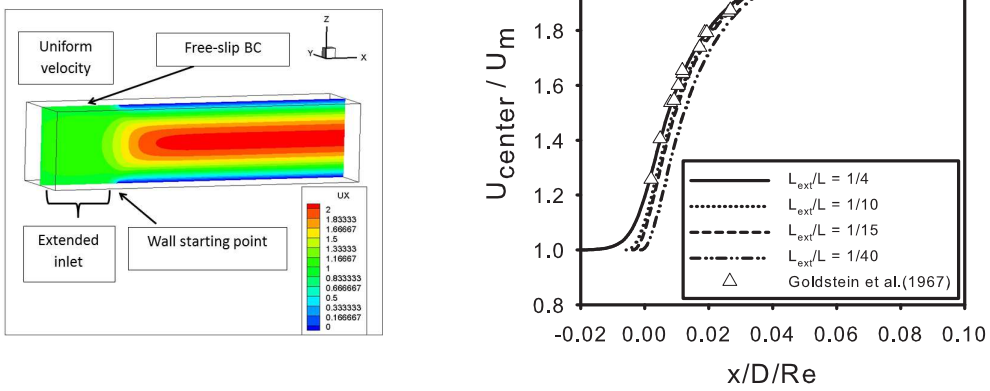

(a) (b)

Figure 7.5: (a) Sketch of developing flow in a square duct and contour of the streamwise velocity in the middle plate. The extended domain is used and uniform velocity is given in the inlet of the domain. (b) Comparison of the streamwise velocity from FFD PR-DNS with Goldstein and Kreid (1967) experimental data (denoted by the triangle) along the center of the square duct in laminar flow. The lines represent the FFD PR-DNS results using the different ratio of extended lengths L_{ext} to the total length L of the computational domain. The bulk fluid velocity is $U_m\left(x_{\|}\right) = \frac{1}{A_f}\int_{A_f} U dA$. The Reynolds number is based on the duct height D and inlet uniform velocity.

the flow is almost developed since velocity profile is close to the analytical solution for the fully–developed duct flow. Thus, the FFD PR-DNS can be used to simulate wall-bounded flows with inflow/outflow boundary conditions accurately.

Similar to the setup of the hydrodynamic problem, the heat transfer in the same square duct is simulated with the inlet uniform temperature and isothermal walls. Figure 7.7 shows that variation of local Nusselt number along the axial location in the duct flow at steady state. The local Nusselt number is defined as

$$\mathrm{Nu_x} = \frac{hD}{k_f} = \frac{(\partial T/\partial n)_{\,mean}}{T_m - T_s} = \frac{(\partial \phi/\partial n)_{\,mean}}{\phi_m}, \tag{7.20}$$

where D is the height of the square duct, T_m is the bulk fluid temperature, T_s is the wall temperature, and n is the normal direction of duct wall. For convenience, the non–dimensional fluid temperature in Eq. 7.20 is defined as

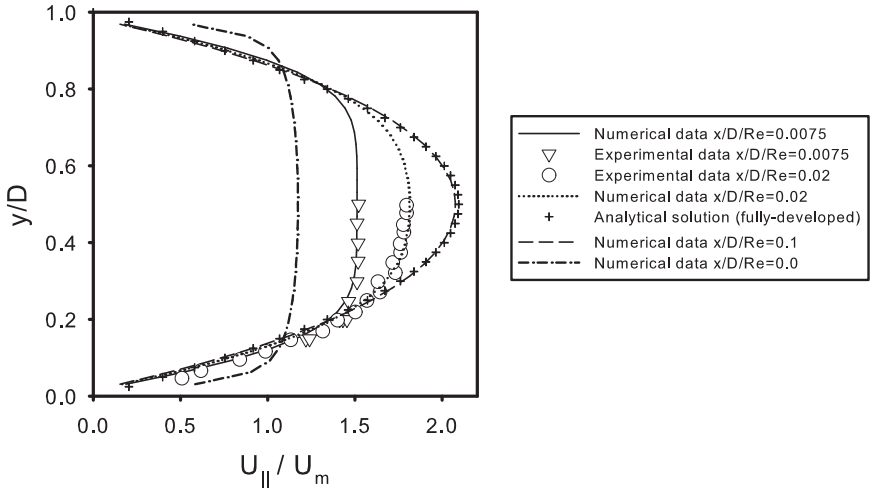

Figure 7.6: Comparison of the velocity profile along the streamwise direction $U_{\|}$ in a square duct flow: FFD PR-DNS compared with Goldstein and Kreid (1967) experimental data (triangles and circles) and the analytical solution of fully–developed flow (plus). U_m is the bulk fluid velocity.The Reynolds number is based on the The lines represent the FFD PR-DNS data, the triangles and circles represent the experimental data, and the crosses represent the analytical solution of the velocity in a fully–developed duct flow. The bulk fluid velocity is $U_m\left(x_{\|}\right) = \frac{1}{A_f}\int_{A_f} UdA$. The Reynolds number is based on the duct height and inlet uniform velocity.

$$\phi = \frac{T - T_s}{T_{m,in} - T_s}, \tag{7.21}$$

and the non–dimensional bulk fluid temperature is

$$\phi_m = \frac{T_m - T_s}{T_{m,in} - T_s}, \tag{7.22}$$

where $T_{m,in}$ is the bulk fluid temperature in the inlet of the domain. The mean temperature gradient in the wall normal direction is computed at each cross section to obtain Nusselt number according to Eq. 7.20. Fig. 7.20 reveals that at the normalized axial location $\hat{x}$ that is greater than 0.04, the flow becomes thermal fully–developed flow and the local Nusselt number approaches the analytical solution of Nusselt number in the thermally fully–developed region (Shah and London (1978)). The entrance effect for heat transfer in the square duct is clearly seen. This test case validates the accuracy of the scalar solver of FFD PR-DNS by demonstrating that it approaches the analytically predicted value of the Nusselt number in a

thermally developing duct flow.

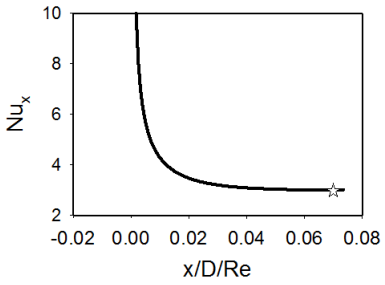

Figure 7.7: Variation of local Nusselt number along the axial location in the developing duct flow. The Reynolds number is based on the height of the square duct D. The line represents the numerical results from FFD PR-DNS data and the star represents the analytical solution of Nusselt number for thermally fully–developed flow in a square duct in Shah and London (1978).

7.5 Gas–solid heat transfer in a duct flow

In order to identify the fully–developed flow region in a duct and the study the wall effect on particles, the convergence characteristics for flow past a sphere with heat transfer is first established in gas–solid flow using FFD PR-DNS. Then the wall effect on drag force and Nusselt number of a fixed sphere in the developing duct flow is investigated by varying the distance between the wall and sphere. Finally, the preliminary results from the case of flow past a fixed particle assembly in a square duct with heat transfer is obtained using FFD PR-DNS. Using these PR-DNS data, the further analysis will be given in the future work.

7.5.1 Convergence test of hydrodynamics and heat transfer in gas–solid flow

In order to choose appropriate numerical parameters for simulations of developing duct flow with particles later, a convergence test of the hydrodynamic and scalar solvers of the FFD PR-DNS is given below for the case of developing flow in a square duct with a fixed sphere. Figure 7.8 shows a sketch of heat transfer on a fixed sphere in a square duct flow. In this case, the height and the length of the square duct are $H/D = 3$ and $L/D = 12$, respectively. The particle Reynolds number $\mathrm{Re_p}$ based on the sphere diameter and inlet uniform velocity is 100.

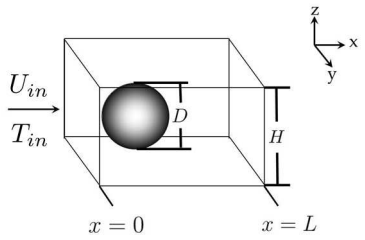

Figure 7.8: Sketch of flow past a fixed sphere in a square duct with heat transfer. D is the diameter of the sphere, H is the height of the square duct, and L is the length of the computational domain. The uniform velocity U_{in} and temperature T_{in} are given at axial location $x = 0$.

Convergence characteristics of the drag coefficient and Nusselt number of the sphere with grid resolution D_m at $\mathrm{Re_p} = 100$ are shown in Fig. 7.9. Fig. 7.9(a) shows variation of the drag coefficient C_D with grid resolution D_m. In this figure, the relative error in the drag coefficient of the sphere between $D_m = 40$ and $D_m = 86$ is about 5%. The drag coefficient converges to a value of 2.2 for $D_m > 40$. For gas–solid heat transfer problem, the Nusselt number of the sphere is defined as

$$\mathrm{Nu_p} = \frac{hD}{k_f}, \tag{7.23}$$

where the heat transfer coefficient is obtained from

$$q_{total} = -\int_{A_s} k_f \frac{\partial T}{\partial n} dA = hA_s \left(T_s - T_{in}\right) \tag{7.24}$$

where q_{total} is the total heat transfer from the sphere to the gas phase, n is the normal direction of the sphere surface, $A_s = \pi D^2$ is the surface area of the sphere. Note that the Prandtl number in this case of gas–solid flow is 0.7 that corresponds to air at standard conditions. Figure 7.9(b) shows that the relative error of the Nusselt number between the grid resolution $D_m = 40$ and $D_m = 66$ is about 3%. For $D_m \geq 40$, the Nusselt number of the sphere converges to a value of 7.9. These results indicates that the hydrodynamic solver requires higher grid resolution to obtain convergent results for the drag coefficient than the scalar solver requires for the Nusselt number. This result is consistent with the fact that for $\mathrm{Pr} = 0.7$ the thermal boundary layer

of the sphere is thicker than the hydrodynamic boundary layer. In the following section, the choice of numerical parameters for the simulation of developing duct flow with particles is based on this results of this convergent test.

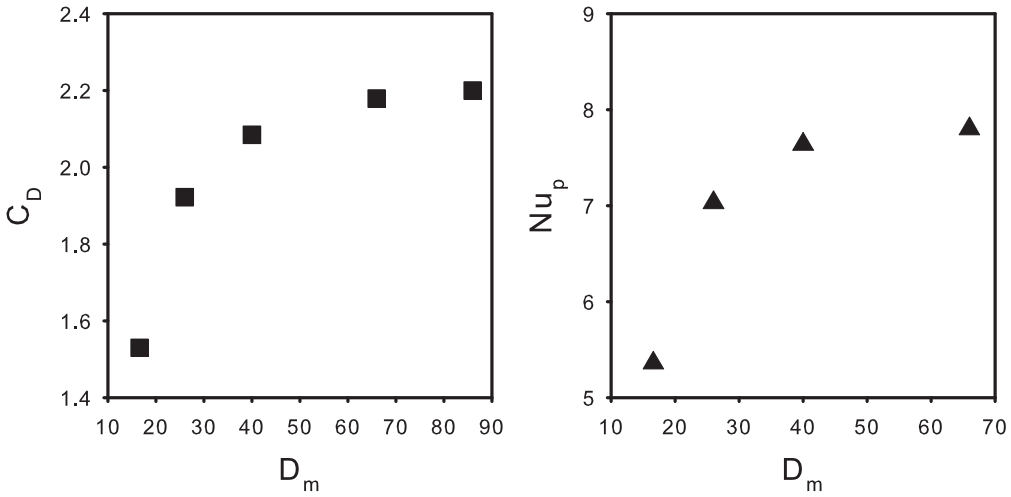

(a) (b)

Figure 7.9: Convergence characteristics of (a) the drag coefficient (square) and (b) Nusselt number (triangle up) of the sphere with grid resolution $D_m = D/\Delta x$ in the computational box of $H/D = 3$ and $L/D = 12$ at $\mathrm{Re_p} = 100$, where Δx is the grid spacing.

7.5.2 Wall effect on drag force of a sphere

Since the presence of walls can affect the flow around a sphere, which can in turn influence the drag force of a sphere, the validated FFD PR-DNS is used to study the wall effect on flow past a fixed sphere in a square duct by varying the ratio of height of the duct to sphere diameter H/D (see Fig 7.8). Due to the restriction of computational resources, a small test domain is used with $L/D = 4$ and the maximum ratio of height to particle diameter $H/D = 4$. The length of the extended domain is 1/10 of the streamwise length L. The sphere is located at $x/L = 0.3$ with a uniform velocity at $x/L = 0$.

Figure 7.10 shows variation of the normalized drag force with the ratio H/D at a sphere Reynolds number of 20. The normalized drag force denoted by the circle symbols decreases with increasing H/D. The decrease of the normalized drag force with H/D results from the

acceleration of flow between the sphere and the wall that produces large stress on the surface of the sphere as seen in Fig. 7.11. Since the mass flow is fixed in this problem (fixed Reynolds number) the reduction in available area (relative to a periodic arrangement of particles) resulting from introduction of the wall causes the flow velocity to increase in the gap between the sphere and the wall. In this figure, it is observed that the pressure and velocity gradient in the normal direction on the particle surface for $H/D = 2$ is larger than the one for $H/D = 4$. The effect of the duct wall on the particle will vanish for $H/D \to \infty$ as Fig. 7.10 shows that the normalized drag force tends to be the value for the drag force of a sphere in a unbounded flow.

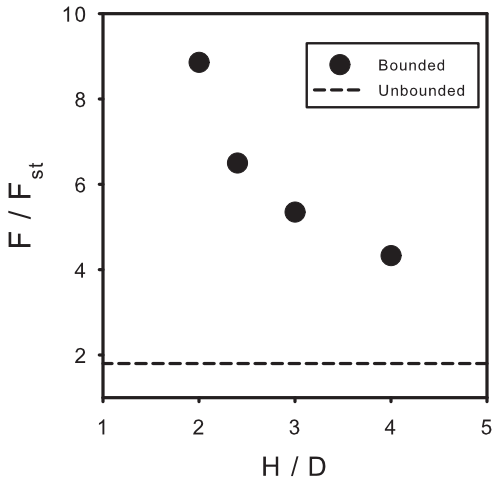

Figure 7.10: Variation of the normalized drag force of a sphere with the ratio H/D at $\mathrm{Re_m} = 20$ and $D_m = 25$ and comparison with the experimental data denoted by dashline from Schlichting (1968) for unbounded flow. The symbols represent the FFD PR-DNS results for the case of flow past a sphere in a square duct.

7.5.3 Heat transfer in dense gas–solid flow within a duct

The main objective to develop FFD PR-DNS approach is to account for wall effect on particle beds that are widely used in industrial applications. In Ch. 2-4, the flow past a fixed particle assembly with heat transfer in the gas–solid flow has been simulated in the thermal fully–developed region using PS PR-DNS. However, in a real fixed bed reactor, there exists the entrance length before the fluid flow transits from developing region into the fully-developed

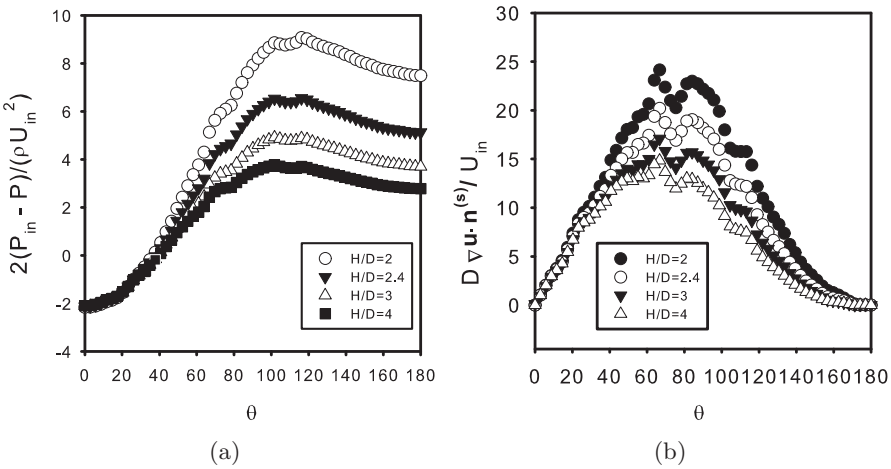

Figure 7.11: (a) The relative pressure and (b) velocity gradient in the normal direction on the sphere surface along the polar angle θ ($0 \leq \theta \leq \pi$) in the $x-y$ plane corresponding to the cases in Fig. 7.8. U_{in} is the inlet velocity and P_{in} is the inlet pressure.

region. In addition, the walls of the reactors also affect the flow with heat transfer. In order to extend the simulations to account for wall effect on particles, we need to go beyond a single particle in a duct and simulate heat transfer in gas–solid flow in a square duct. Before simulating larger domains, a test case of flow past a particle assembly with $L/D = 5$ is simulated in order to obtain some insight regarding the effect of the duct wall on multiple particles. The setup for flow past a particle assembly in a square duct is shown in Fig. 7.12. Differences between this setup and the periodic domain setup used in earlier PS PR-DNS of homogeneous gas–solid flow are worth noting (see details in Ch. 2). In the PS PR-DNS simulation, flow past a homogeneous particle assembly is simulated using periodic boundary conditions in all three directions, whereas in FFD PR-DNS simulation a homogeneous particle assembly ($L/D = 5$ in three directions) is placed in the middle of a square duct. Steady flow in the duct past the particle assembly is simulated using inflow/outflow boundary conditions in the streamwise direction $x_{\|}$ and wall boundary conditions in the y and z directions. In addition, a buffer zone ($B/D = 2$) is needed to obtain the correct inlet velocity distribution, and an extended simulation domain ($T1/D = 1$) at the inlet ensures that all the particles are contained inside the square duct. An extended simulation domain at the outlet ($T2/D = 4$) avoids the reflective

boundary effects at the outlet of the duct. The use of a gap between the duct and the fixed bed of particles ($S/D = 1$) avoids unnecessarily high resolution requirements arising from the need to resolve the distance between the walls and the particles.

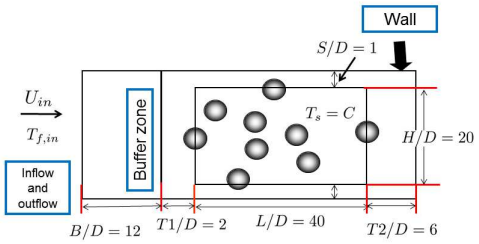

Figure 7.12: Sketch of flow past a homogenous particle assembly with heat transfer in a square duct. D is the diameter of the sphere, H is the width of the square duct, L is the length of the square duct, S is the distance between wall and the boundary of particle bed, B is the length of the buffer zone, $T1$ and $T2$ is an extra length.

In the homogeneous particle assembly region ($L/D = 5$), the solid volume fraction is set to 0.2 (calculated from $N\pi D^3/6L^3$, where N is the number of particles in this region). Uniform velocity U_{in} and temperature $T_{f,in}$ are specified at the inlet to the computational domain. The isothermal boundary condition is imposed at the surfaces of all particles. The initial fluid temperature is higher than the particle temperature. Based on the convergence test results presented in Sec. 7.5.2, we use a grid resolution of $D_m = 25$ for particles at $\mathrm{Re_p} = 50$ since the grid resolution required for this case at low Reynolds number is less than that for a higher Reynolds number.

Figure 7.13(a) shows contours of the fluid velocity field in a plane passing through the center of the square duct at $y/D = 3.5$. It can be seen that the presence of the particle assembly reduces the magnitude of the fluid velocity but the fluid accelerates in the gap between the wall and particles. This phenomena is also observed in a fluidized bed, where the fluid velocity profile is relatively flat in the middle of the bed but is higher near the walls. Figure 7.13(b) shows contours of the non–dimensional fluid temperature field in the same plane. The hot fluid

is cooled down by particles and walls. However, the particles are more effective at transferring heat from the fluid than the wall because of the greater surface area for heat transfer per axial length of the duct.

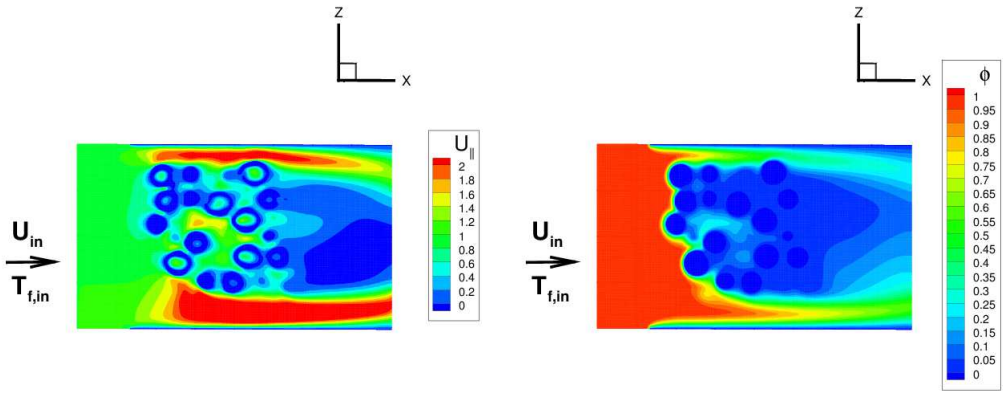

(a) (b)

Figure 7.13: Contour plot of (a) instantaneous axial velocity and (b) non–dimensional fluid temperature field in a plane passing through the center of the square duct ($y/D = 3.5$) for the setup.

Figure 7.14 shows the variation of the bulk fluid velocity with axial location

$$U_m\left(x_{\|}\right) = \frac{1}{A_f}\int_{A_f} U dA, \tag{7.25}$$

and non–dimensional bulk fluid temperature with axial location

$$\phi_m\left(x_{\|}\right) = \frac{\int_{A_f} \phi U dA}{\int_{A_f} U dA}. \tag{7.26}$$

The bulk fluid velocity rapidly increases due to the sudden reduction of the fluid area. The fluctuation of bulk velocity in the bed region mainly results from the small cross-sectional area. With large cross-sectional area, we expect to see a relatively constant value for the bulk fluid velocity in the bed region. Fig. 7.14(b) shows that the non–dimensional bulk fluid temperature decays in both the bed region and in the particle-free region ($x_{\|}/D > 6$). However, the rate of decay in the bed is faster than in the region free of particles. This implies that heat transfer in the bed region is of primary importance. This test case can be considered as a snapshot

of instantaneous flow in a riser and gives insight about the effect of fixed particle assembly on heat transfer in a square duct. Further analysis about this case will be given in the final thesis.

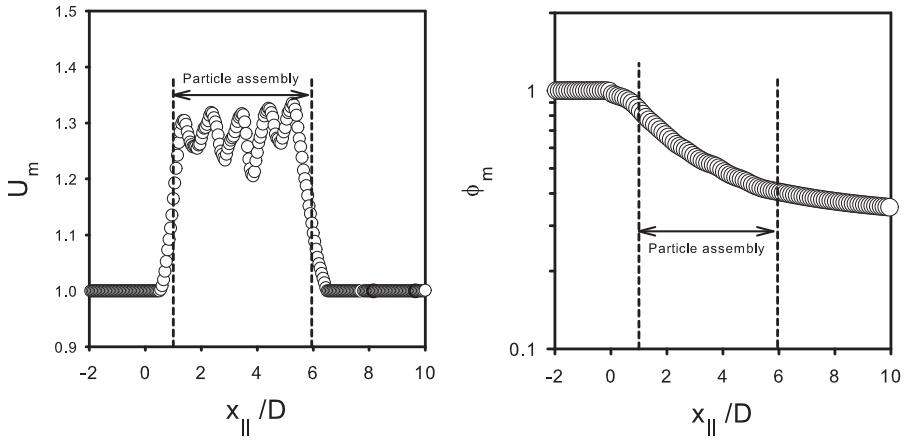

(a) (b)

Figure 7.14: Variation of (a) the bulk fluid velocity U_m and (b) the non–dimensional bulk fluid temperature ϕ_m along the axial location $x_{\|}/D$. The fixed particle assembly is located between the two dash lines. The circles represent the value of bulk fluid velocity and bulk fluid temperature in the two plots.

7.6 Conclusion

A fully finite-difference (FFD) PR-DNS approach was developed based on PUReIBM to account for walls and various boundary conditions. The hydrodynamic and scalar solvers of FFD PR-DNS were parallelized and validated by a suite of test cases including fully developed duct flow, flow past a simple cubic (SC) particle arrangement, flow past a sphere in open field, and developing duct flow with and without a single particle using inflow and outflow boundary conditions. The FFD PR-DNS data obtained from these test cases had a good agreement with analytical solutions, and existing numerical and experimental data. A flow past a fixed particle assembly in a square duct with heat transfer was also simulated. It showed that the effect of entrance length on the velocity and temperature field disappeared fast. Using FFD PR-DNS, the effect of walls on particles can be quantified and modeled in the future work.

CHAPTER 8. DETAILED EXPERIMENTAL AND NUMERICAL INVESTIGATIONS OF VELOCITY FIELD IN A SQUARE DUCT

This chapter is a manuscript titled "Detailed three-dimensional experimental and numerical investigations of hydrodynamic interactions between flow and particles in a square duct" that is under preparation. In this manuscript, my contribution is the development of the numerical approach and performing the simulations to compare with experimental data. The experimental data are provided by Mahdi Ramezani and Michael G. Olsen of Iowa State University.

The purpose of this chapter is to validate the PR-DNS approach by a detailed comparison with experimental data. The PR-DNS approach is used to simulate the flow around spheres in the test section of the experiments of flow through a square duct. The high-resolution particle image velocimetry (PIV) measurement and high-fidelity PR-DNS approach are developed first. Detailed comparisons of the velocity field between experiments and simulations are performed for the cases of pure laminar duct flow, flow past a fixed sphere in a duct, and flow past a train of five spheres inside a duct. All comparisons of the velocity fields between the simulations and experiments show a good agreement. In addition, the effect of the interparticle distance in a train of spheres on the wake behind spheres and the wall boundary layer is discussed. The direct comparisons not only validate both experimental measurement and numerical approach but also establish a standard dataset for by other researchers.

8.1 Introduction

Fundamental understanding of hydrodynamic interactions in gas/liquid-solid flow is important to design industrial reactors such as porous medium or fixed bed reactors. For instance, in these types of reactors, velocity fluctuations in gas/liquid phase are generated due to the

presence of the solid phase. The level of velocity fluctuations affects the quantification of the parameters such as hydrodynamic dispersion (Koch and Brady (1985)) that relies on fluid velocity fluctuations at the microscopic structure. Although theoretical analysis such as boundary layer analysis (Schlichting and Gersten (2003)) can provide some detailed information of hydrodynamic interactions, the limitations of theoretical analysis such as assuming low speed flow or dilute flow are obstacles to providing the detailed information on high-speed dense flow.

As a complement to theoretical analysis, experimental measurements are widely used to provide the detailed information of hydrodynamic interactions. In the early experimental techniques (Wakao and Kaguei (1982); Delgado (2006)) such as frequency response or a pulse input, the measurements of the flow are intrusive. Furthermore, the point-wise measurements cannot quantify velocity fluctuations accurately due to the disturbance from the intrusive flow measurement probes. Recently, nonintrusive planar measurements such as particle image velocimetry (PIV) (Adrian (1991, 2005)) have been developed. Such planar measurements with laser-based techniques have provided accurate, detailed, quantitative measurement of velocity field in gas/liquid-solid flow such as flow past a single sphere. The accuracy of PIV measurements can be improved by increasing the spatial resolution at the cost of reducing the field-of-view (Adrian (2005)).

However, PIV measurements are difficult to deploy in dense gas/liquid-solid flow due to limited optical access. In order to overcome the difficulty in experimental measurements of velocity field in dense gas-solid flow, numerical approaches have been developed to predict flow field. Before using numerical approaches to perform further analysis, a numerical approach has to be validated by experimental data. A standard validation for all numerical approaches is to compare experimental data on flow past a particle in a open field at different Reynolds numbers (Clift et al. (1978)). Beyond the standard test, Johnson and Patel (1999) used dye injection experiments to validate their numerical results of the structure of a wake behind an isolated sphere at high Reynolds number up to 300. Ten Cate et al. (2002) studied a single sphere settling under gravity using PIV measurement to validate the results obtained from lattice-Boltzmann method. They captured the full transient behavior of both the sphere motion and the fluid motion. Tang et al. (2016) performed a pseudo-2D fluidized bed simulation and

compared statistics of axial solids flux between PR-DNS data with PIV experimental data.

In this work, a detailed quantitative comparison between experiments and numerical simulations on flow past the fixed spheres in a square duct is performed. The numerical setup mimics the complete test section of the duct flow experiment. Earlier experimental studies on fixed multiple particles systems have been reported, such as using two spheres (Tsuji et al. (1982); Zhu et al. (1994); Liang et al. (1996); Chen and Wu (2000)), three spheres (Liang et al. (1996); Ozgoren (2013); Pinar et al. (2013)) or more than four spheres (Liang et al. (1996)). Numerical simulations have also been performed for two spheres (Folkersma et al. (2000); Tsuji et al. (2003); Prahl et al. (2007); Yoon and Yang (2007, 2009)) in uniform upstream uniform velocity in a open field. Compared to these existing works, we not only simulate the developing flow around spheres but also account for the effect of the duct wall and inflow/outflow conditions using both approaches.

Once a numerical approach is valid, the approach can be used to extract more detailed information on velocity fluctuations that results from the presence of the spheres even in a laminar flow (Mehrabadi et al. (2015)). The experimental measurement is hard to capture the detailed velocity fluctuations around spheres. The intensity of the velocity fluctuations can be affected by the structure of the wake behind the spheres. The studies of the structure of the wake behind two sphere have been reported by numerical simulations (Tsuji et al. (2003); Prahl et al. (2007); Yoon and Yang (2007, 2009)). They found that the different types of the structure of the wake relies on the interparticle distance that affects the the velocity fluctuations.

The rest of the paper is organized as follows. In Section 8.2, the experimental setup for flow past spheres in a square duct is briefly described. In Section 8.3, the detailed comparisons of velocity fields between experiments and numerical simulations are performed by the cases of an internal flow in a square duct, steady flow past a fixed sphere and a train of five spheres in a square duct. In the case of flow past a train of five spheres, a discussion on the effect of the interparticle distance on the structure of the wake behind spheres and the wall boundary layer growth is also given. Finally, the principal findings of this work are summarized in Section 8.4.

8.2 Experimental setup

In order to validate PR-DNS data by experimental data, the cases of an internal flow in a square duct, steady flow past a sphere and a train of five spheres in a square duct are considered in both experiments and simulations. Since the PR-DNS approach has been developed in Chapter 7, only the experimental approach and setup are briefly given in this chapter for completeness. The details on the experimental method, apparatus, and results are provided by Ramezani and Professor Olsen of Iowa State University.

The experimental apparatus used in this study is shown in Fig. 8.1. The test section consists of a square cross section water tunnel with $H_{exp} = 149$mm width and $L_{exp} = 610$mm length made of clear acrylic. A stationary arrangement of fused silica spheres with the diameter of $D = 15$mm are placed inside the duct that are held by means of a 2mm sting attached to the back wall of the section. This wall of the section is removable and allows for varying the arrangement of the spheres from one experiment to the other.

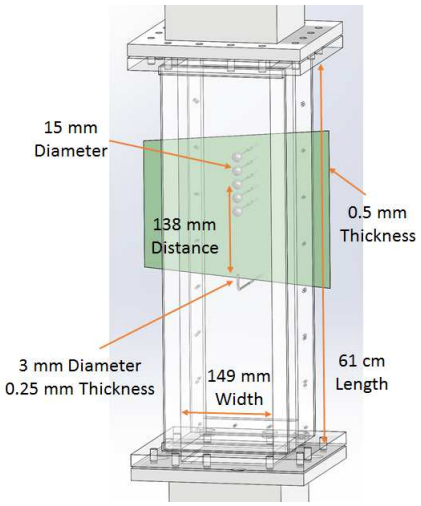

Figure 8.1: Schematic of the test section setup in the experiment. The green sheet represents the position of laser sheet. The case of five sphere arrangement in the apparatus is shown here. All the parameters are marked in the figure. The numerical setup is the same as this experimental setup.

A PIV system from LaVision® Co. is used to measure velocity fields, which incorporates a NewWave Research® Gemini double pulsed Nd-YAG laser illuminating the middle plane of the test section, three double frame FlowMaster 3s cameras recording images of the corresponding

flow field, and the DaVis 7.2 software acquisition and processing data fields. Macro lenses with 50 mm focal length set at an aperture of 5.6 f# were mounted on cameras that gives a sufficient depth of field for the measurements. Simple linear optics are used for maintaining a laser sheet thickness of 1 mm throughout the width of the channel and special care was taken in order to make sure that the plane of laser slices the center plane of the glass spheres. Calibration of the cameras using a pinhole model (Tsai (1987)) is usually considered accurate when the cameras are at a normal angle to the walls of the test section. But since the current setup is considered a 3 media environment, calibration was done using a 3rd order polynomial function (Soloff et al. (1997)) in order to make it possible for accurately matching the images from all the cameras.

The condition of flow at the inlet of the duct plays an important role in the measurements. A digital inverter system controlling the centrifugal pump using an active feedback of an ultrasonic flow meter delivers the desired constant flow rate to the system. In order to attain a uniform inlet flow to the test section, several layers of perforated stainless steel sheets with varying arrangements are installed in the upstream flow conditioner that provides a uniform flow of deionized water into the test section. PIV data of the flow in the duct shows the variation of velocity in the profile to be less than 10 percent across the width and turbulence intensity of flow to be less than 1% for the range of Reynolds number from 500 to 20000 based on the width of the test section (from 50 to 2000 based on the diameter of the spheres).

8.3 Comparison of velocity fields

In order to minimize all possible factors that could result in any difference between numerical and experimental data, the numerical setup is the same as the experimental setup. In the numerical setup, the length from the entrance of the duct to the outlet of the duct is $L/D = 51$ and the width of the duct is $H/D = 10$. Note that in order to avoid the effect of the outlet boundary condition on spheres, the length of the duct in the numerical setup is longer than that in the experimental setup ($L_{exp}/D = 41$). In addition, an extended upstream zone is needed in the numerical setup to capture the correct wall boundary layer growth before the flow enters the square duct is $Z/D = 10$. The validity of using the extended zone in the numerical approach

is given in Section 7.4.4 of the Chapter 7. In the following sections, three cases including a laminar duct flow, steady flow around a single sphere in the duct, and steady flow past a train of five spheres in the duct are compared using numerical and experimental approaches.

8.3.1 Pure laminar duct flow

We first would like to guarantee that the boundary conditions in the numerical approach are the same as the experimental conditions for the case of a laminar duct flow. Our results are compared with the existing experimental results of Goldstein and Kreid (1967) for verification of the experimental facility and numerical approach. Direct comparisons are made in a laminar duct flow by running different experimental and numerical cases at various Reynolds numbers, where the Reynolds number is based on the width of the square duct. Two numerical simulations and experimental tests are presented in Fig. 8.2(a) showing the non-dimensional centreline velocity versus the non-dimensional axial location $x/H\mathrm{Re}_\mathrm{H}$ in the duct. The numerical results at the Reynolds number $\mathrm{Re}_\mathrm{H} = 20$ shows a good agreement with results of Goldstein and Kreid (1967) in the developing and developed regions. The reason to choose the cases at the Reynolds number $\mathrm{Re}_\mathrm{H} = 850$ is to guarantee the same velocity field in both approaches before the case of flow past a sphere is performed at this same Reynolds number. Both the numerical and experimental results match the experimental results of Goldstein and Kreid (1967) very well for the different Reynolds number cases. Note that the experimental facility used here is relatively short in non-dimensional units ($x/H\mathrm{Re}_\mathrm{H}$). The experiments were intentionally designed to be in this flow regime in order to see the interaction of a flat velocity profile rather than a parabolic velocity profile with spherical particles. It is also worth noting that the full length of the experimental setup is in the developing region and covers a relatively short region by design in order to enable a study of the interaction of an almost flat velocity profile with spherical particles.

We also compare the axial velocity profile at $x/H\mathrm{Re}_\mathrm{H} = 0.0023$ from both the numerical and experimental data in Fig. 8.2(b) to check if there is any discrepancy, since a sphere will be installed at this position ($x/H\mathrm{Re}_\mathrm{H} = 0.0023$) in the next test case. Fig. 8.2(b) shows that the axial velocity profile at $x/H\mathrm{Re}_\mathrm{H} = 0.0023$ obtained from PR-DNS falls within the error of

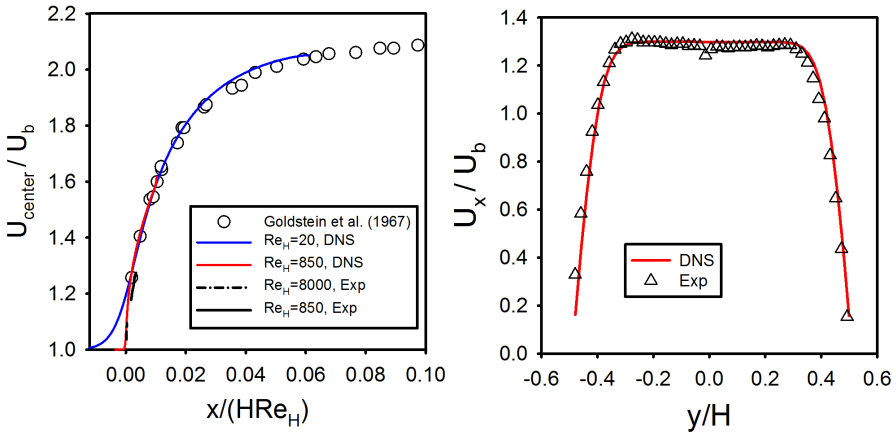

(a) (b)

Figure 8.2: A laminar developing flow comparisons in a duct. (a) Comparison of the centerline velocity U_{center} between the experimental and numerical data. The circles represent the experimental data of Goldstein and Kreid (1967). The blue and red solid lines represent the numerical results obtained from the PR-DNS approach. The other lines represent the present experimental results obtained from PIV measurement. The Reynolds number $\mathrm{Re_H}$ is based on the width or height of the duct and the inlet uniform velocity. (b) Comparison of the axial velocity profile U_x/U_b at $x/H\mathrm{Re_H} = 0.0023$ between the numerical results (the red line) and the present experimental data (the symbols). The bulk fluid velocity is defined as $U_b(x) = \int_{A_f} U_x dA/A_f$, A_f is the fluid cross-sectional area.

the experimental data and is almost same as the time-averaged axial velocity obtained from the experiments. This implies that the wall boundary layer growth in the experiment is the same as the prediction from the numerical approach. The comparison of axial velocity profiles is taken to be an indication that the boundary conditions imposed in our PR-DNS approach, such as inflow/outflow boundary condition is the same as those in the experiments. Therefore, in the next test case, we add spheres into the duct flow for comparison of the velocity fields using both approaches.

8.3.2 A single sphere

In order to validate the capability of the PR-DNS approach to capture the flow field around a sphere accurately, we compare the velocity field obtained from experiments with the PR-DNS data for the case of steady flow past a single sphere in a square duct. The center of the

sphere is located at $x_p/D = 27.2$ in the experiment. The same setup is used in the PR-DNS configuration for the sphere. Note that for convenience, we set the center of the sphere at the origin in the following figures.

Figure 8.3 shows contours of the axial velocity U_x (top panel) and the cross-stream velocity U_y (bottom panel) from PR-DNS and the contour lines from experimental measurements in the square duct at $\mathrm{Re_D} = 85$ (the Reynolds number is based on the diameter of the sphere D). Here the experimental field of view is very small and is focused on the area around the sphere in order to provide a higher resolution for velocity vectors around the sphere and to avoid any complication with resolving the near zero velocity in the vortex region downstream the sphere due to the dynamic range of PIV. In the top panel of Fig. 8.3, the length of the wake behind the particle obtained from PR-DNS data is almost same as that obtained from experimental measurement. The solid lines representing the experimental data match very well with the color contour levels representing the PR-DNS data. In the bottom panel, there are a few differences in the cross-stream velocity between the PR-DNS data and experimental data that results from the challenge of experimental measurement of small magnitudes of the cross-stream velocity. The length of the wake L_w in the simulation shows $L_w/D = 1.20$ and the experiment shows $L_w/D = 1.25$ even though the width of the wake is not affected. The length of the wake for a sphere in a free flow is expected to be $L_w/D = 0.9$ (Taneda (1956)) and our case shows a longer wake due to the containment inside the duct.

Other comparisons can be extracted from the field data of Fig. 8.3 that provide an easier verification of the results. Figure 8.4 shows the comparison of the streamwise variation of the axial velocity along the centreline of the duct. The streamwise variation of the axial velocity from PR-DNS matches very well with experimental data at location upstream of the sphere. There exists the slight difference of velocities between PR-DNS and experiment downstream of the sphere. This difference results from the change of the momentum of the fluid in the experiment due to the sting attached to the sphere. After four particle diameters, the velocity from PR-DNS again overlaps the experimental data. It implies that the disturbance of the sting disappears.

We also compare cross-sectional profile of the axial velocity between PR-DNS and experi-

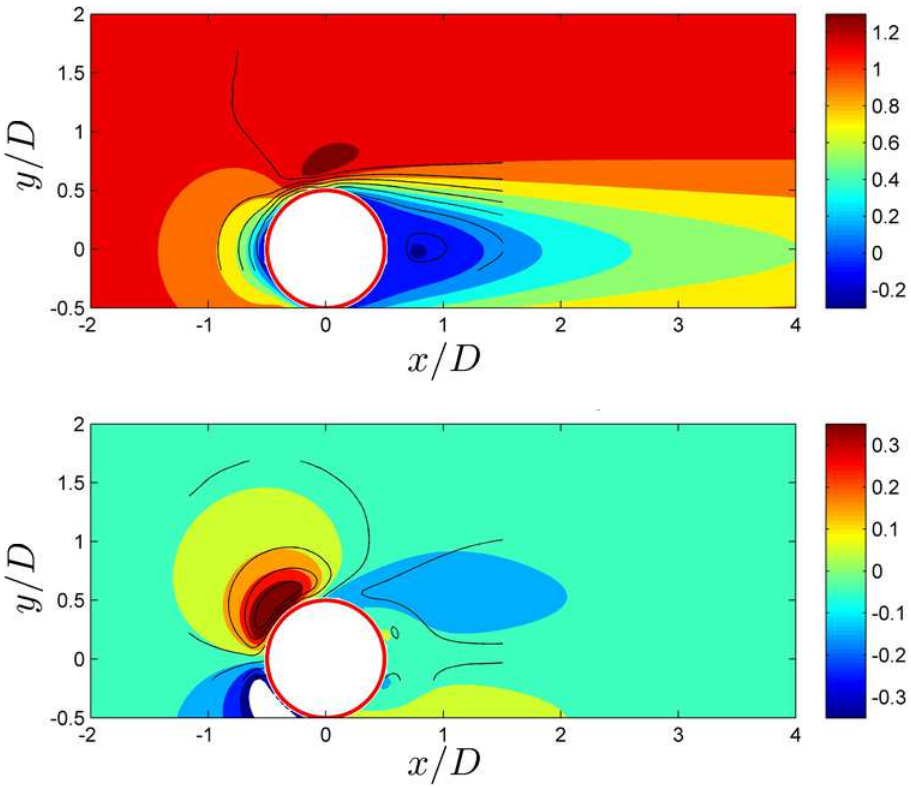

Figure 8.3: Contour of the axial velocity (top) and cross-stream velocity (bottom) obtained from PR-DNS data (color contours) and experimental measurement (contour lines) at $\mathrm{Re_D} = 85$ in a square duct with the height $H/D = 10$ and the position of the sphere at $x_p/D = 27.2$.

mental data in the cross-sectional lines as shown in Fig. 8.5. Four locations in Fig. 8.5(b) that are close to the sphere are chosen to check if the details of velocity field around the sphere can be captured. For the four different locations, we observe that the cross-sectional profile of the axial velocity profile obtained from PR-DNS data fall within the error of the experimental data. The comparisons from different locations indicate that PR-DNS data is validated by the experimental data and can capture details around the sphere accurately.

8.3.3 Five spheres

After validating the PR-DNS data by experimental data for the single sphere case, we compare the velocity fields obtained from experiments and PR-DNS data for two cases of a train of five spheres in a square duct. In the experimental setup, the five sphere are aligned

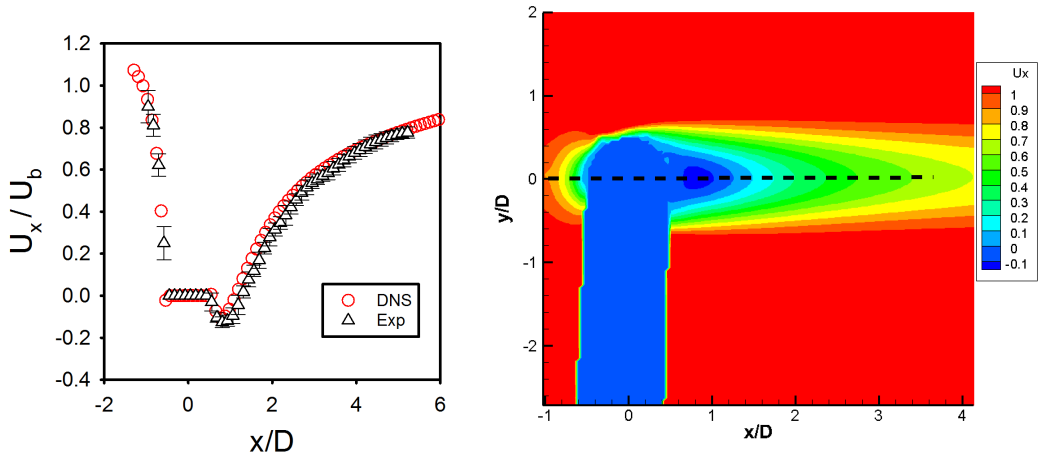

(a) (b)

Figure 8.4: (a) Comparison of the streamwise variation of the axial velocity between the PR-DNS and experimental data along the centreline of the square duct at $\mathrm{Re_D} = 85$ for the position of the sphere $x_p/D = 27.2$. The red circles represent the PR-DNS data and the black triangles present the experimental data along the centreline shown in (b). The error bars represent the standard deviation obtained by time-averaging from experiments. (b) The contour of the axial velocity from experimental data indicates the position of the extracted data ($y/D = 0$).

along the centerline of the duct and the center of the middle of five spheres is located at $x_p/D = 29.6$. The interparticle distance L_s between the center of two neighbor spheres is equal and is $L_s/D = 1.38$ for the first case in Fig. 8.6 and $L_s/D = 2.19$ for the second case in Fig. 8.7. All the experimental data collection for these cases with five spheres are performed at the Reynolds number $\mathrm{Re_D} = 100$, which corresponds to $\mathrm{Re_H} = 1000$ based on the width of the square duct. The flow inside the duct is in the developing region in order to have a flat velocity profile interact with the train of spheres. The reason to choose the two cases with different interparticle distances is to study the effect of the interparticle distance on the wake behind the spheres.

Comparisons of the results between simulations and experiments are first shown as overlaid contours of axial and cross-stream components of velocity. Figs. 8.6 and 8.7 show the contour plots of numerical results in color and the experimental results as lines both showing similar levels. This is a very detailed comparison and even though the uncertainty bands cannot be shown. It is clear that the results from simulation and experiment agree with each other. Note

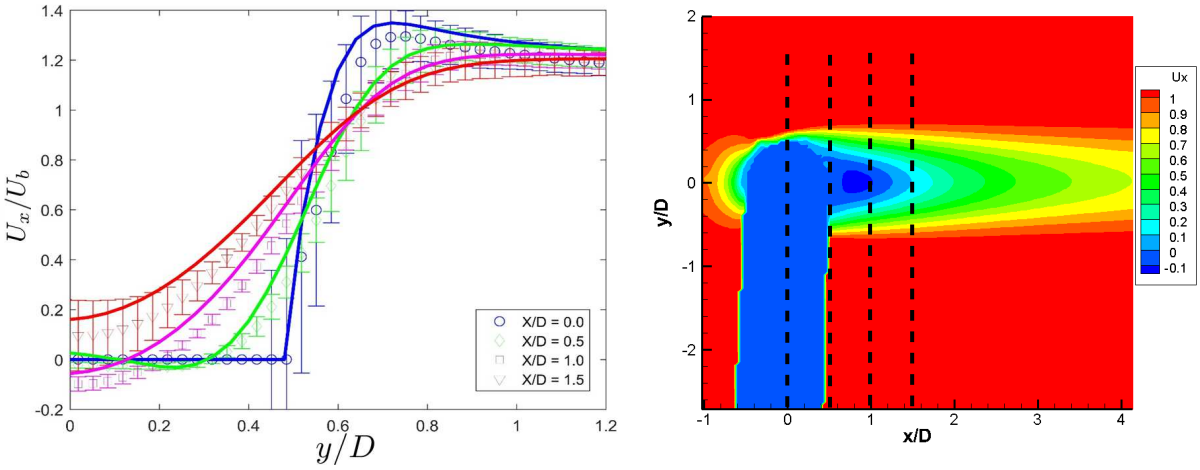

(a) (b)

Figure 8.5: (a) Comparison of the cross-sectional profile of the axial velocity between PR-DNS and experimental data along the cross-sectional lines (shown in (b)) of the square duct at $\mathrm{Re_D} = 85$ for the position of the sphere $x_p/D = 27.2$. The lines represent the PR-DNS data and the symbols present the experimental data. The error bars are obtained by time-averaging from experiments. (b) Contours of the cross-sectional profile of the axial velocity from experimental data. The dashed lines represent the positions of the extracted data ($x/D = 0$, 0.5, 1, and 1.5) corresponding to the profiles in (a).

that the contour levels of the experimental and numerical approaches correspond very closely in the regions close to the train of spheres. However, some discrepancies are seen in the area between the spheres and wall, and also in the wall boundary layer where the experiments show a higher velocity than the simulations. This implies that only using an integrated quantity such as drag force on the sphere as a verification can prove to not be reliable for numerical validation.

In the top panels of Figs. 8.6 and 8.7, the length wakes behind the last sphere are almost the same for two different interparticle distances. This can be confirmed by the axial velocity profile along the centreline of the spheres train in Fig. 8.8. The rate of the increase of the axial velocity after the last sphere (downstream of the train) for $L_s/D = 2.19$ (see Fig. 8.8(b)) is almost the same as that for for $L_s/D = 1.38$ (see Fig. 8.8(a)). The details on axial velocity profile along cross-stream lines downstream the train of five spheres in Fig. 8.9 shows that the axial velocities in the downstream at $x/D = 3.3$, 4.3 and 5.8 for $L_s/D = 1.38$ have almost the

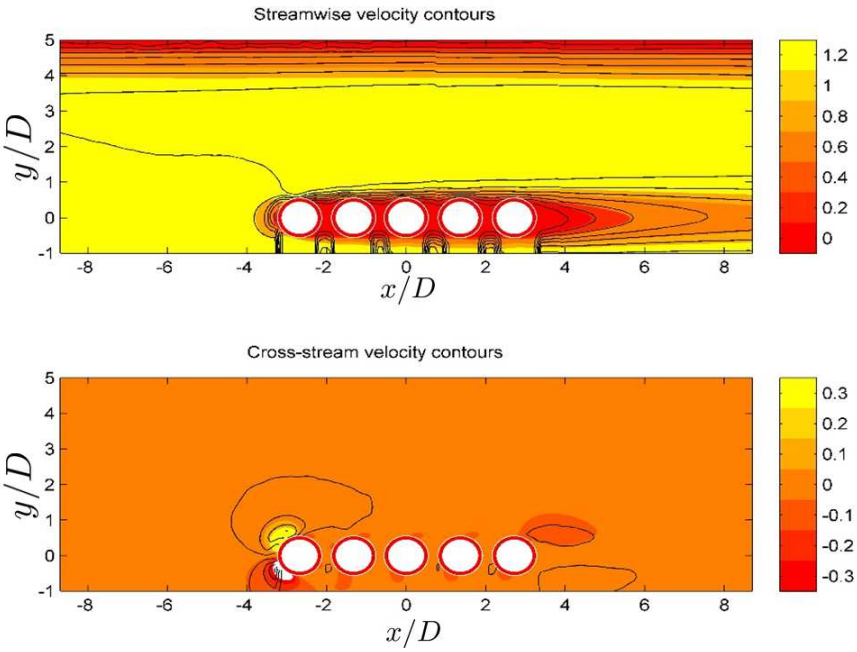

Figure 8.6: Contour of the axial velocity (top) and cross-stream velocity (bottom) obtained from PR-DNS data (color contours) and experimental measurement (contour lines) at $\mathrm{Re_D} = 100$ in a square duct with the height $H/D = 10$ and the interparticle distance $L_s/D = 1.38$.

same growth as those at $x/D = 4.9$, 5.9 and 7.4 for $L_s/D = 1.38$ within one diameter of sphere, respectively. Note that for $L_s/D = 1.38$ the edge of the last sphere is located at $x/D = 3.3$ (see Fig. 8.6) while for $L_s/D = 2.19$ the edge of the last sphere is located at $x/D = 4.9$. The locations correspond to 1, 3, and 6 sphere diameters downstream the last sphere in the train arrangement. For $y/D > 1.5$, the axial velocity in the downstream returns to the mainstream velocity as shown in Fig. 8.9 for the two cases. The flow downstream of the spheres seems to be balancing very similarly irrespective of the configuration of the particle train.

However, for the larger interparticle distance case ($L_s/D = 2.19$), there exists a small wake between spheres as shown in the top panel of Fig. 8.7. The existence of small wakes can also be seen in Fig. 8.8(b). It is seen that the negative velocity between the spheres is higher for the first two sphere and the intensity reduces with moving to the more downstream spheres. However, for the small interparticle distance ($L_g/D = 1.38$), the train of five spheres is similar to a single long particle since the velocity between two neighbor spheres is close to zero as shown in Fig. 8.8(a). The effect of interparticle distance on the wake in the two cases is similar

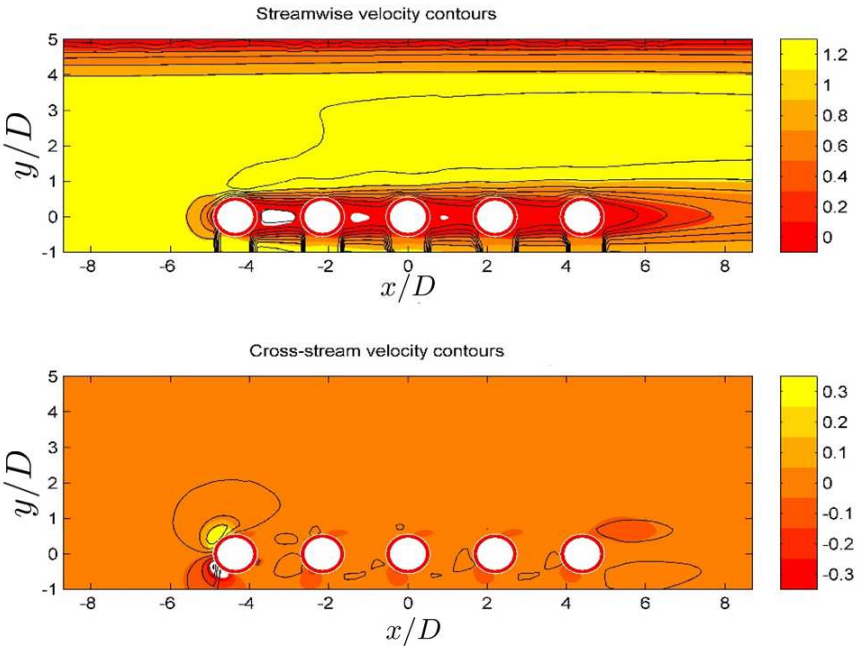

Figure 8.7: Contour of the axial velocity (top) and cross-stream velocity (bottom) obtained from PR-DNS data (color contours) and experimental measurement (contour lines) at $\mathrm{Re_D} = 100$ in a square duct with the height $H/D = 10$ and the interparticle distance $L_s/D = 2.19$.

to the observation and wake analysis in a fixed bed of particles in Chapter 4. In dense flow, small interparticle distance between particles in a fixed bed of particles results in a small wake length behind each particle (see the discussion on the conditionally ensemble-averaged velocity field in Chapter 4). We can only observe the near-wake behind particles in dense flow.

We also investigate the effect of spheres on the duct wall boundary layer using the detailed comparisons. Fig. 8.8 shows that the arrangement of the sphere affects the wall boundary layer growth. For the case of $L_s/D = 1.38$, the velocity at the location ($y/D = 4$) close to the duct wall slowly decreases along the axial location x/D in Fig. 8.8(a) whereas for the case of $L_s/D = 2.19$ the axial velocity at $y/D = 4$ slowly increases, then decreases beyond the last sphere of the train in Fig. 8.8(b). Recall that for a pure laminar duct flow, the axial velocity at such location of $y/D = 4$ decreases along the axial location during the wall boundary layer growth before the flow becomes fully developed. This implies that the larger interparticle distance arrangement slows down the growth of the wall boundary layer within the length of the train of spheres. This effect of the train of spheres on the wall boundary layer can be also

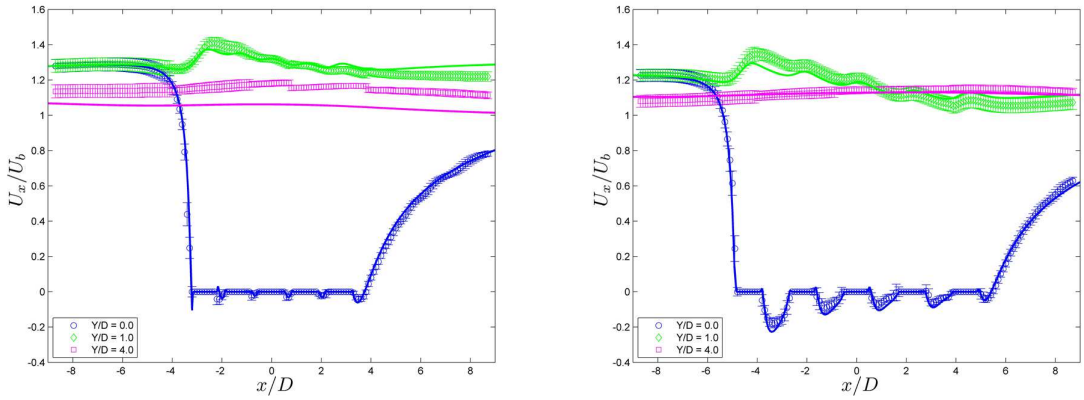

Figure 8.8: Comparison of the axial velocity profile between PR-DNS and experimental data along the centerline ($y/D = 0$) of the square duct, the line close to the train of spheres ($y/D = 1$), and the line inside the wall boundary layer ($y/D = 4$) at $\mathrm{Re_D} = 100$ for the interparticle distance (a) $L_s/D = 1.38$ and (b) $L_s/D = 2.19$. The lines represent the PR-DNS data and the symbols present the experimental data. The error bars are obtained by time-averaging from experiments.

observed at $y/D = 4$ in Fig. 8.9(a) and 8.9(b), although the values of the axial velocity almost overlap each other at different axial locations for the two cases.

Comparison of the cross-stream component of velocity can be more difficult due to the cross-stream velocity components being approximately one order of magnitude smaller than the streamwise velocity component in most of the field. The difficulty is merely due to the inherent limitation of the PIV method for capturing a wide range of velocity vectors, which is limited by the dynamic range of this method (Goldstein and Kreid (1967)). Errors in PIV measurements are minimized by increasing the distance particles move between laser pulses, since this reduces the effect of sub-pixel displacement interpolation errors on the measured velocity. When cross-stream velocities are small relative to streamwise velocities, the measured cross-stream velocities will be more dependent on sub-pixel interpolation and have greater potential measurement error. Moreover, near zero velocity measurements suffer more from any small misalignment in either the laser sheet or the cameras. Despite these potential limitations, comparisons in cross-stream velocity here shown in Fig. 8.10 have an outstanding agreement between simulations and experiments with less than 2% average difference in the results.

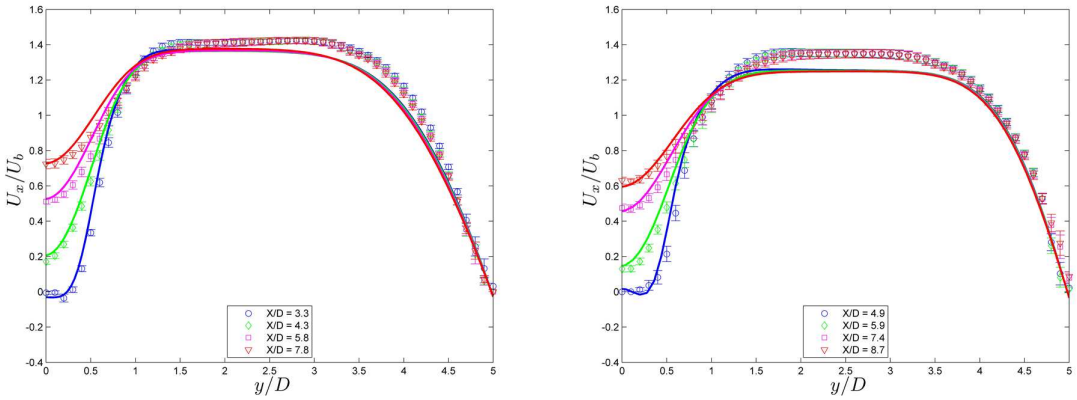

(a)

Figure 8.9: Comparison of the axial velocity profile between PR-DNS and experimental data along different cross-stream lines in the downstream of the train of five spheres at $\mathrm{Re_D} = 100$ for the interparticle distance (a) $L_s/D = 1.38$ and (b) $L_s/D = 2.19$. The locations plotted here correspond to 1, 3, 6, and 10 sphere diameters downstream the last sphere in the train arrangement. The lines represent the PR-DNS data and the symbols present the experimental data. The error bars are obtained by time-averaging from experiments.

Fig. 8.10 shows a comparison of the cross-stream velocity component along axial profiles close to the wall (four sphere diameters from the train centreline) and close to the train of spheres (one sphere diameter from the train centreline). Other locations are not shown due to all values being virtually identical to the $y/D = 4.0$ results. It can be observed that the cross-stream velocity features are well captured by the numerical simulations. The peaks in these figures show that the flow is expelled away from the spheres and the first sphere shows a much higher intensity comparing to the rest of the spheres. In the area between the spheres, for the more packed case studied, there is virtually no entrainment of fluid and the corresponding valleys have positive velocities whereas for the less packed case, there is small negative velocities showing an entrainment of fluid between the particles. The biggest valley on the far right side of the figures corresponds to the vertical wake region downstream the train of particles where a major entrainment of flow occurs.

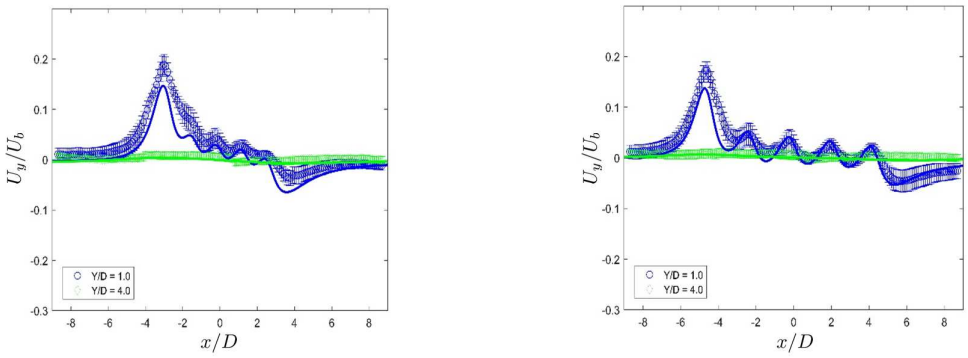

(a) (b)

Figure 8.10: Comparison of the cross-stream velocity between the PR-DNS and experimental data along the line close to the train of spheres ($y/D = 1$) and the line close to the duct wall ($y/D = 4$) at $\mathrm{Re_D} = 100$ for the interparticle distance (a) $L_s/D = 1.38$ and (b) $L_s/D = 2.19$. The lines represent the PR-DNS data and the symbols present the experimental data. The error bars are obtained by time-averaging from experiments.

8.4 Conclusion

In this work we directly compared experimental data with numerical data for a flow past spheres in a square duct in details. We first developed high-resolution PIV measurement and high-fidelity numerical approach. The validation of the PR-DNS approach is established by comparing the axial velocity in the cases of a pure laminar duct flow and flow past a single sphere in a duct. Detailed comparisons of the velocity field between experiments and simulations were performed using the flow inside a duct around a train of five spherical particles. Different interparticle arrangements of the train of five spheres were studied. Comparisons of velocity fields showed a good agreement between the simulations and experiments, especially in the areas closer to the train of particles and also for axial and cross-stream velocity field at different locations. We also found that number of spheres and spacing does not affect the wake length behind the train of spheres but had an effect on the wake between two neighbor spheres and the wall boundary layer growth.

Comparisons shown here verified that the PR-DNS approach is capable of accurately calculating flow for different arrangements of particles. It was also shown that some discrepancies

exist farther from the train of particles. Even though those areas are of less interest in multiphase fluid simulations, further investigations will be performed in order to find the reason for this discrepancy. Current experimental measurements showed only one center slice of the flow field assuming symmetry in the field, but more detailed investigations require a full cross section of the duct to be measured and compared for finding the cause of the differences. Using the PR-DNS approach and PLIF measurement, the comparison will be extended to heat transfer in water-solid flow in future work.

CHAPTER 9. TRANSIENT HEAT TRANSFER IN GAS-SOLID FLOW

This chapter is a part of the manuscript titled "Verification of the assumption of the isothermal particle in gas-solid heat transfer" that is under preparation.

Closure models for gas-solid heat transfer developed in Chapters 3 and 4 are based on the assumption that the particle temperature is constant and independent of time. This assumption may or may not validate in a real system such as biomass fast pyrolysis in which the particle temperature varies with time due to heating or cooling by the flow. In order to validate the range of the closure models presenting, we relax the assumptions of the isothermal particle by considering the variation of the particle temperature in time ($\mathrm{Bi} \ll 1$).

The only way to check the validity of the assumption is to perform simulations of the same identical case of fixed bed particles (used in Chapters 3 and 4) in which the temperature of particles allows to vary with time. However, the thermal fully-developed assumption used in Chapters 3 and 4 may not allow us to use the previous PR-DNS approach since the particle temperature is no more constant. Instead of imposing self-similarity boundary conditions that guarantee the thermal fully-developed flow, the inflow/outflow boundary condition in the streamwise direction has to be imposed. The purpose of this chapter is to extend current FFD code developed in Chapter 7 to account for the variation of the particle temperature in transient gas-solid heat transfer problem with the inflow/outflow boundary conditions. In this case, we do not have the thermal fully-developed assumption. Once the FFD PR-DNS has the capability to simulate transient heat transfer from a sphere, simulation of the transient heat transfer from a fixed bed of particles can be performed in future work.

In this chapter, the particle temperature of the sphere is assumed to be uniform but dependent of time in this transient heat transfer problem. In addition to solving the gas-phase energy equation, the particle temperature evolves by solving the solid-phase energy equation.

The effect of the particle-to-fluid thermal inertia ratio on the particle temperature and average Nusselt number is studied. The time variation of average Nusselt number at the flow and interphase heat transfer time scales is also investigated.

9.1 Introduction

Heat transfer between solid and gas phases plays an important role in many industrial applications such as chemical looping combustion or biomass fast pyrolysis. In order to understand the heat transfer process in an industrial device, computational fluid dynamics (CFD) simulations are widely used to perform device-scale simulations. Specifically, in the absence of mass transfer between phases the average fluid temperature equation in CFD simulations (Syamlal et al. (1993); Garg (2009)) reads as follows:

$$\underbrace{\frac{\partial}{\partial t}\left\{\rho_f \varepsilon_f c_{pf} \langle T^{(f)} \rangle\right\}}_{\text{unsteady term}} = \underbrace{\left\langle \frac{\partial I_f}{\partial x_j} q_j \right\rangle}_{\substack{\text{(1) average gas–solid} \\ \text{heat transfer}}} \underbrace{- \frac{\partial}{\partial x_j} \langle I_f q_j \rangle}_{\substack{\text{(2) average conduction} \\ \text{in the fluid phase}}}$$
$$\underbrace{+ \frac{\partial}{\partial x_j}\left\{\rho_f \varepsilon_f c_{pf} \langle u_j^{(f)} \rangle \langle T^{(f)} \rangle\right\}}_{\text{mean flow convection}} \underbrace{- \frac{\partial}{\partial x_j}\left\{\rho_f c_{pf} \langle I_f u_j''^{(f)} T''^{(f)} \rangle\right\}}_{\substack{\text{(3) transport of temperature-} \\ \text{velocity covariance}}} \underbrace{+ \rho_f \varepsilon_f \langle S_T(\phi_\alpha) \rangle}_{\substack{\text{(4) chemical reaction} \\ \text{source/sink term}}}, \tag{9.1}$$

and it contains the following unclosed terms: (1) average gas–solid heat transfer, (2) average conduction in the fluid phase, (3) transport of temperature-velocity covariance, and (4) chemical reaction source/sink term. In Eq. 3.1, ρ_f and c_{pf} are the density and specific heat of the fluid phase, respectively, $q_j = -k_f \partial T / \partial x_j$ is the heat flux vector, the composition ϕ_α represents the species mass fraction (Y_α) or enthalpy ($c_P T$), S_T is the chemical reaction source/sink term, and $\varepsilon_f = \langle I_f \rangle$ is the volume fraction of the fluid phase, where $I_f(\mathbf{x}, t)$ is the fluid-phase indicator function that is unity if the point $\mathbf{x}$ lies on the fluid-phase at time t, and zero otherwise. If $\psi(\mathbf{x}, t)$ is any field (velocity or temperature), then its phasic average $\langle \psi^{(f)} \rangle(\mathbf{x}, t)$ (average fluid velocity $\langle u_j^{(f)} \rangle$ and average fluid temperature $\langle T^{(f)} \rangle$) is its average value conditional on being

in the fluid phase, which is defined as:

$$\left\langle \psi^{(f)} \right\rangle (\mathbf{x}, t) = \frac{\langle I_f(\mathbf{x}, t)\psi(\mathbf{x}, t)\rangle}{\langle I_f(\mathbf{x}, t)\rangle}. \tag{9.2}$$

We use angle brackets to denote ensemble–averaging of random fields over all particle configurations, and an overbar to indicate spatial averages. Using the phasic average, the fluctuating components of the fluid velocity and temperature in Eq. 3.1 are defined as $u_j''^{(f)} = u_j - \langle u_j^{(f)} \rangle$ and $T''^{(f)} = T - \left\langle T^{(f)} \right\rangle$, where these fluctuations depend on spatial location and time, although for brevity this dependence is not explicitly shown. The average fluid velocity is obtained by solving the averaged momentum and mass conservation equations. In order to solve Eq. 3.1 for the average fluid temperature, closure models are needed for terms (1)–(4). In Chapters 3 and 4 the heat transfer closure models have been developed to model the unclosed terms (1)–(3). The term (4) has been also discussed in Chapter 6.

However, these closure models have been developed based on the assumption of the isothermal particles in fixed beds of particles which the particle temperature is constant and does not vary with time. This assumption of the isothermal particles results in steady-state average Nusselt number that is used in the closure model for average gas-solid heat transfer. Whether or not the steady-state Nusselt number can be still obtained in fixed bed of particles if the assumption does not hold needs to be studied. There are far-reaching implications of the validity of the assumption of the isothermal particle to the closure models since existing time-independent Nusselt number correlations such as the Nusselt number correlation of Gunn (1978) have been widely used in time-dependent CFD simulations (Xue et al. (2011, 2012); Papadikis et al. (2009b)).

One way to validate the assumption of the isothermal particles is to allow the particle temperature to vary in time. This time variation of the particle temperature is known as transient heat transfer in two phases. For instance, in biomass fast pyrolysis that requires moderately high heat to fully convert biomass to liquid at the most efficient rate, the biomass particle is usually heated up from room temperature to the high desired temperature in fixed or fluidized bed reactors. During this process, the time variation of particle temperature affects the reaction rate of species of the biomass particles. The change of the reaction rate can affect

interphase heat transfer between the solid and gas phases and results in the phase change. However, even before examining the dependence of the reaction rate on temperature, there exists an initial stage of fast pyrolysis that temperature variation is significant in time over that the particle temperature influences chemical reactions of biomass. Over that range, it is important to check if the average Nusselt number tends to be constant or not.

This initial stage of fast pyrolysis of biomass has been observed in Di Blasi et al. (2013)'s experiment which measured the time evolution of the temperature of beech wood particles in the fixed bed particles and weight loss of fixed bed particles as shown in Figure 9.1. This figure shows that for less than 100s, the temperature of fixed particles at different positions (from the center to the surface of the fixed bed) increases in time whereas there is no weigh loss of the biomass particles (represented by the dashed lines) during this time scale. This experimental data implies that for $t < 100$s the biomass particles have not been converted into gas or liquid. Based on the properties and flow conditions provided by Di Blasi et al. (2013), the estimated interphase heat transfer time scale ($O(10^{-4})$) is far less than the converting or volatilizing time scale ($O(10^{2})$) for the initial stage of fast pyrolysis of biomass particles in the fixed bed reactor. The transient heat transfer without chemical reactions can be checked in this region.

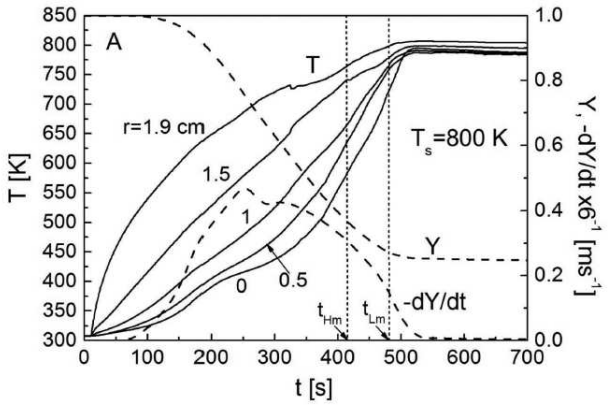

Figure 9.1: Copy of Di Blasi et al. (2013)'s figure about time history of particle temperature (solid lines) at several radial positions ($r = 0$, 0.5, 1, 1.5, 1.9 cm) and weight loss characteristics (dashed line) versus time for the packed bed at a heating temperature $800K$. The positions $r = 0$ and $r = 1.9$cm correspond to the center and the edge of the packed bed of particles.

A few studies of the simple problem of transient heat transfer from a spherical parti-

cle were performed. Michaelides and Feng (1994) and Feng et al. (1996) observed the history effect on the transient heat transfer from the sphere at small Péclet number, analogous to the Basset history force in the particle equation-of-motion. Balachandar and Ha (2001) and Feng and Michaelides (2000) have extended the transient analysis to the case of high Reynolds number and Péclet number, respectively. Both works showed the dependence of the time history of Nusselt number on Reynolds number. We plan to study the transient heat transfer in a fixed bed of particles and validate the assumption of the isothermal particles. However, the earlier works in Chapters 2-4 cannot be easily extended to study the transient heat transfer problem. The PR-DNS approach that has been developed in Chapter 7 has to be used for this problem by imposing inflow/outflow boundary conditions. In this chapter, we first extend the PR-DNS approach in Chapter 7 to study the transient heat transfer from a sphere in flow through a duct. This case is similar to the case of Balachandar and Ha (2001) where they studied the free thermal evolution of a spherical particle subjected to a uniform isothermal ambient flow. Once the approach has the capability to study the transit heat transfer from a single particle, we will study the transient heat transfer from a fixed bed of particles in future work.

The rest of the chapter is organized as follows. In Section 9.2, the energy equation for transient heat transfer in gas-solid flow is described. In Section 9.3 the PR-DNS approach that is extended to solve this transient heat transfer problem is briefly described. In Section 9.4, the time evolution of the particle temperature and average Nusselt number for different particle-to-fluid thermal inertia ratios are shown. Finally, the principal findings are summarized in Section 9.5.

9.2 Description of transient heat transfer in gas-solid flow

Heat transfer in steady flow past isothermal spherical particles by assuming that the Biot number is far less than 0.1 and the ratio of particle-to-fluid thermal inertia for a sphere is infinite has been studied in Chapters 2 and 5. In this steady-state heat transfer, the particle temperature is constant and independent of time. The only way to verify the validity of the assumption of the isothermal particle is to perform simulations of the same identical case of

fixed bed particles with allowing the particle temperature to vary in time. However, the thermal fully-developed assumption used in Chapters 3 and 4 may not allow us to study the non-constant particle temperature case. This results from the fact that the scaled fluid temperature field

$$\theta(\mathbf{x},t) = \frac{T(\mathbf{x},t) - T_s}{\langle T_m \rangle (x_{||},t) - T_s} \tag{9.3}$$

($\langle T_m \rangle$ is the ensemble-average bulk fluid temperature) is no longer statistically homogeneous. In other words, due to the time-dependent particle temperature $T_s(\mathbf{x},t)$, the θ field varies in the streamwise or axial direction $x_{||}$ (Tenneti et al. (2013)), i.e.,

$$\frac{\partial \theta}{\partial x_{||}} = \frac{\partial}{\partial x_{||}} \left(\frac{T(\mathbf{x},t) - T_s(\mathbf{x},t)}{\langle T_m \rangle (x_{||},t) - T_s(\mathbf{x},t)} \right) \neq 0. \tag{9.4}$$

Therefore, the self-similarity boundary condition that is implemented in Chapters 2-4 is not appropriate for the transient heat transfer problem. Instead of imposing self-similarity boundary condition, the inflow/outflow boundary condition has to be used in the streamwise direction. The purpose of this work is to extend current FFD PR-DNS code developed in Chapter 7 to account for the time variation of the particle temperature in the transient gas-solid heat transfer problem.

In order to validate the extended FFD PR-DNS approach, transient heat transfer from a single sphere is first studied. Once the extended FFD PR-DNS has the capability to simulate transient heat transfer on a sphere correctly, the transient heat transfer from a fixed bed of particles can be studied in future work. The test case of steady flow past a sphere with non-constant particle temperature is performed in a square duct. The reason to choose this case is that this case not only consider the time variation of the particle temperature but also the effect of the duct walls. The details of the setup of this case can be seen in Figure 9.2.

The momentum equation and the gas-phase energy equation governing this transient heat transfer problem are described in Chapter 7. In order to evolve the particle temperature $T_s(t)$ with time, the solid-phase energy equation for each particle also needs to be solved. The particle temperature is determined by the solid-phase energy equation that is applied to each particle as

$$\rho_s c_{ps} \frac{\partial T_s}{\partial t} = k_s \frac{\partial^2 T_s}{\partial x_j \partial x_j} + Q_s, \tag{9.5}$$

where Q_s is the heat source term, k_s is the thermal conductivity in the solid phase, ρ_s is the solid density, c_{ps} is the constant pressure specific heat capacity in the solid phase. Note that similar to what Feng and Michaelides (2009) did for the solid phase, the particles that have an uniform temperature is considered, which is valid if Bi $\ll 1$. Therefore, instead of solving the above solid-phase energy equation, the average solid-phase energy equation obtained by integrating the equation over the solid volume V_s is used to determine the transient temperature of the particles as

$$V_s \rho_s c_{ps} \frac{dT_s}{dt} = \int_{A_s} k_s \nabla T_s \cdot \mathbf{n}_s dA + \int_{V_s} Q_s dV, \tag{9.6}$$

where $\mathbf{n}_s$ is the outward normal vector (from solid to fluid). Since the heat flux at the interface between the solid and fluid phases is continuous as $k_s \nabla T_s = k_f \nabla T_f$, the total heat transfer from solid to fluid can be expressed using $k_f \nabla T_f$ as

$$\int_{A_s} k_s \nabla T_s \cdot \mathbf{n}_s dA = -\int_{A_s} k_f \nabla T_f \cdot \mathbf{n}_f dA. \tag{9.7}$$

Therefore, the total energy $\int_{A_s} k_s \nabla T_s \cdot \mathbf{n}_s dA$ can be computed from the gradient of fluid temperature.

It is worth noting that Feng and Michaelides (2009) discussed that for particles that have different temperatures than the fluid, the presence of this term creates a temperature gradient within the fluid, which would modify the fluid properties. For relatively small temperature difference between the particles and fluid, the Boussinesq approximation has been often used to compute the effect of free convection (the purpose to do this is to avoid to change the fluid properties). In our case, in order to avoid to consider the free convection ($\mathrm{Gr}/\mathrm{Re}_\mathrm{D}^2 \ll 1$), the transient heat transfer cases at high particle Reynolds number ($\mathrm{Re}_\mathrm{D} = 100$) are simulated. Thus, this transient heat transfer problem does not need to consider free convection as Feng and Michaelides (2009) did.

9.3 Numerical approach

The equations governing the transient heat transfer problem can be solved using the FFD PR-DNS approach in Chapter 7. Based on the governing equations in the Section 9.2, the equations for simulating this transient heat transfer problem can be described as follows. In FFD PR-DNS approach, the momentum equation is

$$\frac{\partial u_i}{\partial t} + S_i = -\frac{1}{\rho_f} g_i + \nu_f \frac{\partial^2 u_i}{\partial x_j^2} + I_s f_u, \tag{9.8}$$

the gas-phase energy equation is

$$\rho_f c_{pf} \frac{\partial T_f}{\partial t} + u_j \frac{\partial T_f}{\partial x_j} = k_f \frac{\partial^2 T_f}{\partial x_j^2} + I_s f_T, \tag{9.9}$$

and the solid-phase average energy equation is

$$V_s \rho_s c_{ps} \frac{dT_s}{dt} = \int_{A_s} k_f \nabla T_f \cdot \mathbf{n}_f dA + \int_{V_s} Q_s dV. \tag{9.10}$$

where f_u and f_T are the immersed boundary forcing. The details on the procedure of solving the momentum and the gas-phase energy equations can be found in in Chapter 7. The solid-phase average energy equation is solved explicitly as

$$V_s \rho_s c_{ps} \frac{T_s^{n+1} - T_s^n}{\triangle t} = \int_{A_s} k_f \nabla T_f \cdot \mathbf{n}_f dA + \int_{V_s} Q_s dV, \tag{9.11}$$

By solving the above solid-phase average energy equation with gas-phase energy equation in each time step, the transient heat transfer problem can be simulated in our PR-DNS approach. For simplicity, we set the heat source term $Q_s = 0$ and focus on the study of the effect of the particle-to-fluid thermal inertia ratio $\rho_s c_{ps}/\rho_f c_{pf}$ (for biomass fast pyrolysis the value is close to 2000) on heat transfer.

9.4 Result and discussion

In this section, unlike the studies of transient heat transfer from a sphere in a uniform flow (Feng and Michaelides (2000); Balachandar and Ha (2001)), we focus on the transient

heat transfer problem in a duct flow. The inlet condition corresponds to a uniform velocity and temperature. The non-dimensional fluid temperature is defined as

$$\phi = \frac{T - T_{s,i}}{T_\infty - T_{s,i}}, \tag{9.12}$$

where T_∞ is the uniform inlet temperature, $T_{s,i}$ is the initial sphere temperature (non-dimensional time $\hat{t} = t/\tau_f = 0$, where $\tau_f = D/U_\infty$ is the flow time scale, D is the sphere diameter and U_∞ is the inlet velocity). Thus, the non-dimensional inlet temperature is $\phi = 1$. The temperature of the duct wall is the same as the initial sphere temperatures ($\phi = 0$), which is less than the inlet fluid temperature and is constant in time and space. The height of the duct H is $H = 3D$ and the length of the duct L is $L = 10D$. The fixed sphere is located in the center of the duct and its initial temperature is set to $\phi = 0$ as shown in Figure 9.2. Once the flow and temperature fields reach steady-state, the sphere temperature is allowed to evolve in time according to Eq. 9.11.

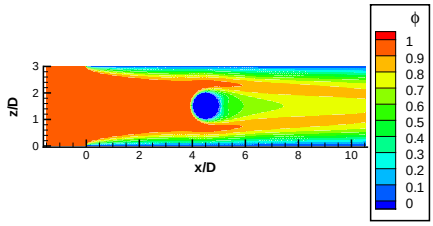

Figure 9.2: Contour plot of flow past a cool sphere ($\phi = 0$) in a duct at the initial time $t = 0$ at $\mathrm{Re_D} = 100$ and $\mathrm{Pr} = 0.7$ in $x - z$ plane. The uniform non-dimensional temperature in the inlet of the duct is $\phi = 1$. The red region presents high temperature region. The duct entrance is located in $x/D = 0$.

Figure 9.3 shows the time history of the non-dimensional particle temperature ϕ_s defined as

$$\phi_s = \frac{T_s(t) - T_\infty}{T_{s,i} - T_\infty} \tag{9.13}$$

for three particle-to-fluid thermal inertia ratio values $\rho_s c_{ps}/\rho_f c_{pf}$ for the same particle Reynolds number (100) based on the sphere diameter and Prandtl number (0.7), where $T_s(t)$ is the time-

dependent sphere temperature. In Fig. 9.3(a) the sphere temperature increases with time while the average Nusselt number (Nu = hD/k_f, where h is the average heat transfer coefficient) decreases and approaches an asymptotic value for $\hat{t} \geq 1$. We observe the same behavior for high thermal inertia ratio in Figs. 9.3(b) and (c) that the Nusselt number goes to an asymptotic value for $\hat{t} \geq 1$ although the average Nusselt numbers are obtained from different thermal inertia ratios. These trends are similar to that found in other works (Feng and Michaelides (2000); Balachandar and Ha (2001)) for unbounded flow past a sphere at Pr = 0.7 for different particle Reynolds numbers.

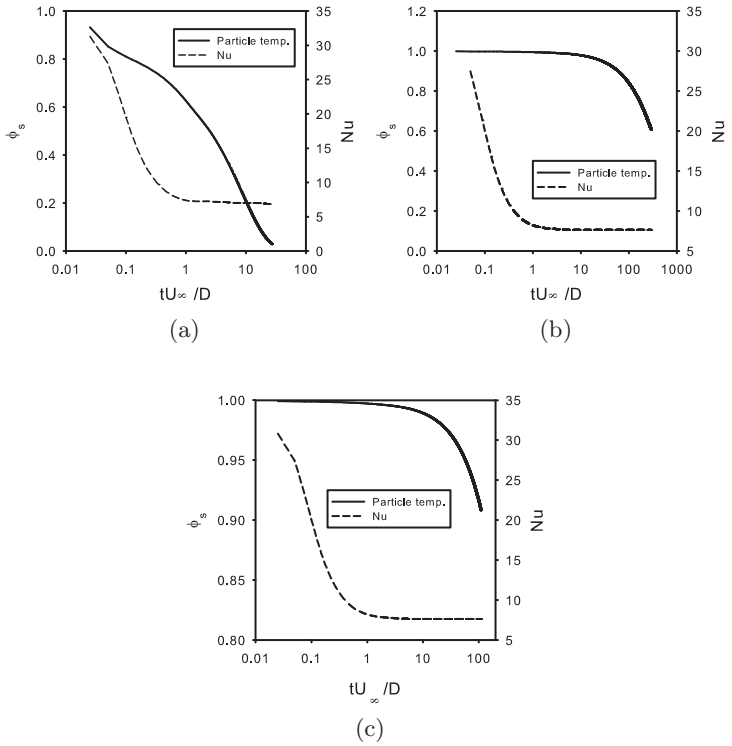

Figure 9.3: Time history of non-dimensional sphere temperature ϕ_s and Nusselt number for the particle-to-fluid thermal inertia ratio $\rho_s c_{ps}/\rho_f c_{pf}$ equal to (a) 10, (b) 1000, and (c) 2000. The solid lines represent the non-dimensional sphere temperature and the dash lines represent the average Nusselt number. U_∞ is the inlet uniform velocity.

The effect of particle-to-fluid thermal inertia ratio $\rho_s c_{ps}/\rho_f c_{pf}$ on the average Nusselt number is not easy to observe whereas the sphere temperature is affected significantly in Fig. 9.3. For for $\rho_s c_{ps}/\rho_f c_{pf} = 10$, the non-dimensional sphere temperature drops to 0.03 at $\hat{t} = 25$

whereas for $\rho_s c_{ps}/\rho_f c_{pf} = 1000$, the non-dimensional sphere temperature is still 0.95 at $\hat{t} = 25$. It is worth noting that for $\rho_s c_{ps}/\rho_f c_{pf} = 2000$ since the sphere temperature only decreases 10% for $\hat{t} = 100$ and Nusselt number does not vary in time for $\hat{t} \geq 1$. Besides the flow time scale, the evolving time can be also normalized by the interphase heat transfer time scale as $\tau_{pf} = V_s \rho_s c_{ps}/hA_s$. Since the flow time scale is far less than the time scale of the interphase heat transfer ($\tau_{pf}/\tau_f = \rho_s c_{ps} V_s \mathrm{PrRe_D}/\rho_f c_{pf} D A_s \mathrm{Nu} > 20$ for $\rho_s c_{ps}/\rho_f c_{pf} \geq 10$ and $\mathrm{Re_D} = 100$), the time scale that the Nusselt number reaches steady-state much faster than the time scale of interphase heat transfer. Therefore, even though the sphere temperature varies in time, there exists the steady value of Nusselt number for the applications such as fast pyrolysis of biomass particle ($\rho_s c_{ps}/\rho_f c_{pf} \approx 2000$).

Although there exists the time scale that the average Nusselt number can reach steady-state in PR-DNS simulation, it is important to know if there also exists in the experiment of biomass fast pyrolysis. If yes, we can conclude that even though the particle temperature varies in time, there exists the steady-state Nusselt number for this transient heat transfer from a sphere. If not, we need to develop Nusselt number correlation to account for the transient heat transfer. Based on the experimental data from Di Blasi and Branca (2003), we can verify the above hypothesis. First, Di Blasi and Branca (2003) estimated the Biot number about $7 - 25$ for the particle radius $2 - 10$ mm at bed temperature $T_r = 807K$. Based on their estimation, the Biot number for our biomass fast pyrolysis is about 1.4 since Xue et al. (2011) assumed the size of the biomass particle to be 400 μm.

Then we can estimate the time scale for fast pyrolysis and verify the above hypothesis. In the experiment of Di Blasi and Branca (2003), the minimum fluidization velocity at atmospheric pressure is 0.036m/s and a superficial velocity is about 8 times higher than that at minimum fluidization conditions for all cases. Therefore, the velocity in the non-dimensional time is $U_\infty = 0.288$m/s. The size of biomass used in Xue et al. (2011) is 400 μm whereas in Di Blasi and Branca (2003) the minimum particle size used is 2mm. However, they gave a correlation on characteristic heating times with particle size as shown in Fig. 9.4. Based on these correlations, the corresponding heating time can be estimated for the small size of biomass such as 400 μm. In this figure, the heating time t_5 represents that the conversion

process is practically terminated. Using t_5 correlation in Fig. 9.4, the heating time t_5 for the size of biomass $D = 400\mu$m is about 16s. Therefore, the non-dimensional time to complete the fast pyrolysis is $\hat{t}_5 = t_5/\tau_f = 11520$. Compared with $\hat{t} \geq 1$, the non-dimensional time $\hat{t}_5 = t/\tau_f = 11520$ indicates that the average Nusselt number becomes a steady value at very early stage of the pyrolysis.

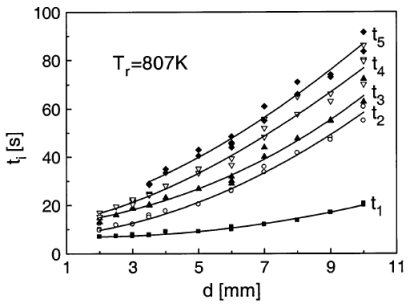

Figure 9.4: Copy of Di Blasi and Branca (2003)'s figure about characteristic heating times $t_1 - t_5$ at the particle center as functions of the particle diameter for the fluidized bed temperature $T_r = 807K$. The times $t_1 - t_5$ represent the stages of heating.

In the other experiment of Di Blasi et al. (2013), they measured the time evolution of the particle temperature at several radical positions and total weight loss of biomass particles in a fixed bed of biomass particles as show in Fig. 9.1. The time history of the total weigh loss of particles shows clearly that there exists the time scale ($\tau_{conv} \approx 100$s) in which there is almost no weight loss or conversion of biomass particles into liquid or gas. This implies that within this time scale the particle temperature increases most due to the high heat rate from external heat flux. Based on the parameters (gas velocity of1.3cm/s and particle diameter of 0.5cm) provided by Di Blasi et al. (2013), the flow time scale is far less than this time scale of conversion of biomass particles ($\tau_f/\tau_{conv} = O(10^{-3})$). Therefore, the steady-state Nusselt number appears in the initial stage of fast pyrolysis of biomass particles. This finding allows us to use the steady-state Nusselt number correlation to develop heat transfer model. The assumption of the isothermal particle does not affect the existence of the steady-state Nusselt number. However, further studies on the effect of the isothermal and non-isothermal particles on the magnitude of Nusselt number needs to be performed. We expect that even in the fixed bed of particles, the steady-state Nusselt number can be still obtained with or without the

assumption of isothermal particles.

9.5 Conclusion

The assumption of the isothermal particle used in model development needs to be validated. Transient heat transfer in a fixed bed of particle is considered as the only way to check the assumption. Before performing simulations of transient heat transfer in a fixed bed of particle, the FFD PR-DNS approach is first extended to account for time-dependent solid-phase temperature. Transient heat transfer for steady flow past a fixed particle in a duct flow is simulated using the extended FFD PR-DNS approach. The sphere temperature is assumed to be uniform inside sphere and is dependent of time. The average solid-phase energy equation is used to evolving the sphere temperature. Then PR-DNS simulations is performed in an inflow/outflow setup for three values of the particle-to-fluid thermal inertia ratio: 10, 1000 and 2000 (the last value corresponds most closely to biomass particles in air). Finally, we show the effect of finite particle-fluid thermal inertia ratio on gas-solid heat transfer based on PR-DNS results. The average Nusselt number became the steady value in a very short time compared with the flow and interphase heat transfer time scales. The existing experimental data (Di Blasi and Branca (2003); Di Blasi et al. (2013)) confirms that in the initial stage of biomass fast pyrolysis the steady-state Nusselt number can be obtained. Future studies on transient heat transfer in a fixed bed of particles will validate the assumption of the isothermal particle and verify if the current heat transfer models in CFD simulation can be still used even though the particle temperature varies in time.

CHAPTER 10. MASS TRANSFER IN STEADY FLOW PAST A NON-POROUS PARTICLE

This chapter is a manuscript titled "Mass transfer from a non-porous sphere in reacting gas-solid flow" that is under preparation.

Mass transfer in reacting gas-solid flow is as much important as heat transfer in industrial applications such as in the process of biomass fast pyrolysis. Simulating mass transfer in such scale-up industrial reactors needs predictive computational models of reacting gas-solid flows. Current mass transfer models which were developed in the late 1970s are used in state-of-the-art computational codes for device-scale simulations of multiphase flow. Model development for mass transfer needs to be performed, which is analogous to heat transfer model development in Chapters 3 and 4. To achieve this objective, the first setup is to fundamentally understand the canonical problem of mass transfer from a single particle in reacting gas-solid flow. In this work, simulation of this mass transfer problem in reacting gas-solid flow is performed. Then mass transfer in a fixed bed of particles will be studied and used to develop mass transfer models in future work.

In this chapter, mass transfer in steady flow past a non-porous sphere with the surface chemical reaction is studied. The convection-diffusion equation is used to describe this mass transfer problem with the surface chemical reaction in gas-solid flow, and the effect of chemical reaction appears as the boundary condition on the sphere surface. By solving the convection-diffusion equation, the steady-state solutions of this mass transfer problem are obtained as a function of relevant characteristic length and time scales. The non-dimensional parameters that results from characteristic length and time scales for this mass transfer problem includes the Reynolds number, the Schmidt number that is defined as the ratio of momentum diffusivity and mass diffusivity, the Péclet number that is defined as the product of Reynolds number and

Schmidt number, and the Damköhler number that is defined by the ratio of mixing time scale to chemical reaction time scale. This mass transfer problem is solved using an analytical approach and particle-resolved direct numerical simulation (PR-DNS), respectively. By imposing the first-order chemical reaction boundary condition on the surface of a sphere, the 1D analytical solution is derived based on the velocity field in Stokes flow, which is valid only for very low Péclet number. The 2D analytical solutions of the concentration field and Sherwood number obtained from Gupalo and Ryazantsev (1972) are used to compare with the 1D analytical solution in Stokes flow for different Damköhler numbers. The PR-DNS approach is extended to study the 3D mass transfer problem with the first-order surface chemical reaction. The PR-DNS results of the mass transfer problem are validated by the 2D analytical solutions of Gupalo and Ryazantsev (1972) at low Reynolds number less than unity. The dependence of mass flux and average sherwood number on Damköhler number is also shown using PR-DNS data.

10.1 Introduction

Mass transfer in reacting gas-solid flow is of fundamental importance in various chemical engineering applications such as chemical looping combustion (CLC) and biomass fast pyrolysis. Since experimental studies of mass transfer in gas-solid flow for industrial device-scale are limited, computational fluid dynamics (CFD) simulation that needs closure models to close the unclosed terms of the averaged equations (Syamlal et al. (1993)) is widely used to simulate heat and mass transfer problem in gas-solid flow. However, current models for average reaction rates as well as heat and mass transfer correlations which were developed in the late 1970s are used in state-of-the-art computational codes for device-scale simulations of gas-solid flow. More accurate models need to be developed for the problems relevant to the mass transfer. In order to improve current closure models, a numerical approach is first developed to solve mass transfer problems in this chapter. Then once the numerical approach is validated, it can be used to perform simulations of fixed or fluidized bed of particles to develop statistical models which are analogous to the models developed for heat transfer problem in Chapters 3 and 4.

Due to the existence of solid phase, whether or not mass transfer and chemical reaction

inside solid phase needs to be considered has to check in reacting gas-solid flow. For instance, one major application of gas-solid mass transfer process is the catalysis of CO_2 such that the exhaust gas CO_2 in CLC is absorbed by the sorbents (solid) such as zeolite particles (Lee et al. (2014)). In the zeolite particles both chemical reaction and pore diffusion exist. Whether or not chemical reactions inside the particle (normally represented by a volumetric chemical reaction rate constant k_V whose SI units are 1/s) are important depends on particle properties and the ratio of the volumetric chemical reaction rate constant to pore diffusion. If most of the gas is consumed at the particle surface very quickly (which responds to a small chemical reaction time scale $\tau_{chem} = D/k_s$ relative to the pore diffusion time scale $\tau_{\text{diff}} = D^2/D_{sA}$, where k_s is the surface chemical reaction whose SI units are m/s and D_{sA} is the pore diffusion coefficient of specie A in solid phase), very little gas will diffuse into the porous particle. This is equivalent to mass transfer with surface chemical reaction in a non-porous particle. Another scenario is that the gas cannot be consumed at the surface of particles, but due to the slow diffusion inside the particles (which responds to a large pore diffusion time scale $\tau_{\text{diff}} = D^2/D_{sA}$), less gas enters the pores and most of the reactions take place at the surface of particle. This case can be also considered as only a surface chemical reaction problem because the ratio of two time scales ($\tau_{\text{diff}}/\tau_{chem} = D^2 k_s/D_{sA}$) is far less than unity. Although many practical cases need to consider volumetric chemical reactions and pore diffusion, the surface chemical reaction is easier to represent first. It is also interesting to see the effect of surface chemical reaction on mass transfer between gas and solid phases that is represented by the Sherwood number. Therefore, in this work, in order to understand the effect of surface reaction on mass transfer, we only consider the surface chemical reaction on a non-porous particle as the first setup.

Mass transfer on a non-porous particle with surface reactions involves more characteristic length and time scales than that in single-phase reactive turbulence. Due to the existence of the particle there exist the characteristic length scale of the particle is the particle diameter D, the diffusion length scale is $\ell_{\text{diff}} = \sqrt{D_{bA} D/U}$ (D_{bA} is the bulk diffusion coefficient of specie A in the gas phase and U is the slip velocity between solid and gas phases), the mixing time scale in gas phase is $\tau_\phi = R^2/D_{bA}$ (R is the particle radii), and the chemical reaction time scale is $\tau_\alpha = R/k_s$. These characteristic length and time scales forms the non-dimensional

parameters which control the behavior of the mass transfer problem. For instance, the Péclet number is defined as Pe $= DU/D_{bA}$ or the product of Reynolds number Re $= DU/\nu_f$ and Schmidt number Sc $= \nu_f/D_{bA}$ (ν_f is the kinematic viscosity) that represents the ratio of the advective transport rate to the rate of diffusive transport. The ratio of the mixing time scale to the chemical time scale is the Damköhler number ($Da = \tau_\phi/\tau_\alpha = k_s R/D_{bA}$, Fox (2003)) which indicates if the chemical reaction controls mass transfer. In the case of CO_2 capture by zeolite particles (Lee et al. (2014)), the Damköhler number is about $Da \approx 2.5 \times 10^{-9}$ indicating that chemical reaction controls gas-solid mass transfer since the chemical time scale is much larger than the mixing time scale. In contrast, for combustion problem fast reactions occurring in thin reaction-diffusion zones result in a large Da (Fox (2003)).

Theoretical studies of mass transfer in reacting gas-solid flow have focused on solving the convection-diffusion equation with surface chemical reactions (Hartunian and Liu (1963); Taylor (1963b); Gupalo and Ryazantsev (1972)). Several analytical solutions of steady mass transfer from a sphere in Stokes flow or at finite low Reynolds number flow have been reported (Hartunian and Liu (1963); Taylor (1963b); Gupalo and Ryazantsev (1972); Bell et al. (2013)). Hartunian and Liu (1963) used matched asymptotic expansions to solve the two-dimensional convection-diffusion equation associated with Oseen's velocity field (Proudman and Pearson (1957)) for flow past a sphere at low Reynolds number flow (Re $\ll 1$). They obtained an analytical solution for the concentration field around the sphere in gas-solid flow and their solution is a function of particle Péclet number and Damköhler number. Gupalo and Ryazantsev (1972) not only considered the effect of Péclet number on the concentration field but also accounted for the dependence of the concentration field on Schmidt number Sc explicitly by using a stream function that is in terms of Schmidt number and Péclet number at small finite Reynolds number.

Based on the analytical solutions for this mass transfer problem with surface chemical reactions, the Sherwood number correlations representing mass transfer between solid and gas phases have been also given. Taylor (1963b) extended the work of Hartunian and Liu (1963) to derive an expression for the Sherwood number with first-order and second-order surface chemical reactions. This Sherwood number correlation depends on Péclet number

(Pe = ReSc,Re $\ll$ 1) and Damköhler number ($0 < Da < \infty$). Since the analytical solution of the concentration field obtained from Gupalo and Ryazantsev (1972) is also a function of Schmidt number, the Sherwood number expression of Gupalo and Ryazantsev (1972) depends not only on Péclet number and Damköhler number, but also explicitly on the Schmidt number.

However, theoretical solutions have the limitations for solving mass transfer on a sphere in a two-phase flow over a wide range of Péclet number, especially at high Reynolds number or high Péclet number. Experimental and numerical approaches have been used to study mass transfer from a sphere at high Reynolds number (Clift et al. (1978)). Based on the experimental and numerical data obtained from the case of fast surface reaction (concentration is zero on the particle surface), several Sherwood number correlations have been proposed, such as $\overline{\mathrm{Sh}} = 1 + [1 + 1/\mathrm{Pe_D}]^{1/3}\mathrm{Re_D^{0.41}Sc^{1/3}}$ from Clift et al. (1978) for mass transfer from a rigid sphere. It is worth noting that existing Sherwood number correlations for high Reynolds number (Clift et al. (1978); Incropera et al. (2006)) are only a function of the Reynolds and Schmidt numbers, but not the Damköhler number. In other words, chemical reaction does not affect the Sherwood number in these correlations for large Damköhler number.

The use of these correlations (Clift et al. (1978); Incropera et al. (2006)) for the mass transfer problems where Damköhler number is low may be not appropriate. This motivates us to use particle–resolved direct numerical simulation (PR-DNS), which is a first-principles method that solves for the instantaneous three–dimensional velocity and scalar fields representing the flow, heat and mass transfer around each particle. Several researchers have successfully simulated heat and mass transfer from a single sphere or multiple spheres in gas-solid flow. Two-dimensional PR-DNS studies (Yu et al. (2006); Feng and Michaelides (2009)) simulating gas–solid flow in an infinite channel with an isothermal particle have been reported. Deen et al. (2012) and Tavassoli et al. (2013) used three-dimensional PR–DNS with inflow/outflow boundary conditions to simulate forced convective heat transfer from a sphere at high particle Reynolds number up to 100. Deen et al. (2014) also used a PR-DNS approach to study coupled heat and mass transfer on particles with fast chemical reaction on the particle surface (zero concentration on the particle surface) in a dense liquid-solid flow at high particle Reynolds number (up to 240). Zhang et al. (2008) and Ren et al. (2013) performed simulations of a flow

past a cylinder with constant heat flux on the cylinder surface. Luo et al. (2016) implemented different type of boundary conditions on the cylinder surface to simulate heat transfer from a cylinder. However, the PR-DNS approach has not been used to study mass transfer in reacting gas-solid flow.

In this chapter, the PR-DNS approach developed in Chapter 7 is extended to account for mass transfer on the surface of a sphere with chemical reaction. Using the extended PR-DNS solver, steady flow past a sphere with the first-order surface chemical reaction in a gas-solid flow ($\mathrm{Sc} \leq 1$) is investigated. The rest of the paper is organized as follows. In Section 10.2, the mass transfer problem in a gas–solid flow is described and the assumptions to simplify this mass transfer problem are discussed. In Section 10.3, 1D and 2D analytical solutions for this mass transfer problem are given and the 1D analytical solution is validated by comparing it with the 2D analytical solution. In Section 10.4, the PR-DNS approach to solve this mass transfer problem is briefly described. In Section 10.5, the PR-DNS data are compared with 2D analytical solutions for low and high Reynolds numbers. The dependence of mass flux and average Sherwood number on Damköhler number is also given. Finally, the principal findings are summarized in Section 10.6.

10.2 Problem statement

We consider gas-solid mass transfer in a uniform flow past a fixed non-porous spherical particle with surface chemical reaction as shown in Fig. 10.1. The velocity and concentration in the far field U_∞ and $C_{A,\infty}$ are assumed to be uniform. The gas-solid flow is characterized by the Reynolds number ($\mathrm{Re_D} = U_\infty D/\nu_f$, D is the particle diameter and ν_f is the fluid-phase kinematic viscosity), the Schmidt number ($\mathrm{Sc} = \nu_f/D_{bA}$, D_{bA} is the diffusion coefficient of specie A in the fluid phase) that is considered to be smaller than unity (gas phase) or the Péclet number ($\mathrm{Pe_D} = DU/D_{bA}$), and the Damköhler number ($Da = k_s R/D_{bA}$). We only consider the first-order surface chemical reaction which is represented by the reaction rate constant k_s.

The assumptions made to simplify this mass transfer problem are similar to Taylor (1963b) and Gupalo and Ryazantsev (1972), namely: (i) decoupling of mass transfer from heat transfer,

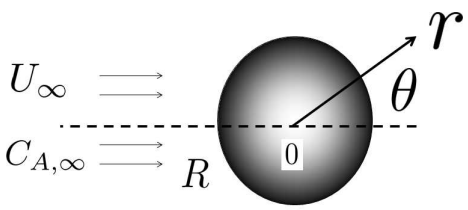

Figure 10.1: Schematic of a steady flow with a uniform velocity U_∞ and concentration $C_{A,\infty}$ through a fixed non-porous particle (the radii R) with the chemical surface reaction rate constant k_s. The spherical coordinate (r and θ) is used to analyze the mass transfer problem.

(ii) neglect of radiation and free convection, (iii) first-order chemical reaction on the particle surface and neglect of pore diffusion inside the particle, (iv) particle properties such as the diameter and density are constant, and (v) steady-state flow. Based on these assumptions, the velocity $\mathbf{u}(\mathbf{x}, t)$ and specie A concentration field $C_A(\mathbf{x}, t)$ obey the following mass, momentum, and convection-diffusion equations:

$$\frac{\partial u_i}{\partial x_i} = 0, \tag{10.1}$$

$$\frac{\partial u_i}{\partial t} + S_i = -\frac{1}{\rho_f} g_i + \nu_f \frac{\partial^2 u_i}{\partial x_j \partial x_j}, \tag{10.2}$$

and

$$\frac{\partial C_A}{\partial t} + S_{C_A} = D_{bA} \frac{\partial^2 C_A}{\partial x_j \partial x_j}, \tag{10.3}$$

respectively. Here ρ_f is the fluid-phase density, g_i is the body force (e.g., hydrostatic pressure gradient or acceleration due to gravity), and $S_i = \partial(u_i u_j)/\partial x_j$ is the convection term ($S_{C_A} = \partial(u_j C_A)/\partial x_j$ is the convection term in the convection-diffusion equation). It is also worth noting that since the steady-state flow is assumed, the unsteady term on the left-hand side of Eq. 10.3 becomes zero for the sufficient time. In other words, the mass gain from the sphere

is balanced by the mass loss in the convective flow if the mass transfer occurs from fluid phase to solid phase.

The boundary conditions for the particle associated with the equations are as follows. Due to the consumption of mass at the particle surface, the first-order chemical reaction boundary condition at the particle surface (also see Taylor (1963b); Gupalo and Ryazantsev (1972)) is

$$D_{bA}\frac{\partial C_A}{\partial r}|_{r=R} = k_s C_{As}, \tag{10.4}$$

where C_{As} is the surface concentration. In this mass transfer problem, since the specie A cannot penetrate the solid surface, the mass flux normal to the surface must be consumed at the surface by the first-order chemical reaction. Based on the flux boundary condition in Eq. 10.4, the non-dimensional flux boundary condition can be derived as

$$\frac{\partial \hat{C}_A}{\partial \hat{r}}|_{\hat{r}=1} = Da\hat{C}_{As}, \tag{10.5}$$

where $Da = k_s R/D_{bA}$ is the Damköhler number, $\hat{C}_{As} = \hat{C}_A|_{\hat{r}=1} = C_A/C_{A,\infty}$ is the non-dimensional surface concentration, and $\hat{r} = r/R$ is the non-dimensional radial coordinate. If the surface chemical reaction is fast relative to mixing (no molecules of specie A at the sphere surface, $Da \to \infty$), then the flux boundary condition at the sphere surface reduces to $\hat{C}_{As} = 0$. This kind of boundary condition is analogous to the isothermal boundary condition for the heat transfer problem in Chapter 7. If $\partial \hat{C}_A/\partial \hat{r}|_{\hat{r}=1} = 0$ ($Da \to 0$), then this implies that reaction rate controls the spatial variation of surface concentration.

10.3 Analytical solution

In order to solve this mass transfer problem, the 3D mass transfer problem can be simplified into a 1D homogeneous problem or 2D axisymmetric problem to obtain an analytical solution in Stokes flow or at low Reynolds number. The analytical solution can be derived since the velocity field in Stokes flow (or Oseen's velocity field) is know from the stream function. There exist several works that discuss the 2D analytical solutions, but the 1D analytical solution is not discussed because it seems to be an oversimplification. We show that it is reasonable for very

low Péclet number (near the conduction limits). For completeness, we show 1D homogeneous problem in Stokes flow since this analytical solution is useful for understanding the mass transfer problem.

10.3.1 1D and 2D Analytical solutions

The 3D mass transfer problem is simplified to a 1D homogeneous problem to obtain an analytical solution in Stokes flow. Note that in order to obtain the 1D analytical solution, the 1D analytical velocity field in Stokes flow needs to be used. Since the velocity field solution of Stokes flow is a function of the radical direction and angular direction as shown in Fig. 10.1, we only use the velocity field solution in Stokes flow at $\theta = 0$ for the 1D analytical solution. This is of course a gross oversimplification and its validity can be examined. The 1D analytical solution for the concentration field in non-dimensional form (see detailed derivation in Appendix N) is:

$$\hat{C}_A\left(\hat{r}\right) = \frac{1 + Da\int_1^{\hat{r}} e^{\mathrm{Re_D Sc}\mathcal{W}(r')}dr'}{1 + Da\int_1^{\infty} e^{\mathrm{Re_D Sc}\mathcal{W}(r')}dr'}, \tag{10.6}$$

where the weight function $\mathcal{W}$ is

$$\mathcal{W}\left(\hat{r}\right) = \frac{1}{8\hat{r}^2} + \frac{3}{4}\ln\hat{r} - \frac{1}{2}\hat{r} - \frac{2}{\mathrm{Re_D Sc}}\ln\hat{r} + \frac{3}{8}. \tag{10.7}$$

The 1D analytical solution for the concentration field is a function of the Péclet number ($\mathrm{Pe_D} = \mathrm{Re_D Sc}$) and the Damköhler number. Although the 1D analytical solution was derived using the velocity field for Stokes flow along the symmetric line $U(r, \theta = 0)$, we expect that the 1D solution can only be used for low Péclet number. This is because the spherical symmetry assumption that was used to simplify the 3D mass transfer problem into a 1D problem is valid only in the diffusion limit (negligible fluid inertia case, low Péclet number) as Eq. 10.8 that is the steady-state non-dimensional concentration equation derived from Eq. 10.3 as

$$\frac{\partial\left(\hat{U}_j\hat{C}_A\right)}{\partial\hat{x}_j} = \frac{1}{\mathrm{Pe_D}}\frac{\partial^2\hat{C}_A}{\partial\hat{x}_j\partial\hat{x}_j}. \tag{10.8}$$

If low Péclet number is far less than unity, the effect of the convection term on the left-hand side of the above equation can be neglected. In other words, the velocity distribution does not

affect the concentration field much.

The 3D mass transfer problem can be more accurately approached by the analysis of a 2D axisymmetric mass transfer problem (Taylor (1963a); Gupalo and Ryazantsev (1972)) since the velocity distributions in Stokes flow or in Oseen's solution (Proudman and Pearson (1957); Clift et al. (1978)) in spherical coordinates are known to be axisymmetric. Note that although Oseen's solution is a function of Reynolds number, the flow is still a creeping flow, or low Reynolds number with Reynolds number far less than unity. The 2D steady-state axisymmetric convection-diffusion equation describing the 2D mass transfer problem in axisymmetric spherical coordinates in non-dimensional form is

$$\hat{U}_r \frac{\partial \hat{C}_A}{\partial \hat{r}} + \frac{\hat{U}_\theta}{\hat{r}} \frac{\partial \hat{C}_A}{\partial \theta} = \frac{1}{\mathrm{Pe_D}} \left[\frac{1}{\hat{r}^2} \frac{\partial}{\partial \hat{r}} \left(\hat{r}^2 \frac{\partial \hat{C}_A}{\partial \hat{r}} \right) + \frac{1}{\hat{r}^2 \sin\theta} \frac{\partial}{\partial \theta} \left(\sin\theta \frac{\partial \hat{C}_A}{\partial \theta} \right) \right], \tag{10.9}$$

where θ is the angular coordinate from the uniform velocity direction (see Fig. 10.1), $\hat{U}_r$ and $\hat{U}_\theta$ are the non-dimensional velocity in radial and angular directions, respectively. The corresponding boundary conditions for the 2D steady-state axisymmetric mass transfer problems are the far field boundary condition $\hat{C}_A(\infty, \theta) = 1$ and the flux boundary condition $\left(\partial \hat{C}_A / \partial \hat{r}\right)_{\hat{r}=1} = Da \hat{C}_A(1, \theta)$. The analytical solutions for concentration or temperature fields based on the velocity field in Stokes flow (Acrivos and Taylor (1962); Bell et al. (2013)) and Oseen's velocity solution (Hartunian and Liu (1963); Taylor (1963a); Gupalo and Ryazantsev (1972)) have been derived using the matched asymptotic expansions approach. Since the analytical solutions for concentration field derived in Stokes flow is a special case for that derived from Oseen's velocity solution, we only focus on the 2D analytical solutions obtained based on Oseen's velocity solution (Taylor (1963a); Gupalo and Ryazantsev (1972)).

Using the matched asymptotic expansions approach, Gupalo and Ryazantsev (1972) obtained the analytical solution for concentration field and average Sherwood number correlation with the first-order surface chemical reaction. The expression for the Sherwood number correlation obtained from Gupalo and Ryazantsev (1972) is

$$\mathrm{Sh} = 2 \left[q + \frac{1}{2} q^2 (\mathrm{Pe_g} + {\mathrm{Pe_g}}^2 \ln \mathrm{Pe}_g + \frac{1}{2} q \mathrm{Pe}_g^3 \ln \mathrm{Pe}_g) + \frac{1}{2} q^2 Q(q, \mathrm{Sc}) \mathrm{Pe}_g^2 + O\left(\mathrm{Pe}_g^3\right) \right], \tag{10.10}$$

where $q = Da/(Da+1)$, $\mathrm{Pe_g} = \mathrm{Pe_D}/2$, and

$$Q\left(q,\mathrm{Sc}\right) = \frac{1}{2}q - \frac{119}{80} + 0.577216 - \frac{3}{32}\left(2-q\right)^{-1} + \frac{1}{2}\mathrm{Sc}^2 - \frac{1}{4}\mathrm{Sc} - \frac{1}{2}\left(\mathrm{Sc}-2\right)\left(\mathrm{Sc}+1\right)^2 \ln\left(1+\mathrm{Sc}^{-1}\right).$$

Note that this Sherwood number depends on the Da through q. The average Sherwood number correlation is obtained from the definition of

$$\overline{\mathrm{Sh}}_{\mathrm{old}} = \int_{-1}^{1}\left(\frac{\partial \hat{C}_A}{\partial \hat{r}}|_{\hat{r}=1}\right) d\cos\theta. \tag{10.11}$$

However, in this definition, the effect of concentration difference $(C_{As} - C_{\infty})$ which drives the mass flux at the particle surface was neglected. Truly speaking, this integral calculation is analogous to an average mass flux not "Sherwood number". In the following section, we carefully derive a expression to compute average Sherwood number in this mass transfer problem.

10.3.2 Average Sherwood number

The local Sherwood number based on particle diameter is defined as follows:

$$\mathrm{Sh} = \frac{h_{m,loc}D}{D_{bA}}, \tag{10.12}$$

where $h_{m,loc}$ is the local mass transfer coefficient (SI units:m/s). The local mass transfer coefficient can be obtained from the local mass flux at the particle surface J_A as

$$h_{m,loc} = J_A/\left(C_{As} - C_{A,\infty}\right) = D_{bA}\frac{\partial C_A}{\partial r}|_{r=R}/\left(C_{As} - C_{A,\infty}\right). \tag{10.13}$$

Then the average Sherwood number for a sphere can be written in non-dimensional form as

$$\overline{\mathrm{Sh}} = \frac{\overline{h}_m D}{D_{bA}} = \frac{D\int_{-1}^{1} h_{m,loc} d\cos\theta}{D_{bA}} = -\frac{D}{4\pi R^2}\int_0^{\pi}\frac{\frac{\partial C_A}{\partial r}|_{r=R}}{\left(C_{As}-C_{A,\infty}\right)} 2\pi R^2 \sin\theta d\theta = -\int_0^{\pi}\frac{\frac{\partial \hat{C}_A}{\partial \hat{r}}|_{\hat{r}=1}}{\left(\hat{C}_A|_{\hat{r}=1}-1\right)}\sin\theta d\theta. \tag{10.14}$$

Compared to the definition of the average Sherwood number in Eq. 10.14, the average Sherwood number expressions of Taylor (1963a) and Gupalo and Ryazantsev (1972) (see Eq.10.11) do

not consider the effect of concentration difference between the far field and the surface in the denominator.

Based on the above definition in Eq. 10.14 and the 1D analytical solution in Eq. 10.6, the average Sherwood number obtained from 1D homogeneous analytical solution can be calculated as

$$\overline{\mathrm{Sh}} = -\int_0^{\pi} \frac{\frac{\partial \hat{C}_A}{\partial \hat{r}}|_{\hat{r}=1}}{\hat{C}_A|_{\hat{r}=1} - 1} \sin\theta d\theta = \frac{-\frac{2Da}{1 + Da\int_1^{\infty} e^{\mathrm{Re_D Sc}\mathcal{W}(r')} dr'}}{\frac{1}{1 + Da\int_1^{\infty} e^{\mathrm{Re_D Sc}\mathcal{W}(r')} dr'} - 1} = \frac{2}{\int_1^{\infty} e^{\mathrm{Re_D Sc}\mathcal{W}(r')} dr'}. \tag{10.15}$$

This expression for the 1D approximation shows that the average Sherwood number is independent of Da and only depends on the Péclet number in Stokes flow. We compare the analytical solutions for the concentration fields and Sherwood numbers in the following section.

10.3.3 Comparison of 1D and 2D analytical solution

We compare the 1D analytical solution with the 2D analytical solutions of Gupalo and Ryazantsev (1972) for verifying the valid range of 1D analytical solution. Figure 10.2 shows a comparison of the concentration fields from the 1D and 2D analytical solutions in Stokes flow for two values of the Damköhler number. In the 1D mass transfer problem, the solution only depends on the radial location r (due to $\theta = 0$). Fig. 10.2 shows that the concentration profile in the 1D analytical solution (red line) has a good agreement with the 2D analytical solution at several different angles (blue lines) at $Da = 100$ and $Da = 0.1$ with the average relative error of 2%. This result shows that the axisymmetric mass transfer problem can be well approximated by a spherically symmetric 1D formulation for Stokes flow when the flow has negligible inertia. The reason of this good approximation results from the small Péclet number. If Péclet number is small (for this case Péclet number is equal to 0.0007) the convection term in the left-hand side of Eq. 10.8 is negligible. Therefore, the 1D analytical solution in gas-solid flow becomes a solution of pure diffusion problem.

In addition, the Damköhler number Da has a large effect on the concentration fields. For large Da, the concentration at the particle surface is almost equal to zero as shown in Fig. 10.2(a). This tells us that at large Da the chemical reaction is fast and the problem is diffusion-

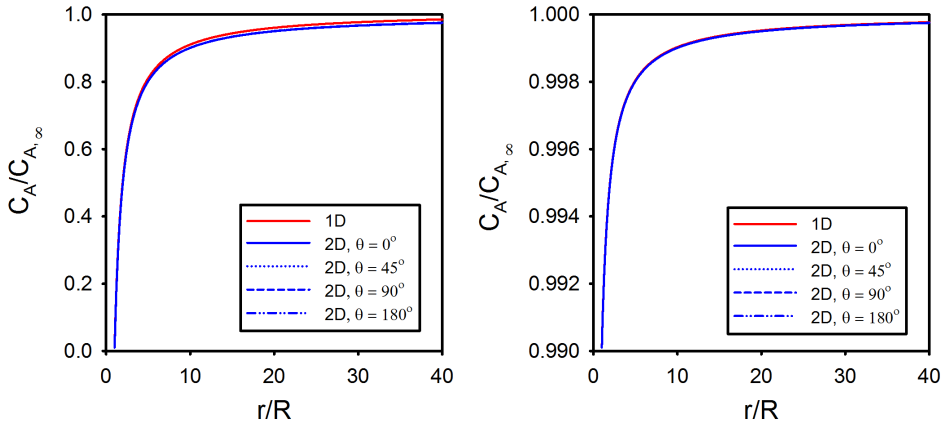

Figure 10.2: Variation of the concentrations obtained from 1D and 2D analytical solutions with the non-dimensional radial location r/R at $\mathrm{Re_D} = 0.001$ and $\mathrm{Sc} = 0.7$ for (a) $Da = 100$ and (b) $Da = 0.1$. The red line represents the 1D homogeneous analytical solution in Eq. 10.15 and the blue lines represent the 2D analytical solutions of the concentrations obtained from Gupalo and Ryazantsev (1972) for different angles.

rate-controlled. For small Da, Fig. 10.2(b) shows that the concentration at the particle surface tends to the far-field concentration $C_{A,\infty}$, which corresponds to a reaction-rate-controlled problem.

However, we find that in Stokes flow, the Sherwood number does not depend on the Damköhler number Da because the effect of $C_{As} - C_{A,\infty}$ cancels out the dependence in the denominator. Table 10.1 shows the average Sherwood number obtained from 1D and 2D analytical solutions by varying the Damköhler number Da. The values in the second column of Table 10.1 represents that the average Sherwood number $\overline{\mathrm{Sh}}$ that is computed by considering the concentration difference in Eq. 10.15, while the values in the third column represent the normalized mass flux that is defined as

$$\frac{\bar{J}_{Da}}{\bar{J}_{Da\to\infty}} = \frac{\int_{A_s} D_{bA} \dfrac{\partial C_A\,(Da)}{\partial r}|_{r=R} dA}{\int_{A_s} D_{bA} \dfrac{\partial C_A\,(Da\to\infty)}{\partial r}|_{r=R} dA}, \tag{10.16}$$

where A_s is the surface area of the sphere, $\bar{J}_{Da\to\infty}$ is the mass flux at $Da \to \infty$. This normalized mass flux is proportional to the average Sherwood number $\overline{\mathrm{Sh}}_{\mathrm{old}}$ in Eq. 10.15 that does not

include the effect of the concentration difference. For the 1D mass transfer problem, with increasing Da the average Sherwood number $\overline{\mathrm{Sh}}$ does not vary while the mass flux $\bar{J}_{Da}$ increases and converges to the value of $\bar{J}_{Da\to\infty} = 2$. Even for the 2D analytical solution, we observe the same behavior as shown in the fourth and fifth column of Table 10.1. This implies that although the mass flux (see Eq. 10.16) varies significantly with Da, the Sherwood number always remains the same in Stokes flow. It also tells us that the Sherwood number correlations obtained from Taylor (1963a) and Gupalo and Ryazantsev (1972) represent the average mass flux but not the computation of the average Sherwood number.

Table 10.1: Variation of average Sherwood number and average mass flux with Da in Stokes flow at $\mathrm{Re_D} = 0.001$ and $\mathrm{Sc} = 0.7$. The average Sherwood numbers $\overline{\mathrm{Sh}}$ from 1D analytical solution and 2D analytical solution are computed in Eq. 10.2 and Eq. 10.14, respectively. The normalized average mass flux $\bar{J}_{Da}/\bar{J}_{Da\to\infty}$ is obtained in Eq. 10.16.

Da	1D $\overline{\mathrm{Sh}}$	1D $\bar{J}_{Da}/\bar{J}_{Da\to\infty}$	2D $\overline{\mathrm{Sh}}$	2D $\bar{J}_{Da}/\bar{J}_{Da\to\infty}$
100	2.0061	0.9921	2.0003	0.9905
1	2.0061	0.5054	2.0003	0.5001
0.01	2.0061	0.0099	2.0003	0.0099

Table 10.1 also indicates that the average Sherwood number computed from 1D analytical solution (the second column) is almost same as that computed from 2D analytical solution in Eq. 10.16 (the fourth column). Therefore, the spherically symmetric assumption for the 3D mass transfer problem holds at low Péclet number (less than 0.01) . However, the 1D and 2D analytical solutions are only valid for low Reynolds number (less than unity). The study of the mass transfer problem at high Reynolds number relies on numerical solutions. In the next section, we use the PR-DNS approach to first validate our PR-DNS results and then investigate the effect of surface chemical reaction on the concentration field and the Sherwood number at high Reynolds number.

10.4 PR-DNS approach

The gas-solid mass transfer problem can be solved using a fully finite-difference (FFD) PR-DNS that has been developed in Chapter 7. We extend the scalar solver (see Chapter 7) to account for mass transfer on the surface of particles with the first-order surface chemical

reaction. The hydrodynamic and scalar solver based on the FFD formulation were parallelized in order to simulate gas-solid flow in a large computational domain with high-resolution. The PR-DNS hydrodynamic and scalar solvers are now briefly described.

The mass, momentum and scalar transport equations to solve the constant-density flow are

$$\frac{\partial u_i}{\partial x_i} = 0, \tag{10.17}$$

$$\frac{\partial u_i}{\partial t} + S_i = -\frac{1}{\rho_f} g_i + \nu_f \frac{\partial^2 u_i}{\partial x_j^2} + I_s f_{u,i}, \tag{10.18}$$

and

$$\frac{\partial \phi}{\partial t} + S_\phi = \Gamma_\phi \frac{\partial^2 \phi}{\partial x_j \partial x_j} + I_s f_\phi, \tag{10.19}$$

where I_s is the solid indicator function ($I_s = 1$ for points lying in the solid phase), $f_{u,i}$ and f_ϕ are the additional immersed boundary (IB) direct forcing terms that are nonzero only in the solid phase. The complete details about the direct IB forcing can be found elsewhere (Tenneti et al. (2013, 2011)). The IB forcing accounts for the presence of the solid particles in the domain by ensuring that the no-slip and no-penetration boundary conditions is satisfied on each particle surface. In order to simulate gas-solid mass transfer, the scalar transport equation ($\phi = C_A$ and $\Gamma = D_{bA}$) is solved with a mass flux boundary condition at the surface of the sphere (see Eq. 10.4).

The key to obtaining the correct PR-DNS results is to impose the boundary condition correctly at the particle surface using the IB forcing. The no-slip and no-penetration boundary conditions are imposed by forcing the desired velocity to be particle velocity ($\mathbf{u}^d = \mathbf{u}_p$) (Tenneti et al. (2011)). Similarly, Tenneti et al. (2013) imposed the isothermal boundary condition by forcing the desired temperature $T^d = T_p$ to the particle temperature T_p. It is worthwhile to note that these boundary conditions are Dirichlet boundary conditions. For the mass transfer problem described in the previous section, the boundary condition in Eq. 10.4 is a flux boundary condition. In order to obtain the desired scalar value, we treat the boundary in the following way

$$C_{As}^{d} = C_{As}^{n+1} = \frac{1}{Da}\left(\frac{\partial C_A}{\partial r}|_{r=R}\right)^n, \tag{10.20}$$

where $(\partial C_A/\partial r|_{r=R})^n$ is obtained from the interpolation on the particle surface at the nth time step as

$$\left(\frac{\partial C_A}{\partial r}|_{r=R}\right)^n = \frac{1}{1+Da\triangle r}C_{A,i}^{n}, \tag{10.21}$$

where $C_{A,i}^{n}$ is obtained from interpolating the outside layer and $\triangle r$ is the grid size. This boundary condition strictly validity for steady flows and not for time-dependent solution of unsteady flow. Zhang et al. (2008) also use a similar method to impose the flux boundary condition using an immersed-boundary method. The details on numerical scheme can be found in Chapter 7.

10.5 Results and discussion

Before comparing PR-DNS data with existing analytical solutions or correlations, we summarize the existing data for gas-solid mass transfer from a sphere. Figure 10.3 shows the valid region of the analytical solutions or Sherwood number correlations for gas-solid mass transfer in terms of the Reynolds number, the Péclet number and the Damköhler number. The 1D analytical solution we derived in the previous section (represented by blue box) are obtained for $\mathrm{Pe_D} \approx 0$ while the 2D analytical solutions are limited for $\mathrm{Re_D} < 1$, $\mathrm{Pe_D} < 1$ and no restriction for Damköhler number $0 < Da < \infty$. The Sherwood number correlation of Gupalo and Ryazantsev (1972) (represented by red box) that were developed with considering the Damköhler number $(0 < Da < \infty)$ is limited for $\mathrm{Re_D} < 1$ and $\mathrm{Pe_D} < 1$ whereas the average Sherwood number correlations (represented by green box) that were developed based on the experimental and numerical data for $\mathrm{Re_D} > 1$ are not a function of the Damköhler number or assume $Da \to \infty$. Large Da corresponds to the zero concentration on the particle surface whereas small Da results in the non-zero concentration on the particle surface as the red double arrows of Fig. 10.3 shows. The PR-DNS has no such limitation and can simulate the low and high Reynolds number cases with $0 < Da < \infty$ as shown in the following sections.

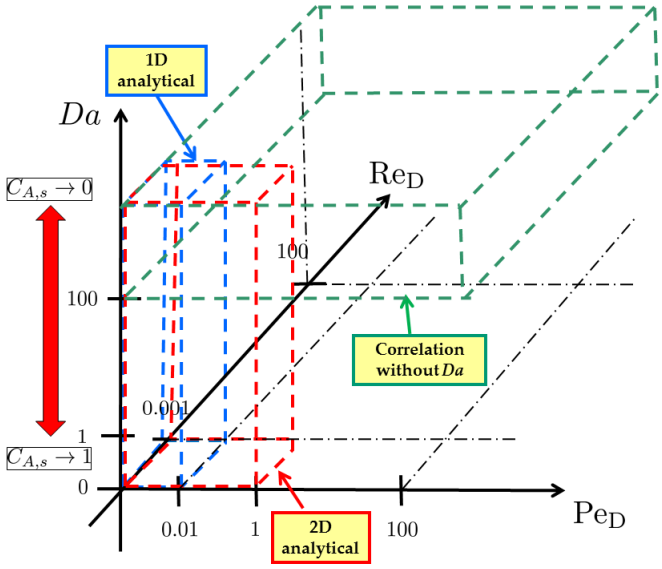

Figure 10.3: Summary of the valid region of existing analytical solutions and Sherwood number correlations for the mass transfer from a sphere in terms of the Reynolds number $\mathrm{Re_D}$, the Péclet number $\mathrm{Pe_D}$, and the Damköhler number Da. The blue dashed box represents the 1D analytical solution derived from this work and the red dashed box represents the 2D analytical solution of Gupalo and Ryazantsev (1972). The green dashed box represents the Sherwood number correlations (not a function of the Damköhler number) obtained from experimental and numerical data which assume the fast reactions on the particle surface. C_{As} represent the concentration of the particle surface. The dash-dotted lines is the reference lines.

10.5.1 Low Reynolds number case

In this section, the uniform flow past a sphere with mass transfer in a open field using PR-DNS at particle Reynolds number of 0.1 and Schmidt number of 0.7 is simulated. The length of the computational domain is $L/D = 20$ in all directions in order to avoid any boundary effects arising from a finite computational domain. A spherical particle is located in the center of the computational domain. In order to validate our PR-DNS results, we first need to match Oseen's velocity field at this Reynolds number, and then compare the concentration field obtained from PR-DNS with the 2D analytical solution of Gupalo and Ryazantsev (1972).

First, the inlet uniform velocity is set to be unity (the blue solid line) as shown in Figure 10.4. We set the location of center of the particle at the origin ($x/R = 0$). The figure shows that due to the limited domain length, the velocity profile cannot match Oseen's velocity field (the red dotted line) (Clift et al. (1978)). In order to match Oseen's solution, instead of setting an

uniform velocity in the inlet of the domain ($x/R = -20$) we use Oseen's solution at $x/R = -20$ as the inlet velocity profile. For this inlet condition the velocity profile obtained from PR-DNS (the black solid line in Fig. 10.4) matches the Oseen's velocity field with a maximum relative error of 3%. The error results from the different slope of the velocity at the inlet. We also observe a velocity difference between PR-DNS data and Oseen's solution at the exit of the domain ($x/R = 20$). This results from that the fact that we use Neumann boundary conditions ($\partial u_x/\partial x = 0$) at the exit of the domain, which cannot capture the slope of Oseen's velocity. The difference can be reduced by increasing the length of the domain. However, due to limitations in computational resources, we only used $L/D = 20$ as the largest domain in our simulations.

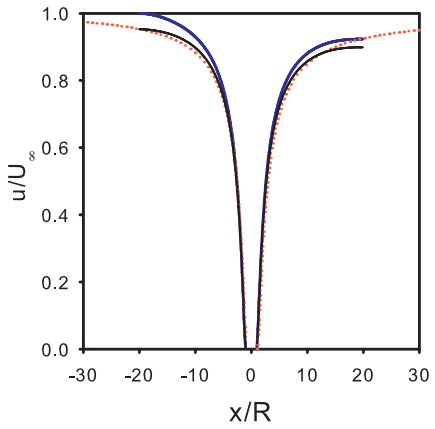

Figure 10.4: Comparison of the centreline velocity profile obtained from PR-DNS data and Oseen's velocity solutions (Clift et al. (1978)) for flow past the spherical particle at $\mathrm{Re_D} = 0.1$. The red dotted line represents the Oseen's velocity solution. The blue solid line and the black solid line represent the centreline velocity profile obtained from PR-DNS data velocity solution using an uniform velocity and Oseen's velocity solution in the inlet of the domain, respectively. The location of the center of the particle is at the origin $x/R = 0$.

Once the velocity field from PR-DNS approximately matches the Oseen's velocity solution, the concentration field is simulated. We compare PR-DNS data with 2D analytical solutions at $Da = 100$ to see the effect of Da on the concentration field and Sherwood number. Figure 10.5 shows the comparison of the concentration field from PR-DNS data with the 2D analytical solution at $Da = 100$. The concentration profile at the centreline obtained from PR-DNS matches well with the 2D analytical solution over the entire line. The difference between PR-

DNS data and the 2D analytical solution is only close to the particle surface, which the surface concentration $\hat{C}_{As}$ from PR-DNS is about 0.01862 but is about 0.01019 from the 2D analytical solution. This difference may result from the implement of boundary condition for the particle surface. The mean concentration on the particle surface from PR-DNS is higher than that of the 2D analytical solutions. For the 2D analytical solution or 3D PR-DNS data, average Sherwood number does not vary with Da for small Reynolds number case. We also compare average Sherwood number between the 2D and 3D solutions. The average Sherwood number from the PR-DNS data (about 1.95) is lower than the analytical solution (about 2.01). The discrepancy between the PR-DNS results and 2D analytical solution is still being investigated.

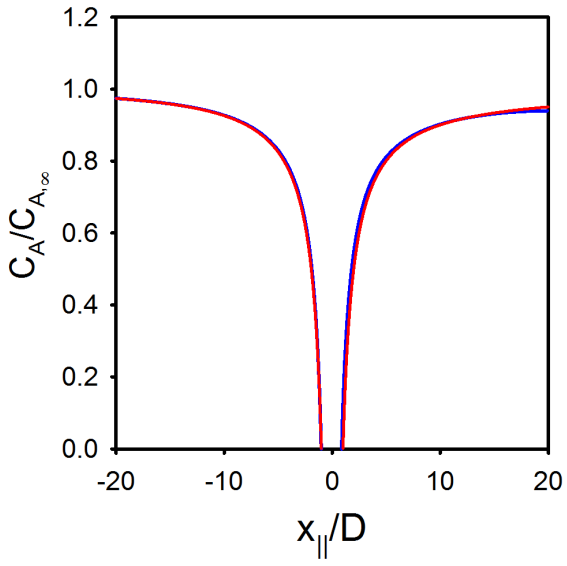

Figure 10.5: Comparison of the non-dimensional centreline concentration profile between PR-DNS data and 2D analytical solutions of Gupalo and Ryazantsev (1972) at $\mathrm{Re_D} = 0.1$ and $\mathrm{Sc} = 0.7$ for $Da = 100$. The solid line represents the concentration profile from the 2D analytical solutions. The dashed line represents the centreline concentration profile obtained from PR-DNS data. The location of the center of the particle is set to be $x/R = 0$.

10.5.2 High Reynolds number case

Current theories for mass transfer are restricted to low Reynolds number where analytical expressions for the velocity field are available. We extend our PR-DNS study to higher Reynolds

numbers of 20 and 100. Figure 10.6 shows variation of concentrations along the centreline of the sphere for Reynolds numbers of 20 and 100 at $Da = 100$. Unlike the low Reynolds number case, the concentration along the centreline ($y/D = 0$ and $z/D = 0$) does not change in the upstream. For the region close to the sphere surface we observe that the concentration drops quickly to the surface concentration. Compared to the case for $\mathrm{Re_D} = 20$, the concentration falls more rapidly is higher for $\mathrm{Re_D} = 100$ as shown in Fig. 10.6.

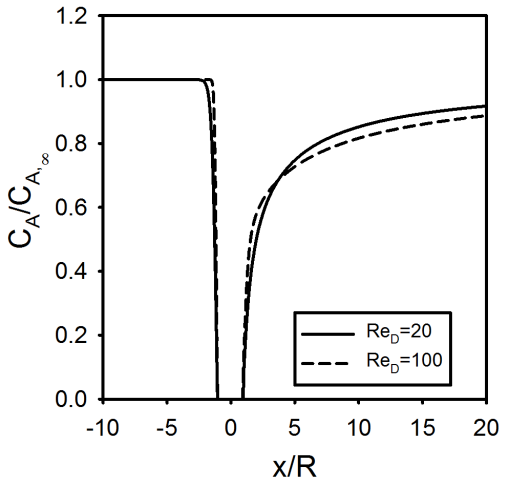

Figure 10.6: Variation of the non-dimensional concentrations along the centreline ($y/D = 0$ and $z/D = 0$) at $\mathrm{Re_D} = 20$ and 100 for $\mathrm{Sc} = 0.7$ and $Da = 100$. The solid line represents the case at $\mathrm{Re_D} = 20$ and the dashed line represents the case at $\mathrm{Re_D} = 100$. The sphere is located at $x/R = 0$.

Based on the PR-DNS data, we can answer the question if the surface chemical reaction has a significant influence on the Sherwood number of a sphere. The computation of average Sherwood number in our PR-DNS approach is defined as

$$\overline{\mathrm{Sh}} = \frac{\overline{h}_m D}{D_{bA}} = -\frac{D}{A_s}\int_{A_s} \frac{\frac{\partial C_A}{\partial r}|_{r=R}}{C_{A,s} - C_{A,\infty}} dA, \tag{10.22}$$

where A_s is the surface area of sphere. Figure 10.7 shows a comparison of average Sherwood number obtained from PR-DNS data and existing Sherwood number correlations for a sphere. In this figure, the PR-DNS data obtained from the case of $Da = 1$ (the squares) and $Da = 100$ (the circles) are close to the Whitaker's correlation (Incropera et al. (2006), $\overline{\mathrm{Sh}} = 2 + \left[0.4\mathrm{Re_D^{1/2}} + 0.06\mathrm{Re_D^{2/3}}\right]\mathrm{Sc}^{0.4} \times [\mu/\mu_s]^{1/4}$) and Clift's correlation (Clift et al. (1978), $\overline{\mathrm{Sh}} = 1 +$

$[1 + 1/\mathrm{Pe_D}]^{1/3}\mathrm{Re_D^{0.41}Sc^{1/3}}$, $1 \leq \mathrm{Re_D} \leq 400$ and $0.25 \leq \mathrm{Sc} \leq 100$). Note that these Sherwood number correlations do not account for surface chemical reaction or the effect of the Damköhler number. For low Reynolds number, the 2D analytical solution of Gupalo and Ryazantsev (1972) at $Da = 100$ (the triangles) is close to these correlations. In this comparison, for high Da we do not find much difference between the PR-DNS data and existing Sherwood number correlations even though we consider surface chemical reaction. This may imply that for high Da, CFD simulations can still use the existing Sherwood number correlations to compute the gas-solid mass transfer. However, for low Da the average Sherwood number from PR-DNS represented by the squares is higher compared to that for high Da. These differences of the average Sherwood number result from the non-zero surface concentration such as $C_{As} = 0.71$ for $Da = 1$ and $\mathrm{Re_D} = 20$. Therefore, the difference of the concentration between the particle surface and far field in Eq. 10.22 plays an important role in determining the magnitude of the average Sherwood number.

In the absence of surface chemical reaction, a high Sherwood number indicates high mass transfer. However, for this mass transfer problem where the surface concentration changes with surface reaction rate, the Sherwood number may not be a good measure of mass transfer between the gas and solid phases. Mass flux is a more direct measure of mass transfer since it does not consider the concentration difference between particle surface and far field. Figure 10.8 shows the variation of the normalized mass flux (see Eq. 10.16) at two Péclet numbers. The normalized mass flux represented by the symbols increases Da with increasing the Péclet number. This finding is similar to the behavior of mass flux obtained from the analytical solution of Gupalo and Ryazantsev (1972) at low Péclet number. This indicates that high Da enhances mass transfer in this gas-solid flow. In addition, the normalized mass flux tends to unity for large Da, which corresponds to fast chemical reaction on the particle surface. The PR-DNS data over a range of Péclet number (> 20) need to be provided to see the effect of low Da on Sherwood number in future work.

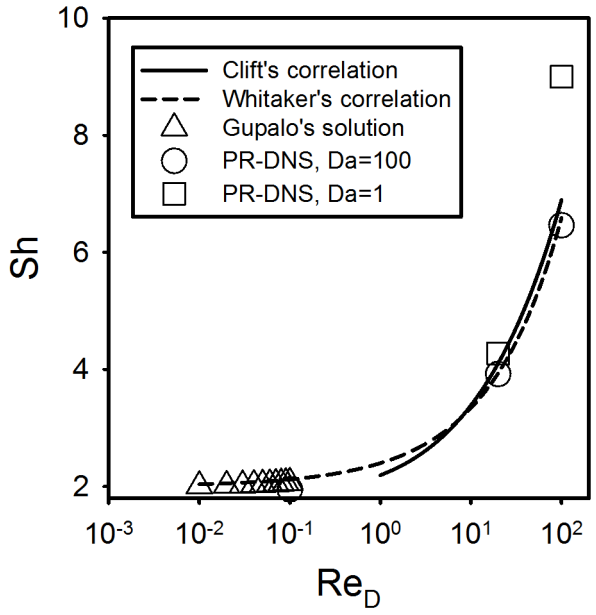

Figure 10.7: Comparison of average Sherwood number between the existing Sherwood number correlations and the PR-DNS data for different Reynolds numbers at Sc = 0.7. The squares and circles represent the PR-DNS data obtained at $Da = 1$ and $Da = 100$, respectively. The solid line and dash line represent the Clift et al. (1978)'s correlation and the Whitaker's correlation (Incropera et al. (2006)) for a rigid sphere, respectively. The triangles represent the Sherwood number correlation from the 2D analytical solution of Gupalo and Ryazantsev (1972) in Eq. 10.14 at $Da = 100$.

10.6 Conclusion

Mass transfer in a steady flow past a sphere with a first-order surface chemical reaction was studied using PR-DNS for Reynolds numbers up to 100. The PR-DNS scalar solver was extended to simulate the mass transfer problem by implementing a boundary condition of the third kind to account for the consumption of species at the surface due to surface reaction. A 1D analytical solution to simplify this mass transfer problem was obtained based on the velocity field in Stokes flow. The 1D analytical solution matches well with published 2D analytical solutions in the literature for the concentration and Sherwood number at low Péclet number ($\mathrm{Pe_D} < 0.01$). The concentration profile in a low Reynolds number case from PR-DNS is found to be close to the analytical solution of Gupalo and Ryazantsev (1972) in low Reynolds number flow. The PR-DNS results for low Reynolds number ($\mathrm{Re_D} = 0.1$) matched well with the 2D

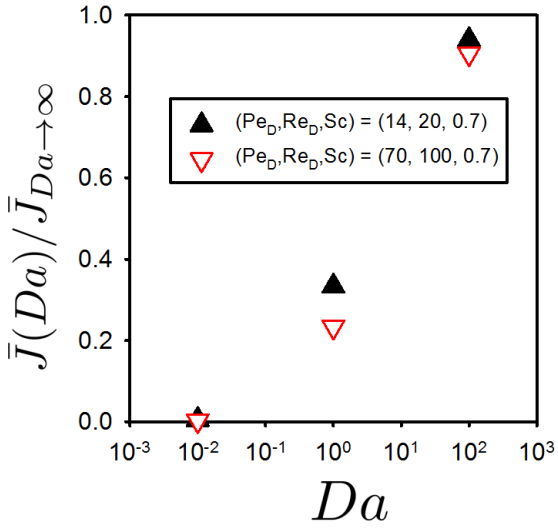

Figure 10.8: Variation of the normalized mass flux with Da in Eq. 10.16 obtained from PR-DNS data at two Péclet numbers at Sc = 0.7. The up-triangles and down-triangles represent the PR-DNS data obtained at $\mathrm{Pe_D} = 14$ and $\mathrm{Pe_D} = 70$, respectively.

analytical solution except on the particle surface. The PR-DNS results for higher Reynolds numbers were used to compare the average Sherwood number from simulation with published correlations in the literature that do not account for surface chemical reaction. We found that for high Da the Sherwood number is close to these existing Sherwood number correlation whereas for low Da the Sherwood number is much higher than the current Sherwood number correlation. However, both 2D analytical solution and PR-DNS data showed that high Da did correspond to higher mass flux in this mass transfer problem. An improved Sherwood number in terms of Da needs to be developed over a wide range of Péclet number in gas-solid flow.

CHAPTER 11. CONCLUSION

In this thesis, the critical challenges in developing improved models for reacting gas–solid flow have been addressed using particle-resolved direct numerical simulation (PR-DNS). Reacting gas–solid flows are an important class of multiphase flows that are frequently occurred in nature and engineering applications. These gas–solid flows are often associated with heat and mass transfer, and chemical reactions in both gas phase and solid phase. Understanding the physical mechanisms of momentum, kinetic energy, heat and mass transfer, and chemical reaction between the gas phase and the solid particles is a crucial step in the industrial process. In industrial process of the design and optimization, device-scale multiphase computational fluid dynamics (CFD) simulations of reacting gas–solid flow are increasingly being used. The device-scale CFD simulations need accurate mathematical models for the interphase transfer phenomena. In order to precisely develop models for device-scale CFD simulations, PR-DNS simulations of reacting gas-solid flow problems can provide the time-dependent three-dimensional velocity, temperature and species mass fraction fields based on the extended Navier-Stokes equations obeying exact boundary conditions at each particle's surface. These simulations give unprecedented insight and improved understanding of flow, mixing and reaction in the interior of particle-laden flows, and provide data on statistics such as average reaction rates and the scalar-velocity covariance for model development. Multiphase reacting flow modeling efforts can greatly benefit from quantitative information regarding velocity, temperature and species mass fraction fields for model development and validation.

In this thesis, the specific objectives related to reacting gas–solid flow problems were studied using PR-DNS approach, such as quantification of the interphase heat and mass transfer, model development for gas–phase velocity and temperature fluctuations, quantification of wall effect on flow and heat transfer in gas–solid flow. The PR-DNS approach was developed to account for

heat and mass transfer in reacting gas–solid flow, and were validated by a suite of test cases. Using the PR-DNS data, the improved models for device-scale CFD simulations of reacting gas–solid flow were proposed. The new model predictions were also compared with previous standard model predictions to assess the improvement in model performance.

The Particle–resolved Uncontaminated–fluid Reconcilable Immersed Boundary Method (Tenneti et al. (2011)) (PUReIBM) has been extended to investigate heat transfer in fixed periodic assemblies and freely evolving suspension of monodisperse spherical particles. This PR-DNS approach is based on the pseudo-spectral (PS) scheme that is used to solve governing equations in Fourier space rather than in physical space. The extension of PUReIBM to solve for heat transfer problem was validated by a suite of test cases such as heat transfer in fully–developed duct flow. Numerical convergence and the validity of the thermal similarity condition in flow past random assemblies and freely evolving suspension of particles and was verified.

PS PR–DNS simulations of gas–solid heat transfer in steady flow through a homogeneous fixed assembly of particles have been used to quantify and model the unclosed terms in the average fluid temperature equation of two–fluid equations. The unclosed terms including average gas–solid heat transfer, average conduction in the fluid phase, and temperature–velocity covariance in gas–solid flow were quantified and modeled using PS PR-DNS data. These models were validated over a wide range of mean slip Reynolds numbers and volume fractions and can be directly implemented in current CFD simulations of gas–solid heat transfer. The modeling efforts for transported PDF approach for two-phase flow have been also discussed and the mixing time scale that appears in the existing closure models is quantified using PS PR-DNS data. In addition, the assumptions underlying the continuum formulation of multiphase flow theory was also verified using PS PR-DNS data. A criterion that ensures the validity of the local homogeneity assumption or scale separation was developed by using a characteristic length scale that defines the scale of inhomogeneity of the average bulk fluid temperature.

A fully finite-difference (FFD) scheme of PR-DNS methodology was also developed based on PUReIBM to account for walls and various boundary conditions. The hydrodynamic and scalar solvers of FFD PR-DNS were parallelized and validated by a suite of test cases including fully–developed duct flow, flow past simple cubic (SC) particle arrangement, flow past a sphere

in open field, and developing duct flow with and without a single particle using inflow and outflow boundary conditions. The FFD PR-DNS data obtained from these test cases has a good agreement with analytical solutions, existing numerical and experimental results.

Using FFD PR-DNS, a detailed comparison between numerical and experimental data in the same setup is performed. The validation with numerical and experimental approaches were given for the cases of pure laminar duct flow, flow past a single sphere and a train of five particles in a duct. Comparisons of the entire velocity fields showed a good agreement between the numerical and experimental data. It was also found that number of spheres and spacing does not affect the wake length behind the train of spheres but has the effect on the wake between two neighbor spheres and the wall boundary layer growth. To study the wall effect on hydrodynamics and heat transfer, a flow past a particle assembly with heat transfer in a square duct was simulated using FFD PR-DNS. The effect entrance length and the wall effect on flow and heat transfer were quantified. The effect of walls on fixed bed of particles will be analysis further in the future work.

Using FFD PR-DNS, the validation of the assumption of the isothermal particle used in model development is expected to be checked. Before performing simulations of transient heat transfer in a fixed bed of particle, the FFD PR-DNS approach is first extended to account for time-dependent solid-phase temperature. The simulation of transient heat transfer from a sphere is performed. The sphere temperature is assumed to be uniform inside sphere and is dependent of time. It is found that even though the solid temperature changes, average Nusselt number goes to a steady value in a short time compared with the flow and interphase heat transfer time scale. The existing experimental data (Di Blasi and Branca (2003); Di Blasi et al. (2013)) confirms that in the initial stage of biomass fast pyrolysis the steady-state Nusselt number can be obtained. Future studies on transient heat transfer in a fixed bed of particles will validate the assumption of the isothermal particle.

For the mass transfer problem, steady flow past a sphere for low and high Reynolds number at low Schmidt number (less than 1) was simulated with a first–order chemical reaction as the boundary condition at the sphere surface. The FFD PR-DNS results were compared with 2D analytical solution for Sherwood number in low Reynolds number flow. The FFD PR-

DNS results for higher Reynolds numbers were used to compare the average Sherwood number correlation from simulation with published correlations in the literature that do not account for surface chemical reaction. This PR-DNS of mass transfer is the initial step to study the coupling of heat and mass transfer in reacting gas-solid flow.

The improved understanding of the reacting gas–solid flow will result in better models and simulation methodologies for interphase heat and mass transfer. The improved models will directly impact device-scale CFD simulation of heat and mass transfer in such fluidized beds and riser. The high-fidelity simulation methodologies such as PR-DNS approach will provide a reliable database to guide the design of industrial reactors.

CHAPTER 12. FUTURE WORK

In this chapter, the proposed future works and their speific plans are listed in Tables 12.1-12.2. In future work, several questions in a reacting gas–solid flow need to be answered:

1. Is heat transfer models developed based on PR-DNS data with assuming isothermal particles valid if the particle temperature varies in time?
2. What is the wall effect on drag force and heat transfer of particles in gas–solid heat transfer?
3. What is the effect of particle clustering on heat transfer models?
4. How should the unclosed momentum transfer term due to the interphase mass transfer be modeled?
5. What is the effect of coupling heat and mass transfer in reacting gas–solid flow?
6. What is the effect of mass transfer in reacting gas–solid flow when accounting for intra-particle phenomena?
7. What is the connection of PR-DNS setup to fluidized bed experiments?

These questions lead to the following works that will be expected to be answered in near future. The specific objectives to answer these questions are discussed below.

The first four questions arise from model development for the unclosed terms in TF and transported PDF approaches (see model development in Table 12.2). As discussed in Chapter 1, the first question can be answered by studying the effect of the transient heat transfer in a fixed bed of particles. It expected that the Nusselt number will reach a steady value after a short

Table 12.1: Future plans to be completed.

Future works	Objectives	Specific plans
Code development	Extend FFD PR-DNS to account for variable density in a reacting gas–solid flow	1. Code implement of a variable density FFD PR-DNS formulation 2. Test cases for variable density solver: (1) Rayleigh Benard natural convection, (2) natural convection of a circular cylinder or a sphere
Flow physics	Couple heat and mass transfer with a simple chemical reaction at a particle surface using FFD PR-DNS	1. Couple of heat and mass transfer at the surface particle with a simple chemical reaction 2. Test cases: dependence of mass transfer on the surface temperature of a particle with two scalar ϕ=$\{c_P T, Y_\alpha\}$ using third type boundary condition
	Extend mass transfer problem to account for flow in porous particles	1. Implement the appropriate boundary conditions on the particle surface and couple the solution of diffusion equation for the concentration field inside porous particle with the gas-phase concentration through the interphase 2. Test case : flow past one biomass particle with chemical reaction
	Build connection of PR-DNS setup to fluidized bed experiments	1. Update the discrete element method (DEM) solver in the PR-DNS approach to perform a fluidized bed simulation with a large number of particles 2. Implement the improved heat and mass models into the TF CFD simulation and compare the results with experimental data

time compared with interphase heat transfer time scale. In that case it can be concluded that the heat transfer models developed in Chapters 3 and 4 are still valid.

The second question arises from the fact that the walls of reactors affect heat transfer on particles. One has to modify heat transfer models to account for the effect of walls. In the hydrodynamic problem, in order to account for the wall effect on the drag force of a particle, the standard drag model is modified by adding an extra term that is a function of the distance between the particle center and the wall (Zeng et al. (2005)). Analogously, the Nusselt number correlation that is used in the average interphase heat transfer model can be modified using

Table 12.2: Future plans to be completed.

Future works	Objectives	Specific plans
Model development	Study the effect of transient heat transfer on a fixed particle assembly	Simulate transient heat transfer on the fixed particle beds with inflow/outflow boundary condition using FFD PR-DNS and quantify Nusselt number in time
	Study the effect of the wall on heat transfer in gas-solid flow	1. Develop a modified Nusselt number correlation for a single particle to account for wall effect 2. Perform the simulations of flow past a fixed bed of particles in a duct or channel with varying the distance between the wall and the center of the fixed beds of particles 3. Develop a modified Nusselt number correlation for fixed bed of particles to account for wall effect
	Study the effect of particle clustering on heat transfer	1.Perform the simulations of flow past a cluster of particles over a range of Reynolds numbers and solid volume fractions and particle pair correlation 2. Develop a Nusselt number correlation to account for heat transfer on particle clustering and homogeneous particle bed

the same approach. In future work (see flow physics in Table 12.1), the first step would be to develop a modified Nusselt number correlation for a single particle that account for the wall effect. Then the Nusselt number correlation would be developed based on data obtained from flow past a fixed bed of particles in a duct or channel. The preliminary results for the effect of walls on a sphere in a duct flow are reported in Chapter 7. In future work, FFD PR-DNS of flow past a fixed particle assembly in a square duct or channel can be performed by varying the distance between the center of fixed bed of particles and the wall. By comparing with the FFD PR-DNS data obtained from the flow past a fixed particle assembly in fully–developed flow without walls, the wall effect on particles will be seen clearly.

The third question is relevant to improve Nusselt number correlation by accounting for particle clustering. The current drag models and Nusselt number correlations in fixed beds or porous media were developed based on the homogeneous particle configurations. However, Mehrabadi et al. (2016) have shown that the mean drag force obtained from the cluster of particles is different from that obtained from homogeneous particle configuration. The difference

results from the particle pair correlation. In future work, PR-DNS of flow past a cluster of particles can be performed over a range of Reynolds number, solid volume fraction, and particle pair correlation. Then using the PR-DNS data, an improved Nusselt number correlation that accounts for particle clustering can be developed.

The answer to the fourth question is unknown since there are very few quantitative studies on source term due to interphase mass transfer. This source term can result from the blowing effect where the mass of particles is ejected to the fluid phase at a high speed. This type of the blowing effect may be considered as an extra mass transfer. In other words, by modifying the Sherwood number correlation, this effect may be taken care of.

The last three questions arise from how to convert the ideal PR-DNS simulation into the realistic PR-DNS simulation (see flow physics in Table 12.1). More physical phenomena need to be considered in the PR-DNS approach. In order to answer the fifth question, FFD PR-DNS is first used to explore the parameter space in the mass transfer problem of flow past a sphere and fixed bed of particles. This can provide PR-DNS data to model the mass transfer problem. Secondly, heat transfer will be coupled with mass transfer in reacting gas–solid flow, extending the preliminary decoupled results in Chapter 10. Two specific objectives will be studied for the coupling between heat and mass transfer problem. One is to impose a simple chemical reaction on the particle surface (see Table 12.1). The reaction rate for this chemical reaction will depend on the local temperature and species mass fraction. Therefore, the mass transfer will depend on the heat transfer at the surface of particles. The other objective is to account for the effect of variable density in the coupling of heat and mass transfer. In order to account for the effect of density variation, a variable-density version of this FFD PR-DNS code need to be developed based on the current frame work of the FFD PR-DNS approach. This extended solver will be tested in several problems such as the natural convection problem (see code development in Table 12.1).

The sixth question arises from the assumption that pore diffusion and volumetric chemical reactions inside the particle are neglected in Chapter 10 since the particle is considered as a non-porous medium. In order to check the effect of pore diffusion on mass transfer, the particle will be assumed to be a porous medium and the diffusion equation governing the

concentration in the porous particle will be solved. In mass transfer to a porous particle, the Thiele modulus that is defined as the ratio of volumetric chemical reaction rate constant to the diffusion inside porous particles will be introduced to determine if the concentration distribution inside particle is uniform. With appropriate boundary conditions on the interface between solid and gas phases, PR-DNS of this mass transfer problem can be solved to provide data that can determine validate if pore diffusion is important in biomass fast pyrolysis.

The last question arises from the challenging question about how to interpret the PR-DNS data with data from experiments in fluidized beds. Although a detailed comparison between experiments and simulations were performed in Chapter 8, this laboratory-scale simulation cannot be easily extended to industrial-scale simulation due to the current computational capability. In addition, once the motion of particle is accounted it is hard to set up the same conditions for experiments and simulations. For instance, Tang et al. (2016) performed the PR-DNS of a small fluidized bed and compare the PR-DNS data with the experimental data obtained from the same pseudo-2D experimental setup. This kind of detailed comparison reveals a good agreement with respect to the time-averaged particle motion and velocity profiles in a statistical sense. Even if the setup of experiments and simulations are the same, there still exist discrepancies that may result from the choice of particle-particle collision model and particle-wall collision model. TF CFD simulation is an alternative way to perform the device-level simulation while the PR-DNS approach provides the detailed data to develop the statistical closure models in the microscale. These microscale models can be used in TF CFD simulation. Therefore, the current PR-DNS setups mostly describe statistics in a representative small subdomain of the fluidized bed experiments.

APPENDIX A. REGIME OF APPLICABILITY OF THE ASSUMPTIONS

The assumptions employed in this work and their regime of validity are discussed in this section. The use of a fixed bed setup for gas–solid flows is justified if the configuration of the particles changes very slowly compared to the time it takes to attain mean momentum balance. The time scale over which the particle configuration changes depends on $\mathrm{Re}_\Theta = D\Theta^{1/2}/\nu_f$, which is the Reynolds number based on the particle fluctuating velocity that is characterized by the particle granular temperature Θ. The particle granular temperature Θ is a measure of the variance in the particle velocities and is defined as $\Theta = 1/3\,\langle \mathbf{v}'' \cdot \mathbf{v}'' \rangle$, where $\mathbf{v}''$ is the fluctuation in the particle velocity defined with respect to the mean particle velocity. Particle–resolved simulations of freely evolving suspensions (Tenneti et al. (2010)) and recent high–speed imaging of particles (Cocco et al. (2010)) show that this value of Re_Θ is $O\,(1)$ for high Stokes number particles that are characteristic of gas–solid flows (e.g., coal particles in air). This indicates that the particle configuration changes slowly relative to fluid time scales.

An important simplification made in this work is the use of a uniform temperature for the particles. The extent of variation of the temperature inside a particle is governed by the Biot number (Bi), which is defined as $\mathrm{Bi} = hD/k_s$. In this definition h is the convection heat transfer coefficient between the particle and the fluid, and k_s is the thermal conductivity of the solid. For many gas–solid systems the thermal conductivity of the solid is greater than that of the gas by more than an order of magnitude (e.g. air–coal, air–Ferrous oxide, air–fused silica) and results in a Biot number that is less than 0.1. The small Biot number encountered in many practical gas–solid systems suggests a lumped capacitance model for the particle temperature, where the spatial variation of temperature inside the particle can be neglected.

In addition to the assumption of uniform temperature of the particle, we also assume that

this uniform temperature is constant in time i.e., we assume the particles are isothermal. This simplification follows from the observation that the thermal response time of the particles is large compared to the time it takes for the fluid to travel a distance equal to the particle diameter. The thermal response time of the particle $\tau_{tp} \sim mc_{ps}/hA_s$, where A_s is the surface area, m is the mass and c_{ps} is the specific heat of the particle, respectively. The time taken by the fluid to travel over a particle $\tau_f \sim D/\left|\langle \mathbf{W} \rangle\right|$, where $\langle \mathbf{W} \rangle$ is the mean slip velocity between the particle and the fluid. The ratio of these time scales

$$\frac{\tau_{tp}}{\tau_f} \sim \left(\frac{\rho_p C_{ps}}{\rho_f C_{pf}}\right)\left(\frac{\mathrm{Re_m Pr}}{\mathrm{Nu}}\right),$$

where ρ_p is the density of the particle, ρ_f is the density of the fluid, C_{pf} is the specific heat of the fluid and Nu is the Nusselt number. Experimental studies (Gunn (1978)) of heat transfer in gas–solid systems reveal that the ratio $\mathrm{Re_m Pr/Nu} \sim O\left(1\right)$. For gas–solid flows the ratio of the density of the particles to the density of the fluid density is very high ($\sim O\left(10^3\right)$). Due to the high thermal inertia of the particles the thermal response time of the particles is about three orders of magnitude larger than the convective time scale of the fluid. Hence, the uniform temperature of a particle can be assumed to be constant in time. In addition to the assumption of a uniform and constant particle temperature, we also assume that all particles in the bed are maintained at the same temperature. The assumption that the particles equilibriate to the same surface temperature is consistent with earlier works (Gunn (1978); Acrivos et al. (1980)).

Neglecting viscous dissipation, radiation and free convection effects limits the gas–solid systems to which our simulation methodology applies. Viscous heating becomes important in flows with Mach numbers comparable or greater than unity and since we are concerned with subsonic flows, viscous dissipation is neglected in this work. Free convection is quantified by the Grashof number, which is defined as

$$\mathrm{Gr} = \frac{g\beta\left(T_f - T_s\right)D^3}{\nu_f^2}, \tag{A.1}$$

where T_f is the free stream temperature, T_s is the temperature of the solid surface, and β is the volumetric thermal expansion coefficient ($\beta = 1/T_f$ for gases). Free convection effects can be neglected if $\mathrm{Gr/Re_m^2} < 1$. For each Reynolds number, this constraint imposes an upper

limit on the particle diameter above which free convection effects cannot be neglected. For a given value of T_f/T_s, the upper limit on the particle diameter D increases with increasing Reynolds number. If a typical value of 5 is taken for the fluid to solid temperature ratio (i.e. $T_f/T_s = 5$), and air is assumed to be the fluid under terrestrial conditions ($g = 9.81\,\mathrm{m}/s^2$), then for a Reynolds number $\mathrm{Re_m} = 1$ the particle diameter has to be less than 150μm for negligible free convection. This restriction on the particle diameter becomes less severe as the Reynolds number increases.

For an isolated particle at T_s with emissivity equal to one, and surrounded by fluid at T_f, the ratio of radiation to forced convection heat transfer can be expressed as

$$\hat{q}_{rc} = \frac{q_{rad}}{q_{conv}} = \frac{\sigma(T_f + T_s)(T_f^2 + T_s^2)}{h_{fs}} = \frac{\sigma D(T_f + T_s)(T_f^2 + T_s^2)}{\mathrm{Nu}k_f},$$

where $\sigma = 5.67 \times 10^{-8}$ W/m^2·K^4 is the Stefan–Boltzmann constant. Assuming air to be the surrounding fluid at $T_f = 1000$K ($k_f = 0.060$ W/m·K) and the particle temperature $T_s = 300$K, for Stokes flow (i.e. $\mathrm{Nu} \approx 2$) the ratio of radiation to forced convection heat transfer increases linearly with particle diameter from 0.66×10^{-4} to 0.66×10^{-2}, for particle diameter in the range 1 to 100 microns. While this estimate is valid in the Stokes flow regime, with increasing Reynolds number the higher value of average Nusselt number reduces the ratio of radiation to forced convection heat transfer, thus relaxing the restriction on particle diameter. These estimates of the relative importance of forced convection to free convection and radiation heat transfer show that the restriction on particle diameter is most severe in the Stokes flow regime, and is progressively less restrictive with increasing Reynolds number. Therefore, the assumptions used in this work are indeed applicable and relevant to practical gas–solid systems.

APPENDIX B. COMPUTATION OF AVERAGE GAS-SOLID HEAT TRANSFER AND FLUID-PHASE AXIAL CONDUCTION

While in internal forced convection in a pipe flow (Incropera et al. (2006)) the heat flux vector at the pipe wall is perpendicular to the solid surface and always lies in the cross-sectional plane for pipes of constant cross-section, in gas–solid heat transfer there exists a component of the local interphase heat flux vector along the streamwise direction. This is due to the fact that the interphase normal at the particle surface changes direction in gas–solid flow with changing axial location. For quantifying the unclosed terms using PR–DNS, it turns out to be convenient to distinguish between two components of the local interphase heat flux: (i) the component along the streamwise or axial direction, which is denoted the *out-of-plane* local interphase heat flux, and (ii) the component of the local interphase heat flux normal to the streamwise direction, or the *in-plane* (see Fig. B.1).

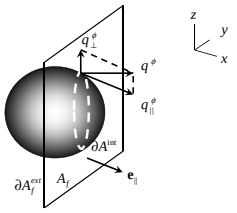

Figure B.1: Sketch of physical domain with a particle intersecting the cross-sectional plane (y-z plane) normal to the streamwise direction. The cross-sectional area occupied by fluid is denoted A_f. The exterior boundary of the fluid phase in the plane is denoted ∂A_f^{ext}. The boundary between the fluid phase and solid phase is denoted ∂A^{int}. The normal vector $\mathbf{e}_{||}$ denotes the streamwise direction. $q_{||}^\phi$ and $q_\perp^\phi$ are the *in-plane* and *out-of-plane* heat fluxes, respectively.

In order to quantify the local interphase heat flux, the PR–DNS instantaneous non-dimensional

fluid temperature equation

$$\frac{\partial \phi}{\partial t} + \frac{\partial (u_j \phi)}{\partial x_j} = -\frac{\partial q_j^{\phi}}{\partial x_j}, \tag{B.1}$$

is integrated over A_f, which denotes the portion of the cross-sectional area that is occupied by fluid, in the $y-z$ plane perpendicular to the streamwise direction. For steady flow we obtain the following equation:

$$\frac{\rho_f c_{pf}}{A} \int_{A_f} \frac{\partial (u_j \phi)}{\partial x_j} dA = \frac{1}{A} \int_{A_f} -\frac{\partial q_j^{\phi}}{\partial x_j} dA. \tag{B.2}$$

The divergence term on the right hand side of Eq. B.2 is first expressed in terms of the *out-of-plane* and *in-plane* components of the heat flux vector $\mathbf{q}^{\phi} = q_{||}^{\phi}\mathbf{e}_{||} + q_{\perp}^{\phi}\mathbf{e}_{\perp}$, and then the divergence theorem is used in the y-z plane for the in–plane component to obtain:

$$\underbrace{\frac{1}{A}\int_{A_f} \frac{\partial q_j^{\phi}}{\partial x_j} dA}_{RHS} = \underbrace{\frac{1}{A}\int_{A_f} \frac{\partial q_{||}^{\phi}}{\partial x_{||}} dA}_{I} + \underbrace{\frac{1}{A}\oint_{\partial A_f^{ext}} q_{j,\perp}^{\phi} \cdot n_{j,\perp}^{(ext)} dl}_{II} - \underbrace{\frac{1}{A}\oint_{\partial A^{int}} q_{j,\perp}^{\phi} \cdot n_{j,\perp}^{(s)} dl}_{III}, \tag{B.3}$$

where l is the perimeter of circles formed by the intersection of particles in the cross-sectional plane, $q_{j,\perp}^{\phi}$ is the *in-plane* interphase heat flux, and $n_{j,\perp}^{(s)}$ is the *in-plane* component of the outward unit normal vector on the surface of particles. Note that since the heat flux is defined in terms of the non–dimensional temperature ϕ, its units are W/(m^2-K). Term I represents the streamwise gradient of *out-of-plane* heat flux in the cross-sectional plane. Term II represents the net conduction of heat flux into this plane from exterior boundaries of the fluid phase at the domain boundary, while Term III represents *in-plane* interphase heat transfer from particle to fluid. Term II is equal to zero due to periodic boundary conditions on the non–dimensional temperature field ϕ in the y and z directions. Term III is defined as the volumetric heat transfer rate per unit temperature difference corresponding to the *in-plane* local interphase heat flux

$$q_{\perp}'''(x_{||};\omega) = \frac{1}{A}\oint_{\partial A^{int}} q_{j,\perp}^{\phi} \cdot n_{j,\perp}^{(s)} dl, \tag{B.4}$$

where the unit for $q_{\perp}'''(x_{||};\omega)$ is W/(m^3-K), and this quantity is specific to the realization ω that corresponds to a particular configuration of particles.

Term I can be decomposed into an axial conduction term and the axial (out-of-plane) contribution to the interphase heat flux using the indicator function in the fluid phase I_f as follows:

$$\frac{1}{A}\int_{A_f}\frac{\partial q_{||}^{\phi}}{\partial x_{||}}dA=\frac{1}{A}\int_{A}I_f\frac{\partial q_{||}^{\phi}}{\partial x_{||}}dA=\frac{1}{A}\int_{A}\frac{\partial I_f q_{||}^{\phi}}{\partial x_{||}}dA+\frac{1}{A}\int_{A}q_{||}^{\phi}\frac{\partial I_f}{\partial x_{||}}dA. \tag{B.5}$$

The first term on the RHS of the above equation is the axial conduction in the fluid phase (this is quantified and modeled in Part 2 of this two–part series). We define the axial conduction in the fluid phase at axial location $x_{||}$ for realization ω as

$$q_{cond}^{'''}(x_{||};\omega)=\frac{1}{A}\int_{A}\frac{\partial I_f q_{||}^{\phi}}{\partial x_{||}}dA. \tag{B.6}$$

The second term on the RHS of Eq. B.5 is the volumetric heat transfer rate corresponding to the *out-of-plane* local interphase heat flux $q_{||}^{\phi}$:

$$q_{||}^{'''}(x_{||};\omega)=\frac{1}{A}\int_{A}q_{||}^{\phi}\frac{\partial I_f}{\partial x_{||}}dA. \tag{B.7}$$

It is clearly seen that due to the presence of particles, Term I includes the axial conduction in the fluid phase and the *out-of-plane* local interphase heat flux. The latter does not appear in single-phase flow.

Combining the *in-plane* and *out-of-plane* local interphase heat flux, we define the local volumetric interphase heat transfer rate $q_{\phi}^{'''}(x_{||};\omega)$ at axial location $x_{||}$ in realization ω as

$$q_{\phi}^{'''}(x_{||};\omega)=q_{||}^{'''}(x_{||};\omega)+q_{\perp}^{'''}(x_{||};\omega). \tag{B.8}$$

Using the definition of ensemble-average in Eq. 3.8, the average gas–solid heat transfer from PR–DNS corresponding to $q_{\phi}^{'''}\left(x_{\parallel};\omega\right)$ is

$$\langle q_{\phi}^{'''}\rangle\left(x_{\parallel}\right)=\int_{\omega\in\Omega}q_{\phi}^{'''}\left(x_{\parallel};\omega\right)\,dP_{\omega}. \tag{B.9}$$

Similarly, we also define average fluid–phase axial conduction at axial location $x_{||}$ corresponding to the local axial conduction in the fluid phase $q_{cond}^{'''}\left(x_{\parallel};\omega\right)$ as

$$\langle q_{cond}^{'''}\rangle\left(x_{\parallel}\right)=\int_{\omega\in\Omega}q_{cond}^{'''}\left(x_{\parallel};\omega\right)\,dP_{\omega}\approx\frac{1}{M}\sum_{\omega=1}^{M}q_{cond}^{'''}\left(x_{\parallel};\omega\right). \tag{B.10}$$

Note that the average fluid–phase axial conduction at axial location $x_{||}$ can also be estimated using M realizations from PR-DNS data. In order to compare with the volumetric mean of average gas–solid heat transfer (see Ch. 3)

$$\overline{\langle q_{\phi}^{'''} \rangle} = \frac{1}{L} \int_0^L \langle q_{\phi}^{'''} \rangle \left(x_{\|} \right) \, dx_{||}, \tag{B.11}$$

the volumetric mean of the axial conduction in the fluid phase is defined as

$$\overline{\langle q_{cond}^{'''} \rangle} = \frac{1}{L} \int_0^L \langle q_{cond}^{'''} \rangle \left(x_{\|} \right) \, dx_{||}, \tag{B.12}$$

where L is the length of the computational domain.

In the cross-sectional plane at every axial location $x_{||}$ we define the local convective heat transfer coefficient $h(x_{||};\omega)$ corresponding to heat transfer between fluid and particles following Bird et al. (2002):

$$A q_{\phi}^{'''}(x_{||};\omega) = h(x_{||};\omega) P(x_{||};\omega) \phi_m(x_{||};\omega), \tag{B.13}$$

where $P(x_{||};\omega)$ is the perimeter formed by cutting the particles in the cross-sectional plane, A is the cross-sectional area, and the non–dimensional bulk temperature $\phi_m(x_{||};\omega)$. The left hand side term in Eq. B.13 represents the heat transfer rate per unit length of interface in the cross-sectional plane and its units are W/(m-K).

Based on the local convective heat transfer coefficient $h(x_{||};\omega)$ at axial location $x_{||}$ a *local Nusselt number* can be defined. The local Nusselt number at axial location $x_{||}$ for realization ω is:

$$\mathrm{Nu}(x_{||};\omega) = \frac{h(x_{||};\omega) D}{k_f} = \frac{A q_{\phi}^{'''}(x_{||};\omega)}{k_f P(x_{||};\omega) \phi_m(x_{||};\omega)} D. \tag{B.14}$$

The local Nusselt number can then used to calculate an *average Nusselt number* at axial location $x_{||}$, where in this context we use the term average to mean an ensemble–average over different particle configurations:

$$\left\langle \mathrm{Nu}(x_{||}) \right\rangle_M = \frac{1}{M} \sum_{\omega=1}^{M} \mathrm{Nu}(x_{||};\omega). \tag{B.15}$$

Similarly, the ensemble-average non–dimensional bulk fluid temperature $\langle \phi_m(x_{||}) \rangle$ at each axial location can also be estimated using M realizations as:

$$\langle \phi_m(x_{||}) \rangle_M = \frac{1}{M} \sum_{\omega=1}^{M} \phi_m(x_{||};\omega). \tag{B.16}$$

For the case of thermally fully developed flow past a homogeneous fixed particle assembly, the Nusselt number is homogeneous in the streamwise direction. Therefore, the average Nusselt number $\langle \mathrm{Nu} \rangle$ can be estimated by integrating Eq. B.15 over the axial length of the box:

$$\langle \mathrm{Nu} \rangle \cong \{\mathrm{Nu}\}_{M,V} = \frac{1}{L} \int_0^L \left\langle \mathrm{Nu}(x_{||}) \right\rangle_M dx_{||}, \tag{B.17}$$

where $\{\mathrm{Nu}\}_{V,M}$ denotes an estimate to the expectation $\langle \mathrm{Nu} \rangle$.

In the context of establishing grid convergence with respect to a single configuration of particles for thermally fully developed flow past a fixed assembly of particles, it is useful to define a volume–averaged Nusselt number for that realization:

$$\{\mathrm{Nu}\}_V(\omega) = \frac{1}{L} \int_0^L \mathrm{Nu}(x_{||}; \omega) dx_{||}. \tag{B.18}$$

APPENDIX C. AVERAGE GAS–SOLID HEAT TRANSFER IN THE TWO–FLUID MODEL

We derive the expression for the average volumetric interphase heat transfer rate in the two–fluid model (Eq. 3.28) for monodisperse spherical particles. Consider a cubical control volume of side L in which there is steady unidirectional flow in the $x_{||}$ direction past N spherical particles each of diameter D, with average fluid temperature $\left\langle T^{(f)} \right\rangle$ and average solid temperature $\left\langle T^{(s)} \right\rangle$. The average volumetric interphase heat transfer rate q'''_{TF} in the domain is given by

$$V q'''_{TF} = A_s \bar{h} \left(\left\langle T^{(s)} \right\rangle - \left\langle T^{(f)} \right\rangle \right), \tag{C.1}$$

where $A_s = N\pi D^2$ is the total surface area of particles, $V = L^3$ is the volume of this domain, and $\bar{h}$ is the average heat transfer coefficient. In the above equation, the ratio of particle surface area to domain volume can be written in terms of the of solid volume fraction ε_s and particle diameter as:

$$\frac{A_s}{V} = \frac{N\pi D^2}{L^3} = \frac{N\pi D^3}{6L^3}\frac{6}{D} = \frac{6\varepsilon_s}{D}. \tag{C.2}$$

Based on the definition of the Nusselt number $\mathrm{Nu_m} = \bar{h}D/k_f$, the average volumetric interphase heat transfer rate in the two–fluid model is obtained as

$$q'''_{TF} = \frac{6\varepsilon_s k_f \mathrm{Nu_m}}{D^2} \left(\left\langle T^{(s)} \right\rangle - \left\langle T^{(f)} \right\rangle \right), \tag{C.3}$$

with units $\mathrm{W/m^3}$. In this expression the difference between average fluid temperature and average solid temperature is used to compute the average volumetric interphase heat transfer rate. Note that since the two–fluid model for the average volumetric interphase heat transfer rate q'''_{TF} is defined in terms of temperature difference, its units are different from that of q'''_{ϕ}. However, Bird et al. (2002) uses the difference between bulk fluid temperature and average solid temperature to compute the average gas–solid heat transfer in a fixed bed of particles. In

the following Appendix, we will show how an improved consistent two–fluid model to compute average volumetric interphase heat transfer is developed based on bulk fluid temperature.

APPENDIX D. IMPROVED MODEL FOR AVERAGE VOLUMETRIC INTERPHASE HEAT TRANSFER RATE

The expression for the average volumetric interphase heat transfer rate in the two–fluid model derived in Appendix C assumes local homogeneity of the average fluid and solid temperature fields. Here we derive an extension of that model that is applicable to a spatially inhomogeneous average fluid temperature field, such as encountered in the gas–solid heat transfer problem simulated by PR–DNS in this work.

We begin with Eq. B.13 that relates the local volumetric interphase heat transfer rate $q_\phi'''(x_{||};\omega)$ at an axial location $x_{||}$ for realization ω with $\phi_m(x_{||};\omega)$, which is the non–dimensional difference between the bulk fluid temperature and the particle surface temperature. Taking the ensemble–average of Eq. B.13 results in

$$\left\langle q_\phi''' \right\rangle (x_{||}) = \langle h \rangle (x_{||}) \frac{\langle P \rangle (x_{||})}{A} \langle \phi_m \rangle (x_{||}), \tag{D.1}$$

where $\langle q_\phi''' \rangle (x_{||})$ (cf. Eq. 3.8) is the average volumetric interphase heat transfer rate per unit temperature difference. We *define* the inhomogeneous average heat transfer coefficient $\langle h \rangle (x_{||})$ to be

$$\langle h \rangle (x_{||}) \equiv \frac{A \left\langle q_\phi''' \right\rangle (x_{||})}{\langle P \rangle (x_{||}) \langle \phi_m \rangle (x_{||})}. \tag{D.2}$$

Note that in general the average of a product of random variables is not equal to the product of the averages, unless the random variables are uncorrelated. Here we are not assuming that the variables on the right hand side of Eq. B.13 are uncorrelated, but we are assuming in the above expression that the dependence of $\phi_m(x_{||};\omega)$ and $P(x_{||};\omega)$ on the particle configuration can be expressed as a dependence on the average solid volume fraction ε_s, and any correlation of the three right hand side terms can be captured in the definition of the inhomogeneous average heat transfer coefficient $\langle h \rangle (x_{||})$ in Eq. D.2. It should however be noted that this model cannot

capture the dependence of the inhomogeneous average heat transfer coefficient on clustered arrangements of homogeneous particle fields where the volumetric interphase heat transfer rate could depend on the pair correlation function of the particles.

Now although the average volumetric interphase heat transfer rate $\left\langle q_\phi''' \right\rangle (x_{||})$ and $\langle \phi_m \rangle (x_{||})$ are inhomogeneous in $x_{||}$ for the gas–solid flow problem considered in this work, the particle configuration is statistically homogeneous. Therefore, the average perimeter $\langle P \rangle (x_{||})$ does not depend on $x_{||}$. An simple expression for the average perimeter $\langle P \rangle$ in terms of the average solid volume fraction is now derived.

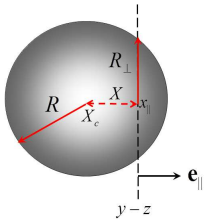

Figure D.1: Sketch of computation of the average perimeter corresponding to the intersection of the $y-z$ plane located at $x_{||}$. The sphere radius is R and $R_\perp$ is the radius of the circle formed by the intersection of the $y-z$ plane with the sphere. The axial coordinate of the sphere center is X_c and a random variable uniformly distributed in $(-R, R)$ is $X = X_c - x_{||}$. The normal vector $\mathbf{e}_{||}$ denotes the streamwise direction.

We need to calculate the average perimeter corresponding to the intersection of the y-z plane located at $x_{||}$ with a random assembly of monodisperse spheres as shown in Fig. D.1. Since the particle field is statistically homogeneous, the y-z plane intersects spheres at various axial locations, and the axial locations reckoned from their respective sphere centers are distributed with equal probability in $(-R, R)$, where R is the sphere radius. In other words, if the axial coordinate of the sphere center is X_c and the y-z plane is located at $x_{||}$, then $X = X_c - x_{||}$ is a random variable uniformly distributed in $(-R, R)$. If the radius of the circle formed by the intersection of the y-z plane with the sphere is $R_\perp$, then

$$\langle P \rangle = \langle N \rangle \int_{+R}^{-R} 2\pi R_\perp \, f_X \, dx, \tag{D.3}$$

where $\langle N \rangle$ is the average number of spheres in the volume $A \times D$ (A being the cross-sectional area of the plane and D being the sphere diameter), $f_X = 1/2R$, and the integration limits

correspond to the traversal of a sphere from just touching the plane with $X_c = x_{||} - R$ to $X_c = x_{||} + R$. Noting that $R_\perp = R\sin\theta = \sqrt{R^2 - X^2}$ the above integral can be simplified to yield

$$\langle P \rangle = 2\pi \langle N \rangle R \frac{\pi}{4} = \frac{\pi^2 \langle N \rangle D}{4}. \tag{D.4}$$

Substituting $\langle N \rangle = n\,A\,D$, where n is the number density that is related to the average solid volume fraction by $\varepsilon_s = n\pi D^3/6$, results in the following expression for $\langle P \rangle / A$:

$$\frac{\langle P \rangle}{A} = \frac{6\pi\varepsilon_s}{4D}, \tag{D.5}$$

which is close to the geometrical factor in the original two–fluid model. This leads to the final expression for the inhomogeneous average volumetric heat transfer rate

$$\left\langle q'''_\phi \right\rangle (x_{||}) = \langle h \rangle (x_{||}) \frac{6\pi\varepsilon_s}{4D} \langle \phi_m \rangle (x_{||}). \tag{D.6}$$

This expression differs from the standard two–fluid model (Eq. 3.28) in two respects. One is that it allows for an inhomogeneous average bulk fluid temperature field, and the other is that the temperature difference is between the average bulk fluid temperature and the average solid temperature. In order for this to be usable in a two–fluid model, we first need to relate the average bulk fluid temperature to the average fluid temperature. This is easily accomplished by Eq. 3.17 that relates the steady average fluid temperature to the average bulk fluid temperature as $\langle \phi^{(f)} \rangle (x_{||}) = \langle \theta^{(f)} \rangle \langle \phi_m(x_{||}) \rangle$. Now we also assume that the flow is locally fully thermally developed, in which case the heat transfer coefficient $\langle h \rangle (x_{||})$ is independent of $x_{||}$ and can be written in terms of the homogeneous average Nusselt number as $\langle h \rangle = k_f \langle \mathrm{Nu} \rangle / D$. The resulting expression is a consistent two–fluid model in terms of the average fluid temperature that allows for its inhomogeneous variation:

$$\left\langle q'''_\phi \right\rangle (x_{||}) = \frac{6\pi\varepsilon_s k_f \langle \mathrm{Nu} \rangle}{4D^2} \frac{\langle \phi^{(f)} \rangle (x_{||})}{\langle \theta^{(f)} \rangle}. \tag{D.7}$$

Now although the above expression is in terms of the inhomogeneous average fluid temperature, the two–fluid model assumes that the average fluid temperature is locally homogeneous. Therefore, we recast our model in terms of quantities that are spatially averaged over the domain length L to obtain the following consistent two–fluid model:

$$q'''_{cTF-model} = \frac{6\pi\varepsilon_s k_f \mathrm{Nu}}{4D^2 \left\langle \theta^{(f)} \right\rangle} \left(\left\langle T^{(s)} \right\rangle - \overline{\left\langle T^{(f)} \right\rangle} \right), \tag{D.8}$$

using the expression for the average non–dimensional fluid temperature as

$$\frac{\overline{\langle T^{(f)}\rangle} - \langle T^{(s)}\rangle}{\langle T_{m,in}\rangle - \langle T^{(s)}\rangle} \equiv \frac{1}{L}\int_0^L \langle \phi^{(f)}\rangle(x_{||})\, dx_{||} = \frac{1}{L}\int_0^L \frac{\left\langle T^{(f)}\right\rangle(x_{||}) - \langle T^{(s)}\rangle}{\langle T_{m,in}\rangle - \langle T^{(s)}\rangle}\, dx_{||}, \tag{D.9}$$

where the volumetric mean of average fluid temperature is

$$\overline{\langle T^{(f)}\rangle} = \frac{1}{L}\int_0^L \langle T^{(f)}\rangle(x_{||})\, dx_{||}. \tag{D.10}$$

Since $\langle T^{(f)}\rangle$ varies significantly along $x_{||}$ in many cases, the two–fluid definition of $\langle T^{(f)}\rangle$ in Eq. 3.28 is appropriately modified using Eq. D.10. Therefore, when we compare q'''_{TF} with PR–DNS data in Section 3.6, we use the following two–fluid model with average Nusselt number from PR–DNS as

$$q'''_{TF} = \frac{6\varepsilon_s k_f \mathrm{Nu}}{D^2}\left(\left\langle T^{(s)}\right\rangle - \overline{\langle T^{(f)}\rangle}\right). \tag{D.11}$$

Note that the units of $q'''_{cTF-model}$ are W/m^3 whereas the units of $\left\langle q'''_{\phi}\right\rangle$ are W/(m^3-K). In order to compare PR–DNS data with $q'''_{cTF-model}$ and q'''_{TF}, we introduce the average volumetric interphase heat transfer rate from PR–DNS $\overline{q'''_{DNS}}$:

$$\overline{q'''_{DNS}} = \frac{1}{L}\int_0^L q'''_{DNS}(x_{||})\, dx_{||} = \frac{1}{L}\int_0^L \left(\langle T_{m,in}\rangle - \langle T^{(s)}\rangle\right)\langle q'''_{\phi}\rangle(x_{||})\, dx_{||}, \tag{D.12}$$

since q'''_{DNS} can be directly extracted from PR–DNS and its unit is W/m^3. Note that the overbar in all the above equations can be dropped if the average fluid temperature satisfies the criterion of local homogeneity.

APPENDIX E. IMPLIED MODEL FOR EFFECTIVE THERMAL DIFFUSIVITY

The model for average bulk fluid temperature allows us to the scaling of effective thermal diffusivity with Péclet number. We derive an model for effective thermal diffusivity based on the exponential decay model for the average bulk fluid temperature as follows.

We have shown that α_{PT} is a function of decay length scale, scaled fluid temperature, and solid volume fraction in Eq. 4.46. Based on this expression, the non-dimensional effective thermal diffusivity can be written as

$$\frac{\alpha_{PT}+\alpha_f}{\alpha_f} = \frac{D\mathrm{Pr}}{\lambda\nu_f}\frac{\left\langle I_f u_{\parallel}^{\prime\prime(f)}\theta\right\rangle}{(1-\varepsilon_s)\left\langle\theta^{(f)}\right\rangle}+1 \tag{E.1}$$

$$= \frac{D}{\lambda}\frac{\mathrm{Pe_D}}{D(1-\varepsilon_s)^2}\frac{\left\langle I_f u_{\parallel}^{\prime\prime(f)}\theta\right\rangle}{|\langle\mathbf{W}\rangle|\left\langle\theta^{(f)}\right\rangle}+1 \tag{E.2}$$

$$= \frac{4}{6\pi\varepsilon_s\langle\mathrm{Nu}\rangle}\frac{\mathrm{Pe_D^2}}{(1-\varepsilon_s)^2}\frac{\left\langle I_f u_{\parallel}^{\prime\prime(f)}\theta\right\rangle}{|\langle\mathbf{W}\rangle|\left\langle\theta^{(f)}\right\rangle}+1., \tag{E.3}$$

where $\langle\mathrm{Nu}\rangle$ is the average Nusselt number that is computed from our Nusselt number correlation in Sun et al. (2015) as

$$\langle\mathrm{Nu}\rangle = \left[-0.46+1.77(1-\varepsilon_s)+0.69(1-\varepsilon_s)^2\right]/(1-\varepsilon_s)^3+\left[1.37-2.4(1-\varepsilon_s)+1.2(1-\varepsilon_s)^2\right]\mathrm{Re}^{0.7}\mathrm{Pr}^{1/3}. \tag{E.4}$$

In the above expression, since $C_1 = \left\langle I_f u_{\parallel}^{\prime\prime(f)}\theta\right\rangle/|\langle\mathbf{W}\rangle|\left\langle\theta^{(f)}\right\rangle$ is not sensitive to Péclet number at a fixed solid volume fraction as shown in figure E.1 (also see discussions in Section 5.3), the non-dimensional effective diffusivity only depends on Péclet number and the decay length scale D/λ for a fixed solid volume fraction.

Therefore, the effective thermal diffusivity can be further simplified as

$$\frac{\alpha_{PT}+\alpha_f}{\alpha_f} = \frac{C_1C_3}{C_2\left(C_4+C_5\mathrm{Re_m^{0.7}Pr^{1/3}}\right)}\mathrm{Pe_D^2}+1, \tag{E.5}$$

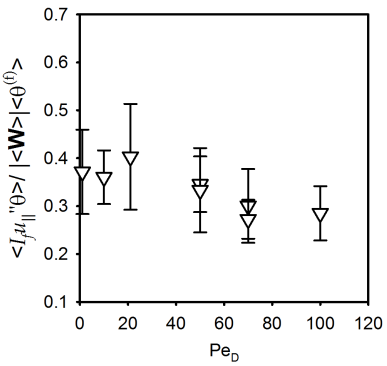

Figure E.1: Variation of $\left\langle I_f u_{\parallel}^{\prime\prime(f)} \theta \right\rangle$ normalized by mean slip velocity $|\langle \mathbf{W} \rangle|$ and the average scaled fluid temperature $\left\langle \theta^{(f)} \right\rangle$ with Péclet number at solid volume fraction of 0.1. The symbols represent $\left\langle I_f u_{\parallel}^{\prime\prime(f)} \theta \right\rangle / |\langle \mathbf{W} \rangle| \left\langle \theta^{(f)} \right\rangle$ obtained using 5 realizations, respectively. The error bars indicate 95% confidence intervals.

where $C_2 = \varepsilon_s (1 - \varepsilon_s)$, $C_3 = 4/6\pi$, $C_4 = \left[-0.46 + 1.77(1 - \varepsilon_s) + 0.69(1 - \varepsilon_s)^2\right] / (1 - \varepsilon_s)^3$, $C_5 = 1.37 - 2.4(1 - \varepsilon_s) + 1.2(1 - \varepsilon_s)^2$. The coefficients $C_1 - C_5$ are only a function of solid volume fraction. For a fixed solid volume fraction ($\varepsilon_s = 0.1$), we compare this derived expression with PR-DNS data as shown in figure 4.10. The values in our this derived model represented by the red solid line at $\mathrm{Pr} = 0.7$ are very close to our PR-DNS data that are obtained from the cases for different Prandtl number. This good agreement with PR-DNS data implies that the effective thermal diffusivity indeed has $\mathrm{Pe_D}^2$ scaling but may contain the boundary layer effect through the expression for the average Nusselt number.

APPENDIX F. PTHF FROM WAKE SCALING ANALYSIS

The unconditional ensemble-averaged PTHF $\left\langle I_f u_\parallel''^{(f)} T''^{(f)} \right\rangle$ is calculated from the wake scaling analysis as the particle number density n_p times an integral over the probability density function (pdf) of the conditionally averaged particle position f:

$$\left\langle I_f u_\parallel''^{(f)} T''^{(f)} \right\rangle = n_p \int_0^{L_w} \int\int f(x_\parallel, y, z)\, dx_\parallel dy dz, \tag{F.1}$$

where $n_p = \langle N_p \rangle / V$ is the particle number density defined as the ratio of the average number of particles $\langle N_p \rangle$ to the volume of the domain V, and L_w is the length of the wake that represents the velocity contour surrounding the particle where the value of the conditionally ensemble-averaged velocity reaches $|\langle \mathbf{W} \rangle|$ (note that since the particles are stationary, the mean slip velocity is equal to the unconditionally averaged fluid velocity). Note that the full length of the far wake is not attained in the computational domain as shown in Fig. 4.11(a) due to hydrodynamic interactions with neighbor particles (note that the two-point velocity correlation has decayed to zero within the computational domain, indicating that the domain is large enough for this to not be an artifact of periodicity). For $\mathrm{Pr} < 1$, the integral in Eq. F.1 can be analyzed in three regions: (a) the near-wake region $x_\parallel < aPe_a < aRe_a$, (b) the intermediate overlap region $aPe_a < x_\parallel < aRe_a$, and (c) the far-wake region $aRe_a < x_\parallel$. In the near-wake and intermediate overlap regions, since the integral over y and z in Eq. F.1 is dominated by a region of $O\left(a^2\right)$ where the fluid velocity disturbance is near $U_\parallel O\left(C_D\right)$ (see Eq. 4.51) we can replace the integral over $dy\, dz$ with a^2. In the far-wake region, there would be some spreading of the momentum wake and one should use $r_{WM} = a\left(x_\parallel / aRe_a\right)^{1/2}$ in Eq. 4.50. Therefore, the ensemble-averaged PTHF can be expressed as

$$n_p \int_0^{L_w} f dx_\parallel dy dz = n_p \left[a^2 \int_0^{aPe_a} f_N dx_\parallel + a^2 \int_{aPe_a}^{aRe_a} f_I dx_\parallel + \int_{aRe_a}^{L_w} f_F r_{WM}^2 dx_\parallel \right], \tag{F.2}$$

where f_N, f_I, and f_F are the functions for the near-wake, intermediate, and far-wake regions based on the expressions in Eqs. 4.51 and 4.53 as

$$f_I \approx \frac{4h}{\rho_f c_{pf} U_\parallel} \frac{aPe_a}{x_\parallel} \left(T_s - \langle T_m \rangle\right) C_D U_\parallel, \tag{F.3}$$

and

$$f_F \approx \frac{4h}{\rho_f c_{pf} U_\parallel} \frac{aPe_a}{x_\parallel} \left(T_s - \langle T_m \rangle\right) \frac{C_D U_\parallel aRe_a}{x_\parallel}. \tag{F.4}$$

Then the PTHF in the three regions can be computed as

$$\begin{aligned} \left\langle I_f u_\parallel''^{(f)} T''^{(f)} \right\rangle_N &= B_1 n_p a^2 \int_0^{aPe_a} \frac{4h}{\rho_f c_{pf} U_\parallel} \left(T_s - \langle T_m \rangle\right) C_D U_\parallel dx_\parallel \\ &= B_1 n_p a^3 \frac{4 \langle Nu \rangle \alpha_f}{D} \left(T_s - \langle T_m \rangle\right) C_D Pe_a, \end{aligned} \tag{F.5}$$

in the near-wake region $x_\parallel < aPe_a < aRe_a$, as

$$\begin{aligned} \left\langle I_f u_\parallel''^{(f)} T''^{(f)} \right\rangle_I &= B_2 n_p a^2 \int_{aPe_a}^{aRe_a} \frac{4h}{\rho_f c_{pf} U_\parallel} \frac{aPe_a}{x_\parallel} \left(T_s - \langle T_m \rangle\right) C_D U_\parallel dx_\parallel \\ &= B_2 n_p a^2 \frac{4 \langle Nu \rangle \alpha_f}{D} \left(T_s - \langle T_m \rangle\right) C_D \int_{aPe_a}^{aRe_a} \frac{aPe_a}{x_\parallel} dx_\parallel \\ &= B_2 n_p a^3 \frac{4 \langle Nu \rangle \alpha_f}{D} \left(T_s - \langle T_m \rangle\right) C_D Pe_a \ln\left(\frac{1}{\mathrm{Pr}}\right) \end{aligned} \tag{F.6}$$

in the intermediate region $aPe_a < x_\parallel < aRe_a$, and as

$$\begin{aligned} \left\langle I_f u_\parallel''^{(f)} T''^{(f)} \right\rangle_F &= B_3 n_p a^2 \int_{aRe_a}^{L_w} \frac{4h}{\rho_f c_{pf} U_\parallel} \frac{aPe_a}{x_\parallel} \left(T_s - \langle T_m \rangle\right) \frac{C_D U_\parallel aRe_a}{x_\parallel} \left(\frac{x_\parallel}{aRe_a}\right) dx_\parallel \\ &= B_3 n_p a^2 \frac{4 \langle Nu \rangle \alpha_f}{D} \left(T_s - \langle T_m \rangle\right) C_D aPe_a \int_{aRe_a}^{L_w} \frac{1}{x_\parallel} dx_\parallel \\ &= B_3 n_p a^3 \frac{4 \langle Nu \rangle \alpha_f}{D} \left(T_s - \langle T_m \rangle\right) C_D Pe_a \ln\left(\frac{L_w}{aRe_a}\right). \end{aligned} \tag{F.7}$$

in the far-wake region $aRe_a < x_\parallel$, where in Eqs. F.5–F.7. Thus, the complete expression for the PTHF is

$$\left\langle I_f u_\parallel''^{(f)} T''^{(f)} \right\rangle = Pe_a \left[k_2 \ln\left(\frac{1}{\mathrm{Pr}}\right) + k_3 \ln\left(\frac{L_w}{aRe_a}\right) + k_1 \right], \tag{F.8}$$

where k_1, k_2, and k_3 are undetermined coefficients that arise from the constants $B_1 - B_3$ and the uncertainty in the limits of integration of the overlap region. Note that the coefficients are not precisely known and their relative magnitude will determine whether or not the logarithmic

dependence on Pr is a dominant contribution in the expression. pseudo–turbulent thermal diffusivity α_{PT} can be obtained based on the PTHF as

$$\alpha_{PT} = -\left\langle I_f u_{\parallel}^{\prime\prime(f)} T^{\prime\prime(f)} \right\rangle \left(x_{\parallel}\right) \Big/ \frac{\partial \left\langle I_f T \right\rangle}{\partial x_{\parallel}} = \left\langle I_f u_{\parallel}^{\prime\prime(f)} T^{\prime\prime(f)} \right\rangle \Big/ \frac{(T_s - \langle T_m \rangle)}{D/\lambda}, \tag{F.9}$$

where the coefficient λ (see Eq. 4.27) is

$$\frac{1}{\lambda} = \frac{4Pe_D}{6\pi\varepsilon_s \langle Nu \rangle} = \frac{8Pe_a}{6\pi\varepsilon_s \langle Nu \rangle}. \tag{F.10}$$

Using the specific expressions for the velocity (cf. Eq. 4.51) and temperature fluctuations (cf. Eq. 4.53) in the three regions, we obtain the effective thermal diffusivity as

$$\begin{aligned} \frac{\alpha_{PT} + \alpha_f}{\alpha_f} &= n_p a^3 \frac{1}{\alpha_f} \frac{D}{\lambda} \frac{4 \langle Nu \rangle \alpha_f}{D} C_D Pe_a \left[B_2 \ln\left(\frac{1}{\mathrm{Pr}}\right) + B_3 \ln\left(\frac{L_w}{aRe_a}\right) + B_1 \right] + 1 \\ &= \frac{a^3 N_p}{V} \frac{D}{\lambda} \frac{4 \langle Nu \rangle}{D} C_D Pe_a \left[B_2 \ln\left(\frac{1}{\mathrm{Pr}}\right) + B_3 \ln\left(\frac{L_w}{aRe_a}\right) + B_1 \right] + 1 \\ &= 0.065 \mathrm{Pe_D^2} \left[B_2 \ln\left(\frac{1}{\mathrm{Pr}}\right) + B_3 \ln\left(\frac{L_w}{aRe_a}\right) + B_1 \right] + 1. \end{aligned} \tag{F.11}$$

where the number density is $n_p = \langle N_p \rangle / V = 3\varepsilon_s/(4\pi a^3)$ and the drag coefficient can be obtained from the normalized average drag force for the case of Reynolds number of 100 and solid volume fraction of 0.1 ($\langle F \rangle = 6.7$ and $U_{\parallel} = |\langle \mathbf{W} \rangle|$) as

$$C_D = \frac{\langle F \rangle 3\pi\mu_f D |\langle \mathbf{W} \rangle| (1-\varepsilon_s)}{\rho_f U_{\parallel}^2 \pi a^2} = \frac{12 \langle F \rangle (1-\varepsilon_s)^2}{Re_m} = 0.65. \tag{F.12}$$

Note that since hydrodynamic interactions with neighbor particles cause the velocity to decay before achieving a far-wake behavior, $\ln(L_w/aRe_a)$ is not present in practice.

The wake analysis of the scaling of the effective thermal diffusivity with Péclet number in Eq. F.11 is compared with PR-DNS data in Fig. 4.10. With assuming $B_1 = 1$, $B_2 = 1$ and the neglect of $\ln(L_w/aRe_a)$ in Eq. F.11, the results obtained from the wake scaling analysis over a range of $0.01 < \mathrm{Pr} < 0.7$ agree very well with the PR-DNS data. The $\mathrm{Pe_D^2}$ scaling itself comes from there being a wake and from realizing that decay length is the scaling to use for mean temperature gradient. Therefore, this analysis of the hydrodynamic and thermal wakes behind the particle gives a physical explanation for the existence of a $\mathrm{Pe_D^2}$ scaling in effective thermal diffusivity in the regime of high Reynolds number and low Prandtl number.

APPENDIX G. DERIVATION OF THE FLUID-PHASE AXIAL CONDUCTION MODEL

The standard model ofBenyahia et al. (2012) for the fluid phase axial conduction term $\partial \langle I_f q_j \rangle / \partial x_j$ in the two-fluid approach is

$$\frac{\partial}{\partial x_j} \langle I_f q_j \rangle = -\varepsilon_f k_f \frac{\partial^2 \langle T^{(f)} \rangle}{\partial x_j \partial x_j}. \tag{G.1}$$

In the case of single-phase turbulence this term would not require closure in the average temperature equation because the operations of differentiation and averaging in single-phase flows commute, leading to the exact relation $\partial \langle q_j \rangle / \partial x_j = -k \partial^2 \langle T \rangle / \partial x_j \partial x_j$. However, in two-phase flows this is a modeling assumption because differentiation of terms such as $I_f q_j$ that involve the indicator function results in additional terms.

We prefer to develop the average conduction model in terms of non-dimensional temperature ϕ, which represents the difference between the fluid and solid temperature non-dimensionalized by a reference temperature scale $(T_{m,in} - T_s)$, because this avoids any spurious dependence of the modeled terms on the choice of reference temperature. We begin by expanding the average conduction term in Eq. 4.1 written in terms of the non-dimensional temperature ϕ as:

$$\begin{aligned} \frac{\partial}{\partial x_j} \left\langle I_f q_j^{\phi} \right\rangle &= \frac{\partial}{\partial x_j} \left\langle -I_f k_f \frac{\partial \phi}{\partial x_j} \right\rangle \\ &= \frac{\partial}{\partial x_j} \left\langle -k_f \frac{\partial I_f \phi}{\partial x_j} + k_f \phi \frac{\partial I_f}{\partial x_j} \right\rangle (x_j) \\ &= -k_f \frac{\partial^2 \langle I_f \phi \rangle}{\partial x_j \partial x_j} + k_f \frac{\partial}{\partial x_j} \left\langle \phi \frac{\partial I_f}{\partial x_j} \right\rangle, \end{aligned} \tag{G.2}$$

where in the last expression it is assumed that the fluid thermal conductivity k_f is constant. The second term on the right hand side of Eq. G.2 is zero because of continuity of the temperature field at the gas-solid interface. Substituting the definition for the phasic average of ϕ from

Eq. 4.2 into the first term on the right hand side of Eq. G.2, and noting that ε_f is a constant due to statistical homogeneity of the particle field in the problem considered in this work, results in the standard model for average conduction in the fluid phase:

$$\frac{\partial}{\partial x_j}\left\langle I_f q_j^{\phi}\right\rangle = -k_f\varepsilon_f \frac{\partial^2\left\langle \phi^{(f)}\right\rangle}{\partial x_j \partial x_j}. \tag{G.3}$$

Recalling that in our problem setup there is no average heat flux in the cross-stream directions due to periodicity, results in the standard model for average axial conduction in the fluid phase:

$$\frac{\partial}{\partial x_{\parallel}}\left\langle I_f q_{\parallel}^{\phi}\right\rangle = -k_f\varepsilon_f \frac{\partial^2\left\langle \phi^{(f)}\right\rangle}{\partial x_{\parallel} \partial x_{\parallel}}. \tag{G.4}$$

Equivalently, this model can be written in terms of the average heat flux in the fluid phase as:

$$\left\langle I_f q_{\parallel}^{\phi}\right\rangle = -k_f\left\langle I_f \frac{\partial \phi}{\partial x_{\parallel}}\right\rangle = -k_f\left\langle \frac{\partial I_f \phi}{\partial x_{\parallel}}\right\rangle = -k_f\varepsilon_f \frac{\partial\left\langle \phi^{(f)}\right\rangle}{\partial x_{\parallel}}, \tag{G.5}$$

where ε_f is assumed constant due to the statistical homogeneity of the particle field.

We would like to evaluate this model using PR-DNS data. Both expressions (Eq. G.4 and G.5) involve taking derivatives of $\left\langle \phi^{(f)}\right\rangle$, which is a phasic average that must be estimated from a finite number of PR-DNS realizations. Therefore, we first examine the effect of statistical variability in $\left\langle \phi^{(f)}\right\rangle$ (arising from a finite number of realizations) on the average heat flux in the fluid phase. Figure G.1 shows the variation of average non-dimensional fluid temperature and its gradient from PR-DNS data for $\mathrm{Re_m} = 100$ and $\varepsilon_s = 0.4$.

As the left panel (Fig. G.1(a)) shows, the gradient of the non-dimensional average fluid temperature $-D\partial\left\langle I_f\phi\right\rangle/\partial x_{\parallel}$ denoted by blue open circles (I, bottom left) using 5 MIS has high fluctuations even though the average non-dimensional fluid temperature $\left\langle \phi^{(f)}\right\rangle$ (top left) has relatively small variation with axial location. With a large number of MIS (50) the fluctuation of $-D\partial\left\langle I_f\phi\right\rangle/\partial x_{\parallel}$ is reduced as shown in the bottom right panel (Fig. G.1(b)) by the blue open circle (I). This is because the variation of the average non-dimensional fluid temperature $\left\langle \phi^{(f)}\right\rangle$ (top right panel, Fig. G.1(b)) with 50 MIS is much lower than the one using 5 MIS. However, small fluctuations in the gradient of the average fluid temperature still remain.

The left panel (bottom left, Fig. G.1(a)) also shows that the axial variation of the average non-dimensional fluid-phase temperature gradient $-D\left\langle I_f\partial\phi/\partial x_{\parallel}\right\rangle$ (denoted by red open circles (II)) has high fluctuations using 5 MIS. According to Eq. G.5, $-D\left\langle I_f\partial\phi/\partial x_{\parallel}\right\rangle$ (II) should

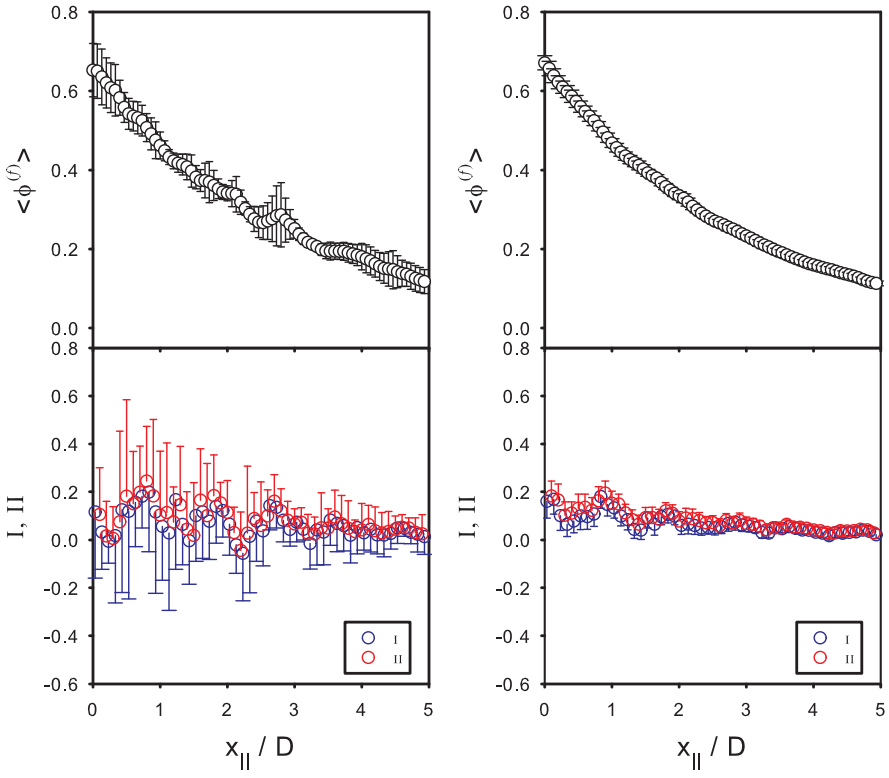

(a) 5 MIS (b) 50 MIS

Figure G.1: Variation of average non-dimensional fluid temperature $\left\langle \phi^{(f)} \right\rangle$ and normalized temperature gradient in the fluid phase from PR-DNS data using (a) 5 MIS and (b) 50 MIS at $\mathrm{Re_m} = 100$ and $\varepsilon_s = 0.4$. The white open circles are average non-dimensional fluid temperature. The blue open circles (I) represent $-D\partial \left\langle I_f \phi \right\rangle / \partial x_{\|}$ and the red open circles (II) represent $-D \left\langle I_f \partial\phi / \partial x_{\|} \right\rangle$ (see Eq. G.2). Error bars in both panels represent 95% confidence intervals inferred from (a) 5 MIS and (b) 50 MIS, respectively. For clarity, only half error bars for the blue and red open circles are shown in this figure.

be equal to $-D\partial \left\langle I_f \phi \right\rangle / \partial x_{\|}$ (I). However, in the bottom left panel, the difference between $-D\partial \left\langle I_f \phi \right\rangle / \partial x_{\|}$ (I) and $-D \left\langle I_f \partial\phi / \partial x_{\|} \right\rangle$ (II) can be seen clearly if only a few realizations (5 MIS) are simulated. This difference arises from two sources. One is that there is always statistical variability in averaging the non-dimensional fluid-phase temperature gradient $I_f \partial\phi / \partial x_{\|}$ from a finite number of realizations. Note that the variation of the average non-dimensional fluid-phase temperature gradient using 50 MIS is much smaller compared to the one obtained from 5 MIS. Correspondingly, the difference between $-D\partial \left\langle I_f \phi \right\rangle / \partial x_{\|}$ (I) and $-D \left\langle I_f \partial\phi / \partial x_{\|} \right\rangle$ (II) due to statistical variability also becomes smaller for a large number of realizations (50

MIS), as shown in the bottom right panel (Fig. G.1(b)). The average relative error between $-D\left\langle I_f \partial\phi/\partial x_\parallel \right\rangle$ and $-D\partial\left\langle I_f\phi\right\rangle/\partial x_\parallel$ is less than 15% using 50 MIS. The other reason for the difference between (I) and (II) is that, as shown above, statistical variability in $\left\langle \phi^{(f)} \right\rangle$ arising from a finite number of realization results in small scale spatial variation. Taking derivatives of $\left\langle \phi^{(f)} \right\rangle$ amplifies these variations. Thus, using PR-DNS data, we verify that the average non-dimensional fluid-phase temperature gradient $-D\left\langle I_f \partial\phi/\partial x_\parallel \right\rangle$ can be approximated by $-D\partial\left\langle I_f\phi\right\rangle/\partial x_\parallel$ in a fixed homogeneous particle assembly. However, it should be noted that since fluctuations in the average temperature gradient exist, these will result in more noise in the second derivative of average temperature.

APPENDIX H. STATISTICAL REPRESENTATION OF TWO-PHASE FLOW

The statistical representation of a two-phase flow using the Eulerian-Eulerian (EE) approach is present. In the EE approach, the two-phase flow is represented as a random field (Drew (1983)). Fundamental events and corresponding probabilities associated with a two-phase flow in the EE framework are briefly described as follows. More details can be found in Pai and Subramaniam (2009).

H.1 Random-field representation

In order to consider a realization ω of a two-phase flow with two distinct phases, the indicator function for the EE description $I_\beta(\mathbf{x}, t)$ is introduced. Let the two-phase flow be composed of a carrier phase (such as gas phase) and a dispersed phase (such as solid phase). The indicator function $I_\beta(\mathbf{x}, t)$ for the βth phase at a single space-time location in a single realization is defined as

$$I_\beta(\mathbf{x}, t) = \begin{cases} 1 & \text{if } \mathbf{x} \text{ is in phase } \beta \text{ at time } t, \\ 0 & \text{if } \mathbf{x} \text{ is not in phase } \beta \text{ at time } t, \end{cases} \tag{H.1}$$

In two-phase flow, the phase indicator functions satisfy the relation

$$\sum_{\beta=\{f,s\}} I_\beta(\mathbf{x}, t) = 1, \tag{H.2}$$

where $\beta = \{f, s\}$, and f represents the carrier phase and s represents the dispersed phase.

In each realization, the instantaneous two-phase velocity field $\mathbf{U}(\mathbf{x}, t)$, the instantaneous composition field $\boldsymbol{\phi}(\mathbf{x}, t)$ and the thermodynamic mass density field $\rho(\boldsymbol{\phi})$, which are defined

in all phases, are vector fields defined at every location $\mathbf{x}$ in physical space. The mass density ρ only depend on the set of compositions $\boldsymbol{\phi}(\boldsymbol{x},t)$ (details can be found in Pope (1985)), where the set of compositions containing the species

$$\phi_\alpha = \begin{cases} Y_\alpha, & \alpha = 1,...n-1 \\ c_p T, & \alpha = n \end{cases} \tag{H.3}$$

and the enthalpy

$$\phi_\alpha = c_p T,\ \alpha = n$$

provides a complete description of the thermo-chemical properties of the carrier-phase mixture.

The events can be used to characterize the state of a two-phase flow at a single space-time location $(\mathbf{x},t)$, and each leads to different probabilities. A complete Eulerian single-point joint probability density function (PDF) description of the two-phase flow will require the event

$$E_1 = \left[\mathbf{U}(\boldsymbol{x},t) \in (\boldsymbol{V}, \mathbf{V}+\mathrm{d}\mathbf{V}), \boldsymbol{\phi}(\boldsymbol{x},t) \in (\boldsymbol{\psi}, \boldsymbol{\psi}+\mathrm{d}\boldsymbol{\psi}), I_\beta(\boldsymbol{x},t) = 1\right], \tag{H.4}$$

where $\mathbf{U}(\boldsymbol{x},t)$ and $\boldsymbol{\phi}(\boldsymbol{x},t)$ are random variables, $\mathbf{V}$ and $\boldsymbol{\psi}$ are the sample space variable corresponding to the random variable $\mathbf{U}(\boldsymbol{x},t)$ and $\boldsymbol{\phi}(\boldsymbol{x},t)$. Corresponding to the joint event E_1, two marginal events are

$$E_2 = \left[\mathbf{U}(\boldsymbol{x},t) \in (\boldsymbol{V}, \mathbf{V}+\mathrm{d}\mathbf{V}), \boldsymbol{\phi}(\boldsymbol{x},t) \in (\boldsymbol{\psi}, \boldsymbol{\psi}+\mathrm{d}\boldsymbol{\psi})\right], \tag{H.5}$$

and

$$E_3^{(\beta)} = \left[I_\beta(\boldsymbol{x},t) = 1\right]. \tag{H.6}$$

There are two important conditional events

$$E_4 = \left[\mathbf{U}(\boldsymbol{x},t) \in (\boldsymbol{V}, \mathbf{V}+\mathrm{d}\mathbf{V}), \boldsymbol{\phi}(\boldsymbol{x},t) \in (\boldsymbol{\psi}, \boldsymbol{\psi}+\mathrm{d}\boldsymbol{\psi}) \,|I_\beta = 1\right], \tag{H.7}$$

and

$$E_5 = \left[I_\beta(\boldsymbol{x},t) = 1 | \mathbf{U} = \mathbf{V}, \boldsymbol{\phi} = \boldsymbol{\psi}\right]. \tag{H.8}$$

where E_4 is the event that $\mathbf{U}(\boldsymbol{x},t)$ belongs to $(\boldsymbol{V},\mathbf{V}+\mathrm{d}\mathbf{V})$ and $\boldsymbol{\phi}(\boldsymbol{x},t)$ belongs to $(\boldsymbol{\psi},\boldsymbol{\psi}+\mathrm{d}\boldsymbol{\psi})$ conditional on the presence of phase β at location $\boldsymbol{x}$, while E_5 is the event that the location $\boldsymbol{x}$ is occupied by phase β conditional on $\mathbf{U}=\mathbf{V},\boldsymbol{\phi}=\boldsymbol{\psi}$ at the same location.

Based on these above events, the probabilities corresponding to each of the above events are

$$P\left[E_2\right]=P\left[\mathbf{U}(\boldsymbol{x},t)\in(\boldsymbol{V},\mathbf{V}+\mathrm{d}\mathbf{V}),\boldsymbol{\phi}(\boldsymbol{x},t)\in(\boldsymbol{\psi},\boldsymbol{\psi}+\mathrm{d}\boldsymbol{\psi})\right]=f_{\mathbf{U}\phi}(\mathbf{V},\boldsymbol{\psi};\boldsymbol{x},t)\mathrm{d}\mathbf{V}\mathrm{d}\boldsymbol{\psi}, \quad \text{(H.9)}$$

$$P\left[E_5\right]=P\left[I_\beta(\boldsymbol{x},t)=1|\mathbf{U}=\mathbf{V},\boldsymbol{\phi}=\boldsymbol{\psi}\right]=p_\beta(\boldsymbol{x},t\,|\mathbf{V},\boldsymbol{\psi}), \quad \text{(H.10)}$$

$$\begin{aligned} P\left[E_1\right] &= P\left[I_\beta(\boldsymbol{x},t)=1|\mathbf{U}=\mathbf{V},\boldsymbol{\phi}=\boldsymbol{\psi}\right]P\left[\boldsymbol{U}(\boldsymbol{x},t)\in(\boldsymbol{V},\mathbf{V}+\mathrm{d}\mathbf{V}),\boldsymbol{\phi}(\boldsymbol{x},t)\in(\boldsymbol{\psi},\boldsymbol{\psi}+\mathrm{d}\boldsymbol{\psi})\right] \\ &= p_\beta(\boldsymbol{x},t\,|\boldsymbol{V},\boldsymbol{\psi})f_{\mathbf{U}\phi}\mathrm{d}\boldsymbol{V}\mathrm{d}\boldsymbol{\psi}, \end{aligned} \quad \text{(H.11)}$$

$$P\left[E_3^{(\beta)}\right] = \iint P\left[I_\beta=1\,|\mathbf{U}=\boldsymbol{V},\boldsymbol{\phi}=\boldsymbol{\psi}\right]f_{\boldsymbol{U}\phi}\mathrm{d}\boldsymbol{V}\mathrm{d}\boldsymbol{\psi}=\iint p_\beta f_{\boldsymbol{U}\phi}\mathrm{d}\boldsymbol{V}\mathrm{d}\boldsymbol{\psi}=\alpha_\beta(\boldsymbol{x},t), \quad \text{(H.12)}$$

$$\begin{aligned} P\left[E_4\right] &= P\left[\mathbf{U}(\boldsymbol{x},t)\in(\boldsymbol{V},\mathbf{V}+\mathrm{d}\mathbf{V}),\boldsymbol{\phi}(\boldsymbol{x},t)\in(\boldsymbol{\psi},\boldsymbol{\psi}+\mathrm{d}\boldsymbol{\psi})\,|I_\beta=1\right] \\ &= \frac{p_\beta f_{\boldsymbol{U}\phi}}{\alpha_\beta(\boldsymbol{x},t)}\mathrm{d}\boldsymbol{V}\mathrm{d}\boldsymbol{\psi}, \end{aligned} \quad \text{(H.13)}$$

where p_β is a phase probability function, $\alpha_\beta\in[0,1]$ is a probability mass function in phase β.

H.2 Random-field statistical representation

Analogous to the single-phase PDF, in order to account for the mass in two-phase flow it is necessary to work with mass-weighted or Favre quantities. The Favre fine-grained mass density of $\mathbf{U}\left(\mathbf{x},t\right)$ and $\boldsymbol{\phi}\left(\mathbf{x},t\right)$ conditional on phase β at location $\mathbf{x}$ and time t is defined as

$$\mathcal{F}'_{\mathbf{U}\boldsymbol{\phi}|I_\beta} = \rho\left(\boldsymbol{\phi}\right) I_\beta\left(\mathbf{x},t\right)\delta\left(\mathbf{U}\left(\mathbf{x},t\right)-\mathbf{V}\right)\delta\left(\boldsymbol{\phi}\left(\mathbf{x},t\right)-\boldsymbol{\psi}\right). \tag{H.14}$$

The expectation of $\mathcal{F}'_{\mathbf{U}\boldsymbol{\phi}|I_\beta}$ defines the Favre mass density conditional on phaseβ :

$$\mathcal{F}_{\mathbf{U}\boldsymbol{\phi}|I_\beta}\left(\mathbf{V},\boldsymbol{\psi},\mathbf{x},t\right) = \left\langle \mathcal{F}'_{\mathbf{U}\boldsymbol{\phi}|I_\beta} \right\rangle. \tag{H.15}$$

where the angled bracket $\langle\cdot\rangle$ represents an expectation over all possible realizations in the $\mathbf{V}-\psi$ space. There is a useful connection between the Favre mass density conditional on phaseβ $\mathcal{F}_{\mathbf{U}\boldsymbol{\phi}|I_\beta}$ and the PDF $f_{\mathbf{U}\boldsymbol{\phi}}$ or density-weighted PDF $\tilde{f}_{\mathbf{U}\boldsymbol{\phi}|I_\beta}$ as

$$\begin{aligned}
\mathcal{F}_{\mathbf{U}\boldsymbol{\phi}|I_\beta} &= \left\langle \rho\left(\boldsymbol{\phi}\right) I_\beta\left(\mathbf{x},t\right)\delta\left(\mathbf{U}\left(\mathbf{x},t\right)-\mathbf{V}\right)\delta\left(\boldsymbol{\phi}\left(\mathbf{x},t\right)-\boldsymbol{\psi}\right)\right\rangle \\
&= \int \delta\left(\mathbf{V}'-\mathbf{V}\right)\delta\left(\boldsymbol{\psi}'-\boldsymbol{\psi}\right)\left\langle \rho\left(\boldsymbol{\phi}\right) I_\beta \,|\mathbf{U}=\mathbf{V}',\boldsymbol{\phi}=\boldsymbol{\psi}'\right\rangle f_{\mathbf{U}\boldsymbol{\phi}}\left(\mathbf{V}',\boldsymbol{\psi}'\right)\mathrm{d}\mathbf{V}'\mathrm{d}\boldsymbol{\psi}' \\
&= \left\langle \rho\left(\boldsymbol{\phi}\right) I_\beta \,|\mathbf{V},\boldsymbol{\psi}\right\rangle f_{\mathbf{U}\boldsymbol{\phi}}\left(\mathbf{V},\boldsymbol{\psi}\right) \\
&= \left\langle \rho I_\beta\right\rangle \tilde{f}_{\mathbf{U}\boldsymbol{\phi}|I_\beta}\left(\mathbf{V},\boldsymbol{\psi}\right).
\end{aligned} \tag{H.16}$$

Note that the integration of $\mathcal{F}_{\mathbf{U}\boldsymbol{\phi}|I_\beta}$ over all velocity-composition space results in

$$\int_{\mathbf{V}}\int_{\boldsymbol{\psi}} \mathcal{F}_{\mathbf{U}\boldsymbol{\phi}|I_\beta}\left(\mathbf{V},\boldsymbol{\psi},\mathbf{x},t\right)\mathrm{d}\mathbf{V}\mathrm{d}\boldsymbol{\psi} = \left\langle \rho I_\beta\right\rangle\left(\mathbf{x},t\right). \tag{H.17}$$

The relationship between the mass density and the mass-weighted phasic velocity PDF is given by $\mathcal{F}_{\mathbf{U}\boldsymbol{\phi}|I_\beta} = \left\langle \rho I_\beta\right\rangle \tilde{f}_{\mathbf{U}\boldsymbol{\phi}|I_\beta}$. Density-weighted means can be defined as

$$\left\langle \widetilde{Q\left(\mathbf{U},\boldsymbol{\phi}\right)} \right\rangle\left(\mathbf{x},t\right) = \frac{1}{\left\langle \rho I_\beta\right\rangle}\int_{\mathbf{V}}\int_{\boldsymbol{\psi}} Q\left(\mathbf{V},\boldsymbol{\psi}\right)\mathcal{F}_{\mathbf{U}\boldsymbol{\phi}|I_\beta}\,\mathrm{d}\mathbf{V}\mathrm{d}\boldsymbol{\psi} = \int_{\mathbf{V}}\int_{\boldsymbol{\psi}} Q\left(\mathbf{V},\boldsymbol{\psi}\right)\tilde{f}_{\mathbf{U}\boldsymbol{\phi}|I_\beta}\,\mathrm{d}\mathbf{V}\mathrm{d}\boldsymbol{\psi}. \tag{H.18}$$

APPENDIX I. DERIVATION OF PDF TRANSPORT EQUATION USING THE DELTA FUNCTION APPROACH

The object of this Appendix is to derive the phase-conditioned single-point velocity-composition joint PDF transport equation for Favre mass density PDF $\mathcal{F}_{\boldsymbol{U}\phi|I_\beta}$. Pai and Subramaniam (2009) have used the delta function method to derive the a phase-conditioned single-point velocity PDF. Following the similar procedure, a phase-conditioned velocity-composition PDF transport equation can be derived. Although the transport equation for the two-phase PDF can be obtained from the PDF $f'_{\boldsymbol{U}\phi|I_\beta}$ (see Appendix H), it is necessary to work with mass-weighted quantities. Based on the instantaneous continuity equation

$$\frac{\partial \rho}{\partial t} + \frac{\partial \rho U_j}{\partial x_j} = 0, \tag{I.1}$$

the momentum equation

$$\rho \frac{DU_i}{Dt} = \rho A_i, \tag{I.2}$$

and the composition equation

$$\rho \frac{D\phi_\alpha}{Dt} = \rho \Theta_\alpha, \tag{I.3}$$

where $\boldsymbol{A}$ is the acceleration

$$\rho A_i(\boldsymbol{x}, t) = \frac{\partial \tau_{ji}}{\partial x_j} - \frac{\partial p}{\partial x_i} + \rho g_i, \tag{I.4}$$

and $\boldsymbol{\Theta}$ is the rate of change of composition that is composed of a diffusion and a reaction source term

$$\rho\Theta_\alpha(\boldsymbol{x},t) = -\frac{\partial J_i^\alpha}{\partial x_i} + \rho S_\alpha, \tag{I.5}$$

the transport equation for the fine-grained mass density $\mathcal{F}'_{\boldsymbol{U}\phi|I_\beta}$ can be derived from two expressions of $\mathcal{F}'_{\boldsymbol{U}\phi|I_\beta}$. The first expressions forms the substantial derivative of $\mathcal{F}'_{\boldsymbol{U}\phi|I_\beta}$ as

$$\frac{D\mathcal{F}'_{\boldsymbol{U}\phi|I_\beta}}{Dt} = \frac{\partial \mathcal{F}'_{\boldsymbol{U}\phi|I_\beta}}{\partial t} + U_k \frac{\partial \mathcal{F}'_{\boldsymbol{U}\phi|I_\beta}}{\partial x_k}. \tag{I.6}$$

Using chain rule, the second term in the right-hand side of Eq. I.6 becomes

$$U_k \frac{\partial \mathcal{F}'_{\boldsymbol{U}\phi|I_\beta}}{\partial x_k} = \frac{\partial U_k \mathcal{F}'_{\boldsymbol{U}\phi|I_\beta}}{\partial x_k} - \mathcal{F}'_{\boldsymbol{U}\phi|I_\beta}\frac{\partial U_k}{\partial x_k} = V_k \frac{\partial \mathcal{F}'_{\boldsymbol{U}\phi|I_\beta}}{\partial x_k} - \mathcal{F}'_{\boldsymbol{U}\phi|I_\beta}\frac{\partial U_k}{\partial x_k}. \tag{I.7}$$

Eq. I.6 can be rewritten as

$$\frac{D\mathcal{F}'_{\boldsymbol{U}\phi|I_\beta}}{Dt} = \frac{\partial \mathcal{F}'_{\boldsymbol{U}\phi|I_\beta}}{\partial t} + V_k \frac{\partial \mathcal{F}'_{\boldsymbol{U}\phi|I_\beta}}{\partial x_k} - \mathcal{F}'_{\boldsymbol{U}\phi|I_\beta}\frac{\partial U_k}{\partial x_k}. \tag{I.8}$$

The second expression forming the substantial derivative of $\mathcal{F}'_{\boldsymbol{U}\phi|I_\beta}$can be obtained from chain rules as

$$\frac{D\mathcal{F}'_{\boldsymbol{U}\phi|I_\beta}}{Dt} = \frac{\partial \mathcal{F}'_{\boldsymbol{U}\phi|I_\beta}}{\partial V_k}\frac{DU_k}{Dt} + \frac{\partial \mathcal{F}'_{\boldsymbol{U}\phi|I_\beta}}{\partial \psi_\alpha}\frac{D\phi_\alpha}{Dt} + \frac{\partial \mathcal{F}'_{\boldsymbol{U}\phi|I_\beta}}{\partial \rho I_\beta}\frac{D\rho I_\beta}{Dt}. \tag{I.9}$$

The first term of Eq. I.9 can be written using Appendix H.6-8 of Pope (2000) as

$$\frac{\partial \mathcal{F}'_{\boldsymbol{U}\phi|I_\beta}}{\partial U_k}\frac{DU_k}{Dt} = -\frac{\partial}{\partial V_k}\left[\left(\frac{DU_k}{Dt}\right)\mathcal{F}'_{\boldsymbol{U}\phi|I_\beta}\right]. \tag{I.10}$$

The third term of Eq. I.9 is expressed based on the definition of the fine-grained mass density $\mathcal{F}'_{\boldsymbol{U}\phi|I_\beta}$ as

$$\frac{\partial \mathcal{F}'_{\boldsymbol{U}\phi|I_\beta}}{\partial \rho I_\beta}\frac{D\rho I_\beta}{Dt} = \delta(U_k(\boldsymbol{x},t) - V_k)\delta(\phi_\alpha(\boldsymbol{x},t) - \psi_\alpha)\frac{D\rho I_\beta}{Dt} = \frac{\mathcal{F}'_{\boldsymbol{U}\phi|I_\beta}}{\rho I_\beta}\frac{D\rho I_\beta}{Dt}. \tag{I.11}$$

The second term of Eq. I.9 can be expressed using the sifting of property of the delta function ($\delta^{(1)}(x-a) = -\delta^{(1)}(a-x)$) and $D\rho(\phi_\alpha)/Dt = 0$ as

$$
\begin{aligned}
\frac{\partial \mathcal{F}'_{\boldsymbol{U}\phi|I_\beta}}{\partial \phi_\alpha}\frac{D\phi_\alpha}{Dt} &= \frac{\partial}{\partial \phi_\alpha}\rho(\phi_\alpha)I_\beta(\boldsymbol{x},t)\delta(U_k(\boldsymbol{x},t)-V_k)\delta(\phi_\alpha(\boldsymbol{x},t)-\psi_\alpha)\frac{D\phi_\alpha}{Dt} \\
&= \frac{\mathcal{F}'_{\boldsymbol{U}\phi|I_\beta}}{\rho(\phi_\alpha)}\frac{\partial \rho(\phi_\alpha)}{\partial \phi_\alpha}\frac{D\phi_\alpha}{Dt} + \rho(\phi_\alpha)\left[\frac{\partial}{\partial \phi_\alpha}I_\beta(\boldsymbol{x},t)\delta(U_k(\boldsymbol{x},t)-V_k)\delta(\phi_\alpha(\boldsymbol{x},t)-\psi_\alpha)\right]\frac{D\phi_\alpha}{Dt} \\
&= \frac{\mathcal{F}'_{\boldsymbol{U}\phi|I_\beta}}{\rho(\phi_\alpha)}\frac{D\rho(\phi_\alpha)}{Dt} + \rho(\phi_\alpha)I_\beta(\boldsymbol{x},t)\delta(U_k(\boldsymbol{x},t)-V_k)\delta^{(1)}(\phi_\alpha(\boldsymbol{x},t)-\psi_\alpha)\frac{D\phi_\alpha}{Dt} \\
&= 0-\rho(\phi_\alpha)I_\beta(\boldsymbol{x},t)\delta(U_k(\boldsymbol{x},t)-V_k)\delta^{(1)}(\psi_\alpha-\phi_\alpha(\boldsymbol{x},t))\frac{D\phi_\alpha}{Dt} \\
&= -\rho(\phi_\alpha)I_\beta(\boldsymbol{x},t)\delta(U_k(\boldsymbol{x},t)-V_k)\frac{\partial}{\partial \psi_\alpha}\delta(\psi_\alpha-\phi_\alpha(\boldsymbol{x},t))\frac{D\phi_\alpha}{Dt} \\
&= -\frac{\partial \mathcal{F}'_{\boldsymbol{U}\phi|I_\beta}}{\partial \psi_\alpha}\frac{D\phi_\alpha}{Dt} \\
&= -\frac{\partial}{\partial \psi_\alpha}\left[\left(\frac{D\phi_\alpha}{Dt}\right)\mathcal{F}'_{\boldsymbol{U}\phi|I_\beta}\right]. \qquad \text{(I.12)}
\end{aligned}
$$

Thus, the transport equation for the fine-grained mass density can be written as

$$
\begin{aligned}
\frac{\partial \mathcal{F}'_{\boldsymbol{U}\phi|I_\beta}}{\partial t}+V_k\frac{\partial \mathcal{F}'_{\boldsymbol{U}\phi|I_\beta}}{\partial x_k} &= -\frac{\partial}{\partial V_k}\left[\left(\frac{\partial U_k}{\partial t}+U_j\frac{\partial U_k}{\partial x_j}\right)\mathcal{F}'_{\boldsymbol{U}\phi|I_\beta}\right] \\
&\quad -\frac{\partial}{\partial \psi_\alpha}\left[\left(\frac{\partial \phi_\alpha}{\partial t}+U_j\frac{\partial \phi_\alpha}{\partial x_j}\right)\mathcal{F}'_{\boldsymbol{U}\phi|I_\beta}\right] \\
&\quad +\frac{\mathcal{F}'_{\boldsymbol{U}\phi|I_\beta}}{\rho I_\beta}\left(\frac{\partial \rho I_\beta}{\partial t}+\frac{\partial \rho I_\beta U_k}{\partial x_k}\right). \qquad \text{(I.13)}
\end{aligned}
$$

Using the topological equation by Drew (1983) as

$$
\frac{\partial I_\beta}{\partial t}+U_k^{(I)}\frac{\partial I_\beta}{\partial x_k}=0 \qquad \text{(I.14)}
$$

($U_k^{(I)}$ is the velocity of the phasic interface), the final fine-grained mass density equation becomes

$$
\begin{aligned}
\frac{\partial \mathcal{F}'_{\boldsymbol{U}\phi|I_\beta}}{\partial t}+V_k\frac{\partial \mathcal{F}'_{\boldsymbol{U}\phi|I_\beta}}{\partial x_k} &= -\frac{\partial}{\partial V_k}\left[\left(\frac{\partial U_k}{\partial t}+U_j\frac{\partial U_k}{\partial x_j}\right)\mathcal{F}'_{\boldsymbol{U}\phi|I_\beta}\right] \\
&\quad -\frac{\partial}{\partial \psi_\alpha}\left[\left(\frac{\partial \phi_\alpha}{\partial t}+U_j\frac{\partial \phi_\alpha}{\partial x_j}\right)\mathcal{F}'_{\boldsymbol{U}\phi|I_\beta}\right] \\
&\quad +\frac{\mathcal{F}'_{\boldsymbol{U}\phi|I_\beta}}{\rho I_\beta}\left[\rho(U_k-U_k^{(I)})\frac{\partial I_\beta}{\partial x_k}\right]. \qquad \text{(I.15)}
\end{aligned}
$$

Taking the expectation of Eq. I.15, it becomes

$$\begin{aligned}\frac{\partial \left\langle \mathcal{F}'_{\boldsymbol{U}\phi|I_\beta} \right\rangle}{\partial t} + V_k \frac{\partial \left\langle \mathcal{F}'_{\boldsymbol{U}\phi|I_\beta} \right\rangle}{\partial x_k} &= -\frac{\partial}{\partial V_k}\left\langle \frac{DU_k}{Dt}\mathcal{F}'_{\boldsymbol{U}\phi|I_\beta} \right\rangle \\ &\quad -\frac{\partial}{\partial \psi_\alpha}\left\langle \frac{D\phi_\alpha}{Dt}\mathcal{F}'_{\boldsymbol{U}\phi|I_\beta} \right\rangle \\ &\quad +\left\langle \frac{\mathcal{F}'_{\boldsymbol{U}\phi|I_\beta}}{\rho I_\beta}\left[\rho(U_k - U_k^{(I)})\frac{\partial I_\beta}{\partial x_k}\right] \right\rangle. \end{aligned} \tag{I.16}$$

Therefore, the phase-conditioned single-point velocity-composition joint PDF transport equation is obtained as

$$\begin{aligned}\frac{\partial \mathcal{F}_{\boldsymbol{U}\phi|I_\beta}}{\partial t} + V_k \frac{\partial \mathcal{F}_{\boldsymbol{U}\phi|I_\beta}}{\partial x_k} &= -\frac{\partial}{\partial V_k}\left[\left\langle \rho I_\beta \frac{DU_k}{Dt}\,|\mathbf{V},\boldsymbol{\psi}\right\rangle \frac{\mathcal{F}_{\boldsymbol{U}\phi|I_\beta}}{\langle \rho I_\beta\,|\mathbf{V},\boldsymbol{\psi}\rangle}\right] \\ &\quad -\frac{\partial}{\partial \psi_\alpha}\left[\left\langle \rho I_\beta \frac{D\phi_\alpha}{Dt}\,|\mathbf{V},\boldsymbol{\psi}\right\rangle \frac{\mathcal{F}_{\boldsymbol{U}\phi|I_\beta}}{\langle \rho I_\beta\,|\mathbf{V},\boldsymbol{\psi}\rangle}\right] \\ &\quad +\left\langle \rho(U_k - U_k^{(I)})\frac{\partial I_\beta}{\partial x_k}\,|\mathbf{V},\boldsymbol{\psi}\right\rangle \frac{\mathcal{F}_{\boldsymbol{U}\phi|I_\beta}}{\langle \rho I_\beta\,|\mathbf{V},\boldsymbol{\psi}\rangle}. \end{aligned} \tag{I.17}$$

APPENDIX J. DERIVATION OF PDF TRANSPORT EQUATION USING TEST FUNCTION METHOD

In order to guarantee the derivation of the PDF transport equation correctly using delta function method, we also derive the phase-conditioned PDF transport equation using test function method that is used to derive the single-point PDF transport equation for single-phase flow by Pope (1985). The governing equations used to derive for the phase-conditioned single-point PDF transport equation are the same as the instantaneous equations in Appendix I. The test function method is to equate two independent expression for the material derivative of the test function $Q(\mathbf{U}, \phi)$.

With the aid of the continuity equation

$$\frac{\partial \rho}{\partial t} + \frac{\partial \rho U_j}{\partial x_j} = 0, \tag{J.1}$$

the first expression for two-phase flow based on the material derivative is written as

$$\begin{aligned} \rho \frac{D I_\beta Q}{Dt} &= \rho \left(\frac{\partial I_\beta Q}{\partial t} + U_j \frac{\partial I_\beta Q}{\partial x_j} \right) \\ &= \frac{\partial \rho I_\beta Q}{\partial t} - I_\beta Q \frac{\partial \rho}{\partial t} + \frac{\partial \rho I_\beta Q U_j}{\partial x_j} - I_\beta Q \frac{\partial \rho U_j}{\partial x_j} \\ &= \frac{\partial \rho I_\beta Q}{\partial t} + \frac{\partial \rho I_\beta Q U_j}{\partial x_j}. \end{aligned} \tag{J.2}$$

Then the expectation of the first expression is

$$\begin{aligned}\left\langle \rho(\boldsymbol{\phi})\frac{DI_\beta Q(\mathbf{U},\boldsymbol{\phi})}{Dt}\right\rangle &= \left\langle \frac{\partial \rho I_\beta Q}{\partial t}+\frac{\partial \rho I_\beta Q U_k}{\partial x_k}\right\rangle \\ &= \frac{\partial}{\partial t}\iint \rho(\boldsymbol{\psi})Q(\mathbf{V},\boldsymbol{\psi})\left\langle I_\beta\,|\mathbf{V},\boldsymbol{\psi}\right\rangle f_{\mathbf{U}\boldsymbol{\phi}}\mathrm{d}\mathbf{V}\mathrm{d}\boldsymbol{\psi} \\ &\quad +\frac{\partial}{\partial x_k}\iint \rho(\boldsymbol{\psi})V_k Q(\mathbf{V},\boldsymbol{\psi})\left\langle I_\beta\,|\mathbf{V},\boldsymbol{\psi}\right\rangle f_{\mathbf{U}\boldsymbol{\phi}}\mathrm{d}\mathbf{V}\mathrm{d}\boldsymbol{\psi} \\ &= \iint Q(\mathbf{V},\boldsymbol{\psi})\left\{\rho(\boldsymbol{\psi})\frac{\partial\left\langle I_\beta\,|\mathbf{V},\boldsymbol{\psi}\right\rangle f_{\mathbf{U}\boldsymbol{\phi}}}{\partial t}+\rho(\boldsymbol{\psi})V_k\frac{\partial\left\langle I_\beta\,|\mathbf{V},\boldsymbol{\psi}\right\rangle f_{\mathbf{U}\boldsymbol{\phi}}}{\partial x_k}\right\}\mathrm{d}\mathbf{V}\mathrm{d}\boldsymbol{\psi}.\end{aligned} \tag{J.3}$$

The second expression is obtained using chain rules

$$\frac{DI_\beta Q(\mathbf{U},\boldsymbol{\phi})}{Dt}=I_\beta\frac{DQ(\mathbf{U},\boldsymbol{\phi})}{Dt}+Q(\mathbf{U},\boldsymbol{\phi})\frac{DI_\beta}{Dt}=I_\beta\frac{\partial Q(\mathbf{U},\boldsymbol{\phi})}{\partial U_k}\frac{DU_k}{Dt}+I_\beta\frac{\partial Q(\mathbf{U},\boldsymbol{\phi})}{\partial \phi_\alpha}\frac{D\phi_\alpha}{Dt}+Q(\mathbf{U},\boldsymbol{\phi})\frac{DI_\beta}{Dt}. \tag{J.4}$$

Then the expectation of the above expression is

$$\left\langle \rho(\boldsymbol{\phi})\frac{DI_\beta Q(\mathbf{U},\boldsymbol{\phi})}{Dt}\right\rangle=\left\langle \rho(\boldsymbol{\phi})I_\beta\frac{\partial Q(\mathbf{U},\boldsymbol{\phi})}{\partial U_k}A_k\right\rangle+\left\langle \rho(\boldsymbol{\phi})I_\beta\frac{\partial Q(\mathbf{U},\boldsymbol{\phi})}{\partial \phi_\alpha}\Theta_\alpha\right\rangle+\left\langle \rho(\boldsymbol{\phi})Q(\mathbf{U},\boldsymbol{\phi})\frac{DI_\beta}{Dt}\right\rangle. \tag{J.5}$$

The first term on the right-hand side of Eq. J.5 is

$$\begin{aligned}\left\langle \rho(\boldsymbol{\phi})I_\beta\frac{\partial Q(\mathbf{U},\boldsymbol{\phi})}{\partial U_k}A_k\right\rangle &= \iint\left\langle \rho(\boldsymbol{\phi})I_\beta\frac{\partial Q(\mathbf{U},\boldsymbol{\phi})}{\partial U_k}A_k\,|\mathbf{V},\boldsymbol{\psi}\right\rangle f_{\mathbf{U}\boldsymbol{\phi}}\mathrm{d}\mathbf{V}\mathrm{d}\boldsymbol{\psi} \\ &= \iint \rho(\boldsymbol{\psi})\frac{\partial Q(\boldsymbol{V},\boldsymbol{\psi})}{\partial V_k}\left\langle I_\beta A_k\,|\mathbf{V},\boldsymbol{\psi}\right\rangle f_{\mathbf{U}\boldsymbol{\phi}}\mathrm{d}\mathbf{V}\mathrm{d}\boldsymbol{\psi}.\end{aligned} \tag{J.6}$$

It can be written further as

$$\begin{aligned}\left\langle \rho(\boldsymbol{\phi})I_\beta\frac{\partial Q(\mathbf{U},\boldsymbol{\phi})}{\partial U_k}A_k\right\rangle &= \iint\frac{\partial}{\partial V_k}\left[\rho(\boldsymbol{\psi})Q(\boldsymbol{V},\boldsymbol{\psi})\left\langle I_\beta A_k\,|\mathbf{V},\boldsymbol{\psi}\right\rangle f_{\mathbf{U}\boldsymbol{\phi}}\right]\mathrm{d}\mathbf{V}\mathrm{d}\boldsymbol{\psi} \\ &\quad -\iint Q(\boldsymbol{V},\boldsymbol{\psi})\frac{\partial\rho(\boldsymbol{\psi})\left\langle I_\beta A_k\,|\mathbf{V},\boldsymbol{\psi}\right\rangle f_{\mathbf{U}\boldsymbol{\phi}}}{\partial V_k}\mathrm{d}\mathbf{V}\mathrm{d}\boldsymbol{\psi},\end{aligned} \tag{J.7}$$

where the first term is

$$\iint \frac{\partial}{\partial V_k} \left[\rho(\boldsymbol{\psi}) Q(\boldsymbol{V}, \boldsymbol{\psi}) \left\langle I_\beta A_k \left| \mathbf{V}, \boldsymbol{\psi} \right\rangle f_{\mathbf{U}\boldsymbol{\phi}}\right] \mathrm{d}\mathbf{V}\mathrm{d}\boldsymbol{\psi} = 0. \tag{J.8}$$

The second term on the right-hand side of Eq. J.5 is rewritten as

$$\left\langle \rho(\boldsymbol{\phi}) I_\beta \frac{\partial Q(\mathbf{U}, \boldsymbol{\phi})}{\partial \psi_\alpha} \Theta_\alpha \right\rangle = -\iint Q(\boldsymbol{V}, \boldsymbol{\psi}) \frac{\partial \rho(\boldsymbol{\psi}) \left\langle I_\beta \Theta_\alpha \left| \mathbf{V}, \boldsymbol{\psi} \right\rangle f_{\mathbf{U}\boldsymbol{\phi}}}{\partial \psi_\alpha} \mathrm{d}\mathbf{V}\mathrm{d}\boldsymbol{\psi}. \tag{J.9}$$

The third term on the right-hand side of Eq. J.5 is rewritten as

$$\begin{aligned} \left\langle \rho(\boldsymbol{\phi}) Q(\mathbf{U}, \boldsymbol{\phi}) \frac{DI_\beta}{Dt} \right\rangle &= \iint \left\langle \rho(\boldsymbol{\phi}) Q(\mathbf{U}, \boldsymbol{\phi}) \left(U_k - U_k^{(I)}\right) \frac{\partial I_\beta}{\partial x_k} \left| \mathbf{V}, \boldsymbol{\psi} \right\rangle f_{\mathbf{U}\boldsymbol{\phi}} \mathrm{d}\mathbf{V}\mathrm{d}\boldsymbol{\psi} \\ &= \iint \rho(\boldsymbol{\psi}) Q(\boldsymbol{V}, \boldsymbol{\psi}) \left\langle \left(U_k - U_k^{(I)}\right) \frac{\partial I_\beta}{\partial x_k} \left| \mathbf{V}, \boldsymbol{\psi} \right\rangle f_{\mathbf{U}\boldsymbol{\phi}} \mathrm{d}\mathbf{V}\mathrm{d}\boldsymbol{\psi}. \right. \end{aligned} \tag{J.10}$$

By substituting the second expression in Eq. J.5 into the first expression Eq. J.3, we obtain

$$\begin{aligned} \iint Q(\mathbf{V}, \boldsymbol{\psi}) \Bigg\{ & \frac{\partial \left\langle \rho(\boldsymbol{\phi}) I_\beta \left| \mathbf{V}, \boldsymbol{\psi} \right\rangle f_{\mathbf{U}\boldsymbol{\phi}}}{\partial t} + V_k \frac{\partial \left\langle \rho(\boldsymbol{\phi}) I_\beta \left| \mathbf{V}, \boldsymbol{\psi} \right\rangle f_{\mathbf{U}\boldsymbol{\phi}}}{\partial x_k} \\ & \frac{\partial}{\partial V_k} \left[\left\langle \rho(\boldsymbol{\phi}) I_\beta A_k \left| \mathbf{V}, \boldsymbol{\psi} \right\rangle f_{\mathbf{U}\boldsymbol{\phi}}\right] + \frac{\partial}{\partial \psi_\alpha} \left[\left\langle \rho(\boldsymbol{\phi}) I_\beta \Theta_\alpha \left| \mathbf{V}, \boldsymbol{\psi} \right\rangle f_{\mathbf{U}\boldsymbol{\phi}}\right] \right. \\ & \left. - \left\langle \rho(\boldsymbol{\phi}) \left(U_k - U_k^{(I)}\right) \frac{\partial I_\beta}{\partial x_k} \left| \mathbf{V}, \boldsymbol{\psi} \right\rangle f_{\mathbf{U}\boldsymbol{\phi}} \right\} \mathrm{d}\mathbf{V}\mathrm{d}\boldsymbol{\psi} = 0. \end{aligned} \tag{J.11}$$

Since these terms in the braces $\{\}$ are independent of Q, we obtain the phase-conditioned single-point velocity-composition joint PDF transport equation with the relation $\mathcal{F}_{\mathbf{U}\boldsymbol{\phi}|I_\beta} = \left\langle \rho\left(\boldsymbol{\phi}\right) I_\beta \left| \mathbf{V}, \boldsymbol{\psi} \right\rangle f_{\mathbf{U}\boldsymbol{\phi}}$ as

$$\begin{aligned} \frac{\partial \mathcal{F}_{\mathbf{U}\boldsymbol{\phi}|I_\beta}}{\partial t} + V_k \frac{\partial \mathcal{F}_{\mathbf{U}\boldsymbol{\phi}|I_\beta}}{\partial x_k} &= -\frac{\partial}{\partial V_k} \left[\left\langle \rho I_\beta A_k \left| \mathbf{V}, \boldsymbol{\psi} \right\rangle \frac{\mathcal{F}_{\mathbf{U}\boldsymbol{\phi}|I_\beta}}{\left\langle \rho I_\beta \left| \mathbf{V}, \boldsymbol{\psi} \right\rangle \right.}\right] \\ &\quad -\frac{\partial}{\partial \psi_\alpha} \left[\left\langle \rho I_\beta \Theta_\alpha \left| \mathbf{V}, \boldsymbol{\psi} \right\rangle \frac{\mathcal{F}_{\mathbf{U}\boldsymbol{\phi}|I_\beta}}{\left\langle \rho I_\beta \left| \mathbf{V}, \boldsymbol{\psi} \right\rangle \right.}\right] \\ &\quad + \left\langle \rho \left(U_k - U_k^{(I)}\right) \frac{\partial I_\beta}{\partial x_k} \left| \mathbf{V}, \boldsymbol{\psi} \right\rangle \frac{\mathcal{F}_{\mathbf{U}\boldsymbol{\phi}|I_\beta}}{\left\langle \rho I_\beta \left| \mathbf{V}, \boldsymbol{\psi} \right\rangle \right.}. \end{aligned} \tag{J.12}$$

The above PDF transport equation is the same as the one derived from delta function method.

APPENDIX K. PHASE-CONDITIONED SINGLE-POINT COMPOSITION PDF TRANSPORT EQUATION

Since Pai and Subramaniam (2009, 2012) have already discussed the first and third term on the right-hand side of Eq. J.12, we will only focus on the second term related to the compositions on the right-hand side of Eq. J.12 in this Appendix. The main difference between single-phase and two-phase flows is that in the two-phase flow the interphase transfer term appear in the PDF transport equation. Understanding the effect of the interphase transfer term in two-phase flow will allow us to develop closure model for the interphase transfer term in the PDF transport equation.

The phase-conditioned single-point velocity-composition joint PDF transport equation have been derived in Appendices I and J as

$$\begin{aligned}\frac{\partial \mathcal{F}_{\boldsymbol{U}\phi|I_\beta}}{\partial t}+V_k\frac{\partial \mathcal{F}_{\boldsymbol{U}\phi|I_\beta}}{\partial x_k} &= -\frac{\partial}{\partial V_k}\left[\left\langle \rho I_\beta \frac{DU_k}{Dt}\,|\mathbf{V},\boldsymbol{\psi}\right\rangle \frac{\mathcal{F}_{\boldsymbol{U}\phi|I_\beta}}{\langle \rho I_\beta\,|\mathbf{V},\boldsymbol{\psi}\rangle}\right]\\ &\quad -\frac{\partial}{\partial \psi_\alpha}\left[\left\langle\left(-\frac{\partial I_\beta J_i^\alpha}{\partial x_i}+J_i^\alpha\frac{\partial I_\beta}{\partial x_i}+I_\beta\rho S_\alpha\right)|\mathbf{V},\boldsymbol{\psi}\right\rangle \frac{\mathcal{F}_{\boldsymbol{U}\phi|I_\beta}}{\langle \rho I_\beta\,|\mathbf{V},\boldsymbol{\psi}\rangle}\right]\\ &\quad +\left\langle \rho(U_k-U_k^{(I)})\frac{\partial I_\beta}{\partial x_k}\,|\mathbf{V},\boldsymbol{\psi}\right\rangle \frac{\mathcal{F}_{\boldsymbol{U}\phi|I_\beta}}{\langle \rho I_\beta\,|\mathbf{V},\boldsymbol{\psi}\rangle},\end{aligned} \tag{K.1}$$

where Favre mass density is defined as $\mathcal{F}_{\boldsymbol{U}\phi|I_\beta}(\boldsymbol{V},\boldsymbol{\psi},\boldsymbol{x},t)=\langle\rho(\boldsymbol{\phi})I_\beta(\boldsymbol{x},t)\delta(\mathbf{U}(\boldsymbol{x},t)-\mathbf{V})\delta(\boldsymbol{\phi}(\boldsymbol{x},t)-\boldsymbol{\psi})\rangle$. The phase-conditioned single-point composition PDF transport equation can be obtained by the integral of the above equation over the velocity sample space as

$$\begin{aligned}\int\frac{\partial \mathcal{F}_{\boldsymbol{U}\phi|I_\beta}}{\partial t}\mathrm{d}\mathbf{V} &= -\int\frac{\partial}{\partial \psi_\alpha}\left[\left\langle\left(-\frac{\partial I_\beta J_i^\alpha}{\partial x_i}+J_i^\alpha\frac{\partial I_\beta}{\partial x_i}+I_\beta\rho S_\alpha\right)|\mathbf{V},\boldsymbol{\psi}\right\rangle \frac{\mathcal{F}_{\boldsymbol{U}\phi|I_\beta}}{\langle \rho I_\beta\,|\mathbf{V},\boldsymbol{\psi}\rangle}\right]\mathrm{d}\mathbf{V}\\ +\int V_k\frac{\partial \mathcal{F}_{\boldsymbol{U}\phi|I_\beta}}{\partial x_k}\mathrm{d}\mathbf{V} &+\int\left\langle \rho(U_k-U_k^{(I)})\frac{\partial I_\beta}{\partial x_k}\,|\mathbf{V},\boldsymbol{\psi}\right\rangle \frac{\mathcal{F}_{\boldsymbol{U}\phi|I_\beta}}{\langle \rho I_\beta\,|\mathbf{V},\boldsymbol{\psi}\rangle}\mathrm{d}\mathbf{V}.\end{aligned} \tag{K.2}$$

Then the unsteady term becomes

$$\int \frac{\partial \mathcal{F}_{\boldsymbol{U}\phi|I_\beta}}{\partial t}\mathrm{d}\mathbf{V} = \frac{\partial \left[\int \mathcal{F}_{\boldsymbol{U}\phi|I_\beta}\mathrm{d}\mathbf{V}\right]}{\partial t} = \frac{\partial \left[\int \langle \rho(\boldsymbol{\phi}) I_\beta(\boldsymbol{x},t)\delta(\mathbf{U}(\boldsymbol{x},t)-\mathbf{V})\delta(\boldsymbol{\phi}(\boldsymbol{x},t)-\boldsymbol{\psi})\rangle \,\mathrm{d}\mathbf{V}\right]}{\partial t} = \frac{\partial \mathcal{F}_{\phi|I_\beta}}{\partial t}. \tag{K.3}$$

The second term on the left-hand side of Eq. K.2 is rewritten as

$$\int V_k \frac{\partial \mathcal{F}_{\boldsymbol{U}\phi|I_\beta}}{\partial x_k}\mathrm{d}\mathbf{V} = \frac{\partial \int V_k \mathcal{F}_{\boldsymbol{U}\phi|I_\beta}\mathrm{d}\mathbf{V}}{\partial x_k} = \frac{\partial \langle U_k |\boldsymbol{\psi}\rangle \mathcal{F}_{\phi|I_\beta}}{\partial x_k} = \frac{\partial \left[\left\langle \widetilde{U_k^{(\beta)}} \right\rangle \mathcal{F}_{\boldsymbol{\phi}|I_\beta}\right]}{\partial x_k} + \frac{\partial \left[\langle u_k |\boldsymbol{\psi}\rangle \mathcal{F}_{\boldsymbol{\phi}|I_\beta}\right]}{\partial x_k}. \tag{K.4}$$

The first term on the right-hand side of Eq. K.2 is rewritten as

$$\begin{aligned}
& \int \frac{\partial}{\partial \psi_\alpha}\left[\left\langle \left(-\frac{\partial I_\beta J_i^\alpha}{\partial x_i} + J_i^\alpha \frac{\partial I_\beta}{\partial x_i} + I_\beta \rho S_\alpha\right)|\mathbf{V},\boldsymbol{\psi}\right\rangle \frac{\mathcal{F}_{\boldsymbol{U}\phi|I_\beta}}{\langle \rho I_\beta |\mathbf{V},\boldsymbol{\psi}\rangle}\right]\mathrm{d}\mathbf{V} \\
= & \int \frac{\partial}{\partial \psi_\alpha}\left[\left\langle \left(-\frac{\partial I_\beta J_i^\alpha}{\partial x_i} + J_i^\alpha \frac{\partial I_\beta}{\partial x_i} + I_\beta \rho S_\alpha\right)|\mathbf{V},\boldsymbol{\psi}\right\rangle f_{\boldsymbol{U}\phi}\right]\mathrm{d}\mathbf{V} \\
= & \frac{\partial}{\partial \psi_\alpha}\left[\int \left\langle \left(-\frac{\partial I_\beta J_i^\alpha}{\partial x_i} + J_i^\alpha \frac{\partial I_\beta}{\partial x_i} + I_\beta \rho S_\alpha\right)|\mathbf{V},\boldsymbol{\psi}\right\rangle f_{\boldsymbol{U}\phi}\mathrm{d}\mathbf{V}\right] \\
= & \frac{\partial}{\partial \psi_\alpha}\left[\left\langle \left(-\frac{\partial I_\beta J_i^\alpha}{\partial x_i} + J_i^\alpha \frac{\partial I_\beta}{\partial x_i} + I_\beta \rho S_\alpha\right)|\boldsymbol{\psi}\right\rangle f_\phi\right].
\end{aligned} \tag{K.5}$$

Note that $\mathcal{F}_{\phi|I_\beta}(\boldsymbol{\psi},\boldsymbol{x},t) = \langle \rho(\boldsymbol{\phi}) I_\beta |\boldsymbol{\psi}\rangle f_\phi$.

The last term on the right-hand side of Eq. K.2 becomes

$$\begin{aligned}
& \int \left\langle \rho(U_k - U_k^{(I)})\frac{\partial I_\beta}{\partial x_k}|\mathbf{V},\boldsymbol{\psi}\right\rangle \frac{\mathcal{F}_{\boldsymbol{U}\phi|I_\beta}}{\langle \rho I_\beta |\mathbf{V},\boldsymbol{\psi}\rangle}\mathrm{d}\mathbf{V} \\
= & \int \left\langle \rho(U_k - U_k^{(I)})\frac{\partial I_\beta}{\partial x_k}|\mathbf{V},\boldsymbol{\psi}\right\rangle f_{\boldsymbol{U}\phi}\mathrm{d}\mathbf{V} \\
= & \left\langle \rho(U_k - U_k^{(I)})\frac{\partial I_\beta}{\partial x_k}|\boldsymbol{\psi}\right\rangle f_\phi.
\end{aligned} \tag{K.6}$$

Finally, combining all the terms, we obtain

$$\frac{\partial \mathcal{F}_{\boldsymbol{\phi}|I_\beta}}{\partial t} + \frac{\partial \left[\left\langle \widetilde{U_k^{(\beta)}} \right\rangle \mathcal{F}_{\boldsymbol{\phi}|I_\beta} \right]}{\partial x_k} + \frac{\partial \left[\langle u_k \, | \boldsymbol{\psi} \rangle \, \mathcal{F}_{\boldsymbol{\phi}|I_\beta} \right]}{\partial x_k} = -\frac{\partial}{\partial \psi_\alpha} \left[\left\langle -\frac{\partial I_\beta J_i^\alpha}{\partial x_i} \, | \boldsymbol{\psi} \right\rangle \frac{\mathcal{F}_{\boldsymbol{\phi}|I_\beta}}{\langle \rho I_\beta \, | \boldsymbol{\psi} \rangle} \right]$$
$$-\frac{\partial}{\partial \psi_\alpha} \left[\left\langle J_i^\alpha \frac{\partial I_\beta}{\partial x_i} \, | \boldsymbol{\psi} \right\rangle \frac{\mathcal{F}_{\boldsymbol{\phi}|I_\beta}}{\langle \rho I_\beta \, | \boldsymbol{\psi} \rangle} \right]$$
$$-\frac{\partial}{\partial \psi_\alpha} \left[\langle I_\beta \rho S_\alpha \, | \boldsymbol{\psi} \rangle \frac{\mathcal{F}_{\boldsymbol{\phi}|I_\beta}}{\langle \rho I_\beta \, | \boldsymbol{\psi} \rangle} \right]$$
$$+ \left\langle \rho (U_k - U_k^{(I)}) \frac{\partial I_\beta}{\partial x_k} \, | \boldsymbol{\psi} \right\rangle \frac{\mathcal{F}_{\boldsymbol{\phi}|I_\beta}}{\langle \rho I_\beta \, | \boldsymbol{\psi} \rangle}. \tag{K.7}$$

APPENDIX L. TRANSPORT EQUATION FOR SCALAR VARIANCE

In order to see the evolution of the scalar variance in a gas-solid flow, a transport equation for scalar variance need to be established. In this Appendix, we derive scalar-variance transport equation from the phase-conditioned single-point velocity-composition joint PDF transport equation obtained in Appendices I and J as

$$\begin{aligned}\frac{\partial \mathcal{F}_{\boldsymbol{U}\phi|I_\beta}}{\partial t} + V_k \frac{\partial \mathcal{F}_{\boldsymbol{U}\phi|I_\beta}}{\partial x_k} &= -\frac{\partial}{\partial V_k}\left[\langle \rho I_\beta A_k \,|\mathbf{V},\boldsymbol{\psi}\rangle \frac{\mathcal{F}_{\boldsymbol{U}\phi|I_\beta}}{\langle \rho I_\beta \,|\mathbf{V},\boldsymbol{\psi}\rangle}\right] \\ &\quad -\frac{\partial}{\partial \psi_\alpha}\left[\langle \rho I_\beta \Theta_\alpha \,|\mathbf{V},\boldsymbol{\psi}\rangle \frac{\mathcal{F}_{\boldsymbol{U}\phi|I_\beta}}{\langle \rho I_\beta \,|\mathbf{V},\boldsymbol{\psi}\rangle}\right] \\ &\quad +\left\langle \rho(U_k - U_k^{(I)})\frac{\partial I_\beta}{\partial x_k}\,|\mathbf{V},\boldsymbol{\psi}\right\rangle \frac{\mathcal{F}_{\boldsymbol{U}\phi|I_\beta}}{\langle \rho I_\beta \,|\mathbf{V},\boldsymbol{\psi}\rangle},\end{aligned} \tag{L.1}$$

where the Favre mass density function conditional on phase β is

$$\mathcal{F}_{\boldsymbol{U}\phi|I_\beta}(\mathbf{V},\boldsymbol{\psi},\boldsymbol{x},t) = \langle \rho I_\beta(\boldsymbol{x},t)\delta(\mathbf{U}(\boldsymbol{x},t)-\mathbf{V})\delta(\boldsymbol{\phi}(\boldsymbol{x},t)-\boldsymbol{\psi})\rangle\,, \tag{L.2}$$

ρA_k and $\rho\Theta_\alpha$ in the above equation are defined as

$$\rho A_k(\boldsymbol{x},t) = \frac{\partial \tau_{jk}}{\partial x_j} - \frac{\partial p}{\partial x_k} + \rho g_k, \tag{L.3}$$

and

$$\rho\Theta_\alpha(\boldsymbol{x},t) = -\frac{\partial J_i^\alpha}{\partial x_i} + \rho S_\alpha, \tag{L.4}$$

respectively. A scalar-covariance transport equation can be derived first as follows. The derivation of the transport equation for scalar covariance is similar to the one for the Reynolds stress in Pai and Subramaniam (2009). In order to derive the equation for scalar covariance, we

multiply the PDF transport equation in Eq. L.1 by $\psi_\eta''^{(\beta)}\psi_\gamma''^{(\beta)}$, where scalar fluctuation is $\phi_\gamma''^{(\beta)} = \phi_\gamma - \left\langle \widetilde{\phi_\gamma^{(\beta)}} \right\rangle$ and the Favre-averaged scalar is

$$\left\langle \widetilde{\phi_\gamma^{(\beta)}} \right\rangle = \frac{\langle \rho I_\beta \phi_\gamma \rangle}{\langle \rho I_\beta \rangle}, \tag{L.5}$$

and then integrate the equation over the velocity-composition space. Here, the Favre-averaged scalar covariance is defined as

$$\widetilde{\Phi_{\gamma\eta}^{(\beta)}} = \frac{\left\langle \rho I_\beta \phi_\gamma''^{(\beta)} \phi_\eta''^{(\beta)} \right\rangle}{\langle \rho I_\beta \rangle} = \int\int \psi_\eta''^{(\beta)} \psi_\gamma''^{(\beta)} \mathcal{F}_{\boldsymbol{U}\phi|I_\beta} \mathrm{d}\mathbf{V}\mathrm{d}\boldsymbol{\psi}. \tag{L.6}$$

After multiplying the PDF transport equation in Eq. L.1 by $\psi_\eta''^{(\beta)}\psi_\gamma''^{(\beta)}$, we obtain

$$\begin{aligned}
\psi_\eta''^{(\beta)}\psi_\gamma''^{(\beta)}\frac{\partial \mathcal{F}_{\boldsymbol{U}\phi|I_\beta}}{\partial t} + \psi_\eta''^{(\beta)}\psi_\gamma''^{(\beta)} V_k \frac{\partial \mathcal{F}_{\boldsymbol{U}\phi|I_\beta}}{\partial x_k} &= -\psi_\eta''^{(\beta)}\psi_\gamma''^{(\beta)}\frac{\partial}{\partial V_k}\left[\langle I_\beta \rho A_k \,|\mathbf{V},\boldsymbol{\psi}\rangle \frac{\mathcal{F}_{\boldsymbol{U}\phi|I_\beta}}{\langle \rho I_\beta \,|\mathbf{V},\boldsymbol{\psi}\rangle}\right] \\
&\quad -\psi_\eta''^{(\beta)}\psi_\gamma''^{(\beta)}\frac{\partial}{\partial \psi_\alpha}\left[\langle I_\beta \rho \Theta_\alpha \,|\mathbf{V},\boldsymbol{\psi}\rangle \frac{\mathcal{F}_{\boldsymbol{U}\phi|I_\beta}}{\langle \rho I_\beta \,|\mathbf{V},\boldsymbol{\psi}\rangle}\right] \\
&\quad +\psi_\eta''^{(\beta)}\psi_\gamma''^{(\beta)}\left\langle \rho(U_k - U_k^{(I)})\frac{\partial I_\beta}{\partial x_k} \,|\mathbf{V},\boldsymbol{\psi}\right\rangle \frac{\mathcal{F}_{\boldsymbol{U}\phi|I_\beta}}{\langle \rho I_\beta \,|\mathbf{V},\boldsymbol{\psi}\rangle}.
\end{aligned} \tag{L.7}$$

The above equation can be simplified as follows:

1. The first term on the left-hand side of Eq. L.7 is decomposed into two terms

$$\psi_\eta''^{(\beta)}\psi_\gamma''^{(\beta)}\frac{\partial \mathcal{F}_{\boldsymbol{U}\phi|I_\beta}}{\partial t} = \frac{\partial \psi_\eta''^{(\beta)}\psi_\gamma''^{(\beta)}\mathcal{F}_{\boldsymbol{U}\phi|I_\beta}}{\partial t} - \mathcal{F}_{\boldsymbol{U}\phi|I_\beta}\frac{\partial \psi_\eta''^{(\beta)}\psi_\gamma''^{(\beta)}}{\partial t}, \tag{L.8}$$

where the last term can be simplified to

$$\begin{aligned}
\mathcal{F}_{\boldsymbol{U}\phi|I_\beta}\frac{\partial \psi_\eta''^{(\beta)}\psi_\gamma''^{(\beta)}}{\partial t} &= \mathcal{F}_{\boldsymbol{U}\phi|I_\beta}\frac{\partial}{\partial t}\left[\left(\psi_\gamma^{(\beta)} - \left\langle \widetilde{\phi_\gamma^{(\beta)}} \right\rangle\right)\left(\psi_\eta^{(\beta)} - \left\langle \widetilde{\phi_\eta^{(\beta)}} \right\rangle\right)\right] \\
&= \mathcal{F}_{\boldsymbol{U}\phi|I_\beta}\left[-\psi_\eta^{(\beta)}\frac{\partial \left\langle \widetilde{\phi_\gamma^{(\beta)}} \right\rangle}{\partial t} - \psi_\gamma^{(\beta)}\frac{\partial \left\langle \widetilde{\phi_\eta^{(\beta)}} \right\rangle}{\partial t} + \frac{\partial \left\langle \widetilde{\phi_\gamma^{(\beta)}} \right\rangle \left\langle \widetilde{\phi_\eta^{(\beta)}} \right\rangle}{\partial t}\right]
\end{aligned} \tag{L.9}$$

Note that the integral of this term over $\boldsymbol{\psi}$ space is equal to zero.

2. The second term on the left-hand side of Eq. L.7 is also decomposed into two terms

$$\psi_\eta''^{(\beta)}\psi_\gamma''^{(\beta)}V_k\frac{\partial\mathcal{F}_{\boldsymbol{U}\phi|I_\beta}}{\partial x_k}=\frac{\partial\psi_\eta''^{(\beta)}\psi_\gamma''^{(\beta)}V_k\mathcal{F}_{\boldsymbol{U}\phi|I_\beta}}{\partial x_k}-V_k\mathcal{F}_{\boldsymbol{U}\phi|I_\beta}\frac{\partial\psi_\eta''^{(\beta)}\psi_\gamma''^{(\beta)}}{\partial x_k}. \tag{L.10}$$

The last term of the above equation can be written as

$$\begin{aligned}V_k\mathcal{F}_{\boldsymbol{U}\phi|I_\beta}\frac{\partial\psi_\eta''^{(\beta)}\psi_\gamma''^{(\beta)}}{\partial x_k} &= V_k\mathcal{F}_{\boldsymbol{U}\phi|I_\beta}\left(\psi_\eta''^{(\beta)}\frac{\partial\psi_\gamma''^{(\beta)}}{\partial x_k}+\psi_\gamma''^{(\beta)}\frac{\partial\psi_\eta''^{(\beta)}}{\partial x_k}\right)\\ &= -V_k\mathcal{F}_{\boldsymbol{U}\phi|I_\beta}\left(\psi_\eta''^{(\beta)}\frac{\partial\widetilde{\left\langle\phi_\gamma^{(\beta)}\right\rangle}}{\partial x_k}+\psi_\gamma''^{(\beta)}\frac{\partial\widetilde{\left\langle\phi_\eta^{(\beta)}\right\rangle}}{\partial x_k}\right).\end{aligned} \tag{L.11}$$

3. The first term on the right-hand side of Eq. L.7 can be rewritten as

$$\begin{aligned}\psi_\eta''^{(\beta)}\psi_\gamma''^{(\beta)}\frac{\partial}{\partial V_k}\left[\langle I_\beta\rho A_k\,|\boldsymbol{V},\boldsymbol{\psi}\rangle\frac{\mathcal{F}_{\boldsymbol{U}\phi|I_\beta}}{\langle\rho I_\beta\,|\boldsymbol{V},\boldsymbol{\psi}\rangle}\right] &= \frac{\partial}{\partial V_k}\left[\psi_\eta''^{(\beta)}\psi_\gamma''^{(\beta)}\langle I_\beta\rho A_k\,|\boldsymbol{V},\boldsymbol{\psi}\rangle\frac{\mathcal{F}_{\boldsymbol{U}\phi|I_\beta}}{\langle\rho I_\beta\,|\boldsymbol{V},\boldsymbol{\psi}\rangle}\right]\\ &\quad-\left[\langle I_\beta\rho A_k\,|\boldsymbol{V},\boldsymbol{\psi}\rangle\frac{\mathcal{F}_{\boldsymbol{U}\phi|I_\beta}}{\langle\rho I_\beta\,|\boldsymbol{V},\boldsymbol{\psi}\rangle}\right]\frac{\partial}{\partial V_k}\left[\psi_\eta''^{(\beta)}\psi_\gamma''^{(\beta)}\right].\end{aligned} \tag{L.12}$$

Note that the first term on the right-hand side of the above equation is equal to zero.

4. The second term on the right-hand side of Eq. L.7 can be derived as

$$\begin{aligned}&\psi_\eta''^{(\beta)}\psi_\gamma''^{(\beta)}\frac{\partial}{\partial\psi_\alpha}\left[\langle I_\beta\rho\Theta_\alpha\,|\mathbf{V},\boldsymbol{\psi}\rangle\frac{\mathcal{F}_{\boldsymbol{U}\phi|I_\beta}}{\langle\rho I_\beta\,|\mathbf{V},\boldsymbol{\psi}\rangle}\right]\\ =\;&\frac{\partial}{\partial\psi_\alpha}\left[\psi_\eta''^{(\beta)}\psi_\gamma''^{(\beta)}\langle I_\beta\rho\Theta_\alpha\,|\mathbf{V},\boldsymbol{\psi}\rangle\frac{\mathcal{F}_{\boldsymbol{U}\phi|I_\beta}}{\langle\rho I_\beta\,|\boldsymbol{V},\boldsymbol{\psi}\rangle}\right] \qquad\text{(L.13)}\\ &-\left[\langle I_\beta\rho\Theta_\alpha\,|\mathbf{V},\boldsymbol{\psi}\rangle\frac{\mathcal{F}_{\boldsymbol{U}\phi|I_\beta}}{\langle\rho I_\beta\,|\mathbf{V},\boldsymbol{\psi}\rangle}\right]\frac{\partial}{\partial\psi_\alpha}\left[\psi_\eta''^{(\beta)}\psi_\gamma''^{(\beta)}\right]\\ =\;&\frac{\partial}{\partial\psi_\alpha}\left[\psi_\eta''^{(\beta)}\psi_\gamma''^{(\beta)}\langle I_\beta\rho\Theta_\alpha\,|\mathbf{V},\boldsymbol{\psi}\rangle\frac{\mathcal{F}_{\boldsymbol{U}\phi|I_\beta}}{\langle\rho I_\beta\,|\boldsymbol{V},\boldsymbol{\psi}\rangle}\right]\\ &-\left[\psi_\eta''^{(\beta)}\langle I_\beta\rho\Theta_\gamma\,|\mathbf{V},\boldsymbol{\psi}\rangle+\psi_\gamma''^{(\beta)}\langle I_\beta\rho\Theta_\eta\,|\mathbf{V},\boldsymbol{\psi}\rangle\right]\frac{\mathcal{F}_{\boldsymbol{U}\phi|I_\beta}}{\langle\rho I_\beta\,|\mathbf{V},\boldsymbol{\psi}\rangle}. \qquad\text{(L.14)}\end{aligned}$$

5. The last term on the right-hand side of Eq. L.7 can be written as a source term

$$\left\langle S_\rho^{(\beta)}\,|\mathbf{V},\boldsymbol{\psi}\right\rangle=\left\langle\rho(U_k-U_k^{(I)})\frac{\partial I_\beta}{\partial x_k}\,|\mathbf{V},\boldsymbol{\psi}\right\rangle. \tag{L.15}$$

Substituting all above terms into Eq. L.7, we obtain

$$\begin{aligned}
\frac{\partial \psi_\eta''^{(\beta)} \psi_\gamma''^{(\beta)} \mathcal{F}_{\boldsymbol{U}\phi|I_\beta}}{\partial t} &- \mathcal{F}_{\boldsymbol{U}\phi|I_\beta}\left[-\psi_\eta''^{(\beta)} \frac{\partial \widetilde{\left\langle \phi_\gamma^{(\beta)} \right\rangle}}{\partial t} - \psi_\gamma''^{(\beta)} \frac{\partial \widetilde{\left\langle \phi_\eta^{(\beta)} \right\rangle}}{\partial t} + \frac{\partial \widetilde{\left\langle \phi_\gamma^{(\beta)} \right\rangle} \widetilde{\left\langle \phi_\eta^{(\beta)} \right\rangle}}{\partial t}\right] \\
&+ \frac{\partial \psi_\eta''^{(\beta)} \psi_\gamma''^{(\beta)} V_k \mathcal{F}_{\boldsymbol{U}\phi|I_\beta}}{\partial x_k} + V_k \mathcal{F}_{\boldsymbol{U}\phi|I_\beta}\left(\psi_\eta''^{(\beta)} \frac{\partial \widetilde{\left\langle \phi_\gamma^{(\beta)} \right\rangle}}{\partial x_k} + \psi_\gamma''^{(\beta)} \frac{\partial \widetilde{\left\langle \phi_\eta^{(\beta)} \right\rangle}}{\partial x_k}\right) \\
&= \frac{\partial}{\partial \psi_\alpha}\left[\psi_\eta''^{(\beta)} \psi_\gamma''^{(\beta)} \left\langle I_\beta \rho \Theta_\alpha \left| \mathbf{V}, \boldsymbol{\psi} \right.\right\rangle \frac{\mathcal{F}_{\boldsymbol{U}\phi|I_\beta}}{\left\langle \rho I_\beta \left| \mathbf{V}, \boldsymbol{\psi} \right.\right\rangle}\right] \\
&\quad - \left[\psi_\eta''^{(\beta)} \left\langle I_\beta \rho \Theta_\gamma \left| \mathbf{V}, \boldsymbol{\psi} \right.\right\rangle + \psi_\gamma''^{(\beta)} \left\langle I_\beta \rho \Theta_\eta \left| \mathbf{V}, \boldsymbol{\psi} \right.\right\rangle\right] \frac{\mathcal{F}_{\boldsymbol{U}\phi|I_\beta}}{\left\langle \rho I_\beta \left| \mathbf{V}, \boldsymbol{\psi} \right.\right\rangle} \\
&\quad + \psi_\eta''^{(\beta)} \psi_\gamma''^{(\beta)} \left\langle S_\rho^{(\beta)} \left| \mathbf{V}, \boldsymbol{\psi} \right.\right\rangle \frac{\mathcal{F}_{\boldsymbol{U}\phi|I_\beta}}{\left\langle \rho I_\beta \left| \mathbf{V}, \boldsymbol{\psi} \right.\right\rangle}. \qquad \text{(L.16)}
\end{aligned}$$

By integrating the above equation over velocity-composition space, we can obtain the scalar covariance equation as follows. The integral of the third term on the left-hand side of Eq. L.16 is

$$\begin{aligned}
\iint \frac{\partial \psi_\eta''^{(\beta)} \psi_\gamma''^{(\beta)} V_k \mathcal{F}_{\boldsymbol{U}\phi|I_\beta}}{\partial x_k} \mathrm{d}\mathbf{V}\mathrm{d}\boldsymbol{\psi} &= \frac{\partial}{\partial x_k}\left\{\int V_k \left[\int \psi_\eta''^{(\beta)} \psi_\gamma''^{(\beta)} \mathcal{F}_{\boldsymbol{U}\phi|I_\beta} \mathrm{d}\boldsymbol{\psi}\right] d\mathbf{V}\right\} \\
&= \frac{\partial}{\partial x_k}\left\{\int V_k \left\langle \rho I_\beta \phi_\eta''^{(\beta)} \phi_\gamma''^{(\beta)} \left| \mathbf{V} \right.\right\rangle d\mathbf{V}\right\} \\
&= \frac{\partial}{\partial x_k}\left\{\int \left\langle \left(u_k^{(\beta)} + \widetilde{\left\langle U_k^{(\beta)} \right\rangle}\right) \rho I_\beta \phi_\eta''^{(\beta)} \phi_\gamma''^{(\beta)} \left| \mathbf{V} \right.\right\rangle \mathrm{d}\mathbf{V}\right\} \\
&= \frac{\partial}{\partial x_k}\left[\left\langle \rho I_\beta u_k^{(\beta)} \phi_\eta''^{(\beta)} \phi_\gamma''^{(\beta)} \right\rangle + \left\langle \rho I_\beta \phi_\eta''^{(\beta)} \phi_\gamma''^{(\beta)} \right\rangle \widetilde{\left\langle U_k^{(\beta)} \right\rangle}\right]. \qquad \text{(L.17)}
\end{aligned}$$

The integration of the fourth term on the left-hand side of Eq. L.16 becomes

$$
\begin{aligned}
&\iint V_k \left(\psi_\eta''^{(\beta)} \frac{\partial \widetilde{\left\langle \phi_\gamma^{(\beta)} \right\rangle}}{\partial x_k} + \psi_\gamma''^{(\beta)} \frac{\partial \widetilde{\left\langle \phi_\eta^{(\beta)} \right\rangle}}{\partial x_k} \right) \mathcal{F}_{\boldsymbol{U}\phi|I_\beta} \mathrm{d}\mathbf{V}\mathrm{d}\boldsymbol{\psi} \\
= &\int V_k \left[\left(\psi_\eta''^{(\beta)} \frac{\partial \widetilde{\left\langle \phi_\gamma^{(\beta)} \right\rangle}}{\partial x_k} + \psi_\gamma''^{(\beta)} \frac{\partial \widetilde{\left\langle \phi_\eta^{(\beta)} \right\rangle}}{\partial x_k} \right) \mathcal{F}_{\boldsymbol{U}\phi|I_\beta} \mathrm{d}\boldsymbol{\psi} \right] \mathrm{d}\mathbf{V} \\
= &\int V_k \left[\left\langle \rho I_\beta \phi_\eta''^{(\beta)} \left| \mathbf{V} \right. \right\rangle \frac{\partial \widetilde{\left\langle \phi_\gamma^{(\beta)} \right\rangle}}{\partial x_k} + \left\langle \rho I_\beta \phi_\gamma''^{(\beta)} \left| \mathbf{V} \right. \right\rangle \frac{\partial \widetilde{\left\langle \phi_\eta^{(\beta)} \right\rangle}}{\partial x_k} \right] \mathrm{d}\mathbf{V} \\
= &\left\langle \rho I_\beta u_k''^{(\beta)} \phi_\eta''^{(\beta)} \right\rangle \frac{\partial \widetilde{\left\langle \phi_\gamma^{(\beta)} \right\rangle}}{\partial x_k} + \left\langle \rho I_\beta u_k''^{(\beta)} \phi_\gamma''^{(\beta)} \right\rangle \frac{\partial \widetilde{\left\langle \phi_\eta^{(\beta)} \right\rangle}}{\partial x_k}.
\end{aligned} \tag{L.18}
$$

The integral of the first term on the right-hand side of Eq. L.16 is equal to zero. The integral of the second term on the right-hand side of Eq. L.16 is

$$
\begin{aligned}
&\iint \left[\psi_\eta''^{(\beta)} \left\langle I_\beta \rho \Theta_\gamma \left| \mathbf{V}, \boldsymbol{\psi} \right. \right\rangle \frac{\mathcal{F}_{\boldsymbol{U}\phi|I_\beta}}{\left\langle \rho I_\beta \left| \mathbf{V}, \boldsymbol{\psi} \right. \right\rangle} + \psi_\gamma''^{(\beta)} \left\langle I_\beta \rho \Theta_\eta \left| \mathbf{V}, \boldsymbol{\psi} \right. \right\rangle \frac{\mathcal{F}_{\boldsymbol{U}\phi|I_\beta}}{\left\langle \rho I_\beta \left| \boldsymbol{V}, \boldsymbol{\psi} \right. \right\rangle} \right] \mathrm{d}\mathbf{V}\mathrm{d}\boldsymbol{\psi} \\
= &\left\langle I_\beta \rho \Theta_\gamma \phi_\eta''^{(\beta)} \right\rangle + \left\langle I_\beta \rho \Theta_\eta \phi_\gamma''^{(\beta)} \right\rangle \\
= &\left\langle \left(-\frac{\partial J_i^\gamma}{\partial x_i} + \rho S_\gamma \right) I_\beta \phi_\eta''^{(\beta)} \right\rangle + \left\langle \left(-\frac{\partial J_i^\eta}{\partial x_i} + \rho S_\eta \right) I_\beta \phi_\gamma''^{(\beta)} \right\rangle.
\end{aligned} \tag{L.19}
$$

And the terms the right-hand side of the above equation can be further written as

$$
\left\langle \left(-\frac{\partial J_i^\gamma}{\partial x_i} + \rho S_\gamma \right) I_\beta \phi_\eta''^{(\beta)} \right\rangle = \left\langle -\phi_\eta''^{(\beta)} \frac{\partial I_\beta J_i^\gamma}{\partial x_i} + \phi_\eta''^{(\beta)} J_i^\gamma \frac{\partial I_\beta}{\partial x_i} + \rho I_\beta \phi_\eta''^{(\beta)} S_\gamma \right\rangle. \tag{L.20}
$$

Therefore, final expression for the scalar-covariance transport equation is

$$\begin{aligned}
\frac{\partial}{\partial t}\left[\langle \rho I_\beta \rangle \Phi_{\gamma\eta}^{(\beta)}\right] &+ \frac{\partial}{\partial x_k}\left[\langle \rho I_\beta \rangle \Phi_{\gamma\eta}^{(\beta)} \left\langle \widetilde{U_k^{(\beta)}} \right\rangle\right] + \frac{\partial}{\partial x_k}\left\langle \rho I_\beta u_k^{(\beta)} \phi_\eta^{\prime\prime(\beta)} \phi_\gamma^{\prime\prime(\beta)} \right\rangle \\
&= -\left\langle \rho I_\beta u_k^{(\beta)} \phi_\eta^{\prime\prime(\beta)} \right\rangle \frac{\partial \left\langle \widetilde{\phi_\gamma^{(\beta)}} \right\rangle}{\partial x_k} - \left\langle \rho I_\beta u_k^{(\beta)} \phi_\gamma^{\prime\prime(\beta)} \right\rangle \frac{\partial \left\langle \widetilde{\phi_\eta^{(\beta)}} \right\rangle}{\partial x_k} \\
&\quad + \left\langle -\phi_\eta^{\prime\prime(\beta)} \frac{\partial I_\beta J_i^\lambda}{\partial x_i} + \phi_\eta^{\prime\prime(\beta)} J_i^\lambda \frac{\partial I_\beta}{\partial x_i} + \rho I_\beta \phi_\eta^{\prime\prime(\beta)} S_\lambda \right\rangle \\
&\quad + \left\langle -\phi_\gamma^{\prime\prime(\beta)} \frac{\partial I_\beta J_i^\eta}{\partial x_i} + \phi_\gamma^{\prime\prime(\beta)} J_i^\eta \frac{\partial I_\beta}{\partial x_i} + \rho I_\beta \phi_\gamma^{\prime\prime(\beta)} S_\eta \right\rangle \\
&\quad + \left\langle \phi_\eta^{\prime\prime(\beta)} \phi_\gamma^{\prime\prime(\beta)} S_\rho^{(\beta)} \right\rangle
\end{aligned} \tag{L.21}$$

Then the scalar-variance transport equation is obtained by using $\phi_\eta^{\prime\prime(\beta)} = \phi_\gamma^{\prime\prime(\beta)} = \phi_\alpha^{\prime\prime(\beta)}$ as

$$\begin{aligned}
\frac{\partial}{\partial t}\left[\langle \rho I_\beta \rangle \Phi_{\alpha\alpha}^{(\beta)}\right] &+ \frac{\partial}{\partial x_k}\left[\langle \rho I_\beta \rangle \Phi_{\alpha\alpha}^{(\beta)} \left\langle \widetilde{U_k^{(\beta)}} \right\rangle\right] + \frac{\partial}{\partial x_k}\left\langle \rho I_\beta u_k^{(\beta)} \phi_\alpha^{\prime\prime(\beta)} \phi_\alpha^{\prime\prime(\beta)} \right\rangle \\
&= -2\left\langle \rho I_\beta u_k^{(\beta)} \phi_\alpha^{\prime\prime(\beta)} \right\rangle \frac{\partial \left\langle \widetilde{\phi_\alpha^{(\beta)}} \right\rangle}{\partial x_k} \\
&\quad + 2\left\langle -\phi_\alpha^{\prime\prime(\beta)} \frac{\partial I_\beta J_i^\alpha}{\partial x_i} + \phi_\alpha^{\prime\prime(\beta)} J_i^\alpha \frac{\partial I_\beta}{\partial x_i} + \rho I_\beta \phi_\alpha^{\prime\prime(\beta)} S_\alpha \right\rangle \\
&\quad + \left\langle \phi_\alpha^{\prime\prime(\beta)} \phi_\alpha^{\prime\prime(\beta)} S_\rho^{(\beta)} \right\rangle .
\end{aligned} \tag{L.22}$$

Note that the second term on the right-hand side of Eq. L.22 can be further simplified for the case of flow past a homogeneous fixed particle bed with heat transfer. In this gas-solid heat transfer problem, the scalar variable is non-dimensional fluid temperature $\phi_\alpha = (T - T_s) / (\langle T_{m,in} \rangle - T_s)$ for $\beta = f$ (see details in Chapters 3 and 4). The assumptions made for this heat transfer problem are (i) no chemical reaction source/sink S_α, (ii) neglect of radiation and free convection (iii) no mass transfer at the interface $S_\rho^{(\beta)}$, (iv) a steady flow, and (v) constant density. Thus, the second term on the right-hand side of Eq. L.22 is expanded to

$$\left\langle \phi_\alpha^{\prime\prime(\beta)} \frac{\partial I_\beta J_i^\alpha}{\partial x_i} \right\rangle = \left\langle \frac{\partial I_\beta \phi_\alpha^{\prime\prime(\beta)} J_i^\alpha}{\partial x_i} \right\rangle - \left\langle I_\beta J_i^\alpha \frac{\partial \phi_\alpha^{\prime\prime(\beta)}}{\partial x_i} \right\rangle . \tag{L.23}$$

The first term on the right-hand side of the above expression can be further written as

$$
\begin{aligned}
\left\langle \frac{\partial I_\beta \phi_\alpha^{\prime\prime(\beta)} J_i^\alpha}{\partial x_i} \right\rangle &= -\Gamma_\alpha^{(\beta)} \left\langle \frac{\partial I_\beta \phi_\alpha^{\prime\prime(\beta)} \frac{\partial \phi_\alpha^{\prime\prime(\beta)}}{\partial x_i}}{\partial x_i} \right\rangle \\
&= -\Gamma_\alpha^{(\beta)} \left\langle \frac{\partial I_\beta \frac{1}{2} \frac{\partial \phi_\alpha^{\prime\prime(\beta)} \phi_\alpha^{\prime\prime(\beta)}}{\partial x_i}}{\partial x_i} \right\rangle \\
&= -\frac{1}{2}\Gamma_\alpha^{(\beta)} \left\langle \frac{\partial \left[\frac{\partial I_\beta \phi_\alpha^{\prime\prime(\beta)} \phi_\alpha^{\prime\prime(\beta)}}{\partial x_i} - \phi_\alpha^{\prime\prime(\beta)} \phi_\alpha^{\prime\prime(\beta)} \frac{\partial I_\beta}{\partial x_i} \right]}{\partial x_i} \right\rangle \\
&= -\frac{1}{2}\Gamma_\alpha^{(\beta)} \left\langle \frac{\partial^2 \left[I_\beta \phi_\alpha^{\prime\prime(\beta)} \phi_\alpha^{\prime\prime(\beta)} \right]}{\partial x_i \partial x_i} \right\rangle, \qquad \text{(L.24)}
\end{aligned}
$$

where $\Gamma_\alpha^{(\beta)}$ is the molecular diffusivity in phase β. Note that in the derivation of the above equation, due to the definition of $\phi_\alpha = (T - T_s) / (\langle T_{m,in} \rangle - T_s)$ the non-dimensional fluid temperature at the interphase is equal to zero, which results in $\left\langle \phi_\alpha^{\prime\prime(\beta)} \phi_\alpha^{\prime\prime(\beta)} \partial I_\beta / \partial x_i \right\rangle = 0$.

The second term on the right-hand side of the expression (Eq. L.23) can be further written as

$$
\begin{aligned}
\left\langle I_\beta J_i^\alpha \frac{\partial \phi_\alpha^{\prime\prime(\beta)}}{\partial x_i} \right\rangle &= -\Gamma_\alpha^{(\beta)} \left\langle I_\beta \frac{\partial \phi_\alpha^{(\beta)}}{\partial x_i} \frac{\partial \phi_\alpha^{\prime\prime(\beta)}}{\partial x_i} \right\rangle \\
&= -\Gamma_\alpha^{(\beta)} \left\langle I_\beta \frac{\partial \phi_\alpha^{\prime\prime(\beta)}}{\partial x_i} \frac{\partial \phi_\alpha^{\prime\prime(\beta)}}{\partial x_i} \right\rangle - \Gamma_\alpha^{(\beta)} \left\langle I_\beta \frac{\partial \left\langle \phi_\alpha^{(\beta)} \right\rangle}{\partial x_i} \frac{\partial \phi_\alpha^{\prime\prime(\beta)}}{\partial x_i} \right\rangle \\
&= -\Gamma_\alpha^{(\beta)} \left\langle I_\beta \frac{\partial \phi_\alpha^{\prime\prime(\beta)}}{\partial x_i} \frac{\partial \phi_\alpha^{\prime\prime(\beta)}}{\partial x_i} \right\rangle - \Gamma_\alpha^{(\beta)} \frac{\partial \left\langle \phi_\alpha^{(\beta)} \right\rangle}{\partial x_i} \left\langle I_\beta \frac{\partial \phi_\alpha^{\prime\prime(\beta)}}{\partial x_i} \right\rangle \\
&= -\Gamma_\alpha^{(\beta)} \left\langle I_\beta \frac{\partial \phi_\alpha^{\prime\prime(\beta)}}{\partial x_i} \frac{\partial \phi_\alpha^{\prime\prime(\beta)}}{\partial x_i} \right\rangle. \qquad \text{(L.25)}
\end{aligned}
$$

Note that for the same reason, the term $\left\langle I_\beta \partial \phi_\alpha^{\prime\prime(\beta)} / \partial x_i \right\rangle$ is zero in the above derivation. Therefore, the second term on the right-hand side of Eq. L.22 contains the scalar dissipation and mixing terms. If assuming a constant-density steady flow, the steady scalar-variance transport equation becomes

$$\left\langle \widetilde{U_k^{(\beta)}} \right\rangle \frac{\partial}{\partial x_k} \left[\rho \left\langle I_\beta \right\rangle \widetilde{\Phi_{\alpha\alpha}^{(\beta)}} \right] = -2\rho \left\langle I_\beta u_k^{(\beta)} \phi_\alpha''^{(\beta)} \right\rangle \frac{\partial \left\langle \phi_\alpha^{(\beta)} \right\rangle}{\partial x_k} - \rho \frac{\partial}{\partial x_k} \left\langle I_\beta u_k^{(\beta)} \phi_\alpha''^{(\beta)} \phi_\alpha''^{(\beta)} \right\rangle$$
$$+\Gamma_\alpha^{(\beta)} \frac{\partial^2 \left\langle I_\beta \phi_\alpha''^{(\beta)} \phi_\alpha''^{(\beta)} \right\rangle}{\partial x_k \partial x_k} - 2\Gamma_\alpha^{(\beta)} \left\langle I_\beta \frac{\partial \phi_\alpha''^{(\beta)}}{\partial x_k} \frac{\partial \phi_\alpha''^{(\beta)}}{\partial x_k} \right\rangle$$
$$+2 \left\langle \phi_\alpha''^{(\beta)} J_k^\alpha \frac{\partial I_\beta}{\partial x_k} \right\rangle . \qquad \text{(L.26)}$$

APPENDIX M. PARALLELIZATION OF FFD PR-DNS APPROACH

Development of a parallel solver for our FFD PR-DNS from scratch is a nontrivial task, since it involves many subtasks including efficiency of parallelization and decomposition techniques for parallel algorithms. In our parallel implementation, the hydrodynamic and scalar solvers are parallelized using the open-source Portable, Extensible Toolkit for Scientific Computation (PETSc) software. PETSc is widely used for large-scale simulations because it has many efficient matrix solution options. We use three-dimensional domain decomposition to parallelize our computational domain that is discretized using a uniform Cartesian grid as shown in Fig. M.1. PETSc provides excellent parallel management of uniform grids. In the example shown in Fig. M.1, the computational domain is decomposed into 64 subdomains such that each subdomain is handled by one processor. Each subdomain has ghost cell layers at each box face between two processors. The advantage of the 3D domain decomposition is that it allows us to simulate efficiently the computational domain with a large cross-section area.

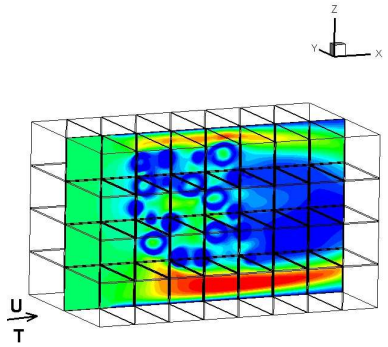

Figure M.1: Schematic plot of the 3D decomposition domain in FFD PR-DNS simulation. Each small box is handled by a processor in parallel simulation. Ghost cells are used to deal with the communication between neighbor processor.

The parallel performance of the FFD PR-DNS solver can be assessed in scale-up tests. In the FFD PR-DNS, since a singular matrix is assembled based on the above Poisson equation, solving this ill-posed matrix costs $70\% - 80\%$ of CPU time in each time step. Therefore, the parallel performance of the solver depends mostly on the time taken to solve the Poisson equation in Eq. 7.9 that arises in the two-step fractional step method. In Eq. 7.9, u_i^* is the intermediate fluid velocity at the half time step, and φ is the correction to the pressure that ensures the final fluid velocity field is solenoidal. Three test cases are simulated to assess the performance of the parallel FFD PR-DNS solver. All the test cases are simulated using the CyEnce cluster at Iowa State University that was funded by an NSF-MRI grant. The first test case involves solving a model 3D Poisson equation that has an analytic solution. This equation is

$$\nabla^2\phi = -\sin(2\pi x)\sin(2\pi y)\sin(2\pi z) \tag{M.1}$$

with the periodic boundary condition $0 \leq x, y, z \leq 1$. The analytical solution for this simple Poisson equation is:

$$\phi = \frac{1}{12\pi^2}\sin(2\pi x)\sin(2\pi y)\sin(2\pi z). \tag{M.2}$$

Figure M.2 shows the accuracy of the numerical solution to Eq. M.1 by comparing its error with respect to the analytical solution in Eq. M.2. The error is defined as

$$\xi = \left[\frac{1}{N}\sum_{i=1}^{N}\left(\phi_{i,num} - \phi_{i,ana}\right)^2\right]^{1/2}, \tag{M.3}$$

where $\phi_{i,num}$ is the numerical solution obtained from Eq. M.1 and $\phi_{i,ana}$ is the analytical solution in Eq. M.2. With reducing grid size the error decays to single precision machine error. The parallel solver is thus validated by comparing the numerical solution with the analytical solution.

Figure M.3 shows the efficiency of solving the 3D Poisson equation in Eq. M.1 using a parallel implementation. The parallel efficiency is defined as t_1/pt_p, where t_1 is the time taken to complete one time step using a single processor for a serial run and t_p is the time taken to complete one time step in each processor for parallel run with p number of processors. This case

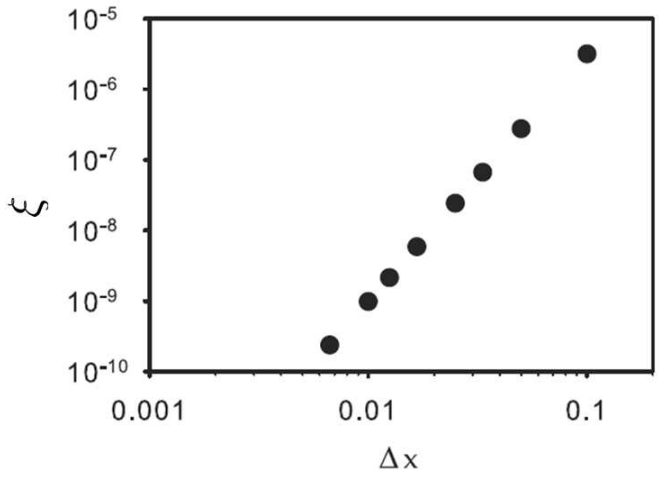

Figure M.2: Error (L2-norm) between numerical solution and analytical solution in solving the 3D Poisson equation in Eq. M.1 with periodic boundary conditions in all three directions. The error ξ is defined in Eq. M.3 and Δx is the grid spacing.

is scaled up to 1600 processors. It shows even using 1600 processors the efficiency of solving Poisson equation is still above 60%. This shows that solving the Poisson equation using PETSc has a good parallel performance.

The second test case is to check the time needed to solve the Poisson equation in Eq. 7.9 and the total time for run one time step using weak scaling. Weak scaling is defined as how the solution time varies with the number of processors for a fixed problem size per processor. Weak scaling was chosen instead of strong scaling to test the parallel efficiency when simulating a long pencil domain that represents a long riser. This simulation is planned in the near future. The test case that has been chosen to assess the performance of the FFD PR-DNS hydrodynamic solver is a periodic duct flow. The metric to assess the performance of our parallel solver is the speedup in weak scaling, which is defined as pt_1/t_p. The ideal speedup for weak scaling results when the time for communication between processors is zero. However, in a real simulation the time for communication between processors is nonzero since the processors need to communicate the variable such as velocity and scalar in the ghost cells. Figure M.4

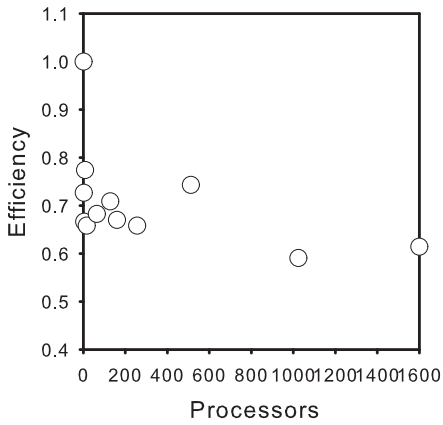

Figure M.3: Parallel efficiency of solving the model 3D Poisson equation. The scale-up is up to 1600 processors.

shows the speedup of solving the Poisson equation and all equations in the FFD PR-DNS hydrodynamic solver. In this test case we are able to successfully scale the FFD PR-DNS solver to 500 processors. The speedup for solving all equations in the FFD PR-DNS (denoted by up-triangle) and solving Poisson equation (denoted by down-triangle) for one timestep is close to 300 using 512 processors, which shows that the efficiency is a little below 60%. This performance implies that even though the communication increases with increasing number of processors, the efficiency is still about 60% with 500 processors. Finally, the third test case is a flow past a fixed sphere in an open field which is a benchmark accuracy test for any numerical simulation approach has been shown in Section 7.4.3.

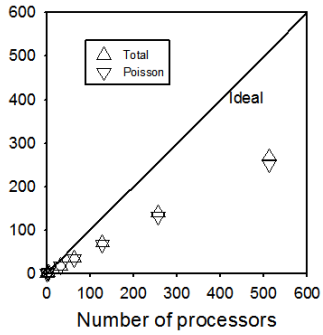

Figure M.4: Parallel speedup in solving the Poisson equation (triangle down) and total time (triangle up) in the weak scaling test: each processor is assigned 32^3 grid nodes. The solid line represents the ideal speedup when the time for communication between processors is zero.

APPENDIX N. 1D ANALYTICAL SOLUTION FOR MASS TRANSFER ON A NON-POROUS SPHERE

The mass transfer in a steady flow past a non-porous sphere with the first-order surface chemical reaction is governed by the momentum equation and convection-diffusion equation. In Stokes flow, this 3D mass transfer problem can be simplified into 1D homogeneous problem. Since the velocity field is known in Stokes flow, the convection-diffusion equation only needs to be solved with appropriate boundary conditions. Therefore, in a spherical coordinate, this mass transfer problem in a steady-state condition is simplified to

$$U\left(r\right)\frac{dC_A}{dr} = D_{bA}\left(\frac{d^2C_A}{dr^2} + \frac{2}{r}\frac{\partial C_A}{\partial r}\right), \tag{N.1}$$

with the far field and the flux boundary conditions

$$C_A(r=\infty) = C_{A,\infty}, \tag{N.2}$$

$$D_{bA}\frac{dC_A}{dr}|_{r=R} = k_s C_{As}. \tag{N.3}$$

Where r is the radial direction, the velocity distribution $U(r)$ in Stokes flow is chosen as

$$U(r) = -U_\infty\left(\frac{R^3}{2r^3} - \frac{3R}{2r} + 1\right). \tag{N.4}$$

Note that the velocity field $U(r,\theta = 0)$ (θ is the angular direction) is assumed in this 1D analysis. Since the concentration $C\left(r\right)$ only depends the r direction, this 1D convection-diffusion equation Eq. N.1 becomes a ordinary differential equation (ODE). For convenience, the above equations and boundary conditions are rewritten as the non-dimensional equations as

$$\hat{U}(\hat{r})\frac{d\hat{C}_A}{d\hat{r}} = \frac{2}{\mathrm{ReSc}}\left(\frac{d^2\hat{C}_A}{d\hat{r}^2} + \frac{2}{\hat{r}}\frac{\partial\hat{C}_A}{\partial\hat{r}}\right), \tag{N.5}$$

with the far field and the flux boundary conditions

$$\hat{C}_A(\hat{r}=\infty) = 1, \tag{N.6}$$

and

$$\frac{d\hat{C}_A}{d\hat{r}}|_{\hat{r}=1} = Da\hat{C}_{As}, \tag{N.7}$$

where $\mathrm{Re} = 2RU_\infty/\nu_f$ is Reynolds number, $\mathrm{Sc} = \nu_f/D_{bA}$ is the Schmit number, $Da = k_sR/D_{bA}$ is the Damkohler number, $\hat{C}_{As} = C_{As}/C_{A,\infty}$ is the surface concentration, and $\hat{r} = r/R$ is the radii of the sphere, $\hat{C}_{As} = \hat{C}_A(\hat{r}=1)$ is the surface concentration , the velocity distribution $U(r)$ in Stokes flow is

$$\hat{U}(\hat{r}) = \frac{U(r)}{U_\infty} = -\left(\frac{1}{2\hat{r}^3} - \frac{3}{2\hat{r}} + 1\right). \tag{N.8}$$

The non-dimensional convection-diffusion equation can be solved using variable separation as follows. Let

$$f_A(\hat{r}) = \frac{d\hat{C}_A}{d\hat{r}}, \tag{N.9}$$

then the equation Eq. N.5 can be written as

$$\left[\frac{\mathrm{ReSc}}{2}\hat{U}(\hat{r}) - \frac{2}{\hat{r}}\right] f_A(\hat{r}) = \frac{df_A(\hat{r})}{d\hat{r}}. \tag{N.10}$$

Using the velocity field in Stokes flow $\hat{U}(\hat{r})$, the expression for $f_A(\hat{r})$ is obtained by integrating Eq. N.10 over $\hat{r}$ as follows

$$\ln\frac{f_A(\hat{r})}{f_A(\hat{r}=1)} = \mathrm{ReSc}\mathcal{W}(\hat{r}), \tag{N.11}$$

where the weight function $\mathcal{W}$ is

$$\mathcal{W}(\hat{r}) = \frac{1}{8\hat{r}^2} + \frac{3}{4}\ln\hat{r} - \frac{1}{2}\hat{r} - \frac{2}{\mathrm{ReSc}}\ln\hat{r} + \frac{3}{8}. \tag{N.12}$$

Thus, the expression for the concentration $\hat{C}_A(\hat{r})$ can be obtained by integrating Eq. N.11 with $f_A(\hat{r}) = d\hat{C}_A/d\hat{r}$ over $\hat{r}$ as

$$\hat{C}_A\left(\hat{r}\right) - \hat{C}_A\left(\hat{r}=1\right) = f_A(\hat{r}=1)\int_1^{\hat{r}} e^{\mathrm{ReSc}\mathcal{W}(r')}dr'. \tag{N.13}$$

Using the boundary conditions in Eqs. N.7 and N.6, the surface concentration $\hat{C}_{A,s} = \hat{C}_A(\hat{r}=1)$ can be written as

$$\hat{C}_A(\hat{r}=1) = (1 + Da\int_1^{\infty} e^{\mathrm{ReSc}\mathcal{W}(r')}dr')^{-1}, \tag{N.14}$$

Therefore, by substituting Eq. N.14 into N.13, the 1D analytical solution for the concentration field with the first-order surface chemical reaction is

$$\hat{C}_A\left(\hat{r}\right) = \frac{1 + Da\int_1^{\hat{r}} e^{\mathrm{ReSc}\mathcal{W}(r')}dr'}{1 + Da\int_1^{\infty} e^{\mathrm{ReSc}\mathcal{W}(r')}dr'}. \tag{N.15}$$

BIBLIOGRAPHY

Abanades, J. C., Anthony, E. J., Lu, D. Y., Salvador, C., and Alvarez, D. (2004). Capture of CO_2 from combustion gases in a fluidized bed of CaO. *Environmental and Energy Engineering*, 50(7):1614–1622. 1, 27, 46, 78

Acrivos, A., Hinch, E. J., and Jeffrey, D. J. (1980). Heat transfer to a slowly moving fluid from a dilute fixed bed of heated spheres. *Journal of Fluid Mechanics*, 101(2):403–421. 11, 15, 28, 32, 47, 48, 50, 82, 86, 95, 109, 250

Acrivos, A. and Taylor, T, D. (1962). Heat and mass transfer from single spheres in Stokes flow. *Physics of Fluids*, 5:387. 9, 226

Adrian, R. J. (1991). Particle-imaging techniques for experimental fluid mechanics. *Annual Review of Fluid Mechanics*, 23(1):261–304. 84, 188

Adrian, R. J. (2005). Twenty years of particle image velocimetry. *Experiments in Fluids*, 39(2):159–169. 84, 188

Anderson, T. B. and Jackson, R. (1967). A fluid mechanical description of fluidized beds. *Industrial & Engineering Chemistry Research*, 6:527–539. 5, 46, 78, 126, 127, 165

Apte, S., Martin, M., and Patankar, N. (2009). A numerical method for fully resolved simulation of rigid particle flow interactions in complex flows. *Journal of Computational Physics*, 228:2712–2738. 14

Azar, C., Lindgren, K., Larson, E., and Mollersten, K. (2006). Carbon capture and storage from fossil fuels and biomass-costs and potential role in stabilizing the atmosphere. *Climatic Change*, 74(1-3):47–79. 27, 46

Bagchi, P. and Balachandar, S. (2003). Effect of turbulence on the drag and lift of a particle. *Physics of Fluids*, 15(11):3496–3513. 14

Bagchi, P. and Balachandar, S. (2004). Response of the wake of an isolated particle to an isotropic turbulent flow. *Journal of Fluid Mechanics*, 518:95–123. 14

Balachandar, S. and Ha, M. (2001). Unsteady heat transfer from a sphere in a uniform cross-flow. *Physics of Fluids*, 13(12):3714–3728. 208, 211, 213

Barker, J. J. (1965). Heat transfer in packed beds. *Industrial and Engineering Chemistry*, 57:43–51. 63

Batchelor, G. K. (2000). *An introduction to fluid dynamics*. Cambridge University Press. 126

Beetstra, R., van der Hoef, M. A., and Kuipers, J. A. M. (2007a). Drag force of intermediate Reynolds number flows past mono- and bidisperse- arrays of spheres. *AIChE Journal*, 53:489. 15, 29, 48, 84

Beetstra, R., van der Hoef, M. A., and Kuipers, J. A. M. (2007b). Numerical study of segregation using a new drag force correlation for polydisperse systems derived from lattice-Boltzmann simulations. *Chemical Engineering Science*, 62:246–255. 7

Bekri, S., Thovert, J. F., and Adler, P. M. (1995). Dissolution of porous media. *Chemical Engineering Science*, 50(17):2765–2791. 83

Bell, C. G., Byrne, H. M., Whiteley, J. P., and Waters, S. L. (2013). Heat or mass transfer from a sphere in Stokes flow at low Peclet number. *Applied Mathematics Letters*, 26(4):392–396. 220, 226

Benyahia, S., Syamlal, M., and O'Brien, T. (2012). Summary of MFIX Equations 2012-1. Technical report. 6, 8, 49, 68, 268

Bird, R. B., Stewart, W. E., and Lightfoot, E. N. (2002). *Transport Phenomena*, volume 2ed. John Wiley and Sons. 255, 257

Boateng, A. A. and Mtui, P. L. (2012). CFD modeling of space-time evolution of fast pyrolysis products in a bench-scale fluidized-bed reactor. *Applied Thermal Engineering*, 33-34:190–198. 4

Boivin, M., Simonin, O., and Squires, K. D. (1998). Direct numerical simulation of turbulence modulation by particles in isotropic turbulence. *Journal of Fluid Mechanics*, 375:235–263. 14

Brenner, H. (1980). Dispersion resulting from flow through spatially periodic porous media. *Philosophical Transactions of the Royal Society A*, 297(1430):81–133. 80, 81, 83, 108

Brenner, H. and Gaydos, L. J. (1977). The constrained Brownian movement of spherical particles in cylindrical pores of comparable radius: models of the diffusive and convective transport of solute molecules in membranes and porous media. *Journal of Colloid and Interface Science*, 58(2):312–356. 80

Bridgwater, A., Meier, D., and Radlein, D. (1999). An overview of fast pyrolysis of biomass. *Organic Geochemistry*, 30(12):1479–1493. 2

Brilliantov, N. V. and Pöschel, T. (2010). *Kinetic theory of granular gases*. Oxford University Press. 126

Brown, R. C. (2011). *Thermochemical processing of biomass : conversion into fuels, chemicals and power*. Wiley Series in Renewable Resource. John Wiley & Sons Inc, New York. 1, 2, 78

Burton, T. M. and Eaton, J. K. (2005). Fully resolved simulations of particle-turbulence interaction. *Journal of Fluid Mechanics*, 545:67–111. 14

Capecelatro, J., Desjardins, O., and Fox, R. O. (2014). Numerical study of collisional particle dynamics in cluster-induced turbulence. *Journal of Fluid Mechanics*, 747:R2. 127

Capecelatro, J., Desjardins, O., and Fox, R. O. (2015). On fluid–particle dynamics in fully developed cluster-induced turbulence. *Journal of Fluid Mechanics*, 780:578–635. 127

Capuani, F., Frenkel, D., and Lowe, C. P. (2003). Velocity fluctuations and dispersion in a simple porous medium. *Physical Review E*, 67(5):056306. 81, 83

Carbonell, R. G. and Whitaker, S. (1983). Dispersion in pulsed systems-II: Theoretical developments for passive dispersion in porous media. *Chemical Engineering Science*, 38(11):1795–1802. 108

Carrara, M. and DesJardin, P. (2006). A filtered mass density function approach for modeling separated two-phase flows for LES I: Mathematical formulation. *International Journal of Multiphase Flow*, 32(3):365–384. 8, 147

Carrara, M. and DesJardin, P. (2008). A filtered mass density function approach for modeling separated two-phase flows for LES II: Simulation of a droplet laden temporally developing mixing layer. *International Journal of Multiphase Flow*, 34(8):748–766. 8, 147

Cassiani, M., Franzese, P., and Giostra, U. (2005). A PDF micromixing model of dispersion for atmospheric flow. Part I: development of the model, application to homogeneous turbulence and to neutral boundary layer. *Atmospheric Environment*, 39(8):1457–1469. 161

Celis, C. and da Silva, L. F. F. (2015). Lagrangian mixing models for turbulent combustion: Review and prospects. *Flow, Turbulence and combustion*, 94(3):643–689. 146

Chapman, S. and Cowling, T. G. (1953). *The mathematical theory of non–uniform gases*. Cambridge University Press, 2nd. edition. 126

Chen, R. and Wu, J. (2000). The flow characteristics between two interactive spheres. *Chemical Engineering Science*, 55(6):1143–1158. 189

Clift, R., Grace, J. R., and Weber, M. E. (1978). *Bubbles, Drops and Particles*. Academic Press. xxii, xxviii, xxix, 9, 47, 175, 176, 188, 221, 226, 233, 234, 236, 238

Cocco, R., Shaffer, F., Hays, R., Karri, S. R., and Knowlton, T. (2010). Particle clusters in and above fluidized beds. *Physics of Fluids*, 203(1):3–11. 127, 249

Coutand, D. and Shkoller, S. (2005). On the interaction between quasilinear elastodynamics and the Navier-Stokes equations. *Archive for Rational Mechanics and Analysis*, 179:303–352. 166

Crimaldi, J. P. (2008). Planar laser induced fluorescence in aqueous flows. *Experiments in Fluids*, 44(6):851–863. 84

Cundall, P. A. and Strack, O. D. L. (1978). The Distinct Element Method as a Tool for Research in Granular Media. Technical Report NSF Grant ENG76-20711, National Science Foundation. 39

Cybulski, A., Dalen, M. V., Verkerk, J., and Berg, P. V. D. (1975). Gas-particle heat transfer coefficients in packed beds at low Reynolds numbers. *Chemical Engineering Science*, 30(9):1015–1018. 7

Deen, N. G., Kriebitzsch, S. H., van der Hoef, M. A., and Kuipers, J. A. M. (2012). Direct numerical simulation of flow and heat transfer in dense fluid-particle system. *Chemical Engineering Science*, 81:329–344. 15, 48, 84, 128, 221

Deen, N. G. and Kuipers, J. (2014). Direct numerical simulation of fluid flow accompanied by coupled mass and heat transfer in dense fluid-particle systems. *Chemical Engineering Science*, 116:645–656. 84

Deen, N. G., Peters, E. A. J. F., Padding, J. T., and Kuipers, J. (2014). Review of direct numerical simulation of fluid-particle mass, momentum and heat transfer in dense gas-solid flows. *Chemical Engineering Science*, 116:710–724. 15, 48, 221

Delgado, J. M. P. Q. (2006). A critical review of dispersion in packed beds. *Heat and Mass Transfer*, 42(4):279–310. 13, 84, 188

Di Blasi, C. and Branca, C. (2003). Temperatures of wood particles in a hot sand bed fluidized by nitrogen. *Energy & Fuels*, 17(1):247–254. xxvii, 214, 215, 216, 242

Di Blasi, C., Branca, C., Masotta, F., and De Biase, E. (2013). Experimental analysis of reaction heat effects during beech wood pyrolysis. *Energy & Fuels*, 27(5):2665–2674. xxvii, 207, 215, 216, 242

Drew, D. A. (1983). Mathematical modeling of two–phase flow. *Annual Review of Fluid Mechanics*, 15:261–291. 5, 126, 165, 272, 278

Drew, D. A. and Passman, S. L. (1998). *Theory of Multicomponent Fluids*. Applied Mathematical Sciences. Springer, New York. 28, 46, 78, 126

Edwards, D. A., Shapiro, M., Brenner, H., and Shapira, M. (1991). Dispersion of inert solutes in spatially periodic, two-dimensional model porous media. *Transport in Porous Media*, 6(4):337–358. 80

Eidsath, A., Carbonell, R. G., Whitaker, S., and Herrmann, L. R. (1983). Dispersion in pulsed systems-III: comparison between theory and experiments for packed beds. *Chemical Engineering Science*, 38(11):1803–1816. 108

Elghobashi, S. E. and Truesdell, G. C. (1993). On the two-way interaction between homogeneous turbulence and dispersed solid particles. I: Turbulence modification. *Physics of Fluids A*, 5:1790–1801. 14

Ergun, S. (1952). Fluid flow through packed columns. *Chemical Engineering Progress*, 48:89–94. 164

Feng, Z. G. and Michaelides, E. (2008). Inclusion of heat transfer computations for particle laden flows. *Physics of Fluids*, 20(4):040604. 30

Feng, Z. G. and Michaelides, E. E. (2000). A numerical study on the transient heat transfer from a sphere at high Reynolds and Peclet numbers. *International Journal of Heat and Mass Transfer*, 43(2):219–229. 208, 211, 213

Feng, Z. G. and Michaelides, E. E. (2009). Heat transfer in particulate flows with direct numerical simulation (DNS). *International Journal of Heat and Mass Transfer*, 52:777–786. 15, 48, 84, 210, 221

Feng, Z. G., Michaelides, E. E., and Scibilia, M. F. (1996). The energy equation of a sphere in an unsteady and nonuniform temperature field. *Revue générale de thermique*, 35(409):4. 208

Feng, Z. G. and Musong, S. G. (2014). Direct numerical simulation of heat and mass transfer of spheres in a fluidized bed. *Physics of Fluids*, 262:62–70. 49

Folkersma, R., Stein, H., and Van de Vosse, F. (2000). Hydrodynamic interactions between two identical spheres held fixed side by side against a uniform stream directed perpendicular to the line connecting the spheres centres. *International Journal of Multiphase Flow*, 26(5):877–887. 189

Forestier, M., Pasquetti, R., and Peyret, R. (2000). Spatial development of wakes using a spectral multi-domain method. *Applied Numerical Mathematics*, 33:207–216. 166

Fox, R. O. (2003). *Computational Models for Turbulent Reacting Flows*. Cambridge University Press. 8, 104, 145, 146, 147, 150, 151, 157, 160, 161, 162, 220

Fox, R. O. (2012). Large-Eddy-Simulation tools for multiphase flows. *Annual Review of Fluid Mechanics*, 44:47–76. 127

Fox, R. O., Laurent, F., and Massot, M. (2008). Numerical simulation of spray coalescence in an eulerian framework: Direct quadrature method of moments and multi-fluid method. *Journal of Computational Physics*, 227:3058–3088. 126

Garg, R. (2009). *Modeling and simulation of two-phase flows*. PhD thesis, Iowa State University. 14, 46, 79, 205

Garg, R., Galvin, J., Li, T., and Pannala, S. (2010a). Documentation of open-source mfix-dem software for gas-solids flows. Technical report, National Energy Technology Laboratory, Department of Energy. 39

Garg, R., Narayanan, C., Lakehal, D., and Subramaniam, S. (2007). Accurate numerical estimation of interphase momentum transfer in Lagrangian-Eulerian simulations of dispersed two-phase flows. *International Journal of Multiphase Flow*, 33:1337–1364. 62

Garg, R., Narayanan, C., and Subramaniam, S. (2009). A numerically convergent Lagrangian-Eulerian simulation method for dispersed two-phase flows. *International Journal of Multiphase Flow*, 35(4):376–388. 6

Garg, R., Tenneti, S., Mohd-Yusof, J., and Subramaniam, S. (2010b). Direct numerical simulation of gas–solid flow based on the immersed boundary method. In Pannala, S., Syamlal, M.,

and O'Brien, T. J., editors, *Computational Gas–solid Flows and Reacting systems: Theory, Methods and Practice*. IGI Global. 14, 15, 16, 30, 35, 55, 57, 60, 90, 91, 130, 163, 165, 168

Gladden, L. (1999). Applications of in situ magnetic resonance technique in chemical reaction engineering. *Topics in Catalysis*, 8:87–95. 164

Glowinski, R., Pan, T., Hesla, T., Joseph, D., and Periaux, J. (2001). A fictitious domain approach to the direct numerical simulation of incompressible viscous flow past moving rigid bodies: application to particulate flow. *Journal of Computational Physics*, 169:363 – 426. 14

Godard, K. and Richardson, J. F. (1969). Bubble velocities and bed expansions in freely bubbling fluidized beds. *Chemical Engineering Science*, 24:663. 164

Goldstein, R. and Kreid, D. K. (1967). Measurement of laminar flow development in a square duct using a laser-doppler flowmeter. *Journal of Applied Mechanics*, 34(4):813–818. xxiii, 176, 177, 178, 192, 193, 200

Gordon, M. and Taylor, P. A. (2009). The electric field during blowing snow events. *Boundary-Layer Meteorology*, 130(1):97–115. 1

Guermond, J.-L., Minev, P., and Shen, J. (2005). Error analysis of pressure-correction schemes for the time-dependent stokes equations with open boundary conditions. *SIAM Journal on Numerical Analysis*, 43:239–258. 166

Gunn, D. J. (1978). Transfer of heat and mass to particles in fixed and fluidized beds. *International Journal of Heat and Mass Transfer*, 21:467–476. xiv, xv, 7, 10, 12, 15, 28, 41, 42, 45, 47, 49, 63, 64, 65, 75, 206, 250

Gunn, D. J. and Desouza, J. F. C. (1974). Heat-transfer and axial dispersion in packed-beds. *Chemical Engineering Science*, 29:1363–1371. 7, 11, 12, 47, 63, 83, 84

Gupalo, Y. P. and Ryazantsev, Y. S. (1972). Mass and heat transfer from a sphere in a laminar flow. *Chemical Engineering Science*, 27 (1):61–68. xxviii, xxix, 9, 218, 220, 221, 222, 224, 226, 227, 228, 229, 230, 232, 233, 235, 237, 238

Haeri, S. and Shrimpton, J. S. (2013). A new implicit fictitious domain method for the simulation of flow in complex geometries with heat transfer. *Journal of Computational Physics*, 237:21–45. 48, 84

Halvorsen, B., Guenther, C., and O'Brien, T. (2003). CFD calculations for scaling of a bubbling fluidized bed. In *Proceedings of the AIChE annual meeting*. 78, 145

Handley, D. and Heggs, P. J. (1968). Momentum and heat transfer mechanisms in regular shaped packings. *Transactions of the Institution of Chemical Engineers*, 46:251–264. 11, 47, 84

Hartunian, R. A. and Liu, S. W. (1963). Slow flow of a dissociated gas about a catalytic probe. *Physics of Fluids*, 6(3):349–354. 9, 220, 226

Haworth, D. (2010). Progress in probability density function methods for turbulent reacting flows. *Progress in Energy and Combustion Science*, 36(2):168–259. 8, 144, 146, 148, 157

Hill, R. J., Koch, D. L., and Ladd, A. J. C. (2001a). The first effects of fluid inertia on flows in ordered and random arrays of spheres. *Journal of Fluid Mechanics*, 448:213–241. 7, 15, 29, 48, 84

Hill, R. J., Koch, D. L., and Ladd, A. J. C. (2001b). Moderate Reynolds number flows in ordered and random arrays of spheres. *Journal of Fluid Mechanics*, 448:243–278. 7, 15, 29, 48, 84

Holloway, W., Yin, X., and Sundaresan, S. (2010). Fluid-particle drag in inertial polydisperse gas-solid suspensions. *AIChE Journal*, 56:1995–2004. 29

Hrenya, C. and Morris, A. (2014). Pachinko revisited: Predicting granular flows and their heat transfer. In *Proceedings of 2014 American Institute of Chemical Engineers Annual Meeting*. 47, 80

Hu, H. H., Patankar, N. A., and Zhu, M. Y. (2001). Direct Numerical Simulations of fluid-solid systems using the arbitrary Lagrangian-Eulerian technique. *Journal of Computational Physics*, 169(2):427–462. 14

Incropera, F. P., DeWitt, D. P., Bergman, T. L., and Lavine, A. S. (2006). *Fundamentals of Heat and Mass Transfer*. John Wiley & Sons Inc, New York, sixth edition. xxix, 32, 33, 52, 62, 87, 93, 221, 236, 238, 252

Jeong, N. and Choi, D. H. (2011). Estimation of the thermal dispersion in a porous medium of complex structures using a lattice Boltzmann method. *International Journal of Heat and Mass Transfer*, 54(19):4389–4399. 7, 82

Jin, G. and Braza, M. (1993). A nonreflecting outlet boundary condition for incompressible unsteady Navier-Stokes calculations. *Journal of Computational Physics*, 107:239–253. 166, 170

Johnson, T. and Patel, V. (1999). Flow past a sphere up to a Reynolds number of 300. *Journal of Fluid Mechanics*, 378:19–70. 188

Kashiwa, B. A. and Gaffney, E. S. (2003). Design Basis for CFDLib. Technical Report LA-UR-03-1295, Los Alamos National Lab. 27, 46, 78

Kaviany, M. (2012). *Principles of Heat Transfer in Porous Media*. Springer Science & Business Media. 13, 81

Kim, D. and Choi, H. (2006). Immersed boundary method for flow around an arbitrarily moving body. *Journal of Computational Physics*, 212:662–680. 14

Koch, D. L. (1990). Kinetic-theory for a monodisperse gas-solid suspension. *Physics of Fluids A*, 2:1711–1723. 126

Koch, D. L. (1993). Hydrodynamic diffusion in dilute sedimenting suspensions at moderate Reynolds numbers. *Physics of Fluids A*, 5(5):1143–1155. 109, 124

Koch, D. L. and Brady, J. F. (1985). Dispersion in fixed beds. *Journal of Fluid Mechanics*, 154:399–427. 7, 10, 13, 80, 81, 82, 107, 108, 109, 128, 188

Koch, D. L. and Brady, J. F. (1987a). A non-local description of advection-diffusion with application to dispersion in porous media. *Journal of Fluid Mechanics*, 180:387–403. 80, 128, 140

Koch, D. L. and Brady, J. F. (1987b). Nonlocal dispersion in porous media: nonmechanical effects. *Chemical Engineering Science*, 42(6):1377–1392. 80, 128, 140

Kunii, D. and Smith, J. M. (1961). Heat transfer characteristics of porous rocks. 2. thermal conductivities of unconsolidated particles with flowing fluids. *AIChE Journal*, 7:29–34. 7, 11, 47, 84

Kuwahara, F., Nakayama, A., and Koyama, H. (1996). A numerical study of thermal dispersion in porous media. *Journal of Heat Transfer*, 118(3):756–761. 7, 81, 82

Ladd, A. J. C. and Verberg, R. (2001). Lattice-Boltzmann simulations of particle-fluid suspensions. *Journal of Statistical Physics*, 104:1191–1251. 14

Laird, D. A., Brown, R. C., Amonette, J. E., and Lehmann, J. (2009). Review of the pyrolysis platform for coproducing bio-oil and biochar. *Biofuels, Bioproducts and Biorefining*, 3:547–562. 2

Lee, C.-H., Park, S.-W., and Kim, S.-S. (2014). Breakthrough analysis of carbon dioxide adsorption on zeolite synthesized from fly ash. *Korean Journal of Chemical Engineering*, 31(2):179–187. 219, 220

Liang, S., Hong, T., and Fan, L. (1996). Effects of particle arrangements on the drag force of a particle in the intermediate flow regime. *International Journal of Multiphase Flow*, 22:285–306. 189

Lim, K. S., Zhu, J. X., and Grace, J. R. (1995). Hydrodynamics of gas-solid fluidization. *International Journal of Multiphase Flow*, 21:141–193. 164

Littman, H., Barile, R. G., and Pulsifer, A. H. (1968). Gas-particle heat transfer coefficients in packed beds at low Reynolds numbers. *Industrial & Engineering Chemistry Fundamentals*, 7:554. 7, 11, 47, 83, 84

Littman, H. and Sliva, D. (1970). Gas-particle heat-transfer coefficients in packed beds at low Reynolds numbers. In Grigull, U. and Hahne., E., editors, *Proceedings of the Fourth International Heat Transfer Conference*, volume 7. Elsevier, New York. 63

Liu, J. (2009). Open and traction boundary conditions for the incompressible Navier-Stokes equations. *Journal of Computational Physics*, 228:7250–7267. 166

Lowe, C. P. and Frenkel, D. (1996). Do hydrodynamic dispersion coefficients exist? *Physical Review Letters*, 77(22):4552. 81, 83

Lucci, F., Ferrante, A., and Elgobashi, S. (2010). Modulation of isotropic turbulence by particles of Taylor length-scale size. *Journal of Fluid Mechanics*, 650(5–55). 14

Luo, K., Zhuang, Z., Fan, J., and Haugen, N. E. L. (2016). A ghost-cell immersed boundary method for simulations of heat transfer in compressible flows under different boundary conditions. *International Journal of Heat and Mass Transfer*, 92:708–717. 222

Maier, R. S., Kroll, D. M., Bernard, R. S., Howington, S. E., Peters, J. F., and Davis, H. T. (2000). Pore-scale simulation of dispersion. *Physics of Fluids*, 12(8):2065–2079. 81, 83

Maier, R. S., Kroll, D. M., Bernard, R. S., Howington, S. E., Peters, J. F., and Davis, H. T. (2003). Hydrodynamic dispersion in confined packed beds. *Physics of Fluids*, 15(12):3795–3815. 81, 83

Manz, B., Gladden, L. F., and Warren, P. B. (1999). Flow and dispersion in porous media: Lattice-Boltzmann and NMR studies. *AIChE Journal*, 45(9):1845–1854. 81, 83

Marchisio, D. L., Fox, R. O., Barresi, A. A., and Baldi, G. (2001). On the comparison between presumed and full PDF methods for turbulent precipitation. *Industrial & engineering chemistry research*, 40(23):5132–5139. 8

Mashayek, F. and Taulbee, D. B. (2002). Turbulent gas–solid flows, part I: Direct numerical simulations and Reynolds stress closures. *Numerical Heat Transfer, Part B: Fundamentals*, 41(1):1–29. 14

Massol, A., Simonin, O., and Poinsot, T. (2004). Steady and unsteady drag and heat transfer in fixed arrays of equal sized spheres. Technical Report TR/CFD/04/13, CERFACS, Toulouse, France. 15, 48

Mauret, E. and Renaud, M. (1997a). Transport phenomena in multi-particle systems–I. Limits of applicability of capillary model in high voidage beds–application to fixed beds of fibers and fluidised beds of spheres. *Chemical Engineering Science*, 52:1807–1817. 164

Mauret, E. and Renaud, M. (1997b). Transport phenomena in multi-particle systems–II. Proposed new model based on flow around submerged objects for sphere and fiber beds–transition between the capillary and particulate representations. *Chemical Engineering Science*, 52:1819–1834. 164

Mehrabadi, M., Murphy, E. J., and Subramaniam, S. (2016). Development of a gas-solid drag law for clustered particles using particle-resolved direct numerical simulation. *Chemical Engineering Science*, 152:199–212. 246

Mehrabadi, M., Tenneti, S., Garg, R., and Subramaniam, S. (2015). Pseudo-turbulent gas-phase velocity fluctuations in homogeneous gas–solid flow: fixed particle assemblies and freely evolving suspensions. *Journal of Fluid Mechanics*, 770:210–246. 3, 7, 17, 18, 32, 74, 77, 80, 96, 97, 106, 115, 129, 130, 133, 135, 145, 146, 152, 154, 165, 189

Michaelides, E. E. and Feng, Z. G. (1994). Heat transfer from a sphere in a non-uniform temperature and velocity field. *International Journal of Heat and Mass Transfer*, 37:2069–2076. 208

Miller, D. C., Syamlal, M., Cottrell, R., Kress, J. D., Sun, X., Sundaresan, S., Sahinidis, N. V., Zitney, S. E., Bhattacharyya, D., and Agarwal, D. (2012). *Annual Report: Carbon Capture Simulation Initiative (CCSI) (30 September 2012)*. 46

Minier, J. P. and Peirano, E. (2001). The PDF approach to turbulent polydispersed two-phase flows. *Physics Reports*, 352(1):1–214. 5, 147

Mostaghimi, P., Bijeljic, B., and Blunt, M. (2012). Simulation of flow and dispersion on pore-space images. *SPE Journal*, 17(4):1–131. 81, 83

Nomura, T. and Hughes, T. J. R. (1992). An arbitrary Lagrangian–Eulerian finite element

method for interaction of fluid and a rigid body. *Computer Methods in Applied Mechanics and Engineering*, 95(1):115–138. 14

Oguz, H. N. and Prosperetti, A. (2001). PHYSALIS: A new O(N) method for the numerical simulation of disperse systems: Potential flow of spheres. *Journal of Computational Physics*, 167(1):196–216. 14

Orlanski, I. (1976). A simple boundary condition for unbounded hyperbolic flows. *Journal of Computational Physics*, 21:251–269. 166

Ozgoren, M. (2013). Flow structures around an equilateral triangle arrangement of three spheres. *International Journal of Multiphase Flow*, 53:54–64. 189

Özgümüş, T., Mobedi, M., Özkol, Ü., and Nakayama, A. (2013). Thermal dispersion in porous media-a review on the experimental studies for packed beds. *Applied Mechanics Reviews*, 65(3):031001. 7, 13, 81

Pai, G. M. and Subramaniam, S. (2006). Accurate numerical solution of the spray equation using particle methods. *Atomization and Sprays*, 16(2):159–194. 6

Pai, G. M. and Subramaniam, S. (2009). A comprehensive probability density function formalism for multiphase flows. *Journal of Fluid Mechanics*, 628:181–228. 5, 126, 133, 147, 158, 159, 272, 276, 283, 286

Pai, M. G. and Subramaniam, S. (2012). Two-way coupled stochastic model for dispersion of inertial particles in turbulence. *Journal of Fluid Mechanics*, 700:29–62. 159, 283

Papadikis, K., Gu, S., and Bridgwater, A. V. (2009a). CFD modelling of the fast pyrolysis of biomass in fluidised bed reactors. Part B Heat, momentum and mass transport in bubbling fluidised beds. *Chemical Engineering Science*, 64(5):1036–1045. 4

Papadikis, K., Gu, S., and Bridgwater, A. V. (2009b). CFD modelling of the fast pyrolysis of biomass in fluidised bed reactors: modelling the impact of biomass shrinkage. *Chemical Engineering Science*, 149(1):417–427. 206

Park, W. H., Kang, W. K., Capes, C. E., , and Osberg, G. L. (1969). The properties of bubbles in fluidized bed of conducting particles as measured by an electroresistivity probe. *Chemical Engineering Science*, 24:851. 164

Patankar, N. A., Singh, P., Joseph, D. D., Glowinski, R., and Pan, T.-W. (2000). A new formulation of the distributed Lagrange multiplier/fictitious domain method for particulate flows. *International Journal of Multiphase Flow*, 26(9):1509–1524. 14

Patankar, S. V. (1980). *Numerical heat transfer and fluid flow*. Hemisphere Pub. Corp. 36, 57

Pedras, M. H. J. and de Lemos, M. J. S. (2008). Thermal dispersion in porous media as a function of the solid–fluid conductivity ratio. *International Journal of Heat and Mass Transfer*, 51(21):5359–5367. 7, 82

Peirano, E. and Minier, J.-P. (2002). Probabilistic formalism and hierarchy of models for polydispersed turbulent two-phase flows. *Physical Review E*, 65(4):046301. 147

Pepiot, P. and Desjardins, O. (2010). Direct numerical simulation of dense particle-laden flows investigation of the gas-particles coupling. Proceedings of the Center for Turbulence Research Summer Program. xxii, 175, 176

Peskin, C. S. (1981). The fluid dynamics of heart valves: experimental, theoretical, and computational methods. *Annual Review of Fluid Mechanics*, 14(235-259). 14

Pfeffer, R. and Happel, J. (1964). Analytical study of heat and mass transfer in multiparticle systems at low Reynolds numbers. *AIChE Journal*, 10(5):605 – 611. 9, 10, 28, 47

Pinar, E., Sahin, B., Ozgoren, M., and Akilli, H. (2013). Experimental study of flow structures around side-by-side spheres. *Industrial & Engineering Chemistry Research*, 52(40):14492–14503. 189

Pope, S. (1981). Transport equation for the joint probability density function of velocity and scalars in turbulent flow. *Physics of Fluids*, 24:588–596. 158

Pope, S. (1994). Stochastic lagrangian models for turbulence. *Annual Reviews of Fluid Mechanics*, 26:23–63. 162

Pope, S. B. (1985). PDF methods for turbulent reactive flows. *Progress in Energy and Combustion Science*, 11:119–192. 144, 147, 158, 273, 280

Pope, S. B. (1998). The vanishing effect of molecular diffusivity on turbulent dispersion: implications for turbulent mixing and the scalar flux. *Journal of Fluid Mechanics*, 359:299–312. 81

Pope, S. B. (2000). *Turbulent Flows*. Cambridge University Press, Port Chester, NY. 8, 131, 145, 146, 148, 151, 277

Popov, P. P. and Pope, S. B. (2014). Large eddy simulation/probability density function simulations of bluff body stabilized flames. *Combustion and Flame*, 161(12):3100–3133. 162

Poux, A., Glockner, S., and Azaiez, M. (2011). Improvements on open and traction boundary conditions for Navier-Stokes time-splitting methods. *Journal of Computational Physics*, 230:4011–4027. 166, 170, 171

Pozorski, J. and Minier, J.-P. (1999). Probability density function modeling of dispersed two-phase turbulent flows. *Physical Review E*, 59(1):855. 147

Prahl, L., Hölzer, A., Arlov, D., Revstedt, J., Sommerfeld, M., and Fuchs, L. (2007). On the interaction between two fixed spherical particles. *International Journal of Multiphase Flow*, 33(7):707–725. 189

Prasad Vegendla, S., Heynderickx, G. J., and Marin, G. B. (2012). Probability density function simulation of turbulent reactive gas-solid flow in a FCC riser. *AIChE Journal*, 58(1):268–284. 161, 162

Proudman, I. and Pearson, J. (1957). Expansions at small Reynolds numbers for the flow past a sphere and a circular cylinder. *Journal of Fluid Mechanics*, 2(03):237–262. 220, 226

Pyle, D. L. and Harrison, D. (1967). An experimental investigation of the two-phase theory of fluidization. *Chemical Engineering Science*, 22:1199. 164

Raman, V., Fox, R. O., and Harvey, A. D. (2004). Hybrid finite-volume/transported PDF simulations of a partially premixed methane–air flame. *Combustion and Flame*, 136(3):327–350. 161

Ren, W., Shu, C., and Yang, W. (2013). An efficient immersed boundary method for thermal flow problems with heat flux boundary conditions. *International Journal of Heat and Mass Transfer*, 64:694–705. 221

Rigby, G. R., Blockland, G. P. V., Park, W. H., and Capes, C. E. (1970). Properties of bubbles in three phase fluidized beds as measured by an electroresistivity probe. *Chemical Engineering Science*, 25:1729. 164

Ronald, W. B. and Christopher, P. G. (2009). Mass transfer in the core-annular and fast fluidization flow regimes of a CFB. *Powder Technology*, 190(3):385 – 389. 28

Scardovelli, R. and Zaleski, S. (1999). Direct numerical simulation of free–surface and interfacial flow. *Annual Review of Fluid Mechanics*, 31:567–603. 14

Schlichting, H. (1968). *Boundary Layer Theory*. McGraw-Hill. xxiv, 182

Schlichting, H. and Gersten, K. (2003). *Boundary-layer theory*. Springer Science & Business Media. 188

Shah, R. and London, A. (1978). *Laminar flow forced convection in Ducts*. Academic Press, New York. xi, xiii, xxiii, 38, 39, 171, 172, 173, 178, 179

Sharma, N. and Patankar, N. (2005). A fast computation technique for the direct numerical simulation of rigid particulate flows. *Journal of Computational Physics*, 205(2):439–457. 14

Shen, J., Kaguei, S., and Wakao, N. (1981). Measurements of particle-to-gas heat-transfer coefficients from one-shot thermal responses in packed-beds. *Chemical Engineering Science*, 36:1283–1286. 11, 47, 84

Shen, L., Zheng, M., Xiao, J., and Xiao, R. (2008). A mechanistic investigation of a calcium-based oxygen carrier for chemical looping combustion. *Combustion and Flame*, 154(3):489–506. x, 1, 27, 46, 74, 78

Sirivat, A. and Warhaft, Z. (1983). The effect of a passive cross-stream temperature gradient on the evolution of temperature variance and heat flux in grid turbulence. *Journal of Fluid Mechanics*, 128:323–346. 96

Soloff, S. M., Adrian, R. J., and Liu, Z.-C. (1997). Distortion compensation for generalized stereoscopic particle image velocimetry. *Measurement Science and Technology*, 8(12):1441. 191

Sorensen, J. P. and Stewart, W. E. (1974). Computation of forced-convection in slow flow through ducts and packed-beds .3. heat and mass-transfer in a simple cubic array of spheres. *Chemical Engineering Science*, 29:827–832. 10, 28, 47

Spalding, D. (1971). Concentration fluctuations in a round turbulent free jet. *Chemical Engineering Science*, 26(1):95–107. 151

Squires, K. D. and Eaton, J. K. (1991). Measurements of particle dispersion obtained from direct numerical simulations of isotropic turbulence. *Journal of Fluid Mechanics*, 226:1–35. 14

Stoyan, D., Kendall, W. S., and Mecke, J. (1995). *Stochastic Geometry and its Applications*. Wiley Series in Probability and Mathematical Statistics. John Wiley and Sons, New York, 2nd edition. 127

Stoyan, D. and Stoyan, H. (1995). *Fractals, Random Shapes and Point Fields*. Wiley Series in Probability and Mathematical Statistics. John Wiley and Sons, New York. 127

Subramaniam, S. (2013). Lagrangian-Eulerian methods for multiphase flows. *Progress in Energy and Combustion Science*, 39:215–245. 5, 126, 127

Subramaniam, S. and Pope, S. (1998). A mixing model for turbulent reactive flows based on Euclidean minimum spanning trees. *Combustion and Flame*, 115(4):487–514. 96

Sun, B., Tenneti, S., and Subramaniam, S. (2015). Modeling average gas–solid heat transfer using particle-resolved direct numerical simulation. *International Journal of Heat and Mass*

Transfer, 86:898–913. 77, 80, 85, 87, 91, 92, 105, 108, 125, 128, 129, 134, 135, 136, 138, 140, 141, 151, 263

Sun, B., Tenneti, S., Subramaniam, S., and Koch, D. L. (2016). Pseudo-turbulent heat flux and average gas–phase conduction during gas–solid heat transfer: flow past random fixed particle assemblies. *Journal of Fluid Mechanics*, 798:299–349. 129, 151

Sun, J., Battaglia, F., and Subramaniam, S. (2007). Hybrid two-fluid DEM simulation of gas-solid fluidized beds. *Journal of Fluids Engineering*, 129(11):1394–1403. 27, 46, 78, 165

Sundaram, S. and Collins, L. R. (1999). A numerical study of the modulation of isotropic turbulence by suspended particles. *Journal of Fluid Mechanics*, 379:105–143. 14, 126

Syamlal, M., Rogers, W., and O'Brien, T. J. (1993). MFIX Documentation: Theory Guide. Technical report, National Energy Technology Laboratory, Department of Energy. 7, 13, 27, 46, 78, 79, 127, 138, 140, 145, 205, 218

Tabaczynski, R. (2001). Future Trends in Fuel Injection Systems and Their Control. In *Proceedings of the Fourteenth Annual Conference on Liquid Atomization and Spray Systems*, page 1. ILASS Americas. 14

Taneda, S. (1956). Experimental investigation of the wakes behind cylinders and plates at low Reynolds numbers. *Journal of the Physical Society of Japan*, 11(3):302–307. 194

Tang, Y., Lau, Y., Deen, N., Peters, E., and Kuipers, J. (2016). Direct numerical simulations and experiments of a pseudo-2D gas-fluidized bed. *Chemical Engineering Science*, 143:166–180. 188, 248

Tavassoli, H., Kriebitzsch, S., van der Hoef, M., Peters, E., and Kuipers, J. (2013). Direct numerical simulation of particulate flow with heat transfer. *International Journal of Multiphase Flow*, 57:29–37. xv, 15, 48, 49, 63, 66, 67, 84, 128, 221

Taylor, T. D. (1963a). Heat transfer from single spheres in a low Reynolds number slip flow. *Physics of Fluids*, 6(7):987–992. 9, 226, 227, 230

Taylor, T. D. (1963b). Mass transfer from single spheres in Stokes flow with surface reactions. *International Journal of Heat and Mass Transfer*, 6(11):993–994. 9, 220, 222, 224

Ten Cate, A., Nieuwstad, C., Derksen, J., and Van den Akker, H. (2002). Particle imaging velocimetry experiments and lattice-Boltzmann simulations on a single sphere settling under gravity. *Physics of Fluids*, 14(11):4012–4025. 188

Tenneti, S. (2013). *Momentum, energy and scalar transport in polydisperse gas-solid flows using particle-resolved direct numerical simulations*. PhD thesis, Iowa State University. 7, 15, 16, 55, 57, 74, 80, 90, 91, 96, 115, 163

Tenneti, S., Garg, R., Hrenya, C. M., Fox, R. O., and Subramaniam, S. (2010). Direct numerical simulation of gas-solid suspensions at moderate Reynolds number: Quantifying the coupling between hydrodynamic forces and particle velocity fluctuations. *Powder Technology*, 203:57–69. 7, 15, 16, 30, 55, 90, 130, 131, 132, 133, 135, 165, 249

Tenneti, S., Garg, R., and Subramaniam, S. (2011). Drag law for monodisperse gas-golid systems using particle-resolved direct numerical simulation of flow past fixed assembiles of spheres. *International Journal of Multiphase Flow*, 37(9):1072–1092. 7, 14, 15, 16, 17, 29, 30, 35, 36, 38, 39, 44, 48, 55, 57, 66, 84, 90, 91, 130, 131, 132, 163, 165, 168, 172, 173, 174, 231, 241

Tenneti, S. and Subramaniam, S. (2014). Particle-resolved direct numerical simulation for gas-solid flow model development. *Annual Review of Fluid Mechanics*, 46:199–230. 6, 13, 15, 51, 55, 90, 128, 129, 131, 137, 164, 165, 168

Tenneti, S., Sun, B., Garg, R., and Subramaniam, S. (2013). Role of fluid heating in dense gas-solid flow as revealed by particle-resolved direct numerical simulation. *International Journal of Heat and Mass Transfer*, 58:471–479. 17, 26, 49, 51, 52, 53, 55, 57, 58, 59, 60, 64, 73, 77, 84, 85, 87, 88, 90, 91, 128, 129, 130, 131, 132, 133, 135, 163, 168, 209, 231

Tsai, R. Y. (1987). A versatile camera calibration technique for high-accuracy 3D machine vision metrology using off-the-shelf TV cameras and lenses. *Robotics and Automation, IEEE Journal of*, 3(4):323–344. 191

Tsuji, T., Narutomi, R., Yokomine, T., Ebara, S., and Shimizu, A. (2003). Unsteady three-dimensional simulation of interactions between flow and two particles. *International journal of multiphase flow*, 29(9):1431–1450. 189

Tsuji, Y., Morikawa, Y., and Terashima, K. (1982). Fluid-dynamic interaction between two spheres. *International Journal of Multiphase Flow*, 8(1):71–82. 189

Tsynkov, S. (1998). Numerical solution of problems on unbounded domains. A review. *Applied Numerical Mathematics*, 27:465–532. 166

Tyagi, M. and Acharya, S. (2005). Large eddy simulations of flow and heat transfer in rotating ribbed duct flows. *Journal of Heat Transfer*, 127:486–498. 51, 87

Uhlmann, M. (2005). An immersed boundary method with direct forcing for the simulation of particulate flows. *Journal of Computational Physics*, 209:448–476. 14

Van Cruyningen, I., Lozano, A., and Hanson, R. K. (1990). Quantitative imaging of concentration by planar laser-induced fluorescence. *Experiments in Fluids*, 10(1):41–49. 84

Van der Hoef, M. A., Beetstra, R., and Kuipers, J. A. M. (2005). Lattice-Boltzmann simulations of low-Reynolds-number flow past mono- and bidisperse arrays of sphere: results for the permeability and drag force. *Journal of Fluid Mechanics*, 528:233–254. 15, 29, 48, 84

Vegendla, S. P., Heynderickx, G., and Marin, G. (2009). Probability density function (PDF) simulation of turbulent reactive gas-solid flow in a riser. *Chemical Engineering Science*, 32(3):492–500. 8, 147, 148, 161, 162

Wakao, N. and Kaguei, S. (1982). *Heat and mass transfer in packed beds*, volume 1 of *Topics in chemical engineering*. Gordon and Breach science. 7, 11, 28, 47, 48, 49, 83, 164, 188

Wakao, N., Kaguei, S., and Funazkri, T. (1979). Effect of fluid dispersion coefficients on particle-to-fluid heat transfer coefficients in packed beds. *Chemical Engineering Science*, 34:325–336. 12, 83

Wakao, N., Tanisho, S., and Shiozawa, B. (1977). Thermal response of packed beds at low Reynolds numbers. *Heat Transfer - Japanese Research*, 6(4):56 – 60. 7, 11, 47, 84

Wall, T. F. (2007). Combustion processes for carbon capture. *Proceedings of the Combustion Institute*, 31(1):31–47. 27

Whitaker, S. (1999). *The Method of Volume Averaging*. Springer Science & Business Media. 13, 81

White, B. L. and Nepf, H. M. (2003). Scalar transport in random cylinder arrays at moderate Reynolds number. *Journal of Fluid Mechanics*, 487:43–79. 82

Williams, P. (1993). CCM continuity constraint method : A finite-element computational fluid dynamics algorithm for incompressible Navier-Stokes fluid flows. Technical Report ORNL/TM-12389, Oak Ridge National Laboratory ORNL/TM-12389. 176

Wright, M., Brown, R. C., and Boateng, A. A. (2008). Distributed processing of biomass to biooil for subsequent production of Fischer-Tropsch liquids. *Biofuels, Bioproducts and Biorefining*, 2 (3):229–238. 2

Xu, J. and Pope, S. B. (1999). Assessment of numerical accuracy of PDF Monte Carlo methods for turbulent reacting flows. *Journal of Computational Physics*, 152(1):192–230. 62

Xu, Y. and Subramaniam, S. (2010). Effect of particle clusters on carrier flow turbulence: a direct numerical simulation study. *Flow, Turbulence and Combustion*, 85:735–761. 41, 50, 87

Xue, Q., Dalluge, D., Heindel, T. J., Fox, R. O., and Brown, R. C. (2012). Experimental validation and CFD modeling study of biomass fast pyrolysis in fluidized-bed reactors. *Fuel*, 97:757–769. x, 4, 74, 206

Xue, Q., Heindel, T. J., and Fox, R. (2011). A CFD model for biomass fast pyrolysis in fluidized-bed reactors. *Chemical Engineering Science*, 66(11):2440–2452. x, 4, 74, 206, 214

Yagi, S., Kunii, D., and Wakao, N. (1960). Studies on axial effective thermal conductivities in packed beds. *AIChE Journal*, 6(4):543–546. 81

Yi, C.-K., Jo, S.-H., Seo, Y., Lee, J.-B., and Ryu, C.-K. (2007). Continuous operation of the potassium-based dry sorbent CO_2 capture process with two fluidized-bed reactors. *International Journal of Greenhouse Gas Control*, 1 (1):31–36. x, 1, 27, 46, 74, 78

Yin, X. and Sundaresan, S. (2009). Drag law for bidisperse gas-solid suspensions containing equally sized spheres. *Industrial & Engineering Chemistry Research*, 48:227–241. 7, 15, 29, 48, 84

Yoon, D.-H. and Yang, K.-S. (2007). Flow-induced forces on two nearby spheres. *Physics of Fluids*, 19(9):098103. 189

Yoon, D.-H. and Yang, K.-S. (2009). Characterization of flow pattern past two spheres in proximity. *Physics of Fluids*, 21(7):073603. 189

Yu, Z., Shao, X., and Wachs, A. (2006). A fictitious domain method for particulate flows with heat transfer. *Journal of Computational Physics*, 217:424–452. 15, 48, 84, 221

Yusof, J. M. (1996). *Interaction of massive particles with turbulence*. PhD thesis, Cornell University. 14, 57

Zeng, L., Balachandar, S., and Fischer, P. (2005). Wall-induced forces on a rigid sphere at finite Reynolds number. *Journal of Fluid Mechanics*, 536:1–25. 245

Zhang, N., Zheng, Z., and Eckels, S. (2008). Study of heat-transfer on the surface of a circular cylinder in flow using an immersed-boundary method. *International Journal of Heat and Fluid Flow*, 29(6):1558–1566. 221, 232

Zhou, Z. Y., Kuang, S. B., Chu, K. W., and Yu, A. B. (2010). Discrete particle simulation of particle–fluid flow: model formulations and their applicability. *Journal of Fluid Mechanics*, 661:482–510. 127

Zhu, C., Liang, S., and Fan, L. S. (1994). Particle wake effects on the drag force of an interactive particle. *International Journal of Multiphase Flow*, 20(1):117–129. 189

Zhu, M., Bray, K., Rumberg, O., and Rogg, B. (2000). PDF transport equations for two-phase reactive flows and sprays. *Combustion and flame*, 122(3):327–338. 5, 147